

Hybrid FRP-Lightweight Concrete Sandwich System for Engineering Structures

THÈSE N°4123 (2008)

PRÉSENTÉE LE 11 JUILLET 2008

À LA FACULTE ENVIRONNEMENT NATUREL, ARCHITECTURAL ET CONSTRUIT
LABORATOIRE DE CONSTRUCTION EN COMPOSITES
PROGRAMME DOCTORAL EN STRUCTURES

ÉCOLE POLYTECHNIQUE FÉDÉRALE DE LAUSANNE

POUR L'OBTENTION DU GRADE DE DOCTEUR ÈS SCIENCES

PAR

Erika SCHAUMANN

Dipl.-Ing., Universität Karlsruhe, Allemagne
et de nationalité allemande

acceptée sur proposition du jury:

Dr E. Denarié, président du jury
Prof. T. Keller, directeur de thèse
Prof. E. Brühwiler, rapporteur
Prof. P. Hamelin, rapporteur
Prof. T. Vallée, rapporteur



ÉCOLE POLYTECHNIQUE
FÉDÉRALE DE LAUSANNE

Suisse
2008

Preface

Fiber-reinforced polymer (FRP) composites have been used for an increasing number of applications in bridge structures over recent years and their effectiveness for strengthening and repair purposes is already well established. More and more new bridges have been constructed as all-FRP or hybrid-FRP structures (FRP combined with traditional materials), primarily thanks to the advantageous properties of FRP composites, such as low self-weight, high strength, a high degree of free formability, and substantial resistance to corrosion and fatigue. The use of FRP bridge decks for rapid deck replacement with minimum traffic interference or new constructions are particularly promising applications, as demonstrated by the first generation of all-FRP bridge decks in the USA. However, this first generation of mainly pultruded bridge decks has also highlighted certain technical weaknesses, in addition to high costs, which have hindered their widespread application. One way of overcoming these drawbacks is the implementation of hybrid-FRP construction, that is, the use of FRP composites in combination with traditional materials, especially concrete.

This thesis presents an innovative concept for a lightweight hybrid-FRP bridge deck. The sandwich construction consists of three layers: an FRP sheet with T-upstands for the tensile skin, lightweight concrete for the core and a thin layer of ultra high performance reinforced concrete as a compression skin. The thesis evaluates the feasibility of this concept and then focuses on the shear behavior of the lightweight concrete core. A novel and original shear model is proposed, which takes into account the fracture behavior of the brittle material.

This research was funded by the New Road Construction Concept (NR2C) project of the 6th European Framework Program (Grant OFES No. 03.0318). I also wish to acknowledge the support of Fiberline Composites A/S, Denmark; Sika AG, Switzerland; Liapor AG, Switzerland; and Prebeton SA, Switzerland, for their support of this project.

Prof. Dr Thomas Keller

Director CCLab and thesis director

Summary

Hybrid slab systems combining fiber-reinforced polymer (FRP) composites with concrete are promising load-bearing structures, and an increasing number of applications has demonstrated their high potential in terms of structural performance and durability. Hybrid slabs are currently manufactured mainly on site however, which limits their economic advantages. The aims of this research are to develop a novel concept for a lightweight hybrid FRP-concrete sandwich slab system, which can be prefabricated and easily installed on site, and provide a corresponding engineering-adapted design method.

The proposed system uses three layers of different materials: an FRP sheet with T-upstands for the bottom skin, which also serves as formwork, lightweight concrete (LC) for the core material and ultra-high performance fiber-reinforced concrete (UHPFRC) for the top skin. No additional shear reinforcements are used, resulting in a simple and cost-effective slab manufacturing process.

Analytical and experimental investigations on the proposed system indicate that one of the governing failure mechanisms is shear failure of the LC core. A fracture mechanics-based model to predict the shear resistance of the hybrid sandwich slab is presented. To verify the modeling, experiments were performed on twelve hybrid beams comprising two different types of LC materials for the core: sand lightweight aggregate concrete (SLWAC) and all lightweight aggregate concrete (ALWAC). The proposed model demonstrates good agreement with experimental results and highlights the importance of considering not only the LC static strength, but also fracture mechanics properties such as characteristic length.

Furthermore, a continuous direct load transmission model is developed to model the behavior of the sandwich slab with loads next to the support. The model consists of a diagonal bottle-shaped strut with an infinite number of transverse ties and is based on the principles of strut-and-tie models for direct load transmission. The statically indeterminate system allows the stress redistribution resulting from post-peak material softening after concrete cracking to be taken into account. This leads to an accurate modeling of the varying experimental responses of eight hybrid short-span beams. Again, the considerable influence of LC brittleness on load-bearing behavior is demonstrated, something which is not taken into consideration in classic strut-and-tie models.

In a final step, design examples demonstrate the feasibility of the hybrid FRP-concrete sandwich slab and illustrate an appropriate selection of material properties in accordance with the proposed design method.

Keywords: Bridge deck, Fracture mechanics, FRP, Hybrid, Lightweight concrete, Shear strength prediction, Structural analysis, Slabs.

Résumé

Les systèmes de dalles hybrides combinant les matériaux composites (FRP) avec du béton sont prometteurs; grâce à leur potentiel en terme de performances structurelles et de durabilité, ils sont de plus en plus utilisés dans les structures porteuses en génie civil. Jusqu'à présent, ce type de dalles était fabriqué sur site, ce qui limite leurs avantages économiques. Les objectifs de cette recherche sont le développement d'un nouveau concept pour une dalle hybride légère, facilement préfabriquable ainsi qu'une proposition de dimensionnement adaptée aux besoins de l'ingénieur.

Le système proposé est composé de trois couches: un profilé en FRP avec des sections T dans la zone inférieure servant aussi de coffrage, du béton léger (LC) pour le noyau et du béton fibré ultra haute performance pour la couche supérieure. Aucune armature de cisaillement n'est utilisée pour garantir un procédé de fabrication simple et économique.

Des considérations analytiques et des résultats expérimentaux du système proposé montrent que la rupture est due au cisaillement du noyau en béton léger. Un modèle basé sur la mécanique de rupture est développé pour prédire sa résistance au cisaillement. Pour confirmer le modèle, douze poutres ont été testées avec deux types de béton léger: du LC avec du sable naturel (SLWAC) et du LC composé exclusivement d'agrégats légers artificiels (ALWAC). Le modèle proposé prédit les résultats expérimentaux de manière satisfaisante et montre l'importance de considérer non seulement les résistances et densité du béton léger mais aussi les caractéristiques mécaniques de ruptures, notamment sa longueur caractéristique.

En plus, un modèle continu qui représente la transmission des charges dans la dalle sandwich près de l'appui a aussi été développé. Ce modèle est basé sur le principe des treillis et se compose d'une bielle en compression archée avec un nombre infini de barres transversales en traction. Ce système statiquement indéterminé permet de tenir compte de la redistribution des contraintes qui est le résultat de l'adoucissement du LC après avoir atteint sa résistance à la traction.

Les différents résultats expérimentaux sur huit poutres de courte portée ont pu être modélisés avec une précision suffisante. Encore une fois, l'influence considérable de la fragilité du béton léger sur le comportement a été démontrée; jusqu'à présent, cet effet n'est pas considéré dans les modèles classiques de treillis.

Dans une dernière étape, des exemples de dimensionnement montrent la faisabilité de la dalle hybride FRP-béton ou, en inversant le problème du dimensionnement, permet de déterminer les propriétés qu'un béton léger devrait avoir pour être appropriée à la conception proposée.

Mots clefs: Béton léger (LC), Cisaillement, Dalles hybrides, Mécanique de rupture, Matériaux composites (FRP), Tablier de pont.

Zusammenfassung

Hybride Plattenelemente aus glasfaserverstärkten Kunststoffen (GFK) und Beton bilden vielversprechende Tragstrukturen, deren hohe Tragfähigkeit und Dauerfestigkeit an zahlreichen Anwendungen gezeigt wurden. Momentan werden sie überwiegend auf der Baustelle hergestellt, was ihre Wirtschaftlichkeit einschränkt. Das Ziel dieser Arbeit ist die Entwicklung eines Konzeptes für leichte hybride Platten, die als Fertigteile produziert und dann schnell auf der Baustelle montiert werden können. Gleichzeitig soll ein Designkonzept erarbeitet werden, das eine breite Anwendbarkeit des Systems ermöglicht.

Eine hybride Sandwichplatte wird vorgestellt, die aus den folgenden drei Materialschichten besteht: Einem GFK-Element mit T-Profilen, welches unterseitig als Bewehrung und als verlorene Schalung dient, einem Kern aus Leichtbeton (LB) und einer oberen Schicht aus Ultra-Hochleistungs-Faserbeton. Auf die Schubbewehrung in der Platte wird verzichtet, um eine möglichst einfache und kostengünstige Herstellung zu garantieren.

Analytische und experimentelle Untersuchungen an den Sandwichplatten liessen als Hauptversagenskriterium Schubbruch im Leichtbetonkern erkennen. Ein bruchmechanisches Modell zur Bestimmung der Plattenschubfestigkeit wird vorgestellt. Um dieses zu überprüfen, wurden Versuche an zwölf hybriden Elementen mit zwei verschiedenen Leichtbetontypen verschiedener Sprödigkeiten durchgeführt: LB mit Natursand (SLWAC) und LB mit Leichtzuschlägen ohne Natursand (ALWAC). Die Berücksichtigung bruchmechanischer Kennwerte, wie z.B. der charakteristischen Länge des LBs, führt zu einer guten Übereinstimmung der Modellierung mit den experimentellen Ergebnissen.

Zusätzlich wird ein Modell entwickelt, das den direkten Lastabtrag der Platten in Auflagernähe simuliert. Es basiert auf der Annahme von klassischen Fachwerkmodellen und besteht aus einem gebogenen Druckglied mit quer laufenden Zuggliedern. Durch die statische Unbestimmtheit des Systems können Lastumverteilungen in den Zuggliedern und somit das Entfestigungsverhalten bei Überschreiten der Zugfestigkeit berücksichtigt werden. Mit Hilfe dieses Modells werden die Unterschiede zwischen acht zusätzlichen Experimenten simuliert. Die Ergebnisse verdeutlichen, dass die LB Sprödigkeit, die in Fachwerkmodellen nicht berücksichtigt wird, einen grossen Einfluss auf das Riss- und Tragverhalten des Systems hat.

Zum Abschluss der Arbeit werden mögliche Einsatzgebiete der hybriden Sandwichplatten aufgezeigt. Das erarbeitete Designkonzept stellt dem Ingenieur Richtlinien zur Verfügung, mit deren Hilfe für unterschiedliche Anwendungen ein Leichtbetontyp mit adäquaten Materialeigenschaften gewählt werden kann.

Stichwörter: Brückenplatte, Bruchmechanik, glasfaserverstärkte Kunststoffe (GFK), Hybrid, Leichtbeton (LB), Schubfestigkeit, Strukturanalyse, Plattenelemente.

Acknowledgements

Over the past four years, I have received support and encouragement from many different people and here I would like to acknowledge those who have made a particularly important contribution.

First, I would like to express gratitude to my thesis director Prof. Thomas Keller for giving me the opportunity to work on this research project, for his support and guidance and our fruitful discussions.

I would like to acknowledge the support of Fiberline Composites A/S, Denmark, supplier of the GFRP Plank elements; Sika AG, Zurich, Switzerland, supplier of the epoxy adhesive; Liapor, Switzerland, supplier of the LC concrete; Holcim BF+P SA Morges, Switzerland, for the fabrication of the S1 beam series and Prebeton SA, Avenches, Switzerland, for the fabrication of beam series S2. This research was funded within the framework of the New Road Construction Concept (NR2C) project of the 6th European Framework Program.

I wish to express my thanks to the thesis defense committee for the time and effort they devoted to reading and evaluating the thesis: Prof. Eugen Brühwiler, MCS-EPFL, Prof. Patrice Hamelin, Université de Lyon 1, France; Prof. Till Vallée, Berner Fachhochschule; and Dr Emanuel Denarié, MCS-EPFL, president of the jury.

A large part of the time dedicated to the preparation of the experimental program was spent in the laboratory. I would like to thank the Holcim team for their help in planning and manufacturing the S1 beam series, especially Dr Jean-Paul Jaccoud and Roger-Albert Mages; Daniel Meyer from Liapor, Switzerland, for his support and assistance in producing very lightweight LC compositions; and Arno Fasel of Prebeton SA, Avenches, Switzerland for manufacturing the S2 beam series.

The time spent on specimen and setup preparation went by quickly thanks to the great assistance provided by Hansjakob Reist, and the guidance and help in preparing the specimens, experimental setups and measuring devices from Sylvain Demierre, Roland Gysler, Gilles Guignet, François Perrin, Patrice Gallay and Laurent Gastaldo.

The research on the hybrid slab system was carried out with the NR2C WP3 working group. I want to express my thanks to our project manager and colleague Brigitte Mahut, to Jean-Marc Tanis, François Toutlemonde, Bruno Godart, Pierre Rossi, Jean-François Carron, Robert Leroy, Jacques Resplendino for their collaboration and helpful remarks. I am most grateful to Dr Holger Basche of Hilti, Liechtenstein, who helped me to understand the LC shear failure mechanism.

I would like to thank my colleagues at CCLab for their help and friendship and for creating an international atmosphere that broadened my understanding of other cultures. Special thanks to Dr Julia de Castro with whom I shared the office and spent a wonderful time

during the first years; Martin Schollmayer, Dr Herbert Gürtler, Dr Florian Riebel, Nina Soddemann, Dr Anastasios Vasilopoulos, Juan Murcia, and to the 'Chinese connection' Ye Zhang, Yu Bai, Ping Zhou, and Dr Aixi Zhou. Not forgetting all the other colleagues and friends from I-Bois, CDM, IS-Beton and MCS - my 'EPFL friends, lunch / coffee partners and fellow sufferers'.

Many thanks to those who helped prepare the thesis document: Prof. Thomas Keller for his careful reading, valuable remarks and interesting suggestions; Prof. Till Vallé for giving encouragement, and helpful advice for the experimental and modeling part; Margaret Howett for converting my German English into proper English and finally Marlène Sommer and Magda Schauenberg for their administrative assistance.

Lastly, I wish to express my sincerest thanks to my parents, Doris and Prof. Gunter Schaumann, as well as friends from all over Europe, for their unconditional support and encouragement, especially my brother Arno Schaumann and his family, Dr Steffi Augter, Daniel Knapp, and Dr Bernhard Stamm for listening to my complaints and worries.

Contents

1	Introduction	1
1.1	Context and motivation	1
1.2	Objectives	1
1.3	Concept of hybrid FRP-concrete slab system	2
1.4	Methodology	4
1.5	Thesis organization	4
2	State of the art	7
2.1	Fiber-reinforced polymers (FRP)	7
2.1.1	Definitions	7
2.1.2	FRP material properties	8
2.1.3	Connection technology	10
2.1.4	Use of FRP in civil engineering structures	11
2.2	Lightweight concrete (LC)	19
2.2.1	Definitions	19
2.2.2	LC material properties	20
2.2.3	LC fracture mechanical properties	24
2.3	Shear capacity of concrete members without shear reinforcement	27
2.3.1	Definitions	27
2.3.2	General remarks concerning modeling of shear failure	28
2.3.3	Shear failure models for members without shear reinforcement	31
2.4	Summary	35
3	Experimental investigation	39
3.1	Overview	39
3.2	Materials used in hybrid sandwich system	40
3.2.1	Material properties of LC cores	40
3.2.2	Material properties of face layer materials	43
3.3	Experiments on hybrid beams	45
3.3.1	Beam description	45

3.3.2	Experimental setup and instrumentation	46
3.3.3	Experimental results - S1 series	48
3.3.4	Experimental results - S2 series	55
3.3.5	Discussion	59
3.3.6	Conclusions	62
3.4	Experiments on direct load transmission	64
3.4.1	Experimental specimen, setup and procedure	64
3.4.2	Experimental results	65
3.4.3	Discussion	74
3.4.4	Conclusions	77
3.5	Summary	78
4	Analysis of experiments and modeling	81
4.1	Failure modes and model concept	81
4.2	Modeling of LC softening behavior	82
4.3	Modeling of beams within the span	84
4.3.1	Modeling of cracking load and load-deflection response	84
4.3.2	Prediction of ultimate loads according to Eurocode 2	86
4.3.3	Prediction of ultimate loads using a fracture mechanics-based model	88
4.3.4	Conclusions	90
4.4	Modeling of direct load transmission region	92
4.4.1	Strut-and-tie models	92
4.4.2	Novel continuous direct load transmission model	94
4.4.3	Results and discussion	102
4.4.4	Conclusions	105
4.5	Summary	105
5	Application of hybrid slab system	107
5.1	Bridge applications	107
5.1.1	Design concept for a hybrid FRP-concrete sandwich bridge deck	107
5.1.2	Design example of a 400-mm-deep, 6-m-wide bridge slab with 2 m girder spacing	110
5.1.3	Design example of a 12-m-wide and 400-mm-deep bridge slab with 6-m girder spacing	117
5.1.4	Optimization study to obtain ductile failure	125
5.2	Building applications	129
5.2.1	Design example of a hybrid FRP-concrete slab in buildings	129

5.3	Summary	132
5.3.1	Bridge applications	132
5.3.2	Building applications	134
6	Conclusions and future research	135
6.1	Conclusions	135
6.1.1	Concept of hybrid FRP-concrete sandwich slab	135
6.1.2	Load-bearing behavior	136
6.1.3	Modeling of load-bearing behavior	137
6.1.4	Application and design method	138
6.2	Contribution to state of the art	138
6.3	Proposal for future research	139
6.3.1	Validation of shear strength prediction and design method	140
6.3.2	Development of a ductile failure mechanism	140
6.3.3	Structural details of slab concept requiring further study	141
6.3.4	Extension of continuous direct load transmission model	141
7	Notation	143
	Bibliography	149
	Curriculum Vitæ	159
A	Direct load transfer model	161
A.1	Description of routine	161
A.2	Influence of strut compression on results	165
B	Materials (on DVD)	169
B.1	Introduction	169
B.2	Experiments on LC core materials	170
B.2.1	SLWAC compositions: LC900 and LC1300	171
B.2.2	ALWAC compositions: LC1000 and LC1000A	175
B.2.3	ALWAC compositions: LC1000P-1/2	177
B.2.4	ALWAC composition: LC1200P	178
B.3	Face layer materials	180
B.3.1	Top layer: normal concrete (NC)	180
B.3.2	Bottom layer: glass fiber-reinforced polymer (GFRP) profile	181
B.3.3	Epoxy resin for GFRP-LC interface	182

C	Long-span beams (on DVD)	183
C.1	Introduction	183
C.1.1	Objectives	183
C.1.2	Experimental program	183
C.2	Experimental specimens	185
C.2.1	Dimensions	185
C.2.2	Manufacture	185
C.3	Experimental procedure	190
C.3.1	Test setup and loading equipment	190
C.3.2	Instrumentation	191
C.4	Results of S1 series	198
C.4.1	Beam 900-1	198
C.4.2	Beam 900-2	212
C.4.3	Beam 900E-1	228
C.4.4	Beam 900E-2	240
C.4.5	Beam 1300-1	253
C.4.6	Beam 1300-2	267
C.4.7	Beam 1300E-1	283
C.4.8	Beam 1300E-2	295
C.5	Results of S2 series	309
C.5.1	Beam 1000	309
C.5.2	Beam 1000E	326
C.5.3	Beam 1000A	340
C.5.4	Beam 1000EA	355
C.6	Summary of main results	370
D	Short-span beams (on DVD)	371
D.1	Introduction	371
D.1.1	Objectives	371
D.1.2	Experimental Program	371
D.2	Experimental procedure	372
D.2.1	Test setup and loading equipment	372
D.2.2	Instrumentation	372
D.3	Results of S3 series	375
D.3.1	Specimen 900Es-1	375
D.3.2	Specimen 900Es-2	382
D.3.3	Specimen 1300s-1	389

D.3.4	Specimen 1300s-2	397
D.3.5	Specimen 1300Es-1	405
D.3.6	Specimen 1300Es-2	412
D.3.7	Specimen 1000s	420
D.3.8	Specimen 1000Es	426
D.4	Summary of main results	434

1 Introduction

1.1 Context and motivation

Fiber-reinforced polymer (FRP) composites have found increased application in bridge structures over recent years. Applications for strengthening and repair are already well established. A growing number of new bridges are constructed as all-FRP or hybrid-FRP structures, in which FRPs are combined with traditional materials such as concrete. This is predominantly due to the advantageous properties of FRP composites, such as low self-weight, high strength, high degree of free formability, and substantial resistance to corrosion and fatigue. Particularly promising applications are FRP bridge decks for rapid deck replacement with minimum traffic interference or new constructions as demonstrated by the first generation of all-FRP bridge decks in the USA [Kel06]. They enable an increase in allowable live loads or the widening of existing bridges via replacement of heavy concrete decks. Furthermore, construction details can be designed much more simply than in the case of concrete decks. The waterproofing layer and associated complicated parapet detailing are not necessary. This first generation of mainly pultruded bridge decks also displays some technical weaknesses however, in addition to the high costs that hinder widespread application. The transverse span between the main girders is limited to approximately 3.0 m maximum (for pultruded decks), and as a result large overhangs are not possible and multi-girder systems are required, which are not economic for longer spans. Compared to concrete decks, a further important drawback is the low stiffness in the main girder direction, which considerably reduces the top chord capacity of the deck in the compositely acting deck-girder cross section [KG06b]. One way of overcoming these drawbacks is to switch from all-FRP to hybrid-FRP construction by using FRP composites together with traditional materials, particularly concrete, as several research projects have already demonstrated.

1.2 Objectives

The aim of this research was to develop a concept for a lightweight hybrid FRP-concrete slab for bridge and building applications. The prefabricated elements should enable easy on-site installation. The following specific objectives were defined:

- development of a concept for a lightweight hybrid FRP-concrete slab, primarily for bridge decks but which can also be used in building applications;
- investigation of deformation behavior, failure modes and influencing parameters;
- development of a model to predict load-bearing behavior;
- proposal of an engineering-oriented dimensioning method.

1.3 Concept of hybrid FRP-concrete slab system

The proposed hybrid bridge deck is primarily developed for application in bridges, while the same slab can be used for building requirements. The sandwich structure consists of three layers of different materials: FRP composites for the tension skin, lightweight concrete (LC) as core material and ultra-high performance fiber-reinforced concrete (UHPFRC) for the compression skin, as shown in Figure 1.1. The FRP layer, consisting of an FRP sheet with T-upstands, also serves as formwork, while the T-upstands should provide composite action through a mechanical interlocking between the basic FRP sheet and the LC core. The fibers in the 25-40-mm-deep UHPFRC layer are required to bear possible local bending moments in this layer due to concentrated wheel loads and the jointless application. A ductile, or at least pseudo-ductile, system behavior should be achieved by failure in the top concrete layer and crushing of the lightweight aggregates. The shear forces in the deck are transferred by the LC and not by the FRP webs, which are sensitive to buckling. No additional shear reinforcements (rebar or studs) are used, resulting in a simple and cost-effective slab manufacturing process. Although no hollow FRP sections are used, the deck is still lightweight due to an LC core density of approximately 1100 kg/m^3 . The target total deck weight is 50% of that of a normal concrete deck. The LC also provides effective thermal insulation for building applications.

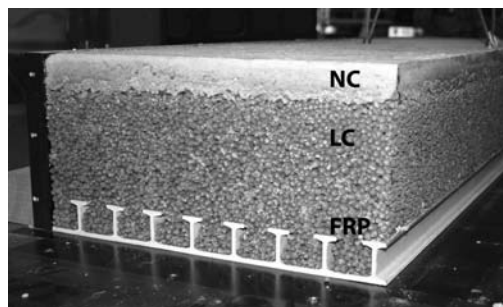


Figure 1.1: Cross section of the hybrid FRP-concrete slab.

The FRP layer together with the LC core is easily prefabricated in large elements (approximately 2.50 m x width of the bridge), while the bond between the LC and FRP skin is achieved either by pure mechanical interlocking through T-upstands integrated into the FRP skin, adhesive bonding or a combination of both. The elements are then transported to the site and rapidly installed on the main girders, see Figure 1.2. The joints between deck elements and between deck and main girders are adhesively bonded (see [KG05a]). Subsequently, the thin UHPFRC layer is jointlessly cast onto the LC core on site. In regions of negative bending moments, FRP reinforcement grids are incorporated into the UHPFRC layer. Since the deck is steel-free and the UHPFRC layer watertight, no waterproofing layer is required and the surfacing is applied directly onto the UHPFRC.

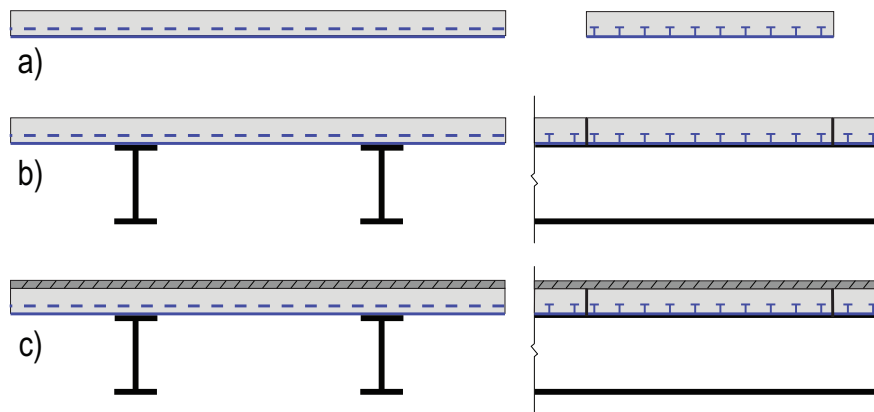


Figure 1.2: Composition and installation of hybrid bridge deck: (a) prefabricated FRP-LC panels; (b) FRP-LC panels bonded together and onto girders and (c) jointless UHPFRC casting.

Similarly to conventional reinforced concrete slabs, two different failure modes can be expected for the hybrid FRP-concrete system: flexural failure, which comprises either crushing of the compression zone or tensile failure of the reinforcement, or shear failure in the core. Shear failure can occur in two different zones: in the span or at the supports, where there is direct load transmission through a compression diagonal. It has been established that the shear span-to-depth ratio, a/d , is an indicator of the dominant failure mode, where a is the distance from the load axis to the support axis, and d the effective depth of the slab. Typically, the region of direct load transmission comprises a/d ratios of up to approximately 2.5, while for higher ratios the beam mechanism predominates.

The flexural failure mode of the hybrid FRP-concrete system is determined by the face layer strengths and can be easily predicted, whereas the shear failure of the hybrid sandwich with LC core is less easy to predict and will be investigated in detail in this research.

In comparison to normal concrete of similar strength, LC is characterized by a more brittle material behavior primarily due to a reduced aggregate interlock, which is caused by crack propagation through the porous lightweight aggregates. Two principal types of LC exist and will be considered in the validation of the concept: sand lightweight aggregate concrete (SLWAC) and all lightweight aggregate concrete (ALWAC), exhibiting considerable differences in fracture mechanics properties, [Fau03]. The dense sand aggregates of the SLWAC prevent crack propagation more effectively than, for instance, the porous expanded glass aggregates of an ALWAC mixture. Hence the concrete brittleness, characterized by the characteristic length of the LC, is usually higher for the latter than the former.

Shear resistance predictions according to standard codes, i.e. [ACI05], [Com04], [SIA03a], do not properly consider the different fracture behaviors of SLWAC and ALWAC concretes and are therefore not always reliable. Predictions need to be improved by introducing the characteristic length into the scale coefficient of the equation for example, or the development of a new shear model that takes concrete brittleness into account.

1.4 Methodology

The methodology used to attain the objectives is as follows:

- conceptual development of a new hybrid FRP-concrete sandwich slab;
- state of the art concerning the materials used and relevant design methods;
- analytical and experimental investigations of the load-bearing behavior of hybrid long-span beams ($a/d=6$) with different LC cores and FRP-LC interfaces;
- analytical and experimental investigations of direct load transmission in hybrid short-span beams ($a/d=1.6$) with different LC cores and FRP-LC interfaces;
- development of fracture-based models to predict the failure behavior of long-span and short-span beams;
- derivation of a design concept for the new hybrid FRP-concrete sandwich slab for bridge and building application;
- conclusions and future prospects.

1.5 Thesis organization

The research presented in this thesis is divided into four main sections: the state-of-the-art review is followed by the experimental investigation of the hybrid FRP-concrete system and

the analysis and modeling of the system. Based on this, a design concept is developed. The general organization of the thesis is shown in Figure 1.3, while in the following a summary of the chapter contents is given.

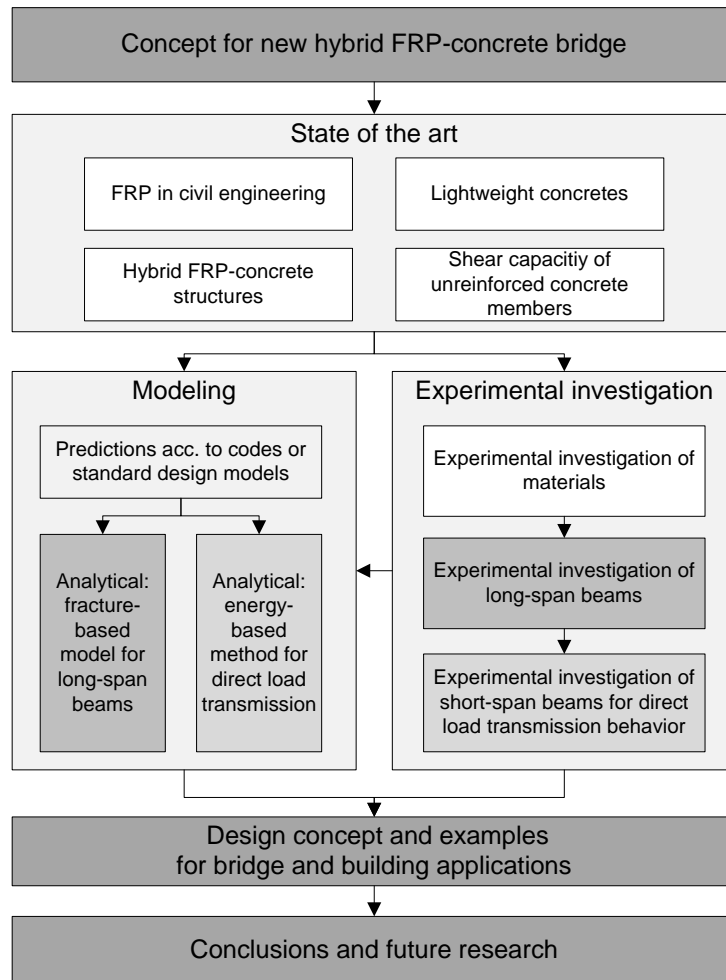


Figure 1.3: Thesis organization and methodology.

Chapter 1: The concept of the hybrid FRP-concrete bridge deck, objectives of the research and thesis methodology are introduced.

Chapter 2: The state of the art presents the general material properties of the materials used, FRP and LC. A summary of existing hybrid FRP-concrete structures is presented. Concluding remarks provide the justification for researching the proposed hybrid bridge slab. A review of existing shear strength prediction methods for concrete beams and slabs without shear reinforcements follows.

Chapter 3: Experimental investigations of LC properties, long-span hybrid beams and direct load transmission are presented.

Chapter 4: A comparison of experimental results with predicted values according to existing models is made. Furthermore, the development of a new fracture mechanics-based model for long-span beams and a continuous shear model for direct load transmission is presented.

Chapter 5: A design concept based on experimental results and modeling is elaborated and studied for several bridge design examples and building requirements.

Chapter 6: The conclusions and major findings of the research are summarized. Suggestions for future research areas are also formulated.

2 State of the art

The proposed new hybrid bridge slab is based on a meticulous analysis of the state of the art in the relevant field. First, the materials involved are discussed and analyzed: FRP composites for the tension skin, lightweight concrete (LC) as core material and ultra-high performance fiber-reinforced concrete (UHPFRC) for the compression skin. Since a first approach beam design showed that the UHPFRC is not the governing material in the system, the state-of-the-art review concentrates on the use of FRP composites in all-FRP and hybrid-FRP engineering structures and lightweight concretes for structural application. The shear forces in the hybrid bridge slab are transferred by the LC and not by the FRP webs, as is often the case in FRP-concrete systems. Hence, a survey of models that take the shear failure of concrete members without shear reinforcements into account is also provided.

2.1 Fiber-reinforced polymers (FRP)

2.1.1 Definitions

Fiber-reinforced polymers (FRPs) consist of load-bearing fibers embedded in a polymer matrix and the reason for using reinforced polymers is to obtain maximum advantage from the reinforcement fibers. The properties of FRPs can be engineered over a wide range due to the large selection of fiber reinforcements, orientations, and polymer matrices.

The reinforcement fibers usually dominate the mechanical properties, especially the tensile strength and stiffness of the composite. The volume fraction of fibers determines dimensional stability and resistance to creep under load. In bridge construction, the three main fiber types used are glass, aramid and carbon fibers. The physical and mechanical material properties can vary significantly and are described in detail in [HH01], [Mur98], [Mur98], [YFZ⁺03].

Two types of polymer resins are used as matrices in FRPs: thermoplastics and thermosetting polymers. Thermoplastics melt when heated and solidify when cooled. In contrast thermosets cure permanently through irreversible cross-linking at elevated temperatures. Mainly thermosets are used for FRP structures today, and the most important of these are unsaturated polyester (UP) resins, epoxy (EP) resins, vinylester (VE) resins and phenolic resins. The polymer encapsulates the fiber in order to fix the fibers in

the desired direction, transfer the loads to the fibers and prevent buckling of the fibers. At the same time it seals the fiber surface and prevents moisture wicking along the fiber.

There are three types of composites, depending on the reinforcement fibers used, designated glass (GFRP), aramid (AFRP) and carbon (CFRP) fiber-reinforced polymers. Material properties greatly depend on fiber fraction, their orientation in the composite and manufacturing process. Typical GFRP profiles manufactured by pultrusion attain tensile strengths of between 200 and 400 MPa parallel to the longitudinal fibers of the profile, whereas the strength perpendicular to the longitudinal fibers ranges from 40 to 180 MPa, [Kel03]. Figure 2.1 illustrates some typical FRP profiles and an FRP bridge deck.

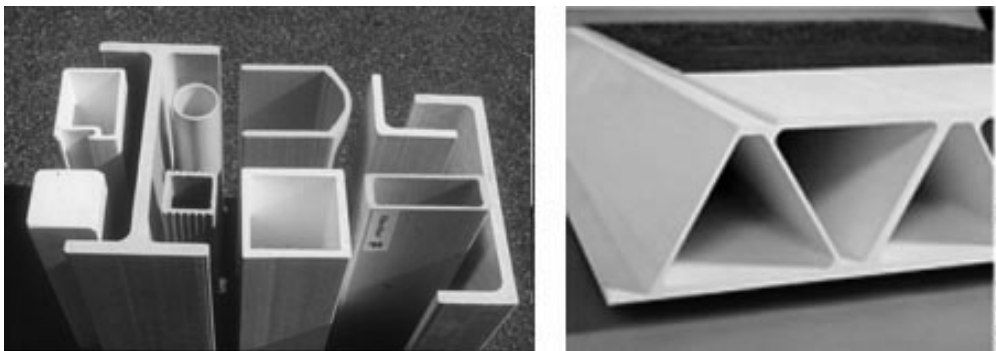


Figure 2.1: GFRP profiles and Asset GFRP deck from Fiberline, taken from [Kel03].

There are a number of techniques for manufacturing FRPs, all of which influence the mechanical properties of the final composite. A manual fabrication method tends to result in lower strength and stiffness values than the automated methods due to a greater degree of compaction in the latter [HH01]. Manufacturing methods can be divided into three groups: (1) the manual process, such as hand lay-up, spray-up; (2) the semi-automated process which includes compression molding and resin injection; (3) the automated process which includes pultrusion, filament winding and resin transfer molding.

2.1.2 FRP material properties

Physical and durability-related properties

FRPs can be optimally engineered to meet customer requirements. Different compositions lead to different properties and a wide range of desirable properties is achievable. The physical durability-related properties, such as density, electrical conductivity, resistance to UV light and temperature, and resistance to chemical effects are dependent on both the fibers and polymers. Nonetheless, some general remarks can be made concerning FRP composites. FRP materials have a high resistance to frost and de-icing salts, which can have a devastating

effect on inadequately protected steel reinforcement. However, glass fibers are sensitive to humidity and alkaline environments while aramid fibers, unsaturated polyester and vinyl ester are sensitive to UV light. Only carbon fibers are generally considered to be stable in most environmental conditions, for further details see also [Ano99], [Fib04], [HH01], [Mur98], [Pot97].

The thermal properties of FRPs vary with the form and relative quantities of their constituents. At the glass transition temperature (T_g) of the matrix, the properties of the FRP, such as strength and modulus of elasticity, decrease significantly. T_g is the temperature at which a polymer changes from hard and brittle to soft and pliable, and ranges from 80°C to approximately 160°C, depending on the polymer. At the more elevated decomposition temperature ($T_d \sim 300^\circ\text{C}$) polymers will decompose. However, temperature-related material properties differ under compression and tension. Under compression, the fibers in the FRP will start to buckle after the T_g of the resin is reached, due to the stiffness loss of the encapsulating polymer, and the FRP structure will consequently lose its structural load-bearing capacity, [BK07], [BVK08]. Elements loaded in pure tension generally retain their strength under high temperature however, since the tensile strength of the fibers is maintained. Following decomposition of the polymer matrix, the fibers can still bear tension forces if anchorage is provided. Consequently, the fire performance of FRPs greatly depends on the loading condition and the region exposed to the fire. Furthermore, one possible method to increase load-bearing behavior during fire exposure is liquid cooling of the FRP profiles, see also [KTH06], [KTZ06a], [KTZ06b], [KZT⁺05].

Mechanical properties

The range of FRP mechanical properties is depends to a great extent on the type of fibers used (glass, aramid or carbon); fiber volume fraction, fiber orientation (unidirectional, bidirectional aligned or randomly orientated) and manufacturing method (ranging from manual to fully automated) and quality control. A further influence on the material properties of the FRP can have the choice of the adequate polymer resin. Typical properties of FRPs for different compositions of fibers and resins are shown in Table 2.1. Additional information can be found in [sps04], [ASM02], [Fib04], [HH01], [Mur98], [YFZ⁺03].

Most fibers are insensitive to fatigue loading and the fatigue strength of FRPs is thus highly dependent on resin properties as well as on composite design, manufacturing process and loading direction. Failure often occurs progressively, starting with fiber debonding and resin cracking. Fatigue failure of FRPs can occur in compression as well as in tension, in contrast to metals which generally develop fatigue cracks only in tension [HH01], [KT04].

Table 2.1: Typical mechanical properties of FRP laminates, from [Ano99], [Kel03], [Unk03].

FRP type, fiber orientation	Type of resin	Tensile strength [MPa]	Tensile modulus [GPa]	Elongation [%]	Density [kg/dm ³]
CFRP (high strength), unidirectional	EP	2500	150	1.6 - 2.0	1,6
AFRP (low modulus), unidirectional	EP	2100	40	5.0 - 5.1	1.4
AFRP (high modulus), unidirectional	EP	2100	70	3.0 - 3.1	1.4
GFRP (E-glass), unidirectional	UP	1200	40	2.9 - 4.3	1.8
GFRP (E-glass), 0/90° symmetrical	UP	350	20	1.8	1.8
GFRP (E-glass), +45/-45° symmetrical	UP	280	15	2.0	1.8

Since the glass, carbon, and aramid fibers have practically zero creep compared to the polymer resin, creep properties are highly dependent on the fiber volume fraction and fiber orientation as well as resin properties and fiber types. Environmental conditions such as temperature and humidity also influence the creep behavior of the FRP, see also [HH01].

2.1.3 Connection technology

Connection FRP - FRP

The connection technology is of great importance in the design of FRP structural components due to the anisotropic non-homogeneous character of the material. The connection techniques that can be used for FRP profiles are bolting, adhesive bonding, a combination of these and also welding for thermoplastic resins, see also [ZK05].

The use of the bolting technique results in high stress concentrations at the holes since FRP materials behave linear elastically and no local plastic deformations are possible. These high stress concentrations combined with the anisotropy of the material lead in most cases to an overdesign of the components. An additional consideration is that holes required for the bolts often expose unprotected fibers to the environment in the region of stress concentration, further reducing the strength of the joint over time. In some cases however design requirements may demonstrate their usefulness, i.e. because the joints must be able to be disassembled.

In comparison to bolting, adhesive bonding is a more material-compatible connection method for FRP [KV05a],[KV05b]. Here the forces are introduced through the resin into the fibers. The adherends remain undamaged by holes but the joints must withstand peeling stresses caused by eccentric loading. Another disadvantage is the difficulty involved in inspection and quality control.

Connections between FRPs and conventional materials

The choice of the technique used to connect FRPs to conventional materials such as steel or concrete greatly depends on the objective of the connection. Three types can be distinguished: the application of FRP to existing and often deficient structures (generally concrete structures) for strengthening purposes; the connection of FRP components to conventional girders, such as FRP bridge slabs to concrete or steel girders; and the combination of materials in new hybrid structures, where concrete is applied directly onto FRP shapes to achieve composite action.

The connection technique most frequently used for strengthening deficient concrete structures is the adhesive bonding of FRP tensile sheets and strips to the existing and deficient concrete structure. FRP bridge decks are usually connected to conventional girders by mechanical fixing, adhesive bonding and hybrid joints, where shear studs are embedded in concrete pockets. The bonding connection ensures composite action between the girder and bridge deck. Research projects on new hybrid structures showed that the adhesive bonding technique is the most efficient way of achieving composite action between the FRP and concrete, [Gür04], [KG05a], [KG05b], [KG06a]. The epoxy is applied to the FRP and the fresh concrete is cast on the epoxy mortar before it has cured. Additional shear connectors are often added in order to increase the interface connection, see also [CHT99], [HHT03], [KAL04], [EHM⁺02].

2.1.4 Use of FRP in civil engineering structures

Strengthening

The aim of strengthening existing structures is to repair structural deterioration and/or to increase the load-bearing capacity of structures. In both cases, existing structures are reinforced using tensile elements. The first method used for strengthening concrete was the bonding of steel plates to the reinforced concrete structure, but in recent years the steel plates have been replaced by FRP plates or sheets. The use of FRPs provides the advantages of easy installation, the high strength-to-weight ratio and high corrosion resistance. The primary strengthening components used are strips, sheet elements, prestressing rods and

external cables. Figure 2.2 shows typical strengthening methods for slabs and beams used on the Duttweiler Bridge in Switzerland from [Kel03].



Figure 2.2: Duttweiler Bridge, Switzerland. Left: strengthening of deck slab with crossed CFRP strips, anchoring of transverse strips in cross-beam. Right: strengthening of cross-beam with strips and crossed L-shaped plates, taken from [Kel03].

FRP reinforcements such as strips, sheets and FRP shells are also used for the containment of concrete columns and walls subjected to seismic action. Improvements of up to tenfold in ductility factors can be realized through the use of FRP column wrapping.

The replacement of conventional concrete bridge decks with FRP composite bridge decks offers a viable solution for the rehabilitation of existing bridges. The benefits of FRP replacement decks are their low weight (increasing the live load capacity of the bridge structure), increased durability (highly resistant to corrosion and fatigue), high strength, rapid installation, lower or competitive life-cycle cost, and high quality manufacturing process under controlled environments. FRP decks weigh up to 80% less than cast-in-place reinforced concrete decks. Some examples of bridge decks will be presented below in the section All-composite new structures.

FRP cables and reinforcements for concrete structures

FRP cables are advantageously used in bridge engineering due to their high strength-to-weight ratio and corrosion resistance. Typical applications are suspension and stay cable bridges, pre-stressed tendons for concrete structures and external reinforcement for beams. Figure 2.3 shows the example of the external CFRP cable reinforcement of the Verdasio Bridge in Switzerland, [Kel03].

The high strength-to-weight ratio is favorable for stay cable bridges, since the maximum span of the bridge is limited by the dead weight of the cables. Using high strength steel, the theoretical limit of the span is approximately 5000 m, whereas the span can be doubled by using aramid cables, [HH01].

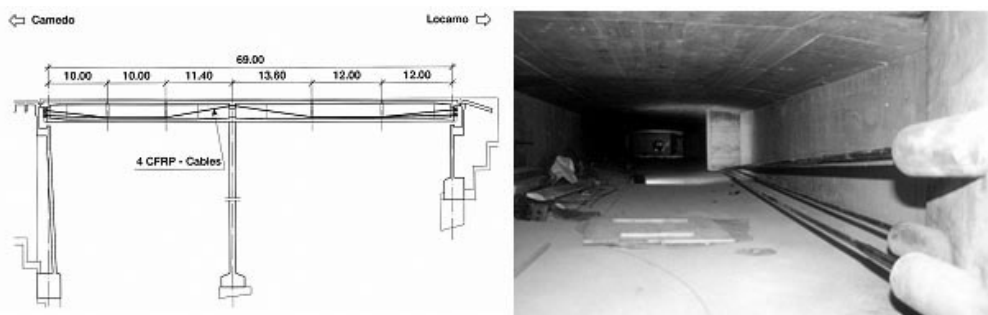


Figure 2.3: Verdasio Bridge, Switzerland repaired in 1998. Left: Longitudinal section of bridge showing carbon fiber cables in polygonal path. Right: External carbon fiber cable reinforcement, taken from [Kel03].

Another application of FRPs is as reinforcement in reinforced concretes. FRP reinforcements include textiles, rebars, internal tendons and short fibers. Apart from the high strength-to-weight ration, the advantages of using FRP reinforcement instead of steel are the high corrosion resistance and low electrical conductivity.

All-composite new structures

All-composite new structures, especially bridge superstructures, are constructed exclusively with FRP materials, while the abutments and piers are usually composed of traditional materials. Since the 1980s mainly pedestrian bridges with trusses consisting of pultruded profiles have been constructed. The pultruded shape connections were generally bolted. However, the Pontresina Bridge in Switzerland built in 1997 was the first pedestrian bridge with adhesively-bonded connections, [BK08], [Kel03]. The Pontresina footbridge and the all-composite cable-stayed footbridge in Kolding, Denmark (1997) are shown in Figure 2.4.



Figure 2.4: All-composite footbridges. Left: Pontresina footbridge in Switzerland, 1997. Right: Kolding footbridge in Denmark, 1997, both taken from [Kel03].

In parallel, pultruded multi-cell panels were developed, such as the modular advanced composite construction system (ACCS) used in footbridges in the UK, [HH01]. Hand-laminated U-shape girders were first incorporated in the Smith Road Bridge in Ohio, USA in 1997, [Kel03].

Furthermore, FRP bridge decks for rapid deck installation were developed, offering simpler construction than concrete decks; for example, the waterproofing layer and associated complicated parapet detailing were no longer necessary. Figure 2.5 shows three different types of FRP bridge deck systems: the pultruded multi-cellular slab *Duraspan* from *Martin Marietta Composites*, USA, the foam core sandwich panel from *Hardcore Composite, Inc.* of New Castle, Delaware, USA, and the honeycomb sandwich manufactured by *Kansas Structural Composites*. However, in addition to their high cost, these bridge decks also

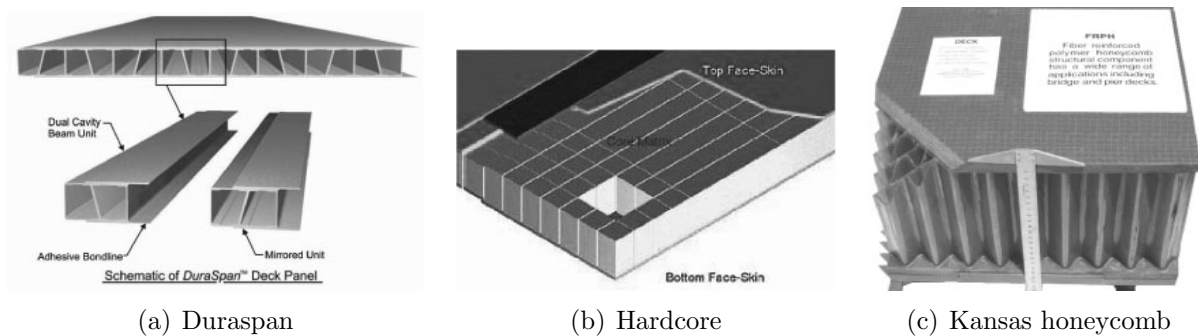


Figure 2.5: Different FRP bridge deck systems, taken from [Kel03].

exhibited some technical weaknesses that hindered their widespread application. For example, for pultruded decks the transverse span between main girders is limited to a maximum of ~ 3 m. Due to this constraint, large overhangs are not possible and multi-girder systems are required, which are not economical for longer spans. Compared with concrete decks, a further significant drawback is the low stiffness in the main girder direction, which considerably reduces the deck's top chord capacity in compositely acting deck-girder cross sections [KG06b]. Moreover, no satisfactory solutions have yet been found for the anchoring of crash barriers in all-FRP decks. One possibility for overcoming these drawbacks is the transition from all-FRP to hybrid-FRP construction by using FRP composites together with traditional materials, particularly concrete, as described below.

Hybrid-FRP structures

In new hybrid bridge structures, FRP materials are combined with concrete. Some hybrid-FRP bridges and design studies are presented below:

The Miyun Bridge in China, built in 1982, was the first hybrid FRP-concrete traffic bridge. The simply supported two-lane bridge consists of six honeycomb sandwich FRP box girders and a 100-mm-deep reinforced concrete slab connected with shear bolts to the box girders [YFZ+03].

In the 1990s Descovic et al. worked on a lightweight hybrid beam concept consisting of a GFRP filament-wound box section with a concrete layer on the top side (the compression zone) and a CFRP strap on the bottom flange (the tension zone), as illustrated in Figure 2.6-a, [DMT95a], [DMT95b], [TM92]. A two-component epoxy adhesive was used to connect the GFRP flange and the concrete. Experiments showed that slightly prestressed shear connectors (in this case steel bolts) improved the GFRP-concrete interface behavior. Furthermore a favorable pseudo-ductile system behavior was achieved.

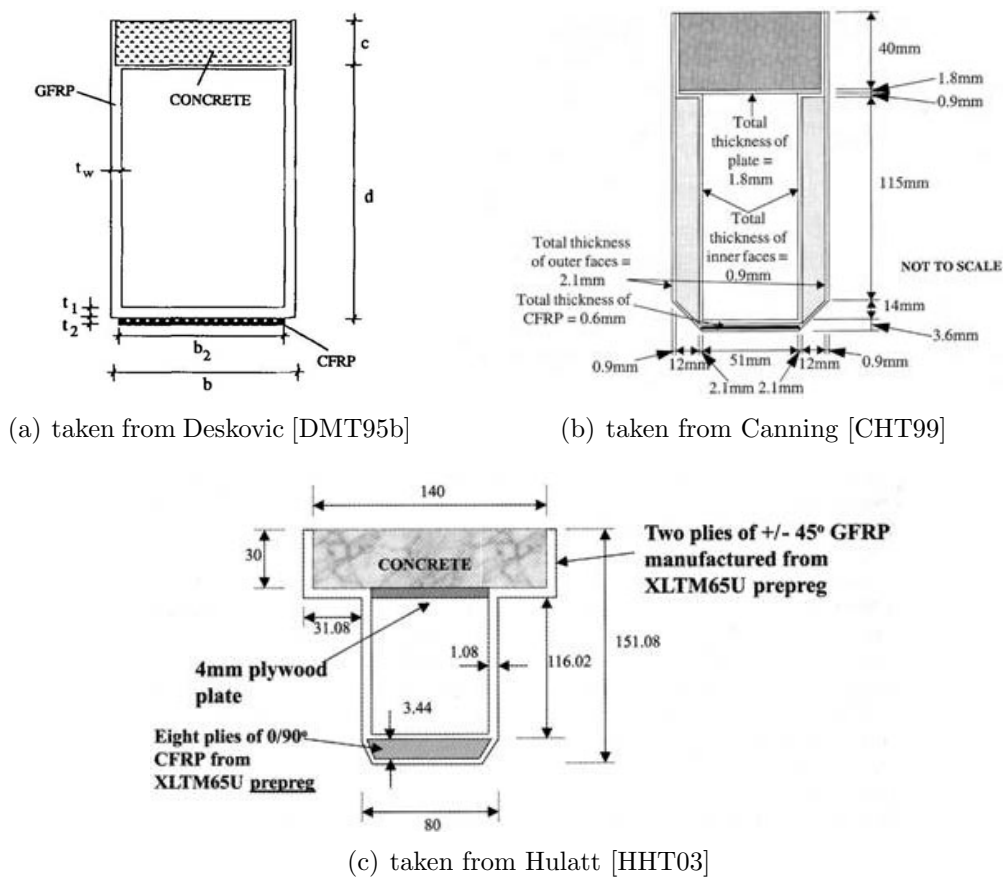


Figure 2.6: FRP-concrete beams proposed by different researchers.

In 1998, Hall and Mottram [HM98] performed experiments on hybrid GFRP-concrete beams consisting of pultruded GFRP panels with T-upstands and normal or lightweight concrete. The concrete was either directly cast onto the FRP panel or onto an intermediate epoxy

adhesive layer that had not yet cured. Four-point bending tests demonstrated that the bonded interface improved the performance of the beams.

Further research on hollow FRP tubes with a thin concrete layer on their upper surface was performed by Canning et al. [CHT99] and Hullat et al. [HHT03], see Figure 2.6-b-c. The investigation of different configurations of hybrid beams showed that the most practical and cost-effective solution for achieving maximum shear/bond resistance (full composite action) was to apply the fresh concrete onto a not yet cured adhesive. The failure mechanism was concrete crushing and local buckling of the FRP.

In 2000, the Kings Stormwater Channel Bridge was built in California following research on carbon shell systems (CSSs) by Seible et al., see Figure 2.7, [Sei01], [SMZH01], [VDEZS03]. The two-span highway bridge is 20 m long (each span 10 m) and 13 m wide. The main girders and piers are made of prefabricated thin filament-wound carbon/epoxy shells filled on-site with lightweight concrete. The shells served as longitudinal reinforcement and circumferential confinement and acted as stay-in-place formwork for the concrete core. The concrete ensured the transfer of the compressive forces and stabilized the thin shells against buckling. The connection between the deck and carbon shell girders consisted of shear connectors, embedded into the carbon shell system during grouting.

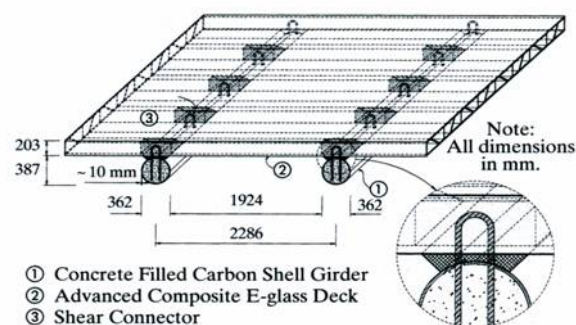


Figure 2.7: Carbon shell system (CSS) from Seible et al. in 2000, taken from [VDEZS03].

In 2002, Van Erp et al. presented results of studies carried out on a composite bridge developed and built in Australia, [EHM⁺02]. The 10-m span bridge consisted of FRP beams placed side by side and bonded together with epoxy adhesive and connected underneath by a transversal laminate to achieve plate behavior and transverse stiffness. The compression zone consisted of a concrete layer, epoxy-bonded onto the FRP to achieve composite action.

In 2004, Kitane et al. presented a hybrid FRP-concrete bridge superstructure, in which the cross section consisted of three trapezoidal GFRP box sections bonded together, as shown in Figure 2.8 [KAL04]. A layer of concrete was placed on the compression side and connected

to the FRP sections by means of FRP shear keys. Static tests on a scale model showed that the bridge meets stiffness requirements and has significant strength reserves.

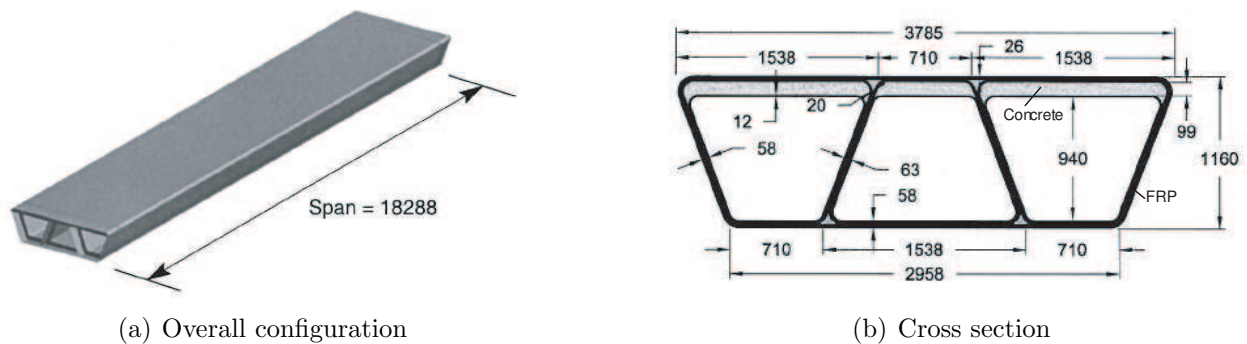


Figure 2.8: Hybrid bridge superstructure from Kitane et al. in 2004, taken from [KAL04].

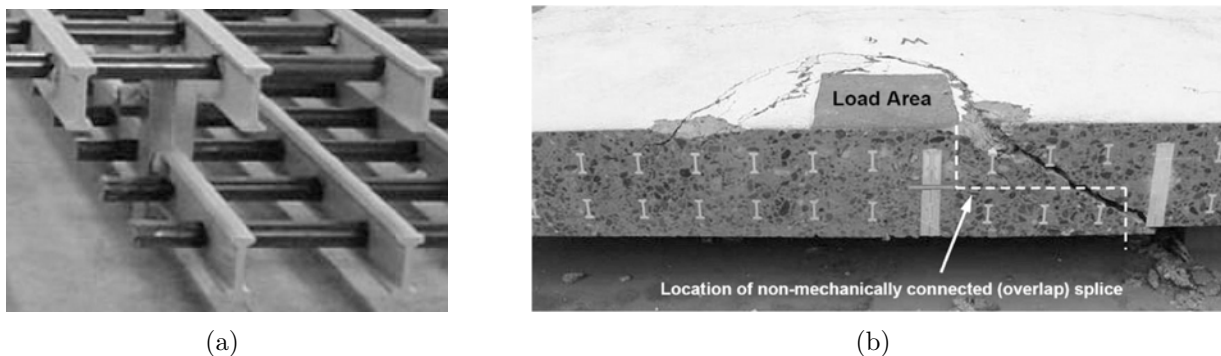


Figure 2.9: Hybrid bridge superstructure from Bank et al. in 2006, taken from [BOR⁺06].

In 2006, Bank et al. presented a case study of prefabricated double-layer pultruded fiber-reinforced polymer FRP grids for bridge deck construction, as illustrated in Figure 2.9. These grids were used to reinforce a 39.6-m-long by 13.7-m-wide bridge deck in Wisconsin, US. The feasibility of the double-layer FRP grids was investigated and the results were presented in [BOR⁺06]. Shear connectors were used to join the top and bottom grids to form an integrated 3D reinforcing module. The reinforcement grids were designed to be moved in a single lift of a crane and placed on the bridge girders. The entire bridge slab reinforcement system was put in place in 10 hours, demonstrating the potential for rapid bridge construction using large prefabricated FRP reinforcements. The authors concluded that the cost of the FRP materials could be reduced appreciably if a better shear connection between the FRP

grid layers was developed, resulting in an overall in-place deck cost much closer to that of a steel-reinforced deck.

Also in 2006, Berg et al., from the same research group, published the construction process and cost analysis for a concrete highway bridge deck built using FRP materials as reinforcements and also as formwork, [BBOR06]. The bridge deck combined three forms of FRP reinforcement: FRP stay-in-place forms, deformed FRP reinforcing bars, and a special prefabricated pultruded FRP reinforcing grid, as illustrated in Figure 2.10. Laboratory testing

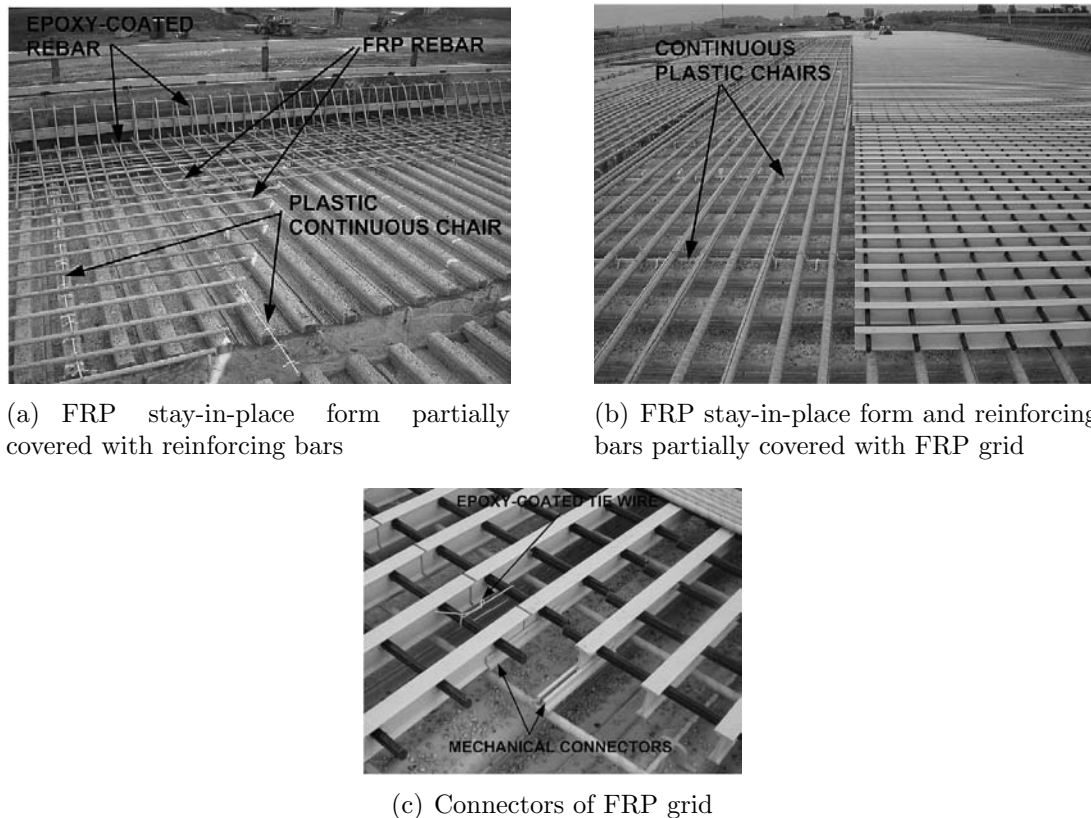


Figure 2.10: Hybrid bridge superstructure from Berg et al. in 2006, taken from [BBOR06].

of the FRP-reinforced deck system was conducted prior to construction. Punching shear, negative and positive moment bending, and fatigue tests were carried out and indicated that the FRP reinforcement system could reliably bear the design loads. Freeze thaw tests demonstrated sufficient durability. Regarding the cost analysis, the bridge construction demonstrated that a 57% saving in labor costs was achieved in comparison to steel-reinforced decks. However, material costs for the FRP-reinforced bridge deck were 60% higher than those for the steel-reinforced bridge deck.

2.2 Lightweight concrete (LC)

2.2.1 Definitions

In comparison to normal concrete (NC) of similar strength, lightweight concrete (LC) is characterized by a lower density due to the use of lightweight aggregates and/or the presence of air in the composition (LC oven-dry density of less than 2000 kg/m^3). Lightweight concretes are usually composed of lightweight aggregates (with diameters of $\varnothing_a \geq 4 \text{ mm}$) embedded in a cementitious matrix. The cementitious matrix basically consists of cement, water, additions and fine aggregates with a diameter of less than $\varnothing_a < 4 \text{ mm}$. According to [ACI05] and [Fau03], two principal types of LC can be distinguished, exhibiting considerable differences in material properties and brittleness: sand lightweight aggregate concrete (SLWAC) and all lightweight aggregate concrete (ALWAC). In SLWAC, the fine aggregates in the composition include normal sand, while in ALWAC fine aggregates consist exclusively of lightweight sand (usually made out of crushed expanded clay) and/or lightweight aggregates. Extensive state of the art reports about the use of LC and its properties are given for example in the ACI 213 [ACI03], Aurich [Aur71] and Faust [Fau03]. The main characteristics are summarized below.

Typical lightweight and normal aggregates used in concretes for civil engineering structures and their densities are listed in Figure 2.11, according to [Fau03].

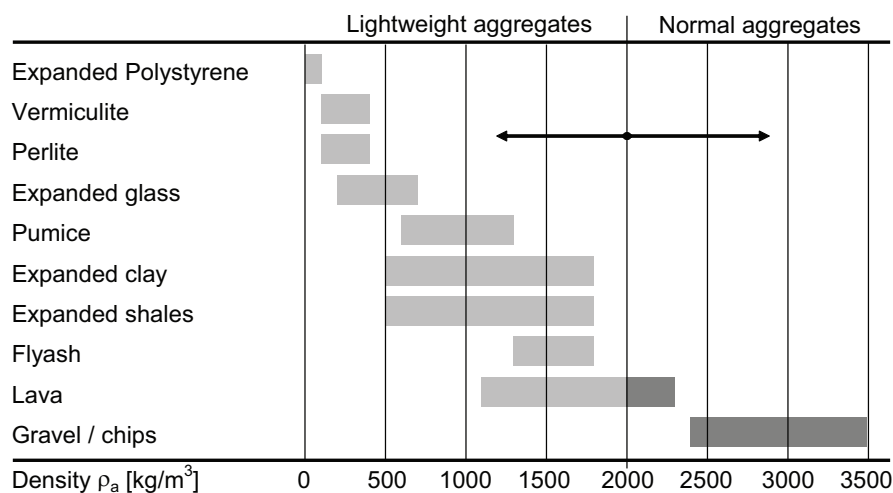


Figure 2.11: Typical aggregates used in concrete for civil engineering structures, acc. to [Fau03].

2.2.2 LC material properties

LC behavior under compression

The compressive strength of lightweight concrete, f_{lc} , is mainly determined by the strength and stiffness relationship between the aggregates and the matrix, and by the volume fraction of both. In NC the aggregates are much stiffer than the cementitious matrix, while in LC the stiffness of the lightweight aggregates is usually lower or in the same range as that of the matrix. This explains the differences in the principle stress trajectories in NC and LC. Figure 2.12 illustrates the stress flow in a simplified concrete section where the components with higher stiffness create the load path of the compressive force flow. In NC the compressive

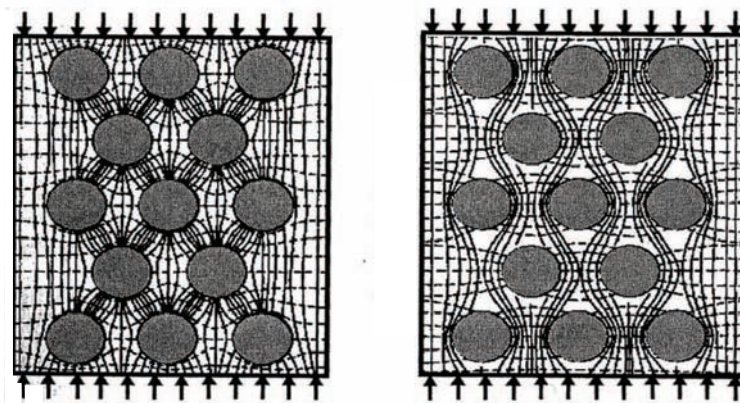


Figure 2.12: Compressive stress flow in normal (left) and lightweight (right) concretes, taken from [Fau03].

force flow proceeds from aggregate to aggregate and the matrix acts as connecting element (Figure 2.12, left), whereas in LC the lightweight aggregates are comparable with voids and the compressive force flow proceeds only in the matrix around the aggregates (Figure 2.12, right). Moreover, the smaller the stiffness differences between aggregates and matrix, the more effective is their interaction.

Figure 2.13 illustrates a simplified model of a compressive failure process in LCs: due to the curved compressive force flow around the aggregates, lateral tensile forces are caused above and below them, as indicated by the black bars in Figure 2.13, left. By increasing the compressive load, the tensile strength of the matrix will be reached and cracks occur in the matrix just above and below the aggregates (Figure 2.13 middle). Subsequently, the lateral tensile stresses redistribute across the lightweight aggregates as illustrated in Figure 2.13, right. Any further increase in compressive load is consequently influenced by the tensile strength of the aggregate. Failure ensues when no further redistribution of lateral tensile stresses can occur and the crack crosses the matrix and entire aggregate.

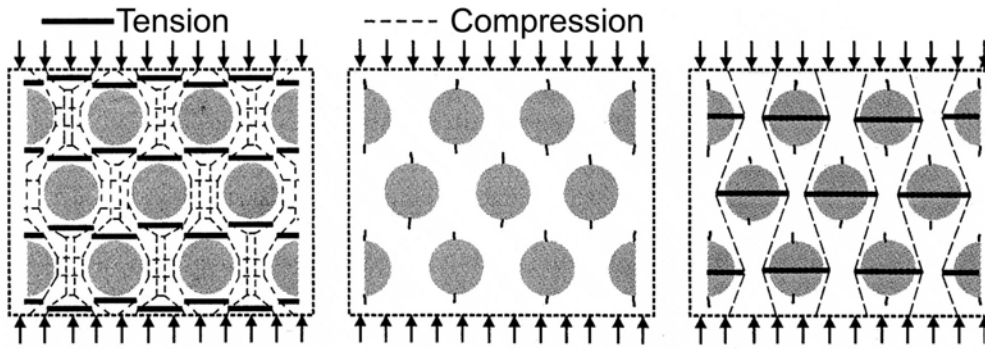


Figure 2.13: Typical compressive failure process in LCs, taken from [Fau03].

The previously described relationships explain why the composition of the matrix and lightweight aggregates not only influences the LC oven-dry density but also LC compressive strength. By changing the volume fraction of both, but maintaining the same LC oven-dry density, different compressive strength ranges can be attained, as shown in Figure 2.14 from [Aur71].

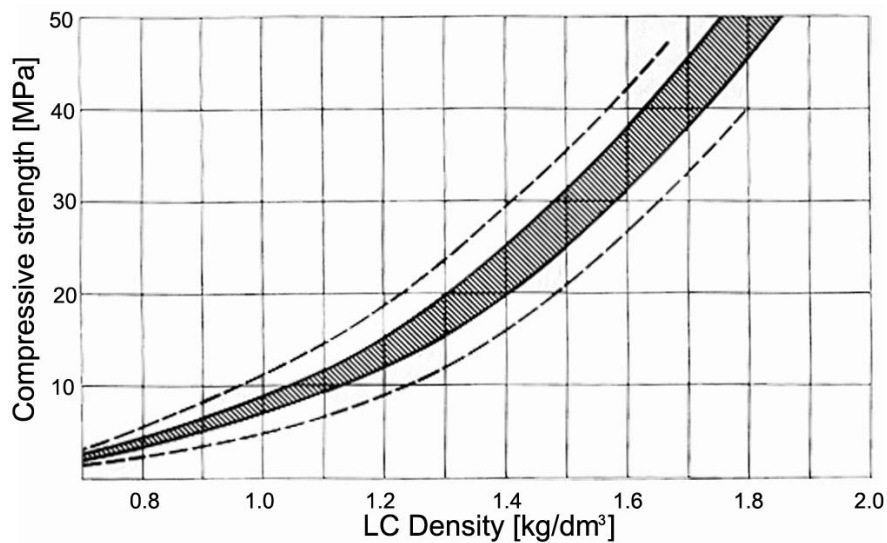


Figure 2.14: Typical compressive strengths vs LC oven-dry density, taken from [Aur71].

The LC Young's modulus, E_{lc} , is usually lower than that of an NC and is essentially determined by the Young's modulus of the lightweight aggregate together with the Young's modulus of the matrix and the efficiency of the contact zone between both. The EC2 [Com04] presents a conversion factor, η_E , for calculating the LC Young's modulus from values obtained

for NCs with similar compressive strength as formulated in Equation 2.1:

$$E_{lc} = \eta_E \cdot E_c \quad \text{with} \quad \eta_E = \left(\frac{\rho}{2200}\right)^2 \quad (2.1)$$

Figure 2.15 illustrates the comparison between the stress-strain relationship of an NC and an ALWAC cylinder under compression with similar compressive strengths. Investigating the NC cylinder, the stress-strain curve is almost linear up to two thirds of the compressive strength. Stiffness then decreases and reaches zero at ultimate strength, where a ductile failure occurs. Regarding the stress-strain behavior of the presented ALWAC specimen, it can be noticed that the LC smaller Young's modulus compared to that of the NC remains fairly constant up to failure. At ultimate strength, the LC cylinder failed immediately. This brittle behavior can again be explained using the simplified model in Figure 2.13. Once the tensile strength of the matrix is reached, hardly and further stress distribution can occur in the LC aggregates and fracture occurs suddenly through the matrix and LC aggregates.

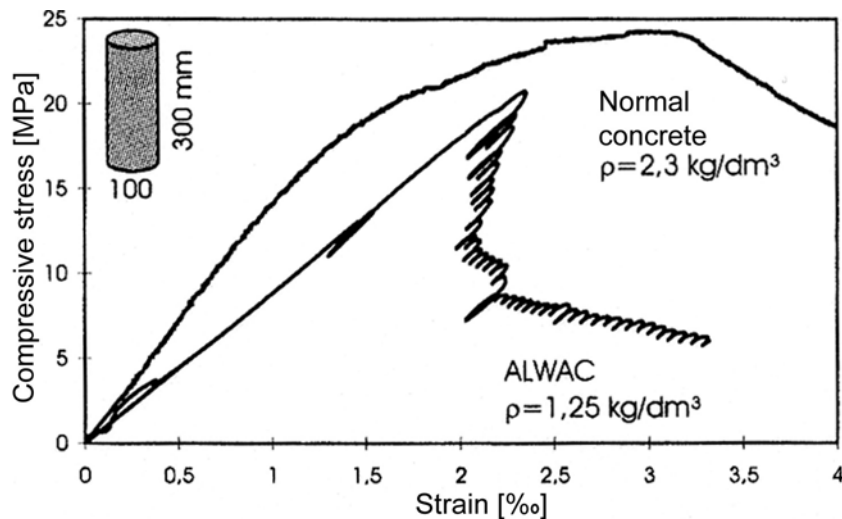


Figure 2.15: Stress-strain relationship of an NC and an ALWAC, taken from [Fau03].

LC behavior under tension

The LC tensile strength, f_{lct} , is again mainly influenced by the tensile strength and stiffness of the aggregates and matrix and the relationship between them and is usually 20% to 35% lower than that of an NC. To take this into account, Eurocode 2 [Com04] introduces a coefficient, η_1 , for determining LC tensile strength from the tensile strengths of NCs with the same compressive strength taking the LC oven-dry density into consideration as formulated in

Equation 2.2:

$$f_{lct} = \eta_1 \cdot f_{ct} \quad \text{with} \quad \eta_1 = 0.4 + \frac{0.6 \cdot \rho}{2200} \quad (2.2)$$

Depending on the loading condition in the experimental investigations, there are three different tensile strengths: the uniaxial tensile strength, f_{lct} , splitting tensile strength, f_{lctsp} and flexural tensile strength, f_{lctfl} , which are determined by tensile tests on cylinders in pure tension, compressive tests on the longitudinal side of cylinders or three- to four-point bending experiments on rectangular sections respectively. The most commonly used experimental method is the splitting tensile test (also called Brazilian test). Investigations carried out by Faust [Fau03] showed that the uniaxial tensile strength can be approximated with 90% of the splitting tensile strength. A general relationship between splitting tensile strength and compressive strength is difficult to formulate since the LC composition and brittleness significantly influence the splitting tensile strength. The EC2 ([Com04]) formulates a relationship between the splitting tensile strength and the compressive strength to a power of $\frac{2}{3}$. A reduction coefficient, k , takes into account whether the relationship is formulated for an NC or LC, as indicated with the black lines in Figure 2.16. The splitting tensile strength is hence the product of $k \cdot f_{lc}^{\frac{2}{3}}$ with $k=0.33$ for NC and $k=0.254$ for LC. The grey line in the graph represents the linear fitting line of all investigated concretes and is of no further interest. In the ACI [ACI05] however, a relationship between the square root of the compressive strength and splitting tensile strength is considered. Furthermore, the ACI

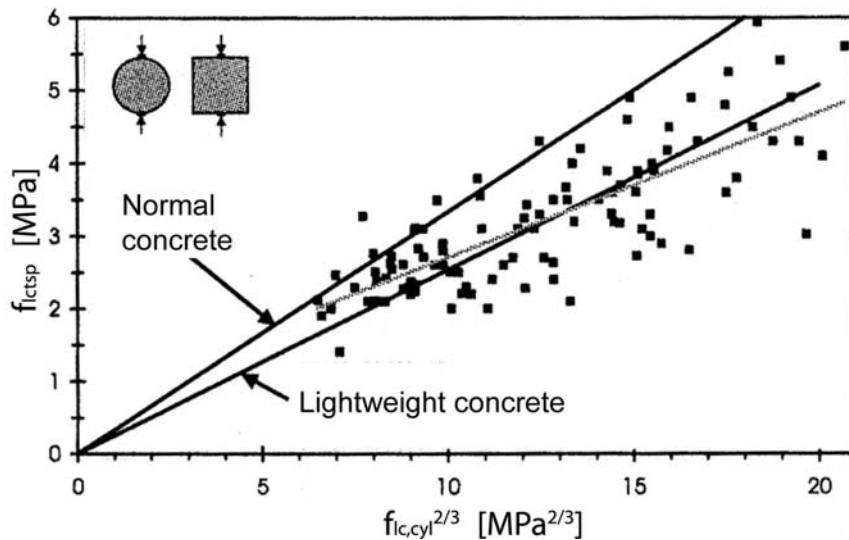


Figure 2.16: Splitting tensile strength vs. compressive strength, taken from [Fau03].

provides a different reducing factor for ALWACs and SLWACs. Consequently, the splitting tensile strength is approximated by 0.415 for ALWACs and $0.473\sqrt{f_{lc}}$ for SLWACs.

2.2.3 LC fracture mechanical properties

As previously described, LC brittleness is much higher than that of NC with similar compressive strengths due to the lower tensile strength and stiffness of the components. The LC brittleness can be described by the fracture energy, G_f , of the material. A way of quantifying this value is to perform wedge splitting tests developed by Wittmann and Brühwiler among others [WRB⁺88] and [BW90], in which a notched specimen is placed on a lower roller and loaded horizontally on the top of the specimen using two steel loading devices both equipped with rollers. The typical test set-up is shown in Figure 2.17. During the experiment, the vertical load (denoted F_v in the diagram) and the crack opening at the top of the specimen are measured. The horizontal splitting force is calculated by taking the wedge angle into consideration.

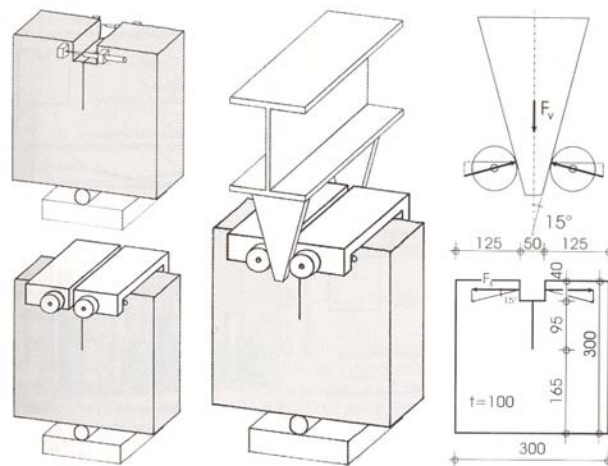


Figure 2.17: Principle of wedge splitting test, taken from [Fau03].

A typical experimentally obtained splitting force vs crack opening curve is illustrated in Figure 2.18, left. From this curve the strain softening curve or post-peak softening behavior of the LC can be determined by subtraction of the elastic displacements, as illustrated in Figure 2.18, right. The fracture energy, G_f , can subsequently be determined. This corresponds to the area below the softening curve, which can be approximated by a bilinear degradation [Fau03], with a kink located at $0.3 f_{lct}$, as illustrated in Figure 2.18. The critical crack opening, w_{crit} , represents the crack width for which no tensile stresses could be transmitted and where the specimen failed.

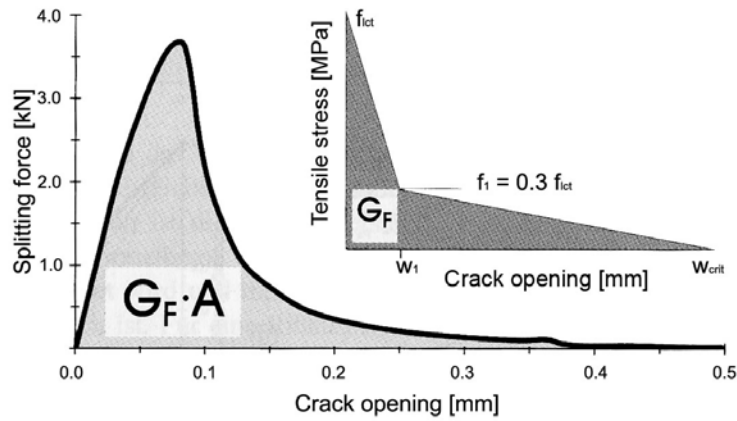


Figure 2.18: Typical splitting force-crack opening curve (left) and corresponding post-peak softening behavior (right) obtained from a wedge splitting test, taken from [Fau03].

A further parameter describing concrete brittleness was introduced by Hillerborg [Hil83] in the form of the characteristic length, l_{ch} , of a material. This represents the length of a tie in which the elastic energy required to create a transverse fracture surface is stored, as formulated using the fracture energy in Eq. 2.3:

$$l_{ch} = \frac{E_{lc} \cdot G_f}{f_{lct}^2} \quad (2.3)$$

Table 2.2 presents typical values for characteristic lengths of LCs compared to NCs and high performance concretes, taken from [BTT04], [Fau03] and [FV99]. Regarding the LCs, different SLWAC and ALWAC were investigated. Their cubic compressive strength, splitting tensile strength and compositions are also summarized in the table, all of them using expanded clay (EC) as lightweight aggregates but with varying aggregate density, ρ_a . The fine aggregates used were normal sand (NS), expanded clay (EC) with a diameter of less than 4 mm, expanded glass (EG) and lightweight sand (LS). A considerable difference was noticed between the SLWAC and ALWAC compositions, the latter always exhibiting lower characteristic lengths for similar compressive strengths.

A further study of different LC compositions was performed by Wille et al. [WDT05]; Table 2.3 presents some of the results. The authors worked with a high performance cementitious matrix including silica fume. Since the achieved compressive strengths were relatively high, the authors denoted the investigated LCs high performance LCs. Again, the characteristic lengths of the ALWAC compositions were lower than those of the SLWAC with comparable compressive strengths.

Table 2.2: Typical values of characteristic lengths of lightweight and normal concretes (NS=normal sand, LS=lightweight sand, EC=expanded clay, EG=expanded glass, taken from [FV99], [Fau03] and * from [BTT04]).

Concrete type	Lightweight aggregates	Fine aggregates	$f_{lc,cube}$ [MPa]	f_{lctsp} [MPa]	l_{ch} [mm]
SLWAC	EC: $\rho_a = 0.83 \text{ kg/dm}^3$	NS	20	2.5	150
SLWAC	EC: $\rho_a = 0.83 \text{ kg/dm}^3$	NS/EC	30	2.2	125
SLWAC	EC: $\rho_a = 1.22 \text{ kg/dm}^3$	NS	30	2.3	225
SLWAC	EC: $\rho_a = 1.22 \text{ kg/dm}^3$	NS/EC	60	3.5	50
SLWAC	EC: $\rho_a = 1.74 \text{ kg/dm}^3$	NS	45	3.2	230
SLWAC	EC: $\rho_a = 1.74 \text{ kg/dm}^3$	NS/EC	60	3.0	130
ALWAC	EC: $\rho_a = 0.83 \text{ kg/dm}^3$	EG	20	1.4	40
ALWAC	EC: $\rho_a = 0.83 \text{ kg/dm}^3$	LS	24	2.3	40
ALWAC	EC: $\rho_a = 1.22 \text{ kg/dm}^3$	LS	20	2.1	75
ALWAC	EC: $\rho_a = 1.22 \text{ kg/dm}^3$	LS	35	3.2	50
ALWAC	EC: $\rho_a = 1.74 \text{ kg/dm}^3$	LS	45	2.7	175
ALWAC	EC: $\rho_a = 1.74 \text{ kg/dm}^3$	EG	30	2.3	75
Normal concrete			-	-	250-750
High performance concrete			-	-	150-250
Steel fiber-reinforced concretes*			-	-	1200-4850

Table 2.3: Material properties of selected high performance lightweight concretes with silica fume investigated by Wille (NS=normal sand, EC=expanded clay, EG=expanded glass, taken from [WDT05]).

LC type	Specification fine aggregates	ρ [kg/m ³]	$f_{lc,cube}$ [MPa]	E_{lc} [GPa]	f_{lctsp} [MPa]	l_{ch} [mm]
SLWAC	NS	1600	41.2	18.3	3.4	67
SLWAC	NS	1730	57.2	22.3	4.7	34
SLWAC	EC/NS	1430	37.5	15.0	2.9	37
SLWAC	EC/NS	1550	58.2	18.2	4.0	28
ALWAC	EC	1240	32.6	11.9	2.6	23
ALWAC	EC	1310	45.3	14.5	2.8	19
ALWAC	EG	1000	20.2	8.7	1.8	16
ALWAC	EG	1170	29.0	10.9	2.3	21
ALWAC	EG	1390	32.7	14.6	2.8	29

2.3 Shear capacity of concrete members without shear reinforcement

2.3.1 Definitions

In concrete beams or slabs without shear reinforcement, two different failure modes can be expected [ASC98]: flexural failure, which entails either crushing of the compression zone or tensile failure of the reinforcement, or shear failure in the core. Shear failure can occur in two different zones: within the span or at the supports, where the load is directly transmitted through a compression diagonal. It has been recognized that the shear span-to-depth ratio, a/d , is an indicator of the governing failure mode, where a is the distance from the load axis to the support axis, and d the effective depth of the slab. As a decreases, shear resistance increases, because the load can be directly transmitted by a compression diagonal to the support [ASC98], [Kan64], [Kan66], [Kan67]. For longer distances, however, compression diagonals interfere with crossing tension diagonals, which lower the shear resistance compared to the shear resistance over the supports (for concrete without shear reinforcement). Schlaich [SSJ87], [SS93], [SS01] introduced the concept of D- and B-regions, where D stands for discontinuity or disturb (associated to nonlinear strain distributions through the cross section), and B stands for beam or Bernoulli (where a linear strain distribution can be expected). Typically, the region of direct load transmission extends up to a/d ratios of approximately 2.5 [ASC98], while for higher ratios the beam mechanism predominates.

Flexural shear failure within the span

Shear failure occurring within the span (B-region) is designated flexural shear failure where the failure-causing crack develops from a flexural crack. Flexural shear failure can occur in beams or slabs without shear reinforcement. Figure 2.19 illustrates a beam without shear reinforcement with typical flexural cracks along the span which can be observed for beams with

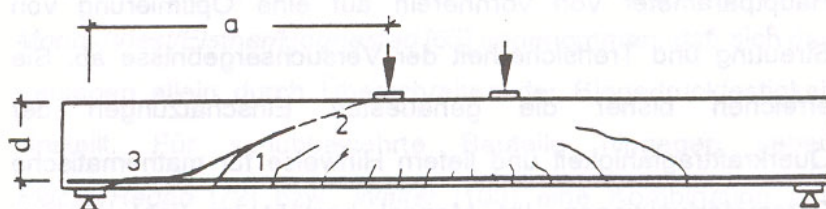


Figure 2.19: Typical flexural shear failure in B-region, taken from [SS95].

a shear span-to-depth ratio $a/d \geq 2.5$. Under increasing load, the outermost flexural crack flattens in the middle of the beam depth (1) and starts to propagate diagonally through the depth of the beam towards the compressive zone (2) and then towards the support at the height of the steel reinforcement (3). This crack development usually occurs very rapidly, so that with the appearance of the diagonal crack, the beam reaches its ultimate load.

Direct load transmission next to supports

Shear failure under direct load transmission occurs for shear span-to-depth ratios ≤ 2.5 , [ASC98]. Figure 2.20 shows the typical cracking pattern (on the left side of the illustrated beam) and the resulting forces (on the right side of the beam). In contrast to flexural shear failure, the beam shows no significant flexural cracks and the diagonal crack appears between the loading plate and the support in the middle of the beam depth, as indicated with (1). Subsequent to this first obvious diagonal crack, the load can increase significantly due to the redistribution of internal stresses. The diagonal crack consequently propagates slowly over the whole beam depth towards the support (2) and the loading plate (3). Subsequent failure usually occurs in a much less brittle manner than under flexural shear failure.

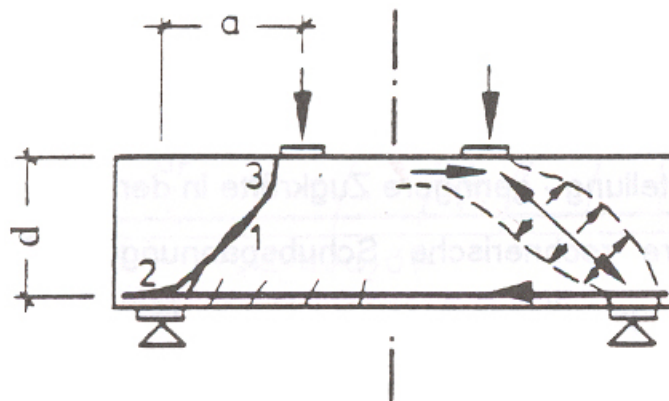


Figure 2.20: Typical shear failure under direct load transmission in D-region, taken from [SS95].

2.3.2 General remarks concerning modeling of shear failure

The prediction of the shear capacity of unreinforced concrete members still represents a challenge for researchers from all over the world and various models have been developed since the early 20th century. The basis for the shear resistance formula in design codes, as presented in the Eurocode [Com04] or the ACI 318 [ACI05] and the Swisscode SIA 262 [SIA03a], is mostly semi-empirical and does not follow any clear mechanical concept. All existing research models based on mechanical justifications assume that in the span regions

of an uncracked concrete member, the shear force is transferred by the total beam depth and results in a maximum shear stress at the mid-depth of the beam, as illustrated in Figure 2.21 in the outer uncracked beam part. In regions where the tensile strength of the concrete is reached in the lower beam section and flexural cracks are formed, the shear stress development through the cross section becomes unevenly distributed over the beam depth. In cracked concrete members, maximum shear stress is no longer at the mid-depth of the beam, but moves to the neutral axis of the cracked member. While the shear stresses are parabolically distributed in the compressive zone above the neutral axis, stress development in the tensile zone is far from constant and requires more precise investigation. According to [ASC98], [Fis97], [SS95], [Zin00], the shear resistance of the cracked concrete beams is basically composed of four portions as illustrated in Figure 2.21: the shear resistance of the compressive zone, V_c ; the shear resistance of the dowel action of the longitudinal reinforcing bars crossing the cracks, V_d ; the shear resistance of the aggregate interlocking, V_i , and the shear resistance of the tensile stresses across the cracks in the fracture process zone, V_{FPZ} .

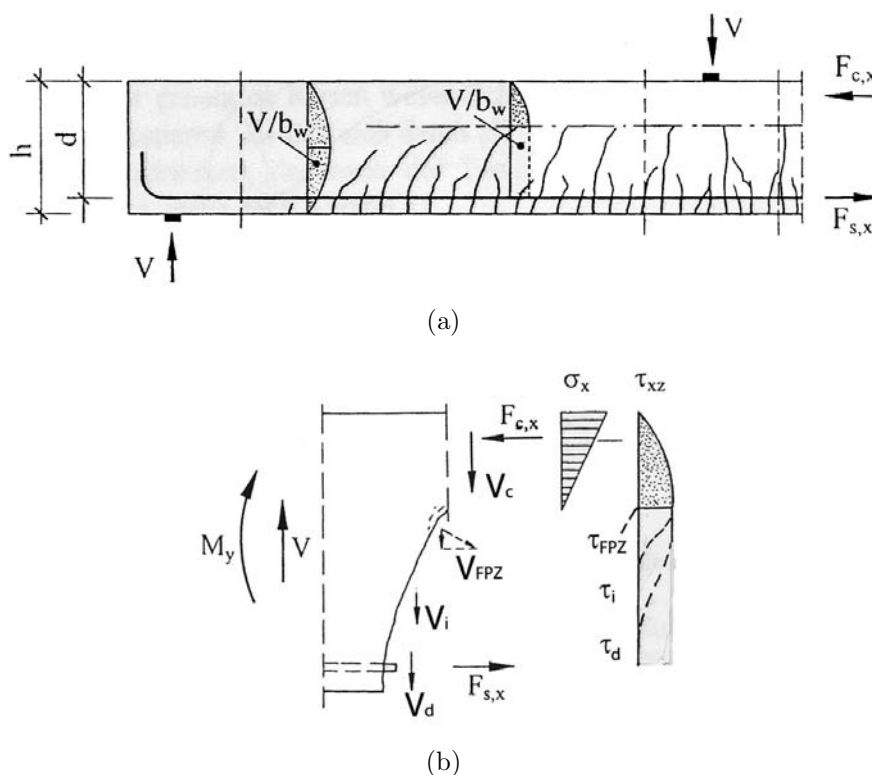


Figure 2.21: Shear stress development through cross section (a) and components contributing to shear resistance (b), refined from [Zin00].

The components of the shear resistance will be further discussed in Section 4.3.3 and only basic definitions are given in the following. The shear resistance of the compressive zone is the portion taken from the concrete above the neutral axis, while dowel action can be defined

as the capacity of longitudinal reinforcing bars to transfer forces perpendicular to their axis. This effect arises when there is slippage of the crack surfaces, which is counteracted by the deformed crossing reinforcing bars, as illustrated in Figure 2.22. According to experimental investigations carried out by Kotsovos et al. [Kot83], [KP97], [KP04], [JPK99], dowel action is usually negligible in members without shear reinforcement, whereas other researchers attach more importance to the effect by including it in their shear models, see also [ESES06a], [ESES06b], [Rei90], [RKKM03], [FP68].

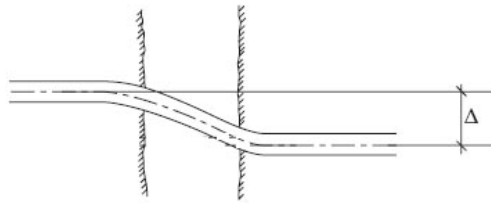


Figure 2.22: Crack surface slip and corresponding deformation of longitudinal reinforcing bar, taken from [JPK99].

The effect of aggregate interlocking occurs when aggregates protruding from the crack surface provide resistance against slip. This effect exists in normal concretes, while it can be disregarded in lightweight concretes, where cracks propagate through the lightweight aggregates. Furthermore, shear resistance is provided in the so-called fracture process zone (FPZ), where the concrete can bridge the crack and transmit tensile forces, as shown in Figure 2.23, refined from Uddin [UO02]. The peak tensile stress at the crack tip equals the tensile strength of the concrete and decreases according to the softening behavior of the material until the critical crack width is reached, beyond which no further stress transmission is possible.

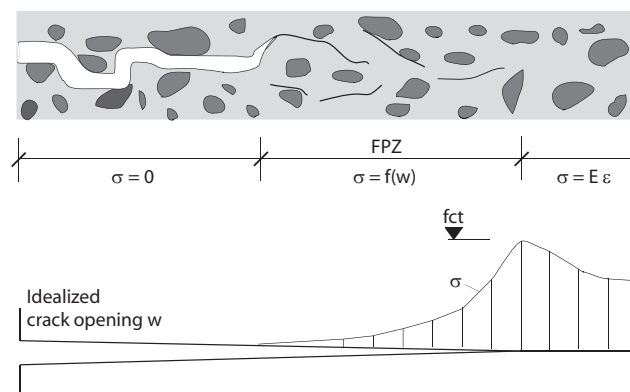


Figure 2.23: Development of through-crack tensile stresses along an emerging crack (revised from [UO02])

The basis for this assumption was taken from investigations by Hillerborg in 1983, [Hil83] who studied the fracture mechanics behavior of concrete, such as concrete fracture energy, G_F , and tensile stresses in the FPZ. In order to take the concrete fracture energy into account, Hillerborg introduced the material characteristic length, l_{ch} , previously defined in Equation 2.3 in Section 2.2. It was furthermore assumed that the length of the FPZ is $0.4 \cdot l_{ch}$. Based on this investigation, the incorporation of the FPZ in shear failure models has been the subject of several research projects, as will be explained in more detail in Section 4.3.3.

2.3.3 Shear failure models for members without shear reinforcement

Many different shear failure models exist for members without shear reinforcement, which can be divided into the following groups: semi-empirical models, strut-and-tie models, tooth models and fracture mechanics approaches. As already stated above, codes and standards, such as the EC2 [Com04], the ACI 318 [ACI05] and the SIA 262 [SIA03a] are semi-empirical models. Due to their generalized form, they offer a conservative and minimum shear resistance value and often do not represent the real shear strength. The EC2 and ACI 318 will be further discussed in Sections 4.3 and 4.4, and therefore only the last three model groups are described in the following.

Strut-and-tie model approaches

Strut-and-tie models are the oldest models and were originally developed to predict the shear strength of reinforced concrete members with reinforcements distributed in all directions (including shear reinforcement). They are useful for the design of concrete structures since they allow the designer to easily visualize the flow of forces and represent them by compressive struts and tension ties. The first truss models were introduced by Ritter [Rit99] in 1899 and Morsch [Mör23] in 1923 for long-span beams. The application of the models required not only longitudinal reinforcements, but also a minimum amount of shear reinforcements to ensure the redistribution of internal stresses on the reinforcements after concrete cracking. The models approximated that the shear of a concrete member was borne by a diagonal compressive strut, inclined by 45° to the longitudinal axis, and that the transverse reinforcement represented the tensile ties for stress equilibration. Any concrete contribution to the tensile stresses was disregarded. The shear capacity of the member was reached when the steel reinforcement started to yield. Comparison with experimental results showed an underestimation of the real shear capacity. One reason for this poor agreement was seen to be related to the approximation of the conservative model geometry with a 45° inclination angle. Thus refined strut-and-tie models focused on truss models having a variable angle of the compressive strut, see also [Kup64], [Leo65]. Other models took the concrete contribution due to its tensile

strength into account as a way of improving strut-and-tie models. Enhanced strut-and-tie models can be found in [GV90], [Kir87], [Kup64], [Rei90], [Rei91].

In short-span beams (or deep concrete members) the load is transmitted directly to the support by a compressive diagonal. This means that shear reinforcements are not necessary for stress equilibration as is the case in long-span beams. It has been experimentally and numerically verified that the compression diagonal, rather than being parallel-sided, is bowed (or bottle-shaped according to the ACI [ACI05]) between the loading point and the support. Consequently tension transverse to the diagonal results, as described in [ASC98], [Bro05], [Fos98], [SSJ87], [WL94a].

Therefore, strut-and-tie models are suitable for modeling the concrete compression diagonal by representing the stress flow as a truss consisting of compressive struts and ties necessary for equilibrium. Two approaches to choosing an appropriate truss geometry from Specht [SS95] and Foster [Fos98] are illustrated in Figure 2.24 and will be discussed in detail in Section 4.4.1.

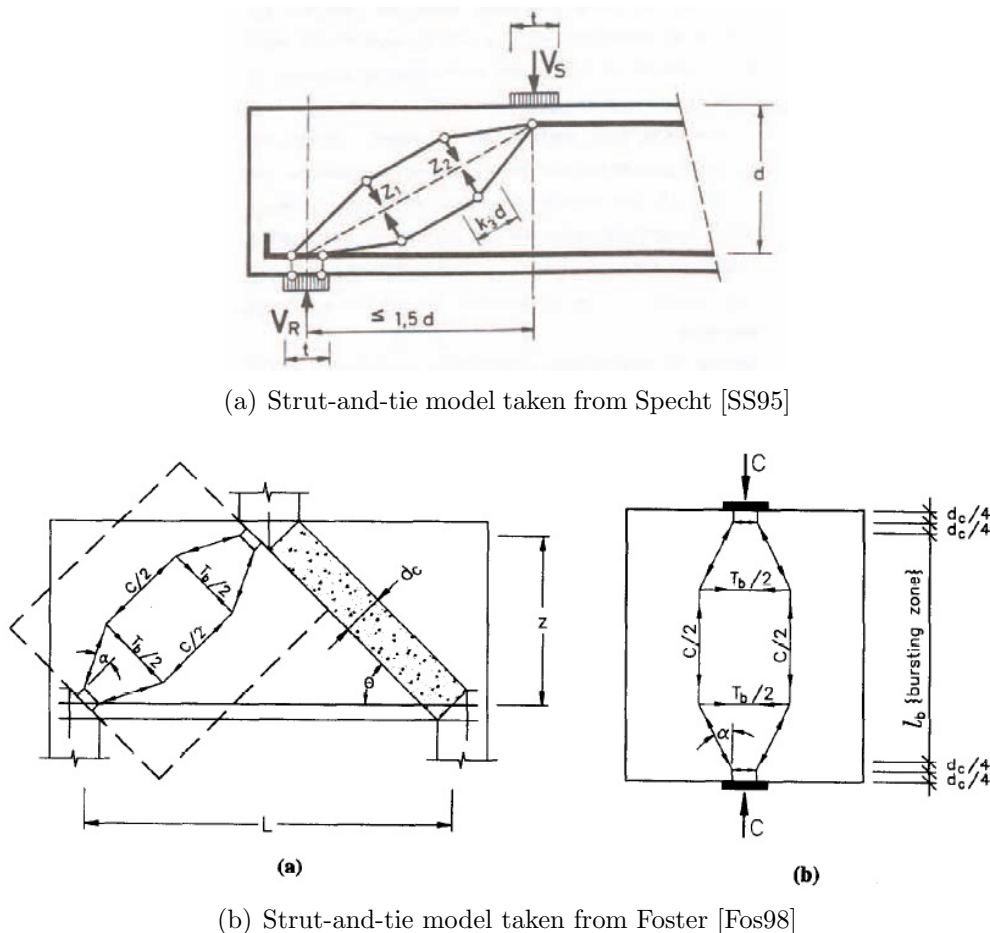


Figure 2.24: Strut-and-tie models representing diagonal strut between load introduction and support, taken from [SS95] and [Fos98].

In contrast to long-span beams, experiments indicated that, after the first cracking is observed, the concrete member can still bear significant loads. Furthermore, research showed that the angle of deviation of the compressive strut change during the loading process. Its maximum value is reached just before cracking; once cracking occurred, the struts become significantly narrower, [Bro05] and [Fos98].

In contrast to the short-span members, truss models for long-span beams without transverse reinforcements, where the force flow is represented by compressive struts and perpendicular concrete ties and the concrete tensile strength plays a major role, require different approaches [ASC98], [SS93], [SSJ87], [SS95]. As an example, Al-Nahlawi and Wight [ANW92] proposed a truss model with concrete compressive struts inclined at 35° to 45° and concrete ties perpendicular to the struts. The ties are assumed to fail when their maximum tensile stress is equal to the tensile strength of the concrete - no softening of the concrete and redistribution of forces were included. Assumptions were made concerning a constant width of the tension tie. The models were seen to be moderately accurate in predicting the measured test result. However, the authors suggest the use of appropriate safety factors to take the scatter between experiments and predictions into account.

Simple tooth model approaches

A tooth or comb-like model was first developed by Kani in 1964 for slightly reinforced concrete beams [Kan64], [Kan66], [Kan67]. The compressive part of a beam under flexural loading can be described as a backbone of a comb, while the tension zone represents the teeth of the comb, where each concrete tooth is fixed in the bone and separated from each other by flexural cracks, as illustrated in Figure 2.25. Assuming that the bond between the steel reinforcement

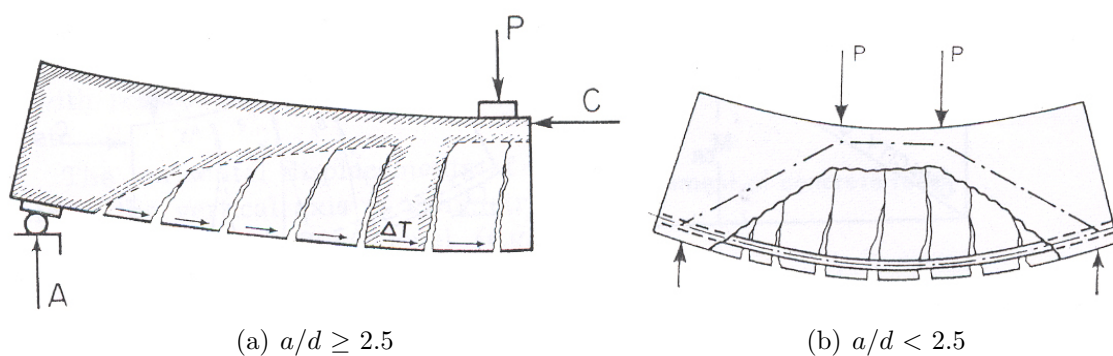


Figure 2.25: Kani's tooth model developed in 1964, taken from [Kan64].

and the concrete is fully effective, the teeth can be described as cantilevers loaded by a simple horizontal load ΔT . Kani supposed that the maximum resistance of the concrete tooth is reached when the tooth reaches its tensile strength in the neutral axis where the cantilever

is fixed. Under increasing load, the concrete teeth break off and the ultimate load is seen to be reached when the steel reinforcement starts to yield. In shorter beams, however, the tensile stresses in the reinforcement remain below the steel tensile strength and the beam is transformed into an arch tie mechanism, as illustrated in Figure 2.25-b. From experimental results, Kani concluded that the change in failure mechanism occurs for shear span-to-depth ratios of 2.5.

In 1968, Fenwick and Paulay confirmed Kani's idea of the tooth and remaining arch mechanism, [FP68]. They specified that in slender long-span beams approximately 20% of beam resistance resulted from the compressive zone, while 60% resulted from the shear transfer mechanism by aggregate interlocking across the crack and a maximum of 20% from dowel action.

Both presented tooth models constitute the basis of further model developments, in particular models which include knowledge of concrete fracture mechanics properties as described in the following and in Section 4.3.

Enhanced models including fracture mechanics approaches

Experimental research on beams without, or with insufficient, shear reinforcements has indicated that shear resistance does not increase proportionally to beam depth, [Kan67], [RKKM03], [SS01], [WL94a]. The fact that the shear resistance-to-beam depth ratio decreases with increasing beam depth is known as the size effect in concrete structures and depends on concrete brittleness and thus the extent of the FPZ.

In 1988, Gustafsson and Hillerborg [GH88] studied this size effect in beams without shear reinforcements by means of a nonlinear fracture mechanics model. Based on the work by Hillerborg [Hil83], the authors concluded that the shear strength of a concrete beam may be equally sensitive to both the fracture energy, G_F , of the concrete and the tensile strength of the concrete. To take the concrete fracture energy and thus the concrete brittleness into account, the authors proposed including the characteristic length, l_{ch} , in existing shear resistance formulae.

In 1990, Reineck presented an enhanced tooth model for slender members without shear reinforcement [Rei90], [Rei91]. The author developed a mechanical model for the explanation of structural behavior from cracking until failure. The shear force was mainly transferred in the tension zone of the member, by friction along the crack surfaces, and by the dowel action of the longitudinal reinforcement. The model demonstrated that the beam depth (size effect) as well as the reinforcement ratio influence the ultimate shear force.

The incorporation of the FPZ in shear failure models has been then subject of several research projects, by Bazant [BK84], Grimm [Gri97], Gustaffson [GH88], Rimmel [Rem94]

and Zink [Zin00] for example. In 2000 Zink, based on Hillerborg [Hil83], proposed a fracture mechanics-based model for the shear resistance prediction of cracked normal and high performance concrete beams, which comprises the portion of the shear resistance of the FPZ. Here the shear strength of the concrete member was provided by the section under compression and the FPZ. This model will be described in detail in Section 4.3.

Existing design codes do in fact take the concrete size effect into account by introducing a scale coefficient, κ : e.g. $\kappa = 1 + \sqrt{(200/d)}$ in the EC2 [Com04] with d = the slab depth, see also Section 4.3. The coefficient reaches a maximum value of 2 for thin concrete members (≤ 200 mm) and decreases for deeper ones. It should be mentioned however that incorporation of the scale coefficient in the EC2 is well established for normal concretes but not yet clearly proved for the use of lightweight concretes. Since the fracture mechanics properties of different lightweight concretes can vary greatly, this generalized scale coefficient should be treated with caution, as will be explained in detail in Section 4.3.

2.4 Summary

The use of FRP in civil engineering structures

The use of FRP materials in bridge engineering structures is still new compared with that of conventional materials. There is still a need for more detailed studies of the constructional concepts and economic aspects of FRP implementation:

- The literature review shows that all-composite structures, as well as hybrid structures, where different materials such as concrete and FRP are combined to create material-adapted structural concepts, offer good potential in bridge engineering, due to their high strength-to-weight ratio and good durability properties. However, each of the developed systems showed certain advantages and disadvantages. The main problems that occurred were premature web buckling of hollow FRP sections, a brittle system behavior, insufficient interface capacity to provide full composite action between the FRP and concrete, and a manufacturing process that is too complicated for practical applications. Thus, in order to fully exploit the potential of FRPs, these concepts have to be replaced with new structural concepts adapted to the specific material properties.
- Since the material and manufacturing costs of FRPs often constitute a considerable drawback, more research should be carried out in the area of design optimization. In particular, faster and more economically efficient production methods need to be investigated.

Lightweight concretes

A wide range of possible LC compositions exists, exhibiting considerable differences in densities, mechanical material properties and fracture mechanics properties. The main LC characteristics should be kept in mind:

- Two different categories of LCs exist: sand lightweight aggregate concrete (SLWAC) and all lightweight aggregate concrete (ALWAC).
- The LC brittleness, quantified by the characteristic length of the LC, is usually higher for ALWAC compositions than for SLWAC compositions.

Shear capacity of concrete members without shear reinforcement

Investigation of the shear failure mechanism in concrete members has represented a challenge for researchers since the late 19th century. The following conclusions can be drawn with respect to the proposed hybrid sandwich bridge slab without additional shear reinforcements:

- Shear failure of concrete members without shear reinforcements can occur in two different zones: in the span or at the supports, where the load is directly transmitted through a compression diagonal. The shear span-to-depth ratio, a/d , is an indicator of the governing failure mode, where a is the distance from the load axis to the support axis, and d the effective depth of the slab. Typically, the region of direct load transmission by a compression diagonal to the support extends up to a/d ratios of approximately 2.5 [ASC98], while for higher ratios the beam mechanism predominates and shear resistance decreases.
- A large number of different shear failure models have been proposed over the last decades. The prediction methods according to common design codes, such as the EC2 [Com04], the ACI 318 [ACI05] and the SIA 262 [SIA03a] are semi-empirical models and often do not represent the real shear resistance. The state of the art review emphasized the importance of taking concrete brittleness into account. Because LC concretes exhibit considerable differences in material brittleness, fracture mechanics-based models seem indispensable with respect to the shear strength prediction of LC specimens, such as the proposed hybrid FRP-concrete sandwich bridge deck with an LC core.

Justification of the proposed hybrid FRP-concrete concept

The proposed hybrid FRP-concrete bridge deck is a sandwich structure consisting of three layers: FRP in the tension zone, LC as a core and a thin layer of UHPFRC as a top layer.

A ductile - or at least pseudo-ductile - system behavior should be achieved by failure in the top concrete layer and crushing of the lightweight aggregates.

- The GFRP sheet with T-upstands in the tensile zone serves as formwork and provides mechanical interlocking (composite action) through the T-upstands between the basic GFRP sheet and the lightweight concrete core.
- The fibers in the UHPFRC layer are required to bear possible local bending moments due to concentrated wheel loads and the jointless application.
- The shear forces in the deck are transferred by the LC and not by the FRP webs, which are sensitive to buckling. To ensure cost-effective and rapid slab manufacture, an LC was chosen for the core instead of a more expensive foam or honeycomb structure. A further advantage of an LC core is the simplicity of the layer interfaces: the bond between LC and FRP profile is achieved either by pure mechanical interlocking through T-upstands or by adhesive bonding, while the UHPFRC layer is directly cast onto the wet LC core.
- Although no hollow FRP sections are used, the deck is still lightweight due to an LC core density of approximately 1100 kg/m^3 . The target total weight of the deck is less than 50% of that of a normal concrete deck.
- Since the deck is steel-free and the UHPFRC layer watertight, no waterproofing layer is required and the surfacing is directly applied onto the UHPFRC.

3 Experimental investigation

3.1 Overview

In order to validate the proposed hybrid FRP-concrete slab concept, experiments on 400-mm-wide and 200-mm-deep beams were performed. As described in Section 1.3, the flexural failure mode of the hybrid FRP-concrete system is determined by the face layer strengths and can be easily predicted. The shear failure of the hybrid sandwich with LC core is more complex however and needs further detailed investigation. Hence, the experimental program consisted of twelve 3600-mm long-span (S1 and S2 series) and eight 1200-mm short-span beam specimens (S3 series), designed to fail due to shear failure in the LC core. The shear span-to-depth ratio of the long-span beams is $a/d = 8.0$, and 1.6 in the case of the short-span beams.

Table 3.1: Experimental configuration (* rounded values).

Beam series	Beam labeling	LC type	LC density [kg/m ³]*	FRP-LC interface	NC anchor blocks	Shear span-to-depth ratio [-]
S1	900-1/2	SLWAC	900	unbonded	no	8.0
S1	900E-1/2	SLWAC	900	bonded	no	8.0
S1	1300-1/2	SLWAC	1300	unbonded	no	8.0
S1	1300E-1/2	SLWAC	1300	bonded	no	8.0
S2	1000	ALWAC	1000	unbonded	no	8.0
S2	1000E	ALWAC	1000	bonded	no	8.0
S2	1000A	ALWAC	1000	unbonded	yes	8.0
S2	1000EA	ALWAC	1000	bonded	yes	8.0
S3	900Es-1/2	SLWAC	900	bonded	no	1.6
S3	1300s-1/2	SLWAC	1300	unbonded	no	1.6
S3	1300Es-1/2	SLWAC	1300	bonded	no	1.6
S3	1000s	ALWAC	1000	unbonded	no	1.6
S3	1000Es	ALWAC	1000	bonded	no	1.6

Experiments were performed on beams rather than a plate in order to create a less complex structural system, enabling a better understanding of basic load-bearing mechanisms. The

top skin was a 30-mm normal concrete (NC) layer, since beam design showed that it was not necessary to use UHPFRC for the experiments. For the bottom FRP skin, standard GFRP pultruded Plank 40HDx500 elements from Fiberline were used. For the sandwich core, three different LCs were used: two SLWAC mixtures (LC900 and LC1300) and one ALWAC (LC1000). Furthermore, two types of FRP-LC interfaces were investigated: unbonded, i.e. pure mechanical interlocking between the LC and FRP T-upstands (the LC was directly cast onto the FRP formwork), and adhesively bonded (first an epoxy adhesive was applied onto the FRP and the LC was then cast onto the wet epoxy). In the case of the two long-span ALWAC beams, the total beam depth over the supports was cast with NC (anchor blocks with epoxy-bonded FRP-NC interface) in order to prevent FRP-LC slippage over the supports. Table 3.1 gives an overview of all investigated specimen configurations and their labeling, while Figure 3.1 illustrates the beam cross section. The experimental investigations of the materials and beams is summarized below, while further details are given in Appendices B to D (on DVD).

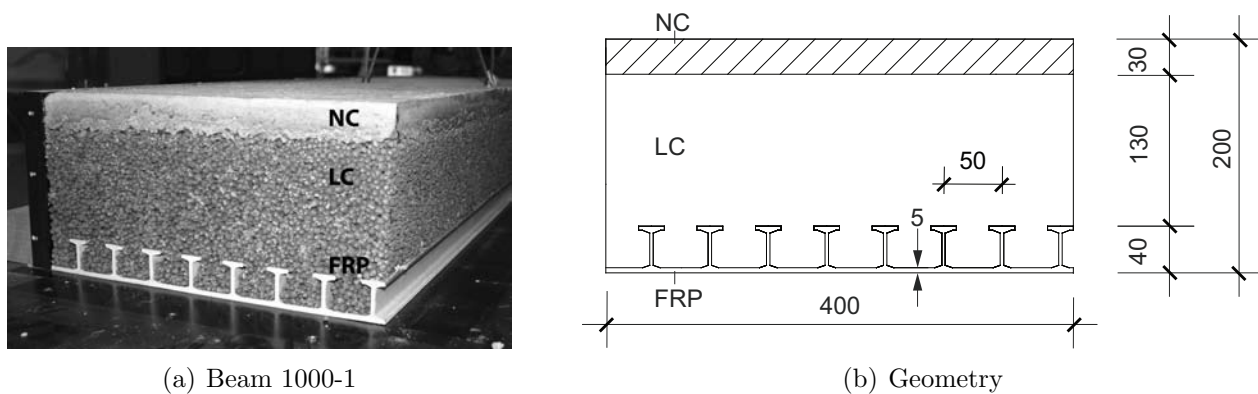


Figure 3.1: Cross section of hybrid beams.

3.2 Materials used in hybrid sandwich system

3.2.1 Material properties of LC cores

3.2.1.1 Composition

The compositions of the three LCs (LC900, LC1300 and LC1000) are given in Table 3.2, while Figure 3.2 shows their macrostructure. The ALWAC beams were cast on two different dates. The LC1000 was produced for beams 1000 and 1000E, while the LC1000A was used for the beams with the anchor blocks (1000A and 1000EA) two weeks later, see also Appendices B and C. Both LC1000 and LC1000A were composed of expanded clay

aggregates (Liapor F3, $\varnothing = 4-8$ mm, aggregate density $\rho_a = 550-650$ kg/m³) and expanded glass aggregates (Liaver, $\varnothing = 1-2$ and $2-4$ mm, $\rho_a = 350$ and 310 kg/m³ respectively), both supplied by Liapor (Switzerland), Portland cement (CEM I 42.5), filler (ZEOTOP supplied by Hauri, Germany), additives (1.0% plasticizer Sikament-10 and 0.5% Sika Stabilizer-229, both supplied by Sika, Switzerland) and water. The SLWAC compositions LC900 and LC1300 consisted of the same expanded clay aggregates (Liapor F3), normal sand, Portland cement and water.

As shown in Figure 3.2, the composition of LC1000 and LC1300 was visually very dense, whereas that of LC900 was porous; the spaces between the aggregates were not completely filled with cement.

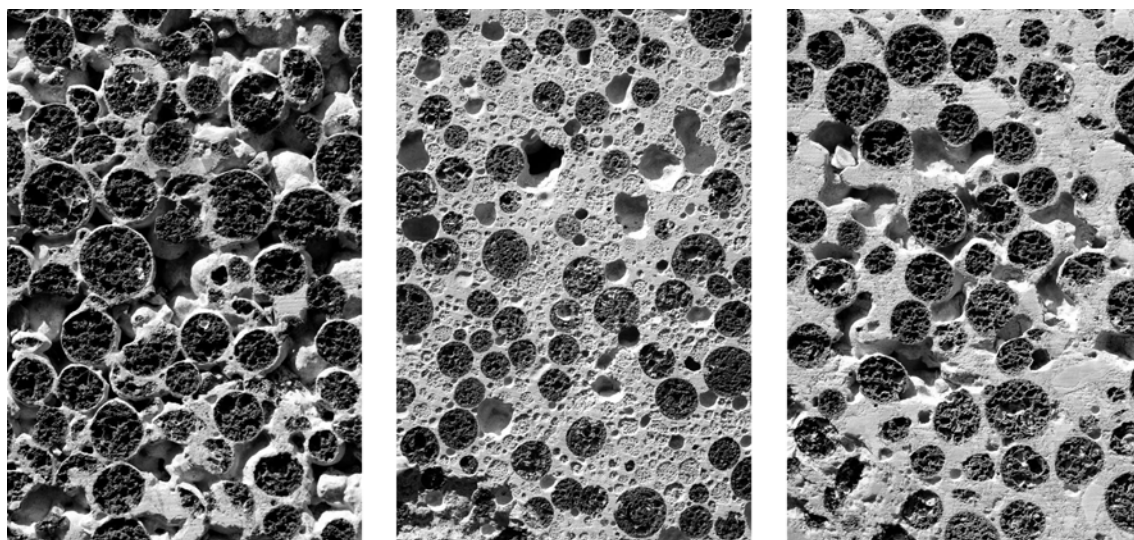


Figure 3.2: Macrostructure of LC concretes, from left to right: LC900, LC1000 and LC1300. (Expanded clay aggregates = porous black spots, expanded glass (LC1000 only) = porous grey spots).

Table 3.2: LC mixtures (*with additional stabilizer and fluidifier) in [kg/m³].

Lightweight concrete	Liapor F3 (4/8 mm)	Liaver (1/2 mm)	Liaver (2/4 mm)	Sand	Cement	Filler	Water
LC900 (SLWAC)	400	-	-	315	250	-	95
LC1000 (ALWAC)	261	55	49	-	452	50	173*
LC1000A (ALWAC)	261	56	50	-	452	50	173*
LC1300 (SLWAC)	295	-	-	570	305	-	195

3.2.1.2 Mechanical properties

Mean compressive strengths, $f_{lc,m}$, and Young's moduli, $E_{lc,m}$, were determined according to Swisscode SIA 162/1 on three to six cylinders ($\varnothing = 160$ mm), which were cast together with the beams. For the SLWAC compositions, five cores of 100-mm diameter for each mixture were taken from the beams after the experiments, mainly to investigate the degree of concrete compaction (denoted by -c). Representative stress-strain curves of the three LC types are shown in Figure 3.3. The stiffness slightly but steadily decreased up to a brittle failure for

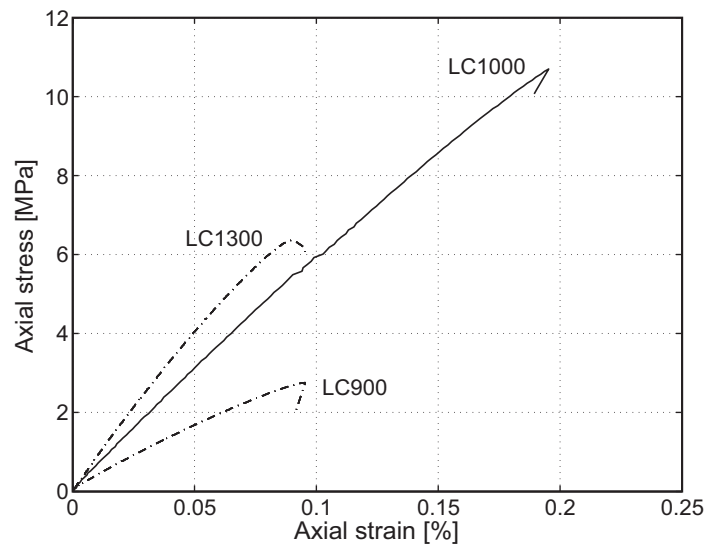


Figure 3.3: Stress-strain responses from representative LC900/1000/1300 cylinders.

all LCs. Magnitudes of stiffness and density showed a good correlation, whereas compressive strength and density exhibited no correlation. In addition, mean splitting tensile strengths, $f_{lctsp,m}$, were determined according to Swisscode SIA 262 for each mixture. The LC densities were also measured on the cylinders after storage in a climate room at 20°C and 95% humidity for 28 days. The variation in the oven-dry density was assumed to be less than 10%. The results of the material properties are summarized in Table 3.3 (average values and standard deviations). For further description of the material properties see Appendix B (on DVD).

3.2.1.3 Assumption concerning material brittleness

The principal results of the investigations by Faust [FV99], [Fau03] and Wille [WDT05] of the fracture mechanical properties of LCs were presented in Section 2.2. Table 3.4 repeats representative values of characteristic lengths of LCs comparable to the experimentally investigated LCs, see also Tables 2.2 and 2.3. The LC compressive strengths of the selected reference LC compositions were determined on cubes and not on cylinders as in the

Table 3.3: Material properties of lightweight concretes.

LC labeling	LC type	LC density [kg/m ³]	Cylindric compressive strength [MPa]	Young's modulus [GPa]	Splitting tensile strength [MPa]
LC900	SLWAC	882 ± 10	2.1 ± 0.7	3.5 ± 0.2	0.65 ± 0.07
LC900-c	SLWAC	870 ± 19	2.0 ± 0.6	-	-
LC1300	SLWAC	1294 ± 70	5.6 ± 1.2	8.7 ± 1.0	1.30 ± 0.17
LC1300-c	SLWAC	1323 ± 100	6.3 ± 3.0	-	-
LC1000	ALWAC	1003 ± 1	10.3 ± 1.1	6.6 ± 0.5	1.44 ± 0.10
LC1000A	ALWAC	991 ± 5	9.03 ± 1.7	6.3 ± 0.2	1.24 ± 0.11

present experimental study. Although LC compressive strengths obtained from cylinders are approximately 10% lower than LC cubic compressive strengths (according to Faust [Fau03]), the chosen LCs exhibited higher compressive strengths than the experimentally investigated LCs.

Table 3.4: Typical values of characteristic length of lightweight and normal concretes taken from [FV99], [Fau03] and [WDT05]; (NS=normal sand, LS=lightweight sand, EC=expanded clay, EG=expanded glass).

Concrete type	Cubic compressive strength [MPa]	l_{ch} [mm]
SLWAC with NS and EC: $\rho_a = 0.83 \text{ kg/dm}^3$	20	150
SLWAC with NS/EC and EC: $\rho_a = 0.83 \text{ kg/dm}^3$	30	125
ALWAC with EG and EC: $\rho_a = 0.83 \text{ kg/dm}^3$	20	40
ALWAC with LS and EC: $\rho_a = 0.83 \text{ kg/dm}^3$	24	40

However, since the experimentally investigated LCs were composed of similar lightweight aggregates (expanded clay aggregates with densities lower than $\rho_a = 0.83 \text{ kg/dm}^3$) and no silica fume was added to the compositions, values of 150 mm and 40 mm were assumed for the SLWAC and ALWAC respectively.

3.2.2 Material properties of face layer materials

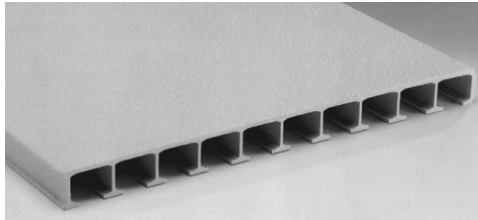
For the NC-layer a standard mixture of self-compacting concrete was used, composed of Portland cement, filler, plasticizer, gravel, sand and water. The NC compressive strength and Young's modulus for each beam pouring were measured on three compression cylinders of $\varnothing = 160 \text{ mm}$ and a height of 320 mm. The results are summarized in Table 3.5 (average values and standard deviations), with the NC labeled according to the corresponding beams.

Additionally, three cylinders from the S2 series were tested for splitting tensile strength. The average value was 3.1 ± 0.2 MPa.

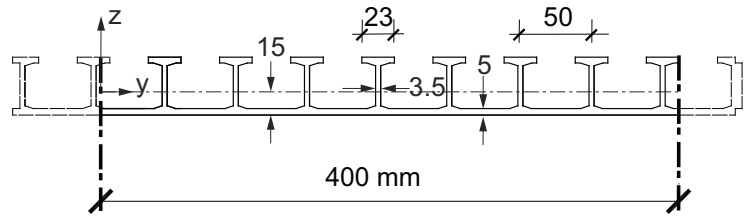
Table 3.5: Material properties of normal concrete.

NC type	Density [kg/m ³]	Compressive strength [MPa]	Young's modulus [GPa]
NC-(900)	2327 ± 13	46.4 ± 1.3	29.9 ± 3.0
NC-(1300)	2317 ± 17	45.1 ± 0.8	31.2 ± 1.3
NC-(1000)	2327 ± 6	59.7 ± 1.8	30.8 ± 0.8
NC-(1000A)	2370 ± 6	53.4 ± 0.8	27.1 ± 4.4

The 40HDx500 GFRP Plank profile from Fiberline, shown in Figure 3.4, consisted of E-glass fibers (approximately 45% by vol.) and a polyester resin and exhibited a tensile strength of 240 MPa and a Young's modulus of 23 GPa, [Fib04]. The Plank profile weighs approximately 17 kg/m². The dimensions of the GFRP profiles used in the experiments are 3600 mm x 400 mm. Therefore both lateral sides of the 40HDx500 Plank profile were cut as in Figure 3.4-b. The sheet depth was 5 mm, the depth and height of the T-upstands were 3.5 and 40, the distance between them 50 mm, and the total weight 17 kg/m². The geometric properties of the Plank are given in Table 3.6.



(a) 40HDx500 Plank profile



(b) Profile dimensions

Figure 3.4: GFRP Plank profile.

Table 3.6: Geometric properties of GFRP Plank profile.

A [mm ²]	I _y [mm ⁴]	Neutral axis z _s [mm]	W _{y,top} [mm ³]	W _{y,bottom} [mm ³]
3615	8.51×10^5	15	56019	34315

The cold-curing two-component epoxy adhesive used for the FRP-LC interface was SikaDur 330 from Sika with an axial tensile strength of 38 MPa, see also [KV05a].

3.3 Experiments on hybrid beams

3.3.1 Beam description

3.3.1.1 Beam dimensions and parameters

The experimental program for the twelve long-span experiments consisted of two series, S1 comprising an SLWAC as core material and S2 comprising an ALWAC. Both series consisted of 3600-mm-long, 400-mm-wide and 200-mm-deep beams. Figure 3.1 on page 40 shows the beam cross section. For the FRP layer, 3.60-m-long standard pultruded 40HDx500 GFRP Plank profiles from Fiberline [Fib04] were used, cut on both sides to a width of 400 mm. A 30-mm-deep normal concrete (NC) layer was applied onto the top.

In series S1, SLWAC concretes of an average density of 900 and 1300 kg/m³ were used (low and high density). In addition, two types of FRP-LC interfaces were investigated as previously described: unbonded and adhesively bonded. The epoxy adhesive used was applied onto the top of the FRP sheet and of the T-upstands. The webs of the T-upstands were only partially covered (lower half approximately) for practical reasons. The weight of the beams with lower LC density was 230 kg/m³ and that of those with higher density 290 kg/m³ and, therefore, 46 or 58% of the weight of a normal concrete beam of the same depth (weight 500 kg/m³).

An ALWAC mixture was used in S2, enabling a low density of 1000 kg/m³ to be maintained by replacing the sand aggregates with expanded glass aggregates, thereby improving compressive strength considerably. Four types of FRP-LC interfaces were investigated in S2: pure mechanical interlocking between the LC and FRP T-upstands and adhesive bonding as already investigated in S1. Both were also investigated with the LC over the supports being replaced by NC anchor blocks, which was predicted to prevent FRP-LC debonding at this location (observed for unbonded S1 beams) and crack propagation over the support (observed for bonded S1 beams). The geometry of the NC anchor blocks is shown in Figure 3.5. For one experiment, the FRP-NC and FRP-LC interfaces were adhesively bonded (similarly to the bonded beams of S1), for the second experiment, only the FRP-NC interface was adhesively bonded and the FRP-LC interface (between the anchor blocks) remained unbonded (only mechanical interlocking). Table 3.1 on page 39 gives an overview of all investigated beam configurations and their labeling. For each configuration two beams were examined in S1 (the first one fully and the second one low instrumented) and one beam in S2.

3.3.1.2 Beam manufacturing

The FRP profiles were equipped with strain gages (see below for disposition) and integrated into a timber formwork in the laboratory. The FRP surface of the bonded beams was roughened with a grinding machine on the T-upstands and with emery paper in between.

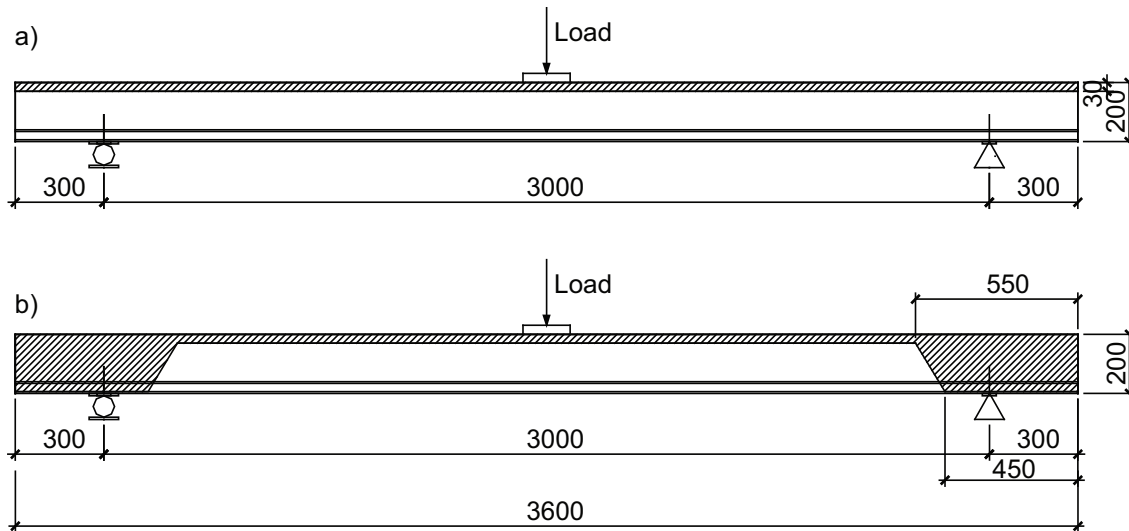


Figure 3.5: Dimensions of (un)bonded and anchored beams.

During the roughening process, special care was taken not to damage the rovings. After roughening, the surfaces were cleaned using acetone. For beams 1000A and 1000EA a special formwork was installed to protect the anchor blocks from the LC casting. At a concrete plant, the epoxy adhesive was then applied and the lightweight concrete was cast onto the wet epoxy, or directly onto the FRP surface for the unbonded beams, and compacted with a vibrator. Compacting was very difficult however, particularly for the lower density LC. In the last step, the NC layer was applied directly onto the fresh LC. For beams 1000A and 1000EA the anchor formworks were removed after the LC had been compacted, the epoxy adhesive was then applied onto the GFRP profiles and the NC was subsequently cast at the beam ends and onto the fresh LC layer. The fluid composition of the thin NC layer enabled good distribution over the beam. In the laboratory, the beams were painted white to better observe the cracking process. While the LC surface of the SLWAC beams was very rough and predominately defined by the lightweight aggregates, the surface of the ALWAC beams was smooth and the lightweight aggregates were fully embedded in the cement paste.

3.3.2 Experimental setup and instrumentation

3.3.2.1 Experimental setup and procedure

The experimental setup and instrumentation are shown in Figure 3.6. All beams were simply supported on rollers with a span length of 3000 mm and subjected to three-point bending using a hydraulic jack. A constant displacement rate of 1 mm/min was introduced at mid-span through a steel plate (300 x 400 mm²) and in order to investigate the degree of system ductility,

up to three load cycles were performed at different displacements. The experiments were performed beyond the ultimate load until a pronounced load decrease occurred.

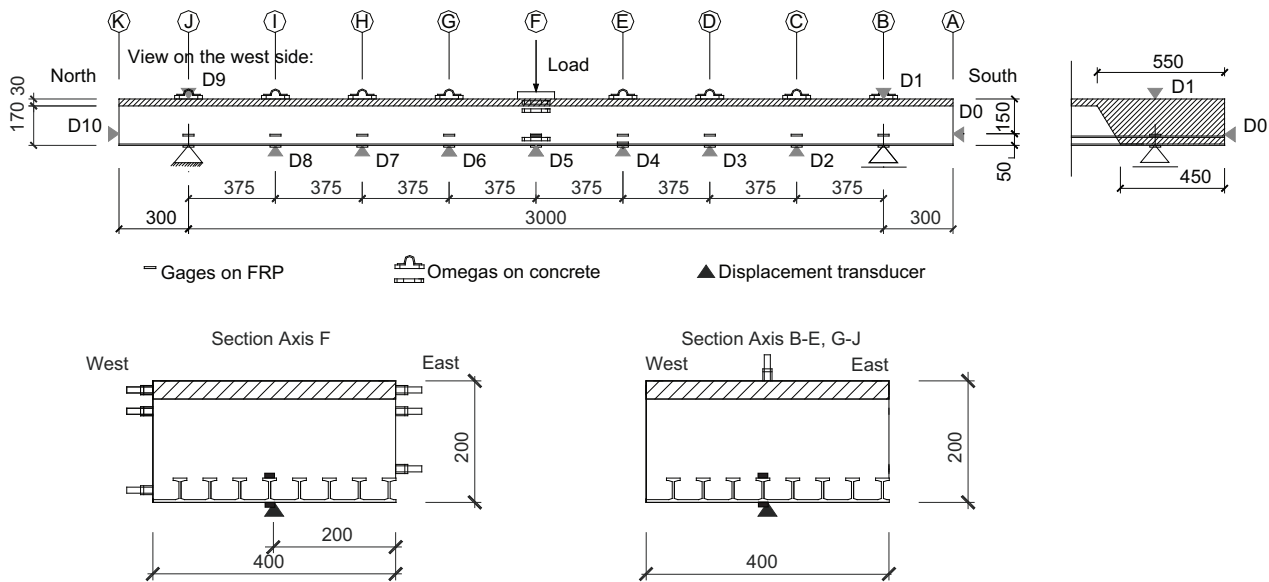


Figure 3.6: Instrumentation of beam series S2.

3.3.2.2 Instrumentation and measurements

The instrumentation of series S1 and S2 was very similar. Figure 3.6 illustrates the typical instrumentation of the S2 beams. The load was measured with load cells between the jack and the steel plate. For all beams, linear voltage displacement transducers (LVDT, accuracy ± 0.10 mm) were used to measure the deflection of the beams along the span in the centerline (D1-9) and the slippage of the LC and NC from the FRP profile at the beam ends (D0, D10). Up to 20 strain gages on the top and bottom faces of the FRP sheet and on top of the T-upstands and up to 30 omega-shaped extensometers on the NC and LC concretes were applied to measure strain distributions through the cross sections at different axes on both beam sides and in the centerline (only FRP sheet with T-upstands). Strain gages of type 6/120 LY 11 produced by HBM (Hottinger Baldwin Messtechnik) with a grid size of 2.8×6 mm and an electric resistance of 120Ω were used. Omega-shaped extensometers of type PI-2-100 produced by Tokyo Sokki Kenkyujo (accuracy ± 0.01 mm) enabled axial concrete displacements over a gage length of 100 mm to be measured. For further details and setup description, see also Appendix C (on DVD).

3.3.3 Experimental results - S1 series

3.3.3.1 Load-deflection response and failure mode of unbonded SLWAC beams

The load-deflection curves at mid-span measured for the unbonded beams with low LC density (beams 900-1, 900-2) and high LC density (beams 1300-1, 1300-2) are shown in Figure 3.7. The four beams showed an almost linear-elastic response up to 6.8-11 kN when the first small vertical cracks appeared in the tension zone of the LC below the loading plate. The cracks always propagated through the LC aggregates, following which the response of the beams with low and high LC densities changed.

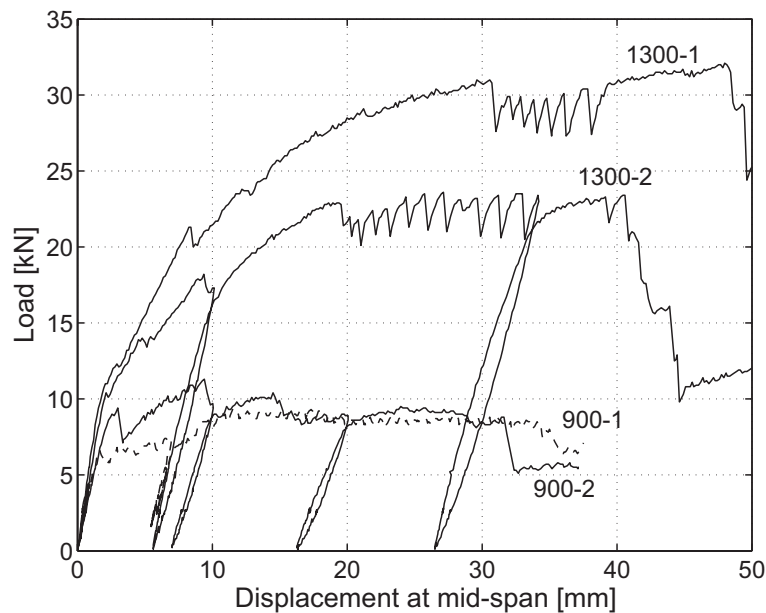


Figure 3.7: Load-deflection response of unbonded beams.

After the first cracking, the load of the beams with high density could be increased significantly up to a first peak (at 31.0 kN for beam 1300-1 and 22.8 kN for 1300-2). During this phase, further cracks formed in the LC below the loading plate region. Also, the LC started to debond from the FRP sheet (at 20.7 kN for 1300-1 and 17 kN for 1300-2) and stiffness decreased slightly. Increased slippage at the beam end was measured from this load on, as shown in Figure 3.8. After this first load peak, an oscillating load phase was observed for both beams as the displacement was increased, while at each intermediate peak a loud crack was audible and the load dropped slightly before increasing again. For beam 1300-2, two additional load cycles (from zero load back to the maximum load) were performed, one before the first load peak and the other after the oscillating phase. Both cycles showed almost unchanged beam stiffness with large remaining deformations. The cracks in the LC did not close during unloading. After the oscillating phase, a slight yet steady load increase was

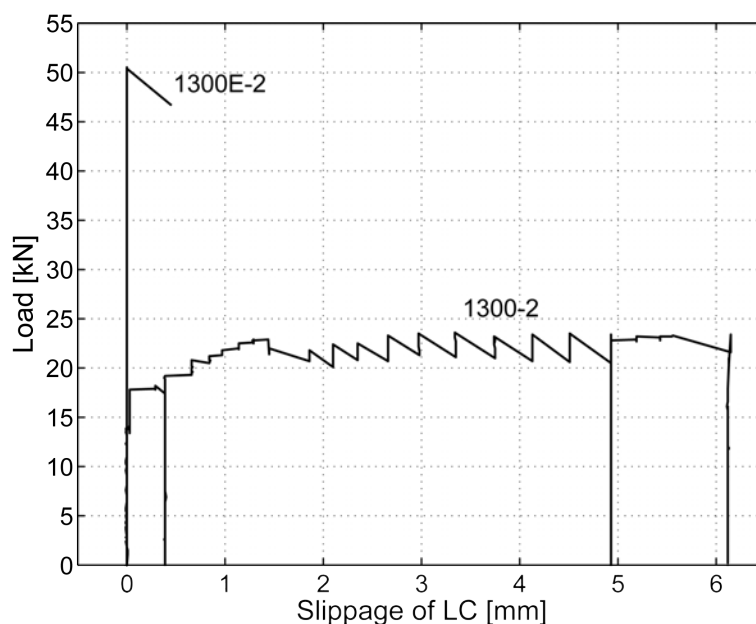


Figure 3.8: LC slippage relative to FRP sheet at beam ends (beams 1300-2 and 1300E-2).

observed up to ultimate load. In this last loading phase, a single crack developed slowly through the whole depth of the beam and then horizontally along the LC-NC interface to the loading plate and along the top of the T-upstands to the support, as shown in Figures 3.9 and 3.10. The same behavior was observed for both 1300-1 and 1300-2 beams. The LC was

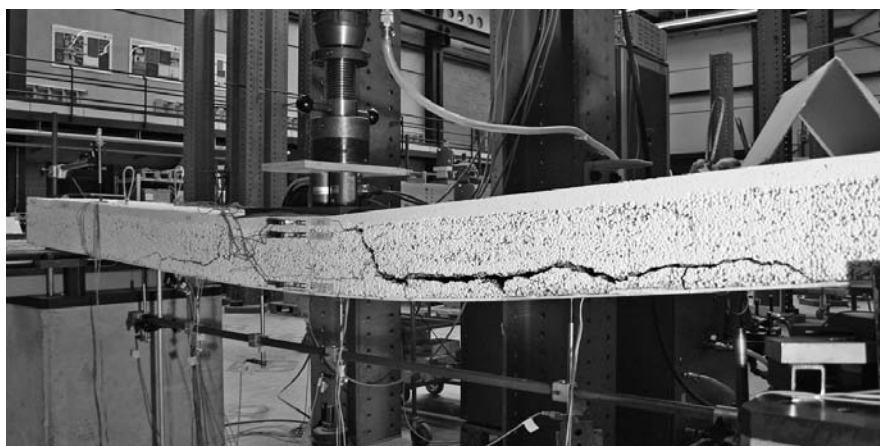


Figure 3.9: Failure pattern of unbonded beam 1300-1.

further pushed out at one beam end as shown in Figure 3.11. After the sudden drop in load, the crack, which always propagated through the LC aggregates, reached the support. The experiments were stopped at this point.

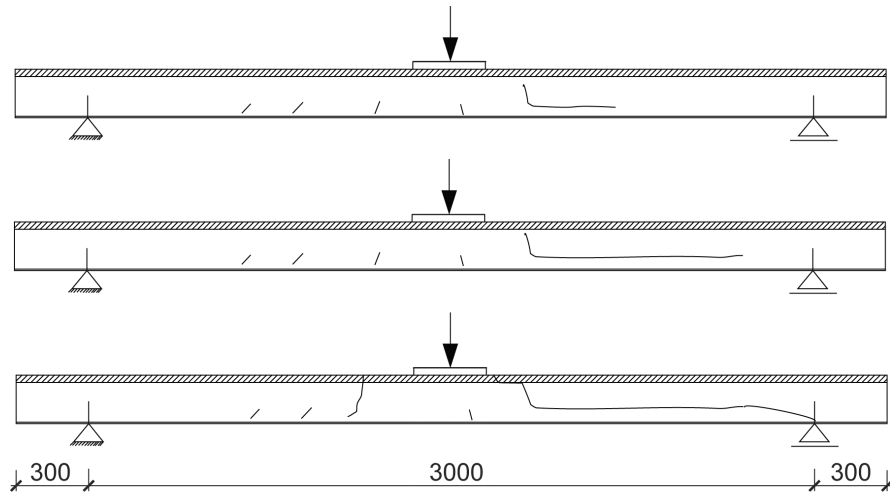


Figure 3.10: Schematic failure process of unbonded beams.

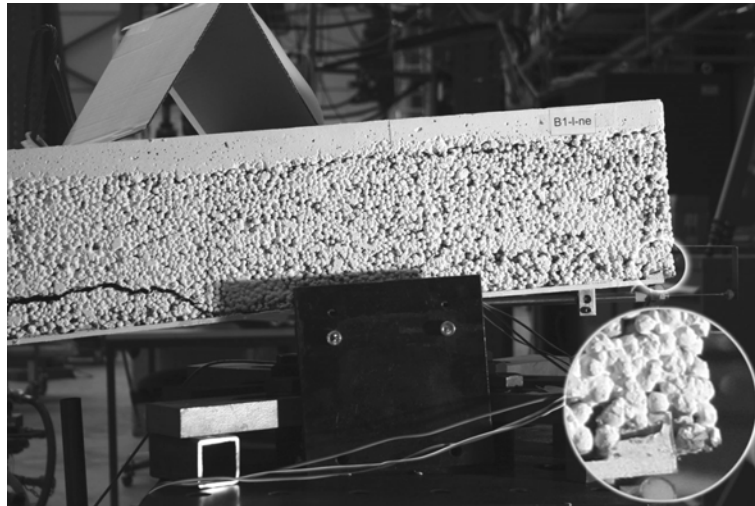


Figure 3.11: LC slippage relative to FRP sheet of unbonded beam 1300-1.

The load of the beams with low density LC could only be slightly increased up to the ultimate load after the first cracks were observed (from 6.8 to 9.3 kN for 900-1 and 9.2 to 11.3 kN for 900-2). During this phase, more cracks formed and stiffness decreased. At ultimate load, the LC started to debond from the FRP sheets and slippage between LC and FRP could be measured at the beam end. A second load cycle (from zero to maximum load) performed for beam 900-1 in this phase showed a remaining deformation of ~ 5 mm. The maximum load of beam 900-1 could be maintained up to a mid-span deflection of ~ 17 mm, after which the load started to decrease slightly up to a 34-mm deflection. After this point a sharp drop in the load was observed. The load of beam 900-2 started to decrease slightly immediately after ultimate load up to a mid-span displacement of 32 mm, when a sharp drop also occurred.

However, two additional loading cycles still showed almost the same beam stiffness as in the first cycle and increasing remaining deformations. During this phase, the same failure mechanism developed as described for the unbonded beams with higher density, although at significantly smaller deflections and lower loads. The cracking and ultimate loads of the four unbonded beams and corresponding mid-span deflections are listed in Table 3.7 on page 54.

3.3.3.2 Axial strain distributions of unbonded beams

The mid-span strain distribution through the depth of unbonded beam 1300-2 is shown in Figure 3.12 at different loads (25, 50, 75, and 100% F_u) up to the ultimate load (F_u). The upper points were calculated from the omega gage displacements on the two concretes

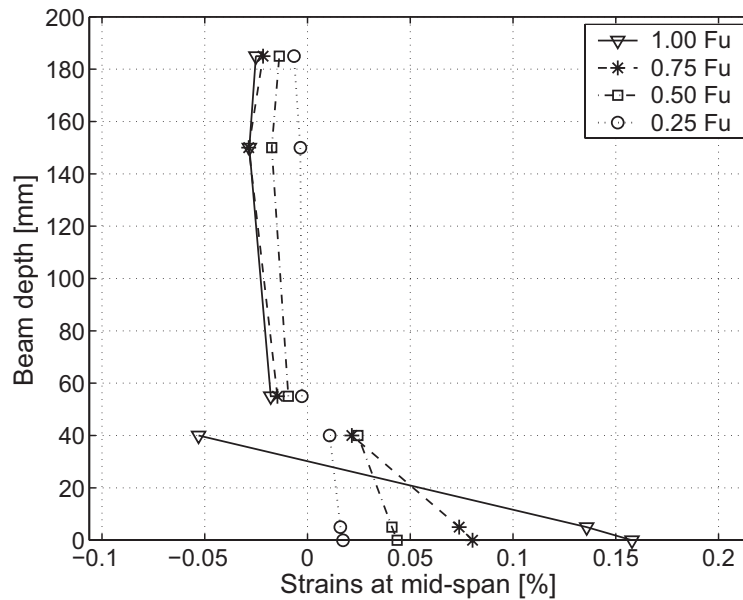


Figure 3.12: Mid-span strain distributions through depth of unbonded beam 1300-2.

(measured displacements divided by gage length), while the lower points were measured from strain gages on the T-upstands and top and bottom sheet surfaces. The two different methods explain the small shift between upper and lower lines (between LC and FRP) at 0.25 F_u (when full composite action was still present). The curves show that the axial strain distributions did not remain plane through the depth of the cross section. Debonding between LC and FRP occurred between 0.50 and 0.75 F_u and an increasing part of the load was borne only by the FRP sheet with the T-upstands. At ultimate failure, compressive strains were even measured in the upper flanges of the T-upstands.

3.3.3.3 Load-deflection response and failure mode of bonded SLWAC beams

The load-deflection curves at mid-span measured for the bonded beams with low density LC (900E-1, 900E-2) and high density LC (1300E-1, 1300E-2) are shown in Figure 3.13.

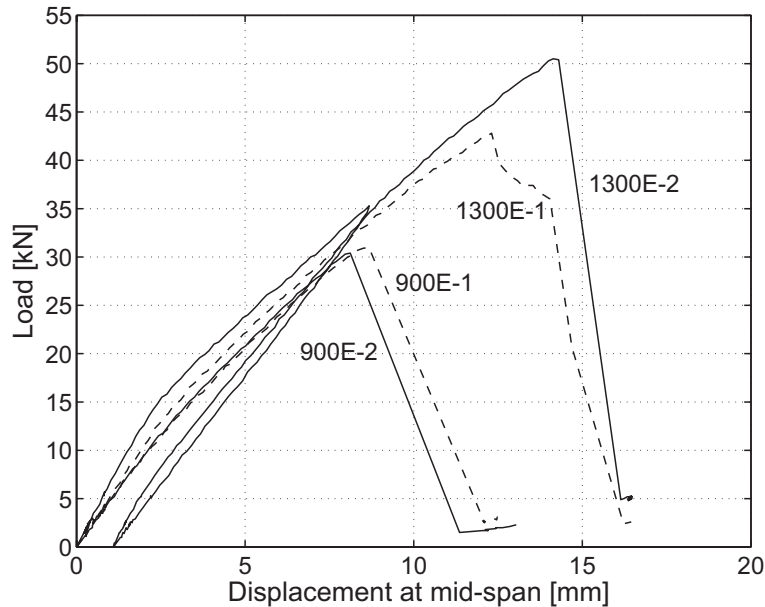


Figure 3.13: Load-deflection response of bonded beams.

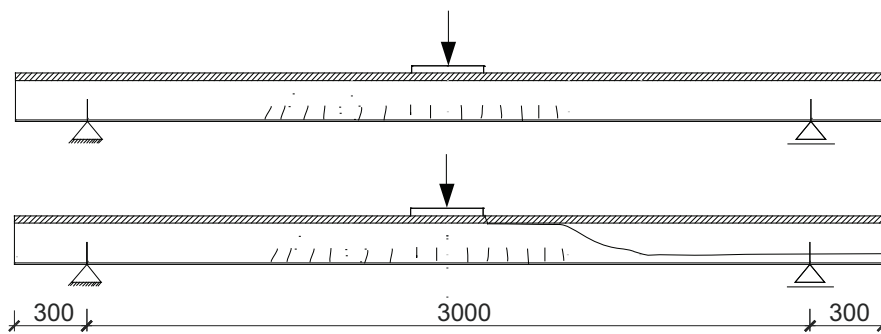


Figure 3.14: Schematic failure process of bonded beams.

The responses of all four beams showed a slight yet steady decrease in stiffness up to ultimate failure, which occurred at 31.2/30.4 kN for beams 900E-1/2 and 42.8/50.5 kN for beams 1300E-1/2. A second cycle performed at 35.4 kN for beam 1300E-2 showed a small remaining deformation of 1.1 mm and a stiffness identical to that observed at the beginning of the experiment. The first cracks in the tension zone of the LC were observed between 10 and 13 kN for all beams. Subsequently, a multitude of small vertical or slightly inclined cracks (up to 15) developed in the tension zone below the loading plate, with an average crack spacing of

110 mm. At ultimate failure, one of the cracks suddenly propagated through the depth of the beam, along the LC-NC interface to the loading plate in one direction and along the top of the FRP T-upstands, just above the FRP-LC interface, to the support and on to the end of the beam in the other direction (Figures 3.14- 3.16). The epoxy-bonded interfaces remained undamaged. The beams showed no debonding of the LC from the FRP and no slippage at the beam end was measured (see beam 1300E-2 in Figure 3.8). After brittle failure, the load dropped and the experiments were stopped. The cracking and ultimate loads of the four bonded beams and corresponding mid-span deflections are also listed in Table 3.7.



Figure 3.15: Failure pattern of bonded beam 1300E-2.

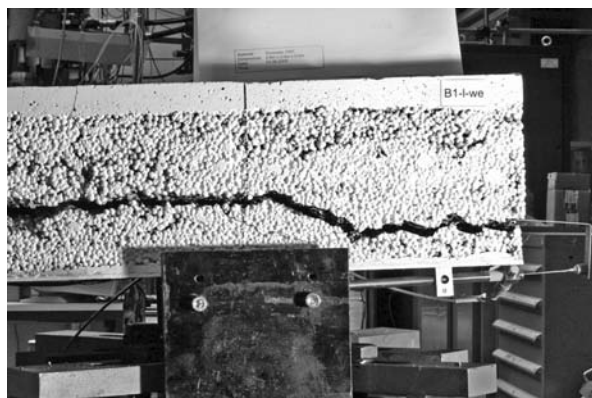


Figure 3.16: Failure pattern of bonded beam 1300E-1 at support.

3.3.3.4 Axial strain distributions of bonded beams

Figure 3.17 shows the mid-span strain distributions through the depth of the bonded beam 1300E-2, again at the four load steps up to the ultimate load (F_u). The axial strain

distributions remained plane up to ultimate load and the strains increased almost linearly with increasing load. The neutral axis was very high, approximately ~ 15 mm below the NC in the LC.

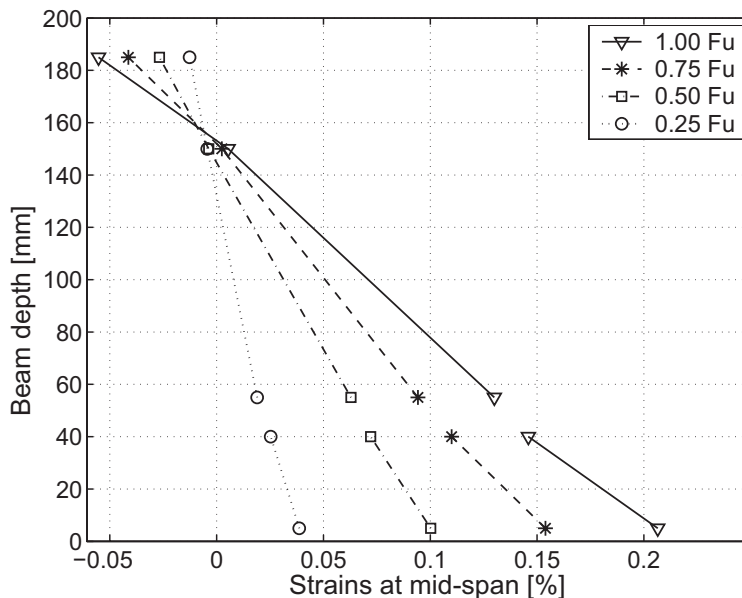


Figure 3.17: Mid-span strain distributions through depth of bonded beam 1300E-2.

Table 3.7: Experimental results at ultimate load for SLWAC beams (negative signs = compression).

Beam	Ultimate load [kN]	Cracking load [kN]	Mid-span deflection [mm]	Axial stress		
				NC [MPa]	LC [MPa]	FRP [MPa]
900-1	9.3	~ 6.5	11.5-17.3	-3.3	-0.8	11.8
900-2	11.5	~ 7.5	9.4	-3.7	0.0	12.6
1300-1	32.1	~ 9.5	47.8	-10.0	0.3	30.5
1300-2	23.3	~ 10.0	40.4	-9.0	0.2	30.2
900E-1	31.2	~ 10.5	8.7	-9.9	-1.7	49.5
900E-2	30.4	~ 11.5	8.1	-8.4	-1.8	35.7
1300E-1	42.8	~ 13.0	12.3	-15.6	-2.5	42.6
1300E-2	50.5	~ 12.5	14.1	-15.6	1.7	47.8

3.3.4 Experimental results - S2 series

3.3.4.1 ALWAC beams 1000 and 1000E

The load-deflection response of the ALWAC beams 1000 (unbonded) and 1000E (bonded) is illustrated in Figure 3.18, while the cracking and ultimate loads of the beams and corresponding mid-span deflections are listed in Table 3.8.

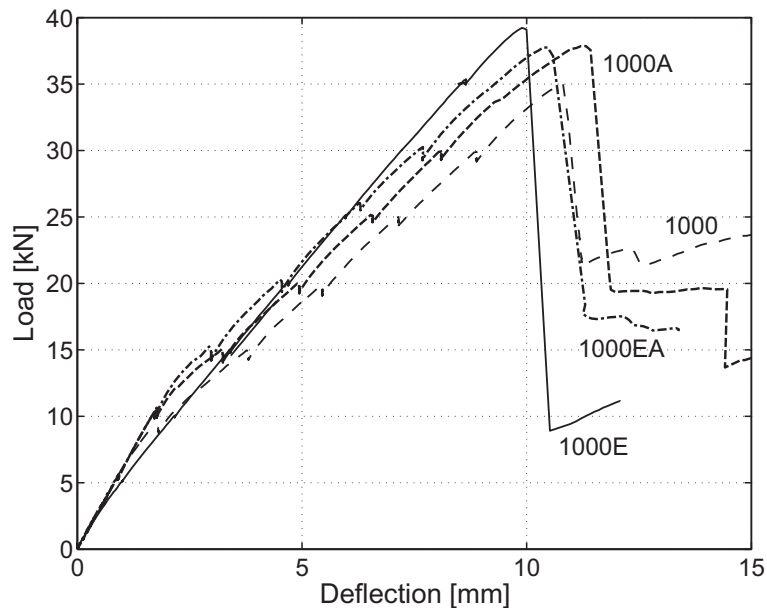


Figure 3.18: Load-deflection response of ALWAC beams.

After the formation of the first cracks in the LC tension zone below the jack at a load of approximately 9 kN, beam 1000 exhibited a slight loss of stiffness, which then remained almost unchanged until the ultimate load of 35.0 kN, although further vertical cracks developed towards the beam supports with crack spacings of approximately 15 cm, see Figures 3.19 and 3.20. The cracks progressed up to the neutral axis of the beam and reached widths of 0.1 to 0.15 mm at 25 kN (last measurement). At 35 kN one crack suddenly opened vertically through the depth of the LC and developed progressively along the LC-NC interface to the loading plate and along the top of the T-upstands towards the support. The corresponding crack pattern of the beam at ultimate load is shown in Figure 3.20. Figure 3.21-a shows that no relative displacement between LC and FRP sheet was measured at the beam end. The LC core debonded from the FRP sheet and slippage occurred only after ultimate failure. This result appears contradictory to the measured axial strain distribution through the depth of the cross section at mid-span, shown in Figure 3.21-b. The curve exhibits a small offset between the LC core and FRP sheet, indicating a loss of full composite action. This offset was observed from the beginning of the experiment however and could be ascribed to the

different types of gages used rather than a loss of composite action (omega gages on the LC and strain gages on the FRP).

The load-deflection response of beam 1000E was similar to that of beam 1000, see Figure 3.18. However, after the first cracking at 8.0 kN, the behavior was markedly stiffer than that of beam 1000. At 25 kN, the cracked region covered half of the span, with an average crack spacing of 8 cm and crack widths of approximately 0.02-0.1 mm. With increasing load, the cracks closest to the beam ends became increasingly inclined, as shown in Figure 3.22. At the ultimate load of 39.2 kN, a new and even more inclined crack suddenly propagated through the depth of the beam, along the LC-NC interface to the loading plate and along the top of the FRP T-upstands to the beam end, see also Figure 3.19. Subsequently the load dropped and the experiment was stopped. The shearing surface was observed predominately above the FRP T-upstands and propagated through the LC aggregates. As shown in Figure 3.21-a, no

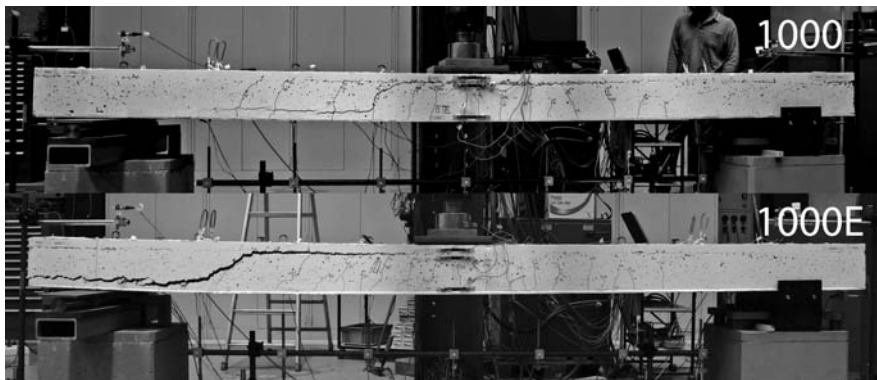


Figure 3.19: Crack patterns at ultimate load for beams 1000 and 1000E.

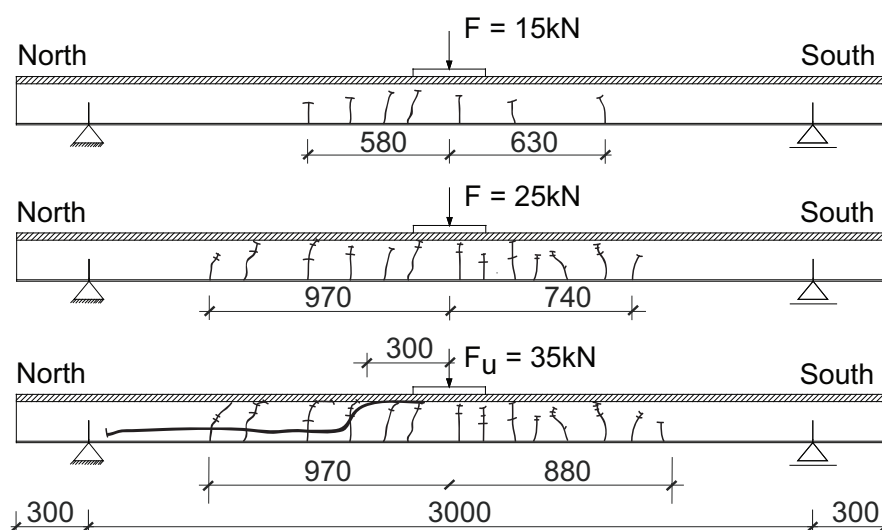


Figure 3.20: Schematic failure process of unbonded beam 1000.

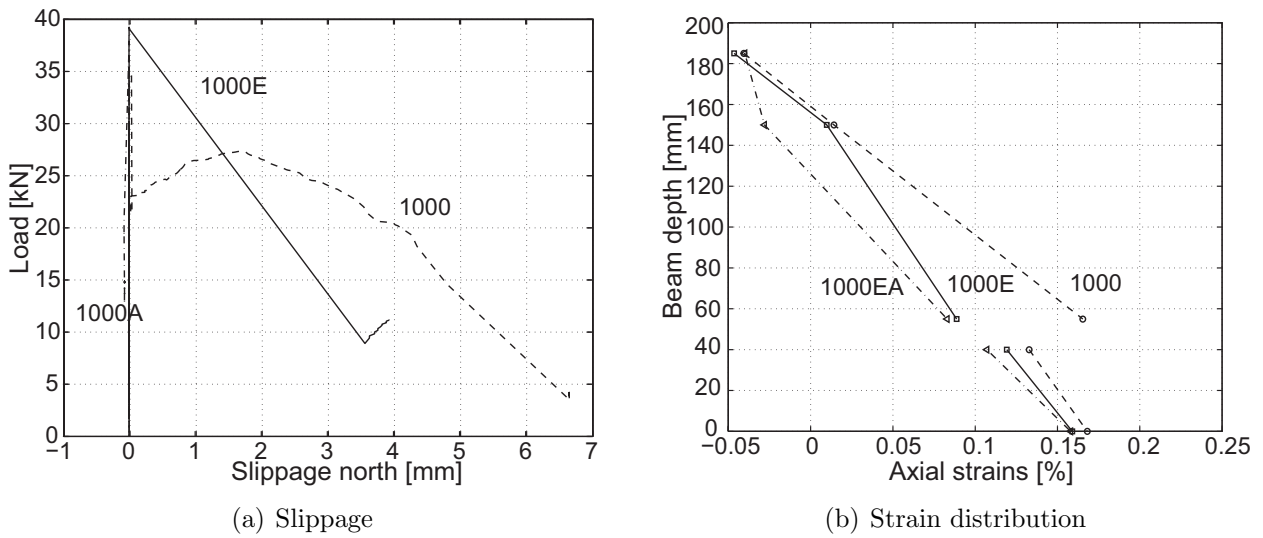


Figure 3.21: Relative displacement between LC and FRP sheet (slippage) at northern beam end and mid-span strain distributions through beam depth at ultimate load.

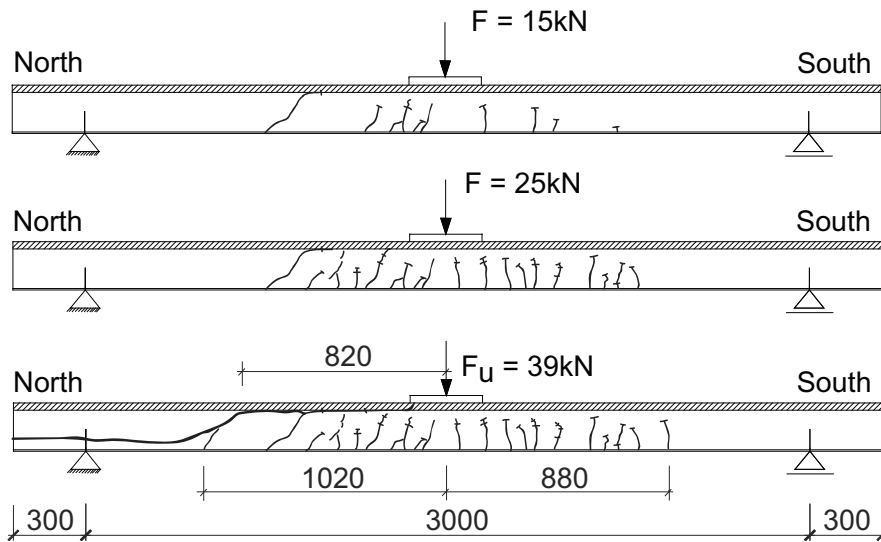


Figure 3.22: Schematic failure process of bonded beam 1000E.

slippage at the beam end was measured until ultimate failure. Figure 3.21-b shows a linear axial strain distribution through the depth of the beam at ultimate load; the continuous distribution indicates full composite action between the cross-sectional parts.

Table 3.8: Experimental results at ultimate load for ALWAC beams (negative signs = compression).

Beam	Ultimate load [kN]	Cracking load [kN]	Mid-span deflection [mm]	Axial stress		
				NC [MPa]	LC [MPa]	FRP [MPa]
1000	35.0	~9.0	11.5	-11.7	1.3	38.7
1000E	39.2	~8.0	9.9	-11.5	1.1	38.6
1000A	37.6	~5.0	11.4	-10.4	0.2	37.3
1000EA	37.1	~5.0	10.6	-10.2	-0.8	36.0

3.3.4.2 ALWAC beams 1000A and 1000EA

The load-deflection curves of beams 1000A and 1000EA lay between those of beams 1000 and 1000E, while beam 1000EA was slightly stiffer than beam 1000A. Similarly, average crack spacings and crack widths ranged between the corresponding values of beams 1000 and 1000E. Visible cracking of both beams initiated at approximately 5 kN; beam stiffness markedly decreased only at 11-12 kN however. During loading, the upper part of one vertical crack started to turn towards midspan for each beam. At the ultimate loads of 37.8 kN (1000A) and 37.2 kN (1000EA), these cracks opened significantly and developed simultaneously along the LC-NC interface towards the loading plate and along the FRP-LC interface towards the NC anchor blocks where propagation stopped. The crack pattern at the ultimate load of beam 1000A is shown in Figure 3.23; beam 1000EA exhibited a similar pattern. No slippage was measured at the beams' ends, as illustrated in Figure 3.21-a for beam 1000A, and an almost linear axial strain distribution through the depth of both beams was found, see Figure 3.21-b for beam 1000EA. The cracking and ultimate loads of the beams with anchor blocks and corresponding mid-span deflections are also listed in Table 3.8.



Figure 3.23: Crack patterns at ultimate loads for beams 1000 and 1000E.

3.3.5 Discussion

3.3.5.1 Failure modes

In all investigated beams, shear failure occurred in the LC in one part of the beam, where one crack started to grow diagonally from a flexural crack through the LC depth and then propagated towards the loading plate along the LC-NC interface and towards the support along the FRP-LC interface at the height of the T-upstands. While in the LC of all bonded beams a multitude of vertical cracks developed up to the sudden shear failure, only a few cracks developed in the unbonded beams. Thus crack development could be described as follows: the highest number of cracks together with the smallest crack widths for totally bonded beams; the lowest number of cracks and the largest cracks for totally unbonded beams; intermediate values for unbonded beams with anchor blocks. Failure in the unbonded ALWAC occurred suddenly followed by debonding of the FRP-LC interface, while a slow and ductile failure occurred in the unbonded SLWAC beams. In the latter case, the LC was constantly pushed out at the beam end, while the main crack slowly progressed along the FRP-LC interface and stopped at the support. The main crack in the bonded beams, however, progressed rapidly over the support up to the beam end, always propagating through the LC aggregates. The LC shear strength was therefore lower than the bonded interface shear strength. The crack stopped at the LC-NC interface of the anchor blocks in these beams.

3.3.5.2 Stiffness

The stiffness of the bonded beams could not be correlated to the density and stiffness of the LC, as shown in Figures 3.13 and 3.18, unlike in Figure 3.3; the stiffness portion from the identical top and bottom skins clearly dominated the slightly different stiffness portions of the different cores. The stiffness of all ALWAC beams was almost identical before cracking (Figure 3.18 on page 55). Similarly to the ultimate load, the beam stiffness after cracking depended on the type of FRP-LC interface, with the highest stiffness being exhibited by the fully bonded interface and the lowest by the totally unbonded interface (only mechanical interlocking, without anchor blocks), see Figure 3.18. Intermediate values were achieved for beams with NC anchor blocks and an unbonded FRP-LC interface.

3.3.5.3 Degree of composite action and ultimate loads

All bonded SLWAC and all ALWAC beams exhibited full composite action up to brittle shear failure in the LC core. In the case of unbonded beam 1000, the mechanical interlocking between the LC and FRP sheet was sufficiently strong to provide full composite action up to a sudden shear failure in the LC core. Only then was debonding of the FRP-LC interface

observed. For the unbonded SLWAC beams however, debonding in the interface occurred at lower loads; subsequently, composite action between the concrete and FRP was partially lost and the FRP sheet participated increasingly in the load transfer with increasing load. Thus, the deflections increased considerably up to ultimate failure. The improvement in the case of the unbonded ALWAC beams was ascribed to the superior mechanical behavior of LC1000 compared to the SLWAC LCs. The much higher compressive strength of the former increased the friction resistance at the interface.

The ratio of the ultimate loads of the bonded to the unbonded beams was correlated to the compressive strength of the LC, as shown in Figure 3.24 (correlation coefficient $R^2=0.83$, beams with anchor blocks were not considered here). Due to reduced composite action in the SLWAC beams, the ultimate loads were much smaller than those achieved with bonding, resulting in average ratios of 3.0 for beams with an LC900 core and 1.7 for beams with an LC1300 core. In the case of the ALWAC beams, the ratio was 1.1, corresponding to almost full composite action up to failure.

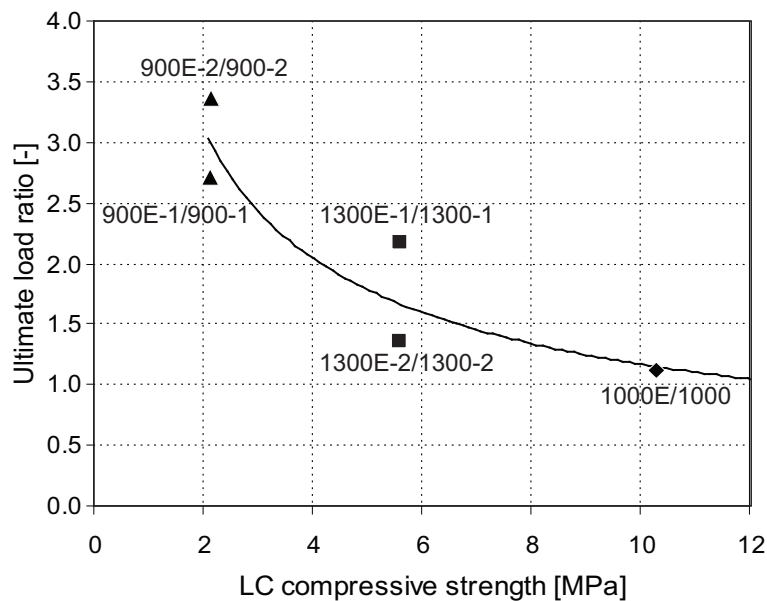


Figure 3.24: Ultimate load ratio of bonded/unbonded beams vs compressive strength of LC core.

The ultimate loads of the beams exhibiting full composite action (bonded SLWAC and all ALWAC beams) were correlated to LC density, with highest values being exhibited by beams with highest densities. This was contrary to the LC compressive strength distribution, where LC1000 recorded the highest compressive strength, as shown in Figure 3.25 (correlation coefficient $R^2=0.22$).

Similarly, almost no correlation was found between the ultimate beam loads and the LC splitting tensile strength, see Figure 3.26 (correlation coefficient $R^2=0.51$). For the ALWAC

beams, the ultimate loads tended to vary with the stiffness of the FRP-LC interface, with descending values from totally bonded interfaces (highest stiffness), to unbonded interfaces with NC anchor blocks, to totally unbonded interfaces (lowest stiffness). The beams with anchor blocks reached similar ultimate loads to those of beam 1000E, indicating that the additional bonding of the FRP-LC interface was not necessary.

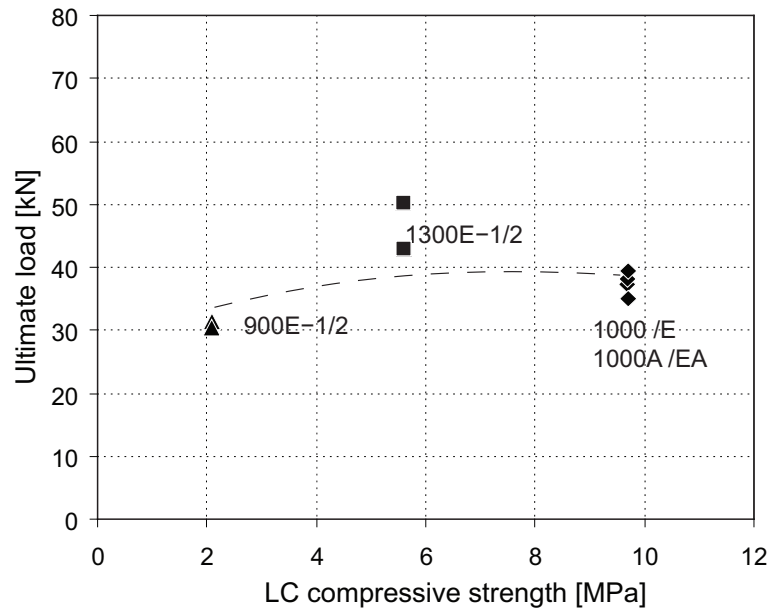


Figure 3.25: Ultimate loads vs compressive strength of LC core.

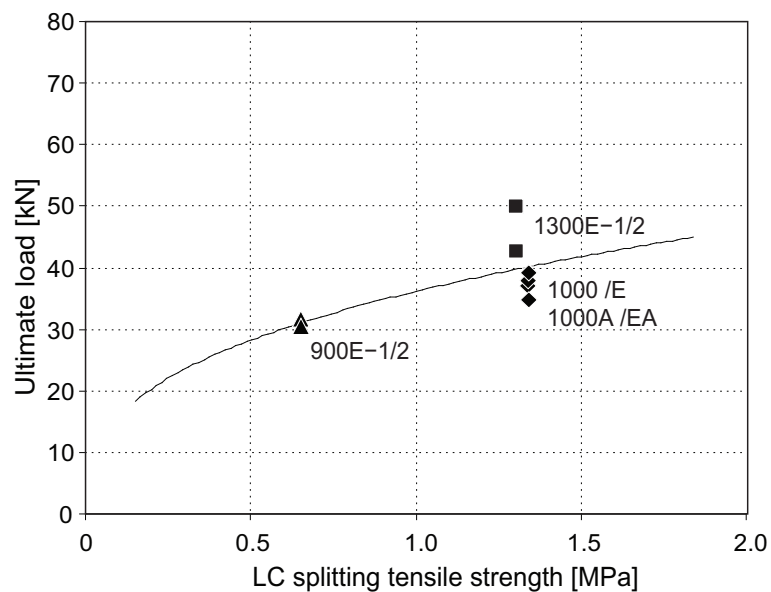


Figure 3.26: Ultimate loads vs splitting tensile strength of LC core.

3.3.5.4 Calculated stresses

Axial stresses were estimated from the measured axial strains at ultimate load and using the Young's moduli given in Tables 3.3 and 3.5 respectively. The results in Table 3.7 and 3.8 respectively (average values from both beam sides) show that the calculated stresses were far below the NC or FRP material strength. This result confirmed that the use of UHPFRC for the experimental beams was not necessary. Furthermore, the FRP sheet was oversized and will require optimization in the next project stage. The LC stresses are very small and sometimes change sign due to the location of measurements close to the neutral axis.

3.3.6 Conclusions

An experimental study was performed on hybrid FRP-concrete sandwich beams. The sandwich core consisted of two different types of lightweight concrete (LC): an SLWAC mixture with expanded clay and sand aggregates and an ALWAC mixture with expanded clay and expanded glass aggregates. All beams exhibited brittle shear failure in the LC core and to summarize, representative load-deflection responses are shown in Figure 3.27. The following conclusions are drawn from the experimental observations:

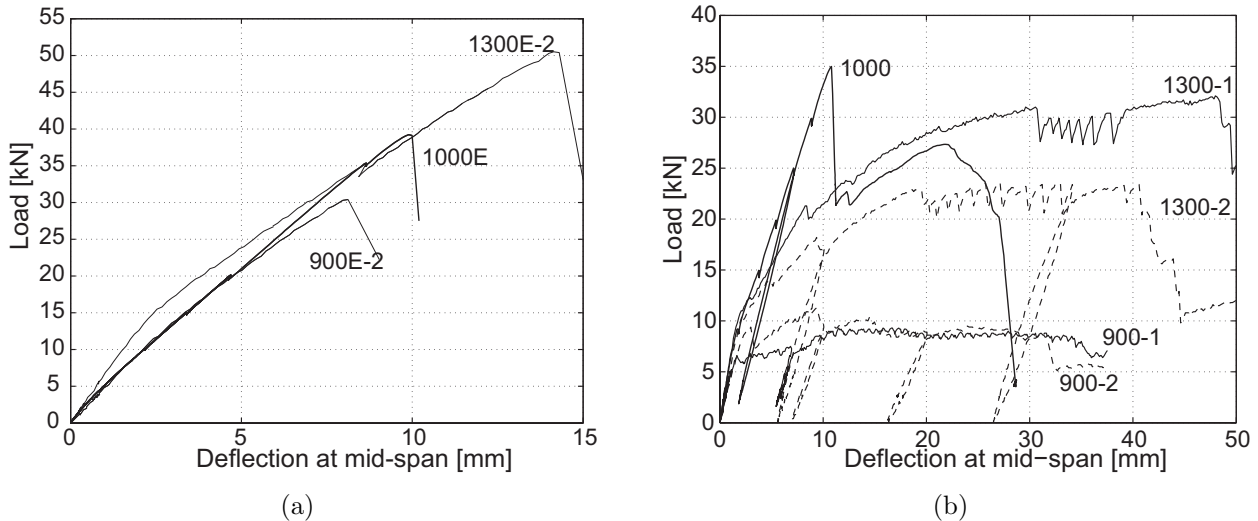


Figure 3.27: Representative load-deflection responses of a) bonded and b) unbonded specimens.

1. The ultimate loads of all beams were correlated to the LC density (higher densities implied higher ultimate loads). No correlation, however, was found between ultimate loads and LC compressive or splitting tensile strength.

2. Beam stiffness could not be correlated to LC density; the stiffness of the identical sandwich skins clearly predominated over the slightly varying stiffnesses of the different cores. For the same LC type, beam stiffness depended on the type of FRP-LC interface: highest stiffness for the adhesively-bonded interface, and lowest stiffness for the unbonded mechanical interlocking between LC and FRP T-upstands.
3. In the case of mechanical interlocking in the FRP-LC interface, interface strength was correlated to LC compressive strength due to the friction mechanism. The unbonded ALWAC beam (with highest compressive strength) exhibited full composite action until ultimate load, in contrast to the unbonded SLWAC beams, which lost their composite action at an early stage due to lower compressive strength. The use of normal concrete anchor blocks with bonded FRP-NC interface can be considered an alternative to the adhesive bonding of the whole FRP-LC interface.
4. Beam manufacture proved to be rapid and easy. Epoxy, LC and NC were applied wet-in-wet without intermediate curing times within less than 30 minutes per beam. From this point of view the fabrication was very economic.

3.4 Experiments on direct load transmission

3.4.1 Experimental specimen, setup and procedure

3.4.1.1 Experimental specimens

In the S3 experimental series, short-span beam specimens 1200 mm long, 400 mm wide and 200 mm deep were cut from the undamaged part of the 3600-mm long beams examined and reported in Section 3.3. The shear span-to-depth ratio was $a/d=1.6$. Figure 3.28 shows the cross section and dimensions of the specimens. The material properties and investigated parameters were described in Sections 3.2 and 3.3. Table 3.1 on page 39 gives an overview of the investigated specimen configurations and their labeling. Eight beam specimens were examined, two specimens for each SLWAC configuration and one specimen for each ALWAC configuration.

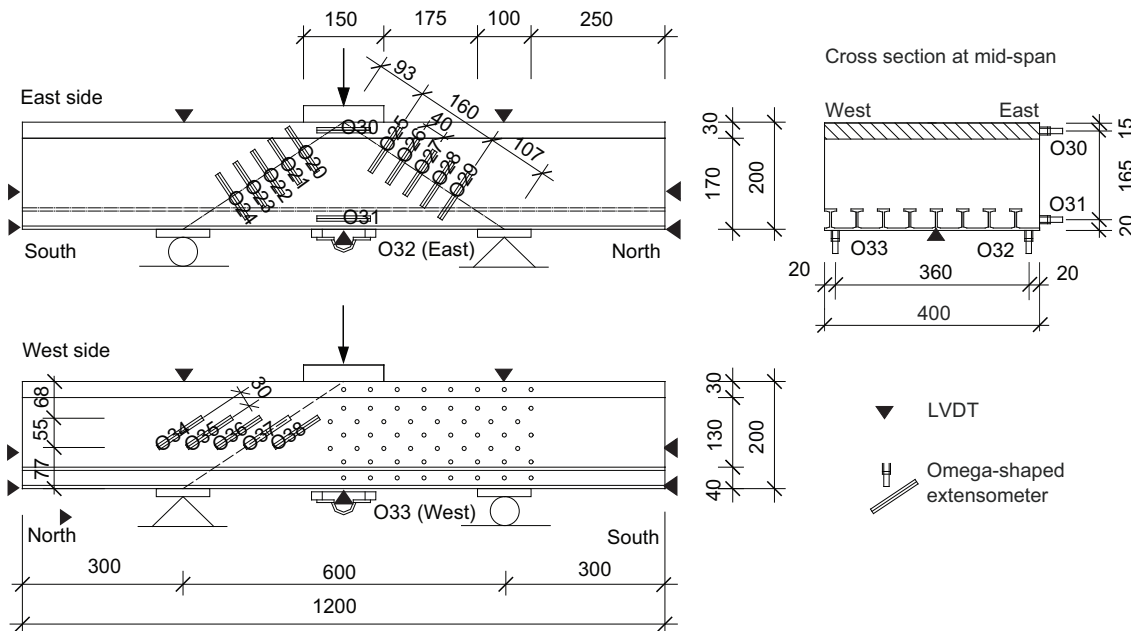


Figure 3.28: Beam dimensions, experimental setup and instrumentation.

3.4.1.2 Setup, instrumentation and measurements

All specimens were simply supported on rollers with a span of 600 mm and subjected to three-point bending using a displacement-controlled hydraulic jack at mid-span on a $150 \times 400 \times 25$ -mm³ steel loading plate (Figure 3.28). The northern roller was fixed, while the southern roller was allowed to move horizontally. The specimens were subjected to a constant displacement rate of 0.12 mm/min until failure. The disposition and labeling of the

instrumentation are shown in Figure 3.28. Linear voltage displacement transducers (LVDTs, accuracy ± 0.10 mm) were used to measure vertical displacements at mid-span, on support sections and differential horizontal displacements between the lightweight concrete and the FRP Plank at both ends of the specimens. Omega-shaped extensometers, type PI-2-100 produced by Tokyo Sokki Kenkyujo (resistance 350 Ω , accuracy ± 0.01 mm), enabled the measurement of deformations (compression and tension) over a gage length of 100 mm on the concrete surface and on the bottom of the FRP sheet. On the east specimen side, 2x5 extensometers (labeled O20-O24 and O25-O29) measured the transverse deformations at distances of 40 mm along each diagonal (lines of direct load transmission from loading axis to the support axes), see also Figure 3.29. On the west side, to measure the longitudinal deformation distribution transverse to the diagonal, extensometers O34-O38 were fixed parallel to the northern diagonal at 30-mm distances (asymmetric arrangement, O37 at diagonal location). In addition, at mid-span, O30 measured the deformations on the NC, O31 on the lower part of the LC (at a height of 20 mm from the bottom of specimen), and O32-O33 on the bottom side of the FRP sheet. For interpretation of the extensometer results, it was assumed that cracks could cross the gage length, as shown in Figure 3.29. Furthermore, a grid of black dots was applied to the western specimen side to record the displacements of the specimen using a digital camera. Due to high scatter and an unsatisfactory analysis of the measurements, the results are not further discussed. For further details see also Appendix D (on DVD).

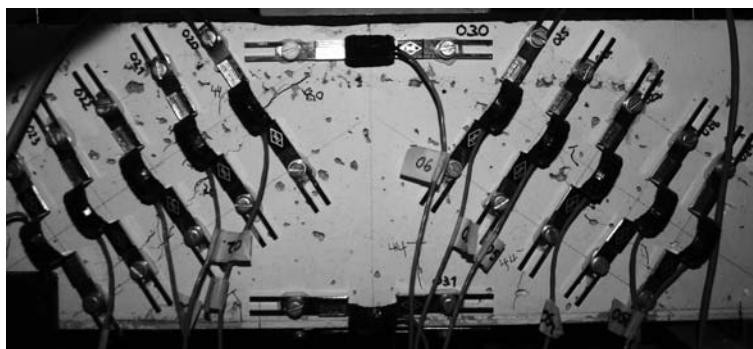


Figure 3.29: Extensometers transverse to compression diagonals (and cracks) and bottom of LC.

3.4.2 Experimental results

3.4.2.1 Unbonded SLWAC specimens

The observed failure process and load-deflection responses of the two unbonded SLWAC specimens (1300s-1 and 1300s-2) were similar; thus only the behavior of specimen 1300s-1 is

described in the following. The load-deflection response, shown in Figure 3.30, was almost linear and no differential horizontal displacements were measured at beam ends up to a load of 40 kN, see Figure 3.31. At this load, a first, almost vertical, crack was noticed 50 mm north of the loading axis. Subsequently, the LC started to be pushed out of the FRP sheet at the northern specimen end (see Figure 3.31) and stiffness decreased (Figure 3.30).

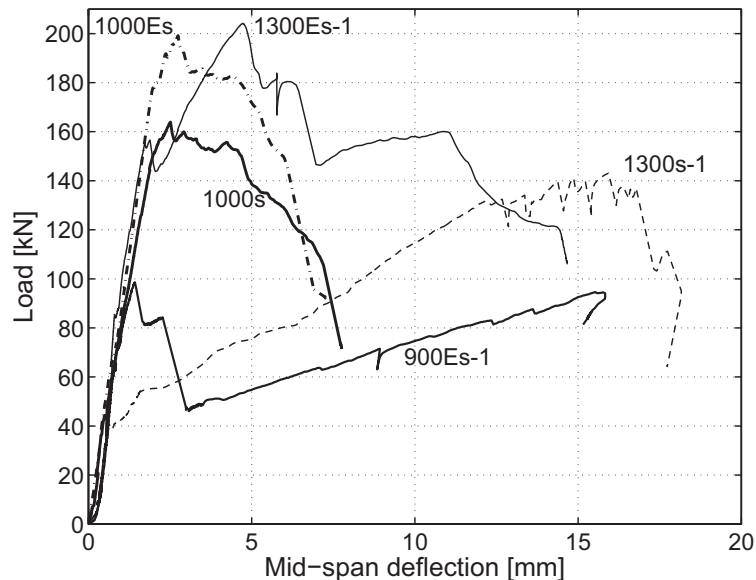


Figure 3.30: Load-deflection responses of representative short-span specimens.

At a load greater than 55 kN, the crack started to propagate through the NC layer, just crossing the O30 gage length. At 132 kN the width of the vertical crack had opened to 15 mm, showing almost complete separation of the northern and southern LC cores. Despite several loud cracks and load drop-offs, the load could be slightly increased up to the ultimate load of 143 kN. At this load the outer T-webs of the FRP sheet exhibited a shear failure at the northern support and the load decreased. Figure 3.32 illustrates the crack pattern of specimen 1300s-1 at ultimate load and Table 3.9 summarizes ultimate loads and loads at the first visual crack of both specimens.

3.4.2.2 Bonded SLWAC specimens

Specimens 900Es-1 and 1300Es-1 behaved similarly to specimens 900Es-2 and 1300Es-2 and therefore only the behavior of the former is described in the following. At 75 kN, a first diagonal crack appeared on the south-east side of specimen 900Es-1. With increasing load, this crack propagated steadily through the whole LC layer, and then propagated horizontally along the LC-NC interface towards mid-span. The ultimate load was reached at 98.3 kN, when a diagonal crack developed next to the northern support. Subsequently the load dropped

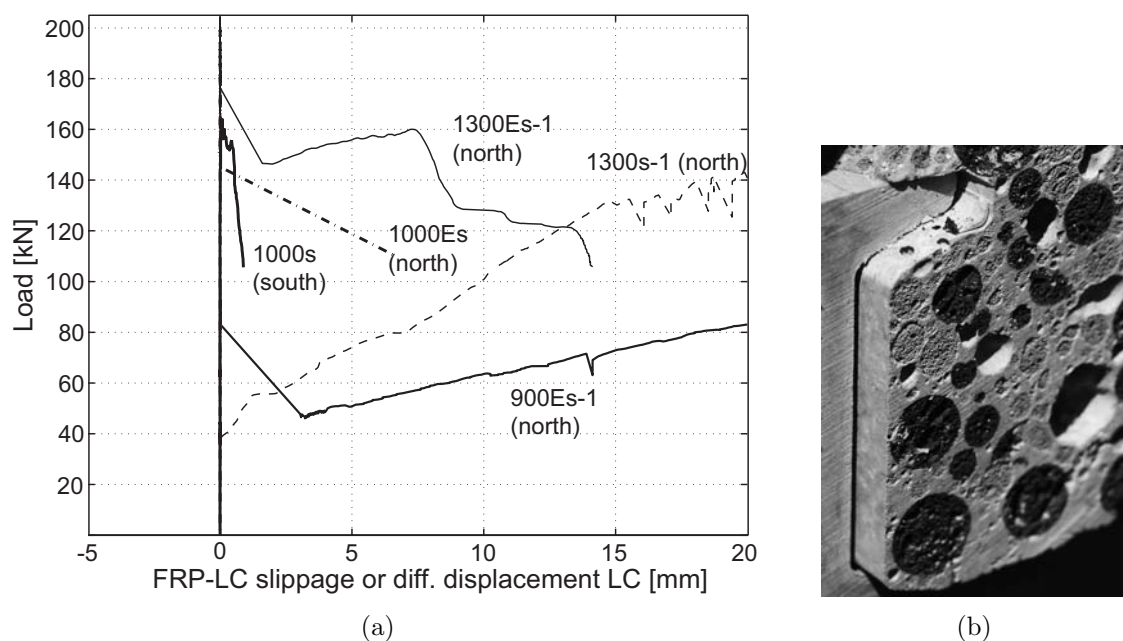


Figure 3.31: Slippage between LC and FRP or differential horizontal displacement within the failed LC at beam end: (a) measured, (b) pushing out of LC from FRP in beam 1000s at end of experiment.

Table 3.9: Ultimate loads, LC cracking loads from visual observation and measurements.

Beam	Ultimate load [kN]	Cracking load at first visual crack [kN]		
		* diagonal crack ** vertical at mid-span	Southern diagonal from O22 [kN]	Northern diagonal from O27 [kN]
1300s-1	143	40**	-	-
1300s-2	146	40**	-	-
900Es-1	98	75*	(72)	70
900Es-2	83	80*	(70-80)	65
1300Es-1	204	85*	87	87
1300Es-2	185	85*	80	80
1000s	164	44*	45	(75)
1000Es	201	35*	50	(68)

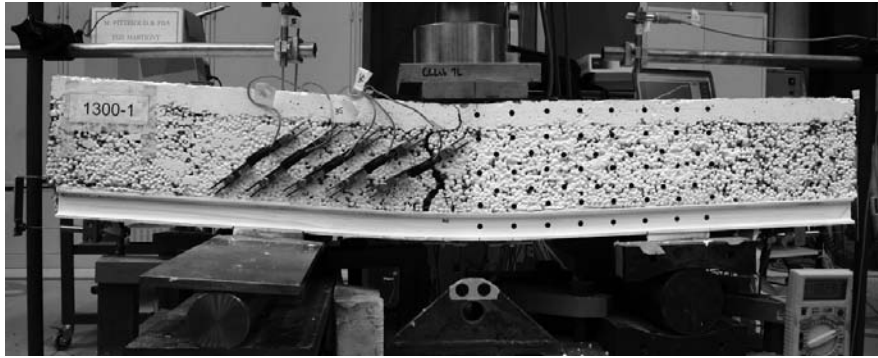


Figure 3.32: Failure pattern of 1300s-1 (unbonded, SLWAC).

slightly and then increased again, while a horizontal crack propagated along the FRP-LC interface towards the northern end of the specimen. The second load peak was attained when the horizontal crack reached the end of the specimen, followed by a significant drop in load. This was followed by large horizontal displacements between the upper LC and lower FRP-LC parts, as shown in Figures 3.31 and 3.33. Near the end of testing, only the FRP sheet, stiffened slightly by the cracked concrete core, maintained some load-bearing capacity until shear failure in the webs of the FRP T-upstands occurred.

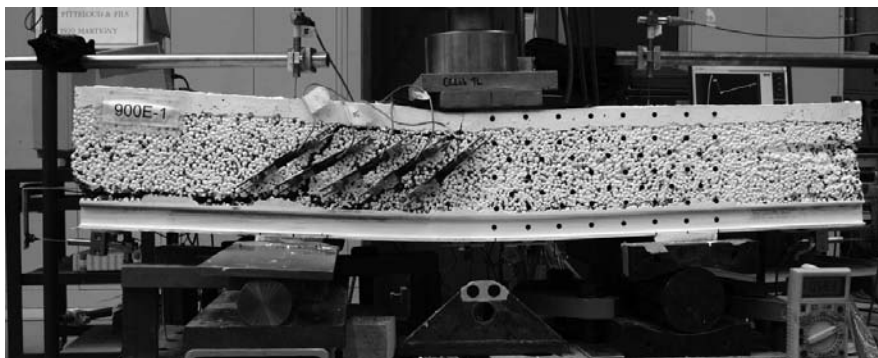


Figure 3.33: Failure pattern of 900Es-1 (bonded, SLWAC).

The first visible diagonal crack in the LC of specimen 1300Es-1 occurred on the north-eastern side at approximately 85 kN. At 155 kN, a diagonal crack on the south-western side had opened significantly, followed by a drop in load to 145 kN, see Figure 3.30. Subsequently, the load could be increased again, with a slightly lower stiffness, up to the ultimate load of 204 kN, when the crack in the northern part opened significantly and simultaneous failure just above the FRP-LC and in the LC-NC interfaces occurred, see Figure 3.34. At this point another load drop was recorded and significant horizontal displacements between the upper and lower LC parts developed at the northern end of the

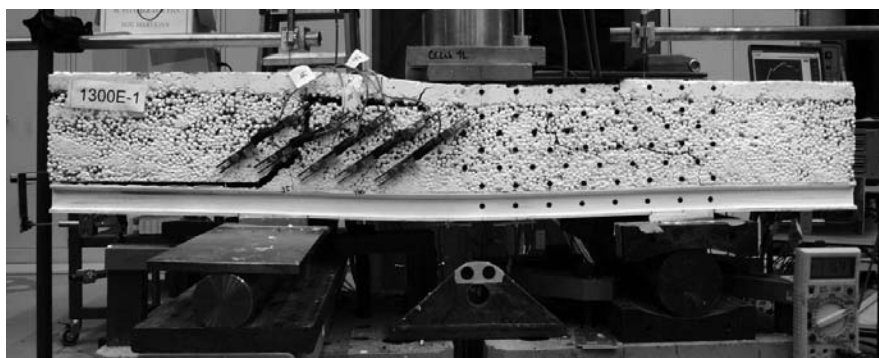


Figure 3.34: Failure pattern of 1300Es-1 (bonded, SLWAC).



Figure 3.35: Typical failure of FRP T-upstands (beam 1300Es-2 at end of experiment).

specimen, see Figure 3.31. The experiment was stopped when failure in the webs of the T-upstands occurred at the northern support, as shown in Figure 3.35. Table 3.9 summarizes the loads at the first visual crack and ultimate loads of the bonded SLWAC specimens.

3.4.2.3 Unbonded and bonded ALWAC specimens

The load-deflection responses of specimens 1000s and 1000Es are shown in Figure 3.30 on page 66.

The first diagonal crack of specimen 1000s was visible on the south-east side at 44 kN. Subsequently, short vertical cracks also appeared on the bottom part of the LC at mid-span. After further cracking, the LC started to be pushed out of the FRP sheet at the southern

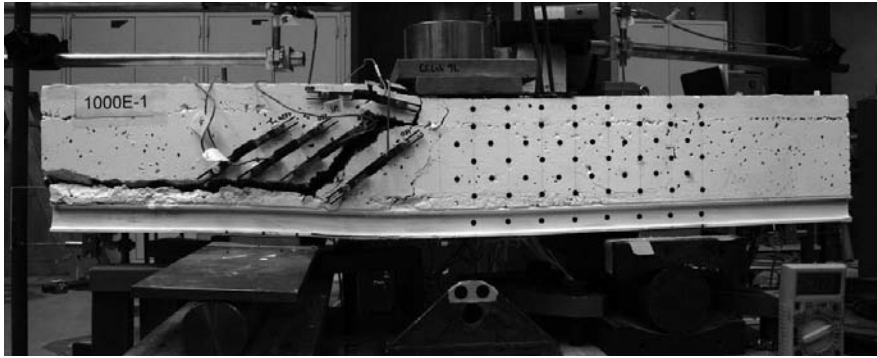


Figure 3.36: Failure pattern of 1000Es (bonded, ALWAC).

end at 150 kN and the corresponding slippage was measured, as illustrated in Figure 3.31. At this point stiffness decreased (see Figure 3.30) while the load could be increased until the ultimate load was reached at 164 kN.

Specimen 1000Es showed an almost linear elastic behavior up to a load of 180 kN, although the first diagonal crack was already observed at 35 kN on the south-eastern side. Subsequent to this first crack, a pattern of diagonal cracks developed progressively on both sides until the ultimate load was reached at 201 kN. One of the northern diagonal cracks opened progressively and propagated horizontally approximately 25 mm above the T-upstands up to the beam end and into the LC-NC interface, see Figure 3.36. The final drop in load occurred when the NC layer failed. Table 3.9 also summarizes the failure loads and loads at the first visual crack.

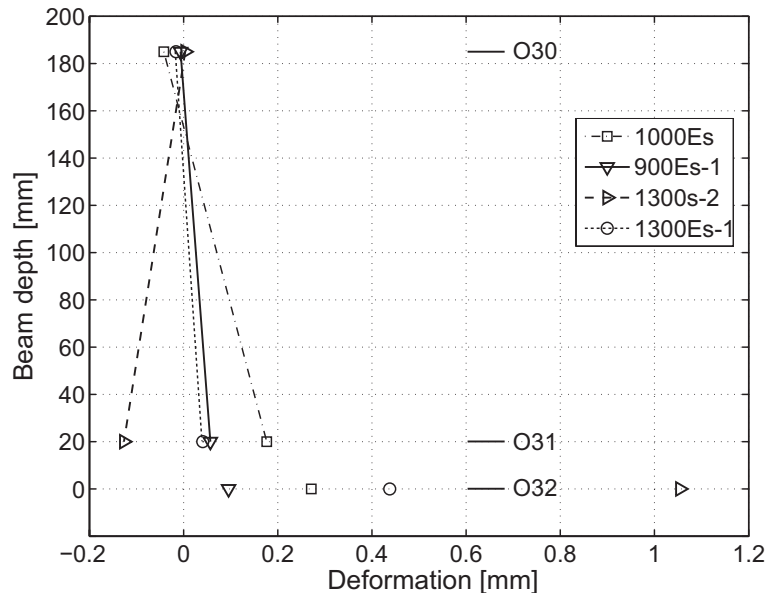
3.4.2.4 Deformations over specimen depth at mid-span

The extensometer responses over the beam depth at ultimate load are summarized in Table 3.10 and illustrated in Figure 3.37 (selected representative specimens). As already pointed out, some of the measurements on the concrete were influenced by cracks propagating through the gage length. The sign of certain values that should normally indicate compression therefore indicated tension instead.

The unbonded specimens 1300s-1/2 exhibited high deformations in the FRP sheet (0.999 and 1.108 mm) compared to values measured on the concrete (see Figure 3.37 for 1300s-2), while the unbonded specimen 1000s showed similar values on the bottom of the LC (0.140 mm) and FRP (0.172 mm), see Table 3.10. The bonded specimens 900Es-1/2, 1000Es and 1300Es-2 exhibited an almost linear distribution through the depth, while the bonded 1300Es-1 exhibited a kink at the bottom.

Table 3.10: Deformations of NC, LC and FRP at mid-span (* crack in gage length of extensometer, negative signs = compression).

Beam	Ultimate load [kN]	Deformation [mm]		
		O30, NC	O31, LC	av. O32/O33, FRP
900Es-1	98	-0.007	0.057	0.095
900Es-2	83	0.007	0.035	0.066
1300s-1	143	1.195*	0.734*	0.999
1300s-2	146	0.003	-0.126	1.108
1300Es-1	204	-0.016	0.041	0.519
1300Es-2	185	0.358*	0.202	0.402
1000s	164	0.264*	0.140	0.172
1000Es	201	-0.042	0.177	0.233

**Figure 3.37:** Distribution of measured deformations through cross section at mid-span and ultimate load.

3.4.2.5 Transverse deformations along diagonal

Selected representative load-deformation responses of extensometers O22 and O27, situated in the middle of the southern and northern diagonals, are shown in Figure 3.38. From these curves, cracking loads (of cracks parallel to the diagonals) could be determined. Crack initiation was assumed when a sudden increase in deformation occurred. The results of this analysis are also summarized in Table 3.9 on page 67. The smaller value measured by the two gages was considered as being the cracking load and compared relatively well to

cracking loads from visual observations. The bonded SLWAC specimens attained significantly higher cracking loads (65-87 kN) than the ALWAC specimens (45 and 50 kN). Only very small deformations (within the accuracy of the gages) could be measured on the unbonded SLWAC specimens and therefore no cracking load could be determined.

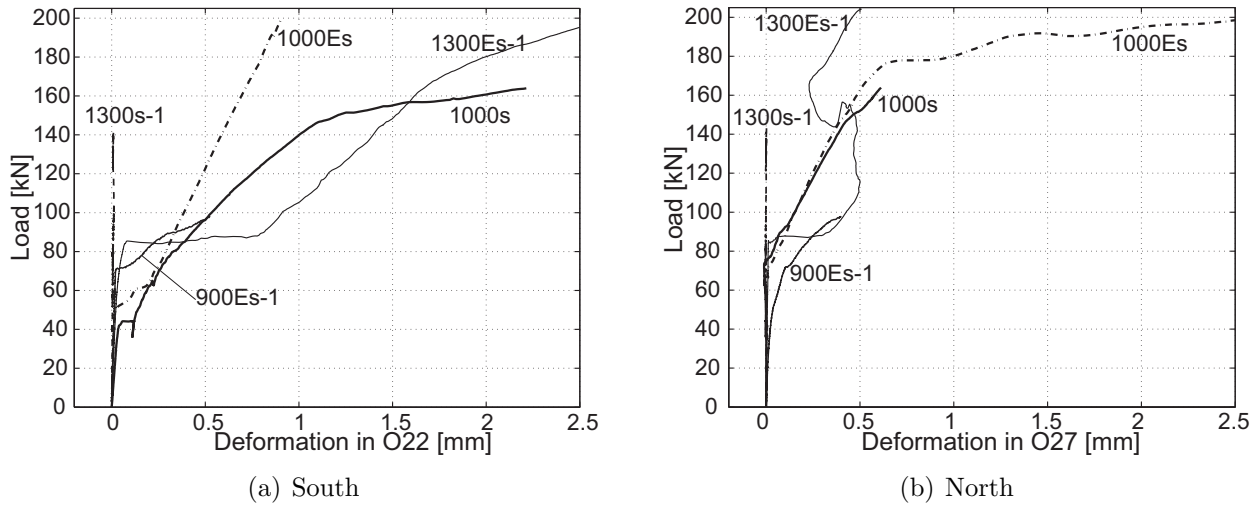


Figure 3.38: Transverse deformation in middle of diagonals.

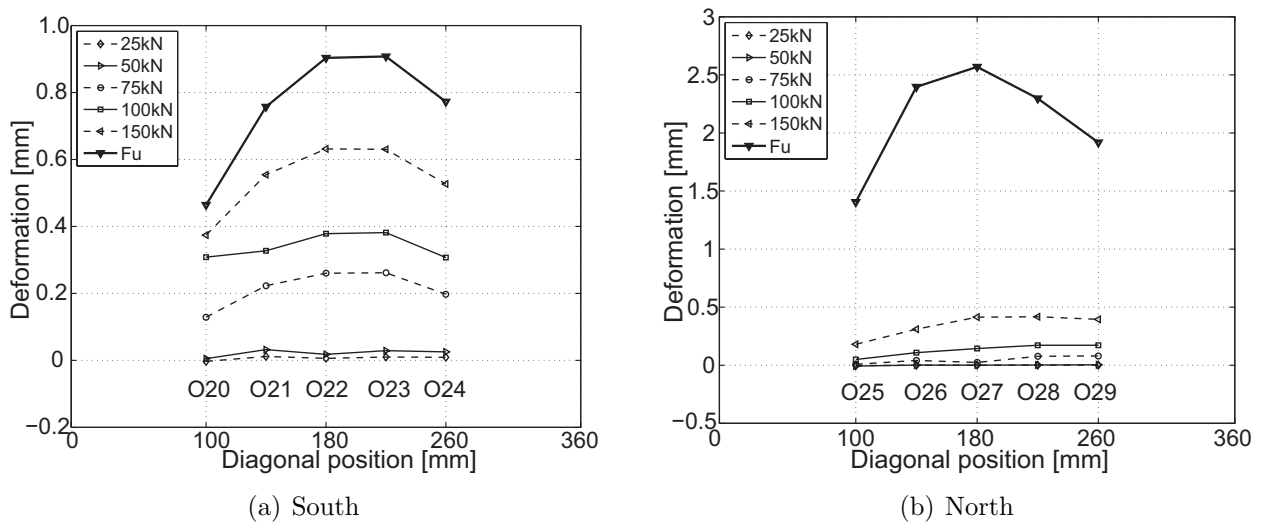


Figure 3.39: Transverse deformations along diagonals from omega gages at different load steps for beam 1000Es.

Typical representative transverse deformation distributions measured along the two diagonals at different load steps are shown in Figure 3.39 (specimen 1000Es). The measurements O20-O24 obtained from the southern diagonal show the development of

a parabolic distribution of deformations with maximum deformations measured by O22, situated in the middle of the diagonal. At ultimate failure, the maximum deformation was 0.90 mm. Along the northern diagonal, the maximum deformation at ultimate load (2.57 mm) was again located almost in the middle of the diagonal, at O27. Table 3.11 gives the maximum transverse deformations at ultimate load for all specimens.

Table 3.11: Transverse deformations along diagonal at ultimate loads.

Beam	Ultimate load [kN]	Transverse deformations at ultimate load	
		Southern diagonal from O22 [mm]	Northern diagonal from O27 [mm]
1300s-1	143	0.00	0.00
1300s-2	146	0.00	0.00
900Es-1	98	0.50	0.44
900Es-2	83	0.28	0.28
1300Es-1	204	3.00	0.75
1300Es-2	185	4.50	4.50
1000s	164	2.22	0.61
1000Es	201	0.90	2.57

3.4.2.6 Longitudinal deformation transverse to diagonal

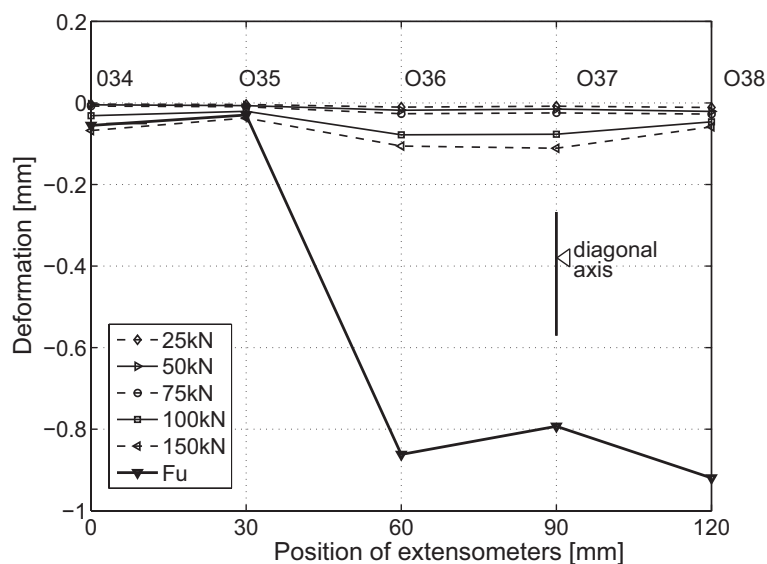


Figure 3.40: Longitudinal deformation transverse to northern diagonal from omega gages at different load steps for beam 1300Es-2 (O37 is on axis of compression diagonal).

Typical deformation distributions due to compression transverse to the diagonals at different load steps up to ultimate load are illustrated in Figure 3.40 (specimen 1300Es-2). Up to the 75-kN load step, deformations were almost evenly distributed over a large width (with a maximum value of -0.03 mm). Subsequently, after cracking at 80 kN, deformations started to increase significantly within a much narrower range of approximately 45 mm on each side of the diagonal. The measurements from O36 to O38 increased considerably, reaching a maximum deformation of -0.8 to -0.9 mm at ultimate load.

3.4.3 Discussion

3.4.3.1 Effect of FRP-LC interface type

The unbonded beams 1300s-1/2 lost composite action in the FRP-LC interface just after cracking. Differential displacements (slippage) between FRP and LC were measured from this load on (see Figure 3.31) and through-depth deformations at mid-span no longer remained linear, see Figure 3.37. The absence of deformation in the diagonals (shown in Figure 3.38) even indicated that the interface was too weak to provide support for the compression diagonals before cracking, which led to the single crack at mid-span. The unbonded beam 1000s exhibited a different behavior: composite action was maintained after cracking up to approximately 91% of the ultimate load. This improvement had already been observed in the beam experiments (Section 3.3.5.3) and was attributed to the much higher compressive strength of the ALWAC mixture, which increased friction resistance at the interface.

The bonded beams exhibited full composite action up to ultimate load. The kink in the through-depth distribution of specimen 1300Es-1 (shown in Figure 3.37) had existed from the beginning of the loading and was regarded as an inaccuracy problem of gage O31. The corresponding value from specimen 1300Es-2 (0.202 mm), given in Table 3.10, matched the linear distribution. The bonded specimens showed significantly higher ultimate loads than the corresponding unbonded specimens. However, the ultimate load ratio of bonded to unbonded specimens (1.35 for 1300Es/1300s and 1.23 for 1000Es/1000s) seemed to correlate with the degree of composite action of the unbonded specimens and to approach unity for full composite action. Failure in the bonded beams over the supports always occurred in the LC (just above the T-upstands) and the LC shear strength was therefore always lower than the bonded interface shear strength.

3.4.3.2 Effect of LC type

The cracking load of the SLWAC specimens was significantly higher than that of the ALWAC specimens, see Table 3.10 on page 71. However, no correlation was found between cracking load and LC splitting tensile strength, as shown in Figure 3.41.

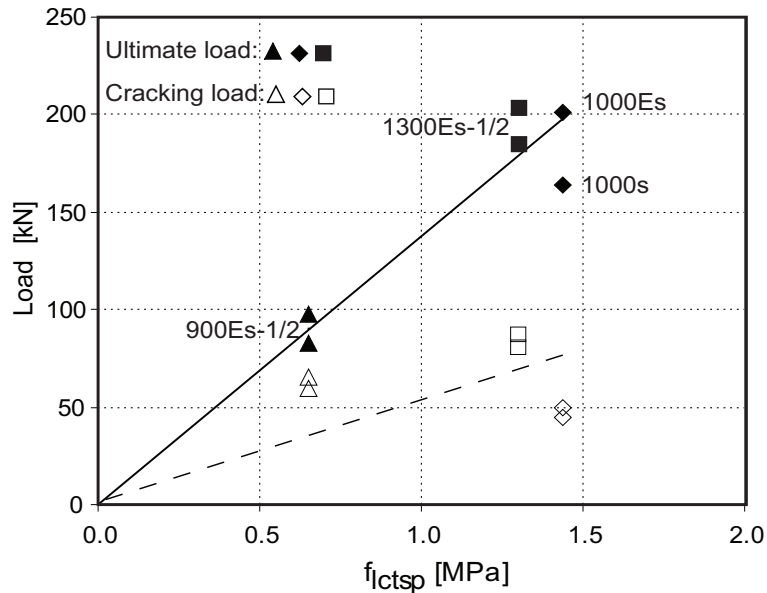


Figure 3.41: Ultimate and cracking loads (from omega gages) vs LC splitting tensile strength.

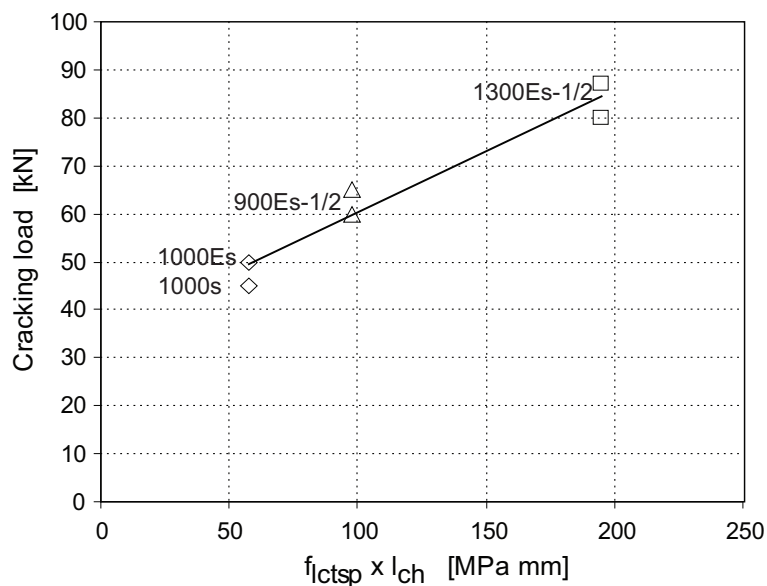


Figure 3.42: Cracking load (from omega gages) vs product of LC splitting tensile strength x characteristic length.

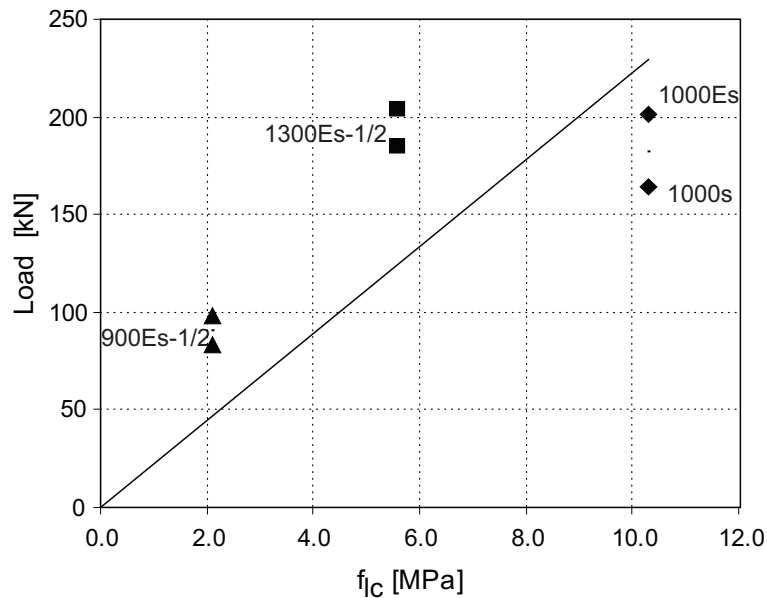


Figure 3.43: Ultimate load vs LC compressive strength.

This had already been observed in the beam experiments and was attributed to the more brittle behavior of the ALWAC concrete as compared with that of the SLWAC mixture. Comparison of cracking load to the product of splitting tensile strength and characteristic length, the latter being an indicator of concrete brittleness, gave a much better correlation, as shown in Figure 3.42 (correlation coefficient $R^2=0.94$). Cracking always started approximately in the middle of the compression diagonal, where maximum transverse deformations due to tension were measured, see Figure 3.39 on page 72.

With the exception of unbonded specimens 1300s-1/2, direct load transfer occurred through the compression diagonal. The deformation was almost evenly distributed across the diagonal at cracking and parabolically distributed at ultimate load, over a much narrower width of approximately 120 mm, see Figure 3.40 (symmetry axis at O37). However, no correlation between LC compressive strength and ultimate failure load was found, as shown in Figure 3.43 (correlation coefficient $R^2=0.36$). The comparison of ultimate loads with LC splitting tensile strength gives a much better correlation, see Figure 3.41 (correlation coefficient $R^2=0.86$).

3.4.3.3 Comparison with beam loading and system optimization

As already discussed, the direct load transmission and beam experiments showed similar results concerning the effects of interface type (composite action) and LC brittleness. Figure 3.44 compares the ultimate loads of corresponding specimens and beams from both

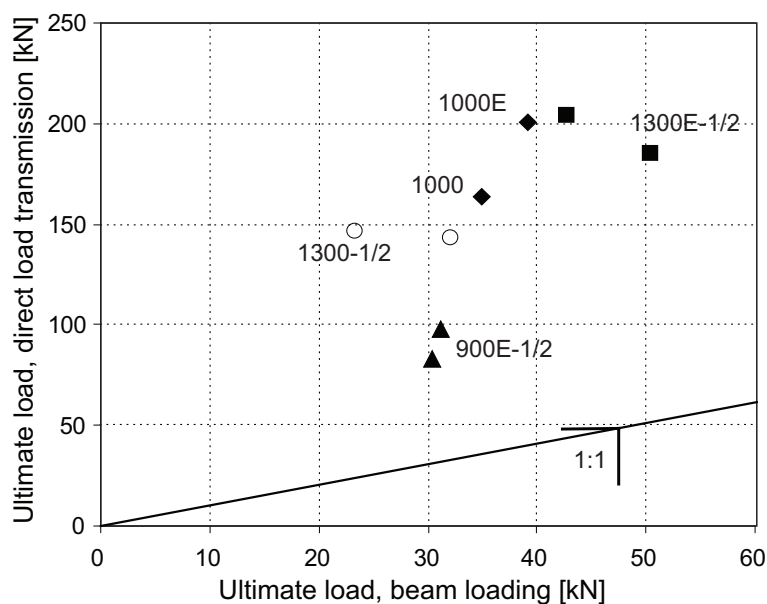


Figure 3.44: Ultimate load, direct load transmission vs ultimate load, beam loading.

experimental series. The former were significantly higher (4.3 times on average) than the latter, as could be expected.

Based on the experimental results, the sandwich system can be further optimized. Firstly, the FRP sheet seems to be overdesigned. Maximum deformations at failure were 0.6 mm on a gage length of 100 mm, corresponding to stresses of approximately 138 MPa, i.e. only 58% of the tensile strength of the sheet. However, more research is required regarding the shear failure of the webs of the T-upstands. Secondly, to increase cracking load and shear resistance, the LC ductility should be improved, by adding short fibers for example, thereby increasing the characteristic length. Thirdly, it seems possible to omit the adhesive bonding of the interface, if the LC deformation strength is high enough to provide sufficient friction and thus full composite action. In this respect, T-upstand geometry could also be improved to ensure better concrete confinement. However, in view of the intended bridge deck application, more research is required regarding the fatigue behavior of interfaces relying only on mechanical interlocking.

3.4.4 Conclusions

Short-span three-point bending experiments on eight hybrid FRP-concrete sandwich specimens provided useful information concerning direct load transmission and the effect of two parameters on static load-bearing behavior: the FRP-LC interface (unbonded or

epoxy-bonded) and the LC composition (low- and high-density SLWAC and ALWAC). The following conclusions were drawn:

1. Specimens with adhesively-bonded interfaces attained significantly higher ultimate loads than corresponding unbonded specimens. The ultimate load ratio of bonded to unbonded specimens correlated with the degree of composite action of the unbonded specimens and approached unity for full composite action. The degree of composite action of the unbonded interfaces depended on the LC compressive strength. Using an ALWAC mixture with high compressive strength provided almost full composite action through pure mechanical interlocking in contrast to an SLWAC mixture with low compressive strength, which lost its composite action following LC cracking.
2. The loads of first cracking occurring in the diagonal were significantly lower than the ultimate loads. Furthermore, the cracking loads of the more ductile SLWAC compositions were significantly higher than those of the more brittle ALWAC mixtures, although splitting tensile strengths were similar.
3. A correlation between ultimate loads and LC splitting tensile strengths was found, although no similar correlation was exhibited for the cracking loads. Combining the splitting tensile strength and characteristic length, a fracture mechanics property characterizing material brittleness, led to a good correlation with cracking loads.

3.5 Summary

An experimental study was performed on long-span and short-span hybrid FRP-concrete sandwich beams. The sandwich core consisted of two different types of lightweight concrete (LC): an SLWAC mixture with expanded clay and sand aggregates and an ALWAC mixture with expanded clay and expanded glass aggregates. Different FRP-LC interface conditions were investigated: pure mechanical interlocking between the FRP and LC (unbonded), adhesive bonding of the LC onto the FRP, and a combination of both. All beams exhibited brittle shear failure in the LC core.

- Long-span and short-span beam experiments showed similar results concerning the effects of interface type (composite action) and LC brittleness. In the case of mechanical interlocking in the FRP-LC interface, interface strength was correlated to LC compressive strength. Furthermore, the cracking loads of the more ductile SLWAC compositions were significantly higher than those of the more brittle ALWAC mixtures, although splitting tensile strengths were similar.

- The ultimate loads of the long-span beams were reached when one of the vertical flexural cracks turned suddenly and developed diagonally through the LC core. The appearance of the diagonal crack was hence the indication of instantaneous failure. In the short-span beams however, loads could be significantly increased after the appearance of the first diagonal cracking. The ultimate loads were up to 3.7 times higher than the corresponding cracking loads.
- The ultimate loads or shear resistances of the short-span beams were significantly higher (4.3 times on average) than those of the long-span beams, since loads were transmitted by a compression diagonal directly to the support. The compression diagonals in the long-span beam experiments interfered with crossing tension diagonals, lowering shear resistances.
- The long-span ultimate loads were correlated to the LC density (higher densities implied higher ultimate loads). No correlation, however, was found between ultimate loads and LC compressive or splitting tensile strength. The ultimate loads of the bonded short-span beams were only correlated to the LC splitting tensile strength and not to density, as was the case for the long-span beams.

4 Analysis of experiments and modeling

4.1 Failure modes and model concept

Thanks to their good durability performance, steel-free bridge slabs have been used in an increasing number of applications. Hybrid fiber-reinforced polymer (FRP) load-bearing structures combining FRP with concrete are promising systems offering high potential with regard to structural performance and manufacturing, see also Section 2.1. A novel concept for a hybrid sandwich bridge deck system was proposed and experimentally investigated in Sections 3.3 and 3.4. The concept consists of three layers: GFRP composites for the tension skin, which also serves as formwork, lightweight concrete (LC) as core material and ultra-high performance fiber-reinforced concrete (UHPFRC) for the compression skin. No additional shear reinforcements (e.g. rebar, studs) were used, resulting in a simple and cost-effective manufacturing procedure for the slab.

As with conventional concrete bridge decks, two main failure modes were expected for the sandwich slab: firstly a flexural failure, which results in crushing of the compression zone or tensile failure of the reinforcement, and secondly a shear failure of the LC core. The shear failure can again be divided into two separate modes: one associated to “beam action“ and one associated to “direct load transmission“, as described in Section 2.3. Schlaich introduced the concept of B and D regions for reinforced concrete structures, where B denotes beam or Bernoulli (where a linear strain distribution can be expected), and D discontinuity or disturb (associated to nonlinear strain distributions in direct load transmission). For beams or slabs, an indicator as to whether a zone is located in a B or D region (beam action or direct loading action respectively) is the shear span-to-depth ratio (a/d), where a is the distance between load and support and d the effective depth of the member.

The beam action (corresponding to $a/d=8$) and direct load transmission ($a/d=1.6$) of sandwich beams with different FRP-LC interfaces were experimentally investigated and presented in Sections 3.3 and 3.4. Emphasis was placed on the shear failure behavior of the LC cores. Therefore, two different categories of LCs were studied and classified according to [Fau03] as sand lightweight aggregate concrete (SLWAC) and all lightweight aggregate concrete (ALWAC). Experimental investigation showed that the concrete brittleness, quantified by the characteristic length of the LC, was higher for the

ALWAC specimens than for the SLWAC specimens. To take material brittleness into account, the modeling of the LC softening behavior is therefore presented in Section 4.2. A fracture mechanics-based model to predict the shear resistance of the unreinforced LC core for high shear-span ratios (beam action) will then be developed in Section 4.3, which demonstrates that not only static strength but also fracture mechanics properties must be considered. Regarding the modeling of the short-span beams, different approaches involving existing strut-and-tie models will be discussed in Section 4.4. In Section 4.4.2 a model will then be developed for the direct loading behavior of the proposed structure, including the softening behavior of the LC core.

4.2 Modeling of LC softening behavior

The two types of lightweight concretes (SLWAC and ALWAC) showed significant differences in material properties and structural performance. The results of the LC properties are given in Table 3.3 on page 43. With regard to the short-span experiments, the cracking load of the ALWAC specimens was significantly lower than that of the SLWAC specimens and no correlation between cracking load and LC splitting tensile strength was found (Figure 3.41). However, good correlation could be achieved when comparing cracking loads to the product of splitting tensile strength and characteristic length, an indicator of concrete brittleness (Figure 3.42). As described in Section 3.2, characteristic lengths of 150 mm and 40 mm were assumed for the SLWAC (normal performance) and ALWAC (high-performance) respectively. To take the influence of concrete brittleness into account, the post-peak softening behavior is considered according to [Hil83]. The fracture energy, G_f , of the LC:

$$G_f = \frac{l_{ch} \cdot f_{lct,m}^2}{E_{lc,m}} \quad (4.1)$$

with $f_{lct,m}$ = uniaxial LC tensile strength (approximately 90% of the LC splitting tensile strength [Fau03], see Table 4.1), corresponds to the area below the softening curve. Assuming a typical bilinear degradation [Fau03], with a kink located at $0.33 f_{lct,m}$ and $0.25 w_{crit}$, the critical crack openings, w_{crit} , could be determined, as shown in Figure 4.1 and are listed in Table 4.1. No tensile stresses can be transmitted through cracks of widths greater than the critical crack opening. Compared to the SLWAC, the lower fracture energy of the ALWAC (see Table 4.1) as compared to the SLWAC resulted in a smaller critical crack opening, and thus, with small deformations, the ALWAC rapidly lost its ability to transmit tensile stresses through a crack.

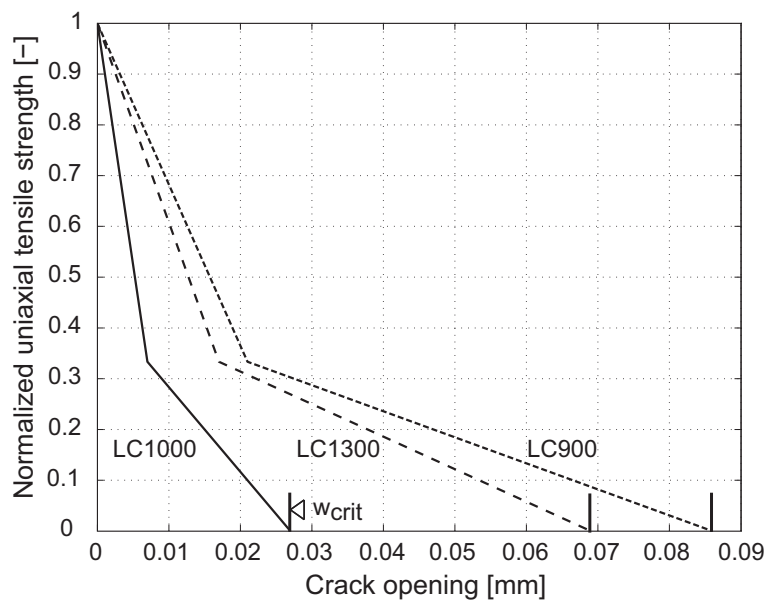


Figure 4.1: Normalized uniaxial tensile strength vs crack opening.

Table 4.1: Calculated properties of lightweight concretes for modeling of softening behavior.

LC type	Uniaxial tensile strength $f_{ict,m}$ [MPa]	Characteristic length l_{ch} [mm]	Fracture energy G_f [Nm/m ²]	Critical crack opening w_{crit} [μ m]	Exp. factor for material softening r [1/mm]
LC900	0.59	150	14.7	86	38
LC1300	1.17	150	23.6	69	48
LC1000	1.30	40	10.2	27	123

4.3 Modeling of beams within the span

4.3.1 Modeling of cracking load and load-deflection response

The mid-span load-deflection response was modeled for the hybrid beams without interface slippage and then compared to representative experimentally investigated load-deflection responses. A bilinear beam stiffness was approximated with a kink at the cracking load where the uncracked section stiffness changed to the cracked section stiffness. The effective section stiffness was always calculated on the basis of a linear strain distribution and an equilibrium of inner compressive and tensile forces. In the case of the uncracked section, the LC layer was assumed to act in compression and in tension. The neutral axis, $x_{n,uncr}$, (counting from the top) was hence calculated by equilibrating tension and compression as illustrated in Figure 4.2, where i denotes the i -th layer of the section (nc , lc and frp), T_i = the corresponding tension and C_i = the corresponding compression in the i -th layer.

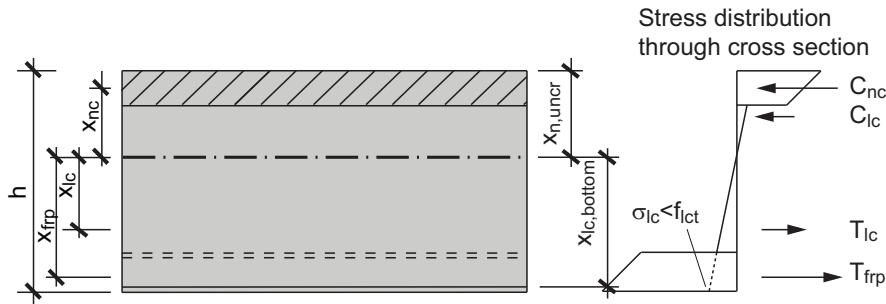


Figure 4.2: Nomenclature for calculation of neutral axis and effective stiffness of uncracked hybrid beam cross section.

The effective stiffnesses $EI_{eff,uncr}$ of the uncracked beams were determined according to Eq. 4.2, with A_i = the area, E_i = the Young's modulus, I_i = the moment of inertia of the i -th layer and x_i = the distance from the neutral axis of the specimen to the gravity center of each layer as also indicated in Figure 4.2. The results are summarized in Table 4.2.

$$EI_{eff(uncr)} = \sum_{i=1}^3 (E_i \cdot I_i) + \sum_{i=1}^3 (E_i \cdot A_i \cdot x_i^2) \quad (4.2)$$

In order to determine the kink of the bilinear stiffness approximation, the cracking load had to be calculated. Therefore, the moment when the maximum tensile stress in the LC core reached the LC tensile strength at $x_{lc,bottom}$ was defined as the cracking moment, M_{cr} , with the corresponding cracking load, $F_{cr} = 4 \cdot M_{cr}/l$ for three-point bending (with $x_{lc,bottom}$ = the distance of the FRP sheet-LC interface from the neutral axis as indicated in Figure 4.2 and l = the beam span of 3 m). The cracking moment, and hence the cracking load, was calculated

using Eq.4.3:

$$\sigma_{lc,bottom} = \frac{M_{cr}}{W_{lc,bottom}} \equiv f_{lct} \quad (4.3)$$

with

$$W_{lc,bottom} = \frac{EI_{eff,uncr}}{E_{lc} \cdot x_{lc,bottom}} \quad (4.4)$$

At this load, the corresponding deflection, u_{cr} , was determined according to Eq. 4.5. The cracking loads and corresponding deflections are also listed in Table 4.2.

$$u_{cr} = \frac{M_{cr} \cdot l^2}{12 \cdot EI_{eff,uncr}} \quad (4.5)$$

After the cracking load had been reached, it was assumed that the lightweight concrete core no longer transmitted any tension. The neutral axis and effective cross section of the cracked beam were hence calculated again according to Figure 4.3 and Eq. 4.2 by considering only the compression part of the LC core. The neutral axis (x_n) and effective stiffness (EI_{eff}) always take the cracked beam section into account in the following sections. The results are also summarized in Table 4.2. It could be noticed that the type of LC core influenced only the stiffness of the uncracked section, while the values for the cracked sections were similar

Table 4.2: Neutral axis and effective stiffness of investigated beams, cracking loads and corresponding deflection for 3-m span beams.

Type of LC core	$x_{n,uncr}$ [mm]	$EI_{eff,uncr}$ [Nmm^2]	F_{cr} [kN]	u_{cr} [mm]	x_n [mm]	EI_{eff} [Nmm^2]
LC900	63	2.78E+12	7.3	1.48	46	2.01E+12
LC1300	76	3.57E+12	8.7	1.38	45	2.03E+12
LC1000	71	3.31E+12	11.0	1.88	45	2.03E+12

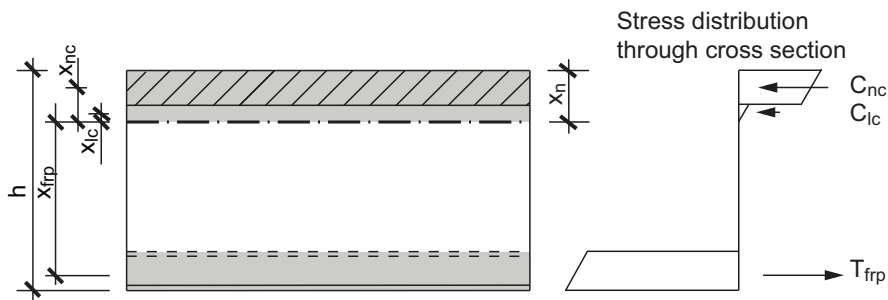


Figure 4.3: Nomenclature for calculation of neutral axis and effective stiffness of cracked hybrid beam cross section.

due to the predominating stiffness portion of the face layers. The highest cracking loads were reached for LC1000, which exhibited the highest splitting tensile strength.

Figure 4.4 illustrates the bilinear load-deflection response from the modeling (dashed lines), with a kink at the cracking load, and the experimental results for representative beams (solid lines). The graphs indicate good agreement between the measured and predicted beam stiffnesses. While the bilinear modeling of the hybrid beam comprising LC900 fits the measured response very well, the modeled LC1300 cracking load was lower than that measured. After cracking, a slight overestimation of the real beam stiffness could be noticed. In the case of beam 1000E with the LC1000 core, no clear stiffness change was observed during the experiment. Hence, the uncracked beam stiffness was slightly overestimated, while the stiffness up to ultimate failure was slightly underestimated. However, good agreement was found between the predicted and experimentally measured deflections. Figure 4.4 shows the load-deflection response up to the experimental ultimate load. The ultimate load prediction will form the subject of the following sections.

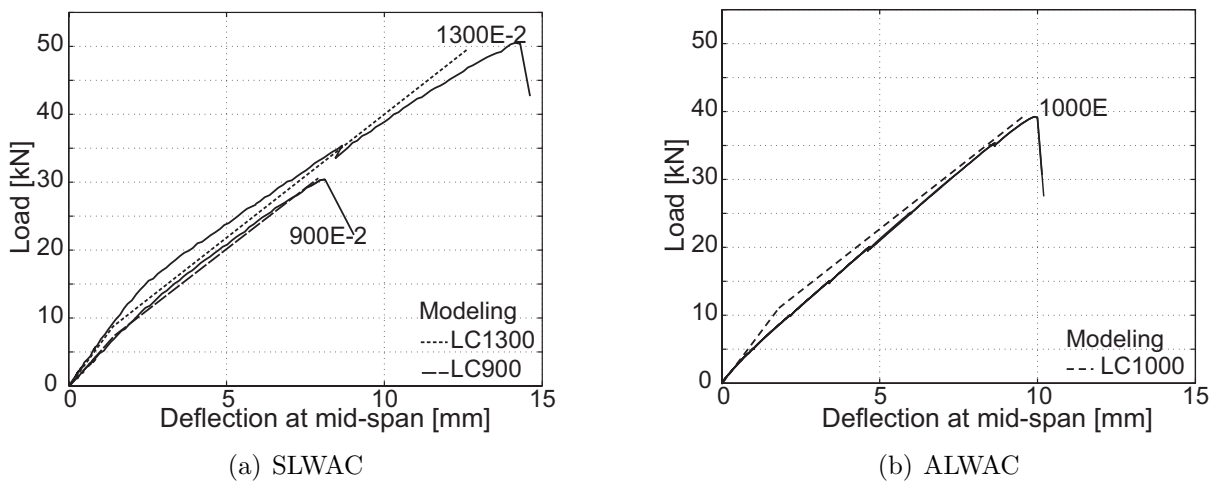


Figure 4.4: Prediction of and experimental results for load-deflection curve for representative SLWAC and ALWAC beams.

4.3.2 Prediction of ultimate loads according to Eurocode 2

The failure mode of all beams was a shear failure in the LC core material. The shear resistance of the beams was estimated on the basis of Eurocode 2 (EC2 [Com04]), using a semi-empirical approach. Since the NC layer was thin compared to the beam depth and the maximum shear stresses occurred in the LC, it could be assumed that the LC would extend up to the top surface of the beam. The mean value of the LC shear resistance of lightweight concrete beams,

$V_{lc,Rm}$, could then be calculated as follows:

$$V_{lc,Rm} = C_{c,Rm} \cdot \eta_1 \cdot \kappa \cdot \sqrt[3]{100 \cdot \rho_l \cdot f_{lc,m}} \cdot b_w \cdot d \quad (4.6)$$

where $C_{c,Rm}$ is an empirical value based on a statistical evaluation of mean resistances of shear beams and lies between 0.18-0.20 [BKN04]; η_1 is a coefficient that takes into account the oven-dry density of the LC, ρ , as follows: $\eta_1 = 0.4 + (0.6 \cdot \rho)/2200$; ρ_l is the steel reinforcement ratio, which can be transformed to consider the FRP sheet as follows: $\rho_l = (A_{frp} \cdot E_{frp}) / (b_w \cdot d \cdot E_{steel})$, where A_{frp} is the area of the FRP sheet (3615 mm²), b_w is the beam width (400 mm), d is the effective depth (185 mm), and E_{steel} is the Young's modulus of steel (210 GPa). The scale coefficient κ depends on the effective depth as follows: $\kappa = 1 + \sqrt{(200/d)}$. Table 4.3 compares experimental ultimate loads, $F_{u,exp}$, and predicted ultimate loads, $F_{u,pred}$. The predicted ultimate loads are twice the LC shear resistance according to beam theory: $F_{u,pred} = 2 \cdot V_{lc,Rm}$. Similarly, Figure 4.5 shows this comparison

Table 4.3: Ultimate load prediction according to EC2 ($C_{c,Rm} = 0.18$, $\kappa = 2.0$ and $\rho_l = 0.0054$).

Beam	$F_{u,exp}$ [kN]	η_1	$F_{u,pred}$ [kN]	$F_{u,exp} / F_{u,pred}$
900E-1/2	31.2 / 30.4	0.64	35.4	1.14 / 1.17
1300E-1/2	42.8 / 50.5	0.75	57.8	1.35 / 1.15
1000/1000E	35.0 / 39.2	0.67	62.0	1.77 / 1.58
1000A/1000EA	37.8 / 37.2	0.67	62.0	1.64 / 1.67

for each beam type (solid lines) and for the mean value of $\eta_1 = 0.68$ (dashed line) as a function of the LC compressive strength. The experimental ultimate loads of the SLWAC beams were overestimated by an average of 19%, and those of the ALWAC beams by up to 67%. Figure 4.5 shows that the trend of the dashed curve fits quite well for the SLWAC beams. The experimental results for the ALWAC beams, however, differ significantly from the prediction.

This result, together with the poor correlation to the splitting tensile strength shown in Figure 3.26 on page 61, led to the conclusion that the shear behavior of LC beams could not be predicted solely on the basis of LC mechanical strength properties such as compressive or tensile strength. Zink [Zin00] proposed an alternative value for the κ scale coefficient used in Eq. 4.6, κ^* , which takes into account not only the cross-sectional geometry, but also characteristic length:

$$\kappa^* = \sqrt[4]{\frac{5 \cdot l_{ch}}{d}} \quad (4.7)$$

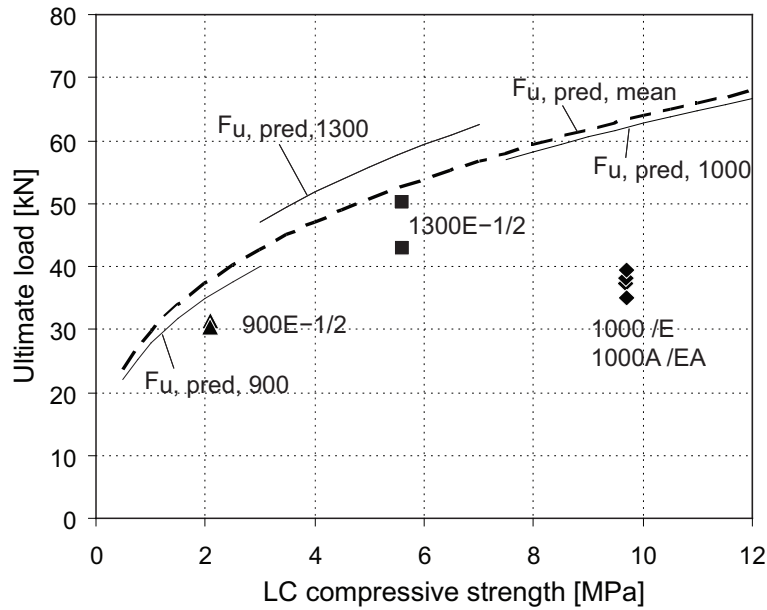


Figure 4.5: Ultimate loads vs compressive strength of LC core and prediction according to EC2.

By incorporating this fracture mechanics-based coefficient into Eq. 4.6, an average underestimation of the ultimate failure loads of 15% for both SLWAC beams and ALWAC beams was achieved, as shown in Table 4.4. The predictions were therefore considerably improved, particularly for the ALWAC beams.

Table 4.4: Ultimate load prediction according to EC2 using a modified κ^* coefficient according to Zink [Zin00].

Beam	l_{ch} [mm]	κ^*	$F_{u,pred}$ [kN]	$F_{u,exp} / F_{u,pred}$
900E-1/2	150	1.42	25.2	0.81 / 0.83
1300E-1/2	150	1.42	41.0	0.96 / 0.81
1000/1000E	40	1.02	31.6	0.90 / 0.81
1000A/1000EA	40	1.02	31.6	0.84 / 0.85

4.3.3 Prediction of ultimate loads using a fracture mechanics-based model

As already explained in Section 2.3, the shear resistance of cracked concrete beams is basically composed of three portions: the shear resistance of a) the compressive zone, b) from the dowel action of the longitudinal reinforcing bars propagating through the cracks, and c) from the shear and tensile stresses across the cracks [ASC98], [Fis97] and [SS95]. The interface shear transfer mechanism for normal concrete is aggregate interlocking, where aggregates protruding from the crack surface provide resistance against slip. This effect is negligible

for LC, since cracks propagate straight through the aggregates. However, concrete cracks occur gradually and tensile stresses across the cracks can be transmitted along the fracture process zone (FPZ), as shown in Figure 2.23 on page 30 in Section 2.3. The FPZ is the zone where the concrete has the ability to bridge the cracks and transmit tensile forces. The peak tensile stress at the crack tip is equivalent to the tensile strength of the concrete and decreases according to the softening behavior of the material until the critical crack width is reached, beyond which no further stress transmission is possible. The incorporation of the FPZ in shear failure models has been the subject of several research projects in the area of fracture mechanics, as described in Section 2.3. In 2000, based on Hillerborg [Hil83], Zink [Zin00] proposed a fracture mechanics-based model for predicting the shear resistance of cracked normal and high-performance concrete beams, which includes the shear resistance of the FPZ. Figure 4.6 shows the components that contribute to the shear resistance of the

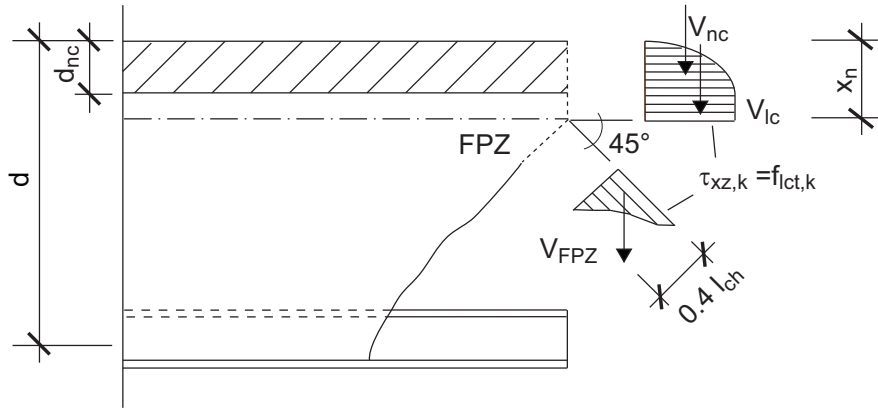


Figure 4.6: Shear resistance components in hybrid sandwich beams.

hybrid sandwich beams, obtained through the interpretation of Zink's model and expressed in the following equation:

$$V_{lc,R} = V_{nc} + V_{lc} + V_{FPZ} = \left[\frac{2}{3}d_{nc} + (x_n - d_{nc}) + 0.4 \cdot \cos 45^\circ \cdot l_{FPZ} \right] b_w \cdot f_{lct,k} \quad (4.8)$$

where V_{nc} = shear portion transferred in NC layer (depth d_{nc}), V_{lc} = shear portion transferred in LC core (above the neutral axis, at depth x_n), V_{FPZ} = shear portion transferred in FPZ, l_{FPZ} = length of FPZ. The shear stresses in the LC at ultimate load at the neutral axis, $\tau_{xz,k}$, can be defined as being equal to the tensile strength $f_{lct,k}$ [Zin00], which is approximately 90% of the splitting tensile strength [Fau03]. V_{nc} and V_{lc} can then be calculated according to Eq. 4.8. The NC layer influenced the shear load-bearing capacity insofar as it raised the location of the neutral axis. Its shear capacity was not fully exploited, since the magnitude of the shear stresses was governed by the tensile strength of the LC layer. The shear stresses

through the NC developed in a parabolic form and were almost constant in the LC layer, since the LC/NC stiffness ratio was low. For the calculation of V_{FPZ} , a crack inclination at the neutral axis of 45° was assumed and the length of the FPZ was defined as $0.4 l_{ch}$ (taken from Hillerborg [Hil83], who suggests a value of between 0.3 and 0.5 of the characteristic length). Furthermore, a parabolic development of the crack opening and a softening proper to the LC in the FPZ are assumed [Zin00] and [Hil83], as schematically shown in Figures 2.23 and 4.6. Since cracking in LC members always occurs through the aggregates and the shearing surface is relatively smooth, the effect of interface shear was disregarded. The dowel action provided by the FRP sheet was also disregarded due to the very small contribution of this component in unreinforced concretes [ASC98]. Table 4.5 shows the results of the shear resistance prediction and the ultimate failure loads of the experimental beams assuming $f_{lct,k}$ as being 90% of the mean splitting tensile strength obtained from the experiments. Good agreement with experimental results was achieved regarding the prediction of ultimate failure loads (98% on average of the experimental values). The NC and LC layers of the SLWAC beams contributed only 68% of the shear resistance, while 32% of the shear was transmitted through the FPZ. The ALWAC beams exhibited a different behavior, whereby the FPZ contributed only 12% of the shear resistance, mainly due to the much shorter characteristic length and corresponding short length of the FPZ.

Table 4.5: Ultimate load prediction according to proposed shear resistance model.

Beam	x_n [mm]	V_{nc} [kN]	V_{lc} [kN]	V_{FPZ} [kN]	$V_{lc,Rm}$ [kN]	$V_{nc+lc}/V_{lc,Rm}$ [-]	$F_{u,pred}/F_{u,exp}$ [-]
900E-1/2	46	4.7	3.7	4.0	12.3	0.68	0.79 / 0.81
1300E-1/2	45	9.4	7.1	7.9	24.4	0.68	1.14 / 0.97
1000/1000E	45	9.6	7.4	2.2	19.3	0.88	1.10 / 0.98
1000A/1000EA	45	9.6	7.4	2.2	19.3	0.88	1.02 / 1.04

4.3.4 Conclusions

An experimental study of hybrid FRP-concrete sandwich beams was performed using two different types of lightweight concretes (LCs), SLWAC and ALWAC mixtures, as core materials. The former LC exhibited a much higher fracture energy and longer fracture process zone (FPZ) than the latter. The modeling of the shear resistance of the beams, all exhibiting a brittle shear failure in the LC core, was discussed and the following conclusions were drawn:

1. Shear resistance prediction according to Eurocode2 [Com04] was not reliable, since the different fracture behaviors of SLWAC and ALWAC concretes is not considered.

Predictions were improved by incorporating the characteristic length into the scale coefficient.

2. Good agreement between predicted and ultimate loads was achieved using a refined shear model originally developed for normal and high-performance concretes that considers the shear resistance of the fracture process zone. The shear resistance of the FPZ of SLWAC beams was 2.7 times higher on average than that of the ALWAC beams, which exhibited a much more brittle behavior with much lower fracture energy and shorter FPZ length.

4.4 Modeling of the direct load transmission region

For small shear span-to-depth ratios, $a/d < 2.5$, the load is directly transmitted by a compressive strut to the support, see also Section 2.3 and [ASC98], [Kan64], [KN99]. Furthermore, it has been experimentally and numerically verified that the compressive strut, rather than being parallel-sided, is bowed between the loading point and the support, and consequently transverse tension is caused [ASC98], [SSJ87] and [Fos98].

4.4.1 Strut-and-tie models

The flow of compressive stresses in concrete members next to supports can be represented by a strut-and-tie model consisting of compressive struts and tension ties necessary for the equilibrium. Several research studies examined truss models, i.e. [ASC98], [SSJ87], [SS01], [WL94b], [ACI05], [Fos98], [Bro02], see also Section 2.3. Three different methods for predicting the strength of the compressive strut of normal concrete ACI 318-05 [ACI05], Specht [SS95] and Foster [Fos98] were applied to predict the strength of the LC strut.

According to ACI 318-05 (Appendix A: strut-and-tie models), the nominal compressive strength, F_{ns} , of bottle-shaped struts without transverse reinforcement is $F_{ns} = f_{ce} \cdot A_{cs}$, with A_{cs} = cross-sectional area at the strut end, f_{ce} = effective compressive concrete strength, defined by $f_{ce} = 0.85 \cdot \beta_s \cdot f'_c$ with efficiency factors $\beta_s = 0.6 \cdot \lambda$, where $\lambda = 1.0$ for normal concrete, 0.85 for SLWAC and 0.75 for ALWAC, and f'_c = specified compressive concrete strength. The ultimate loads resulting from this approach are given in Table 4.6, assuming an approximated minimum strut width of 79 mm at the bottom nodal zone and hence $A_{cs} = 79 \cdot 400 = 31600 \text{ mm}^2$ and $f'_c \simeq f_{c,m}$ as shown in Table 3.3.

Table 4.6: Cracking and ultimate loads predicted by different strut-and-tie models and their accordance with experimental results (ratio F_{pred}/F_{exp}).

	ACI 318-05		Specht $k_3d=43 \text{ mm}$		Foster $l_b=201 \text{ mm}$	
	Ultimate load F_u [kN] (Acc. [-])	Cracking load F_{cr} [kN] (Acc. [-])	Ultimate load F_u [kN] (Acc. [-])	Cracking load F_{cr} [kN] (Acc. [-])	Ultimate load F_u [kN] (Acc. [-])	Cracking load F_{cr} [kN] (Acc. [-])
900Es-1	32 (0.3)	59 (1.0)	130 (1.3)	110 (1.8)	274 (2.8)	110 (1.8)
900Es-2	32 (0.4)	59 (0.9)	130 (1.5)	110 (1.7)	274 (3.2)	110 (1.7)
1300Es-1	86 (0.4)	119 (1.4)	261 (1.3)	219 (2.5)	549 (2.7)	219 (2.5)
1300Es-2	86 (0.5)	119 (1.5)	261 (1.4)	219 (2.7)	549 (3.0)	219 (2.7)
1000s	140 (0.9)	131 (2.9)	289 (1.8)	243 (5.4)	608 (3.7)	243 (5.4)
1000Es	140 (0.7)	131 (2.6)	289 (1.4)	243 (4.9)	608 (3.0)	243 (4.9)

Specht [SS95] determined the cracking load of normal concrete beams with shear span-to-depth ratios of $a/d < 1.5$ based on Schlaich [SSJ87],[SS01]. Diagonal cracking occurred when the ties, T , as illustrated in Figure 4.7, reached their tensile strength at $T = 0.2 \cdot C = k_3 \cdot d \cdot b \cdot f_{ctsp}$. Here C represents the diagonal compressive force and $0.2 \cdot C$ was considered a reasonable approximation of the tensile force, while f_{ctsp} is the splitting tensile strength of normal concrete. The cross section of the ties was defined by the beam width, b , and the effective width of the tie given by the effective depth of the beam, d , and a coefficient, k_3 , derived from experimental results. As suggested by Specht, $k_3 = 0.685/\ln(100d)$. The ultimate load of the beams was again derived from the experimental results and found to be (on average) 2.2 times the cracking load. Applying these assumptions to the LC core led to an effective width of $k_3 \cdot d = 0.23 \cdot 185 = 43$ mm and the cracking and ultimate loads summarized in Table 4.6. The results are discussed in Section 4.4.3.

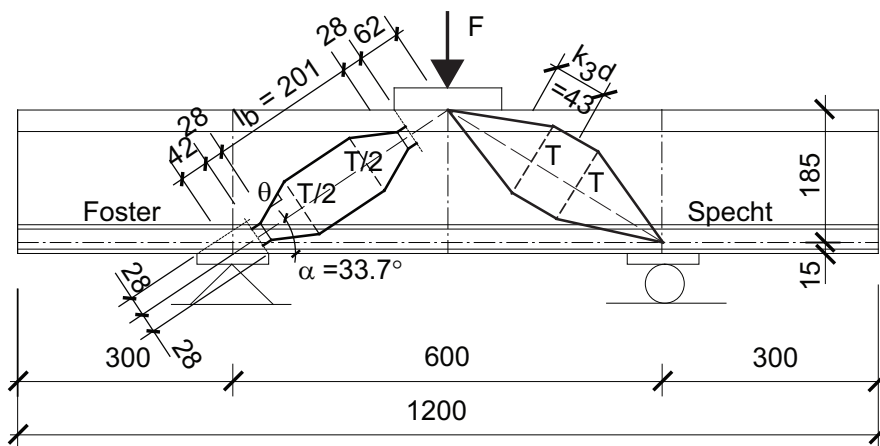


Figure 4.7: Simplified truss models based on Foster (left) [Fos98] and Specht (right) [SS95].

Foster [Fos98] calculated the so-called bursting force, T_b , defined by $T_b = C \cdot \tan\theta = l_b \cdot b \cdot f_{ctsp}$, with C = diagonal compressive force, θ = angle of deviation of the compressive strut, and l_b = length of the so-called bursting zone (see Figure 4.7). This approach is similar to that of Specht, with two differences: firstly, the effective width of the bursting force, the bursting zone length, l_b , was defined as the total length of the compressive strut, minus the length of the nodes and minimum width of the support, as in Figure 4.7, where $l_b = 201$ mm. Secondly, the angle of deviation of the compressive strut from the diagonal - determining the arch rise of the bowed compressive strut - changed during the loading process. Its maximum value was reached just before cracking; once cracking occurred, the struts became significantly narrower. This phenomenon was recently confirmed by Brown [Bro02]. According to Foster, the deviation angle was $\theta = \arctan(1/2) = 26.6^\circ$ before cracking, while after cracking the angle decreased to $\theta = \arctan(1/5) = 11.3^\circ$. Thus for the ultimate state the load was predicted to

increase by 150%, which was slightly higher than that observed by Specht (120%). The resulting cracking and ultimate loads for the LC system are also summarized in Table 4.6 and discussed in Section 4.4.3.

4.4.2 Novel continuous direct load transmission model

A major problem with the previously described strut-and-tie models is the definition of the effective widths on which the compression and tensile forces act. The proposed values were always fitted on experimental results. Furthermore, the systems are statically determined and therefore do not allow load or stress redistribution. In this respect, statically indeterminate systems could be more advantageous, since they allow the stress redistribution resulting from the non-linear LC softening behavior after concrete cracking to be taken into account. In the following, an extension of the truss model with its discrete system of ties to a system based on a continuum, with an infinite number of ties, is proposed. The model consists of a bottle-shaped strut, which transmits the diagonal compressive force and, to fulfill equilibrium, generates continuous tension transverse to the strut in the LC, as illustrated in Figures 4.8 and 4.9.

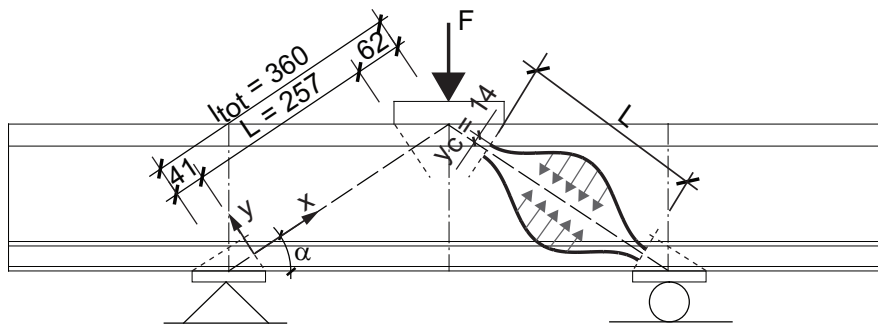


Figure 4.8: Continuous direct load transmission model: bottle-shaped compressive strut and continuously distributed transverse tensile stresses.

4.4.2.1 Basic assumptions and kinematic relationships

Figure 4.9 illustrates the compressive strut with undeformed shape, $y(x)$, and deformed shape (dashed line), $w(x)$, relative to $y(x)$, in the equilibrium state and also represents the kinematic relationships of a dx wide tie. The initially undeformed shape of the compressive force flow is geometrically defined by Eq. 4.9:

$$y(x) = y_0 \sin^2(\pi x/L) + y_c \quad (4.9)$$

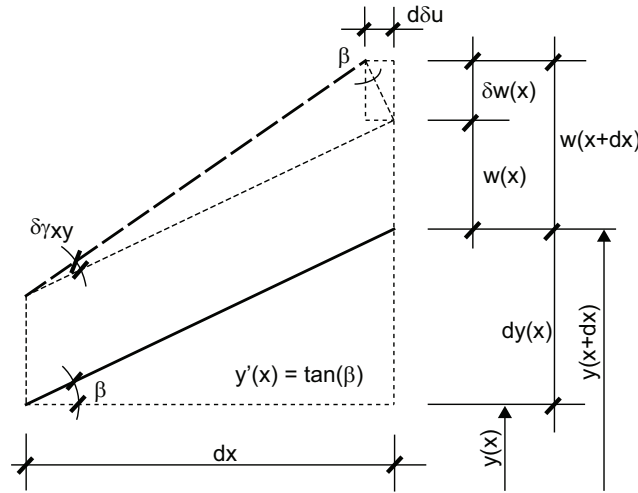


Figure 4.10: Kinematic relationships due to virtual displacements.

where $\delta\pi_i$ is the variation of the inner potential energy and $\delta\pi_o$ is the variation of the outer potential energy, i.e. the potential energy of the external loads:

$$\delta\pi_o = C \cdot \delta u \quad (4.11)$$

The virtual displacement δu is the integration of the reduction of the projected length, $d\delta u$, shown in Figure 4.10, as follows:

$$\delta u = 2 \int_0^{L/2} y'(x) \cdot \delta w'(x) dx \quad (4.12)$$

where $y'(x) = dy(x)/dx$ and $\delta w(x) = \delta w'(x) \cdot dx$ (see also Figure 4.10).

The variation of $\delta\pi_i$ includes contributions from the elongations of the ties and shear deformations resulting from different elongations of two adjacent ties:

$$\delta\pi_i = \int_V \sigma_y \cdot \delta\varepsilon_y dV + \int_V \tau_{xy} \cdot \delta\gamma_{xy} dV \quad (4.13)$$

where V is the volume enclosed by the bottle-shaped strut, σ_y and τ_{xy} are the axial and shear stresses of the ties, and $\delta\varepsilon_y$ and $\delta\gamma_{xy}$ are the virtual strains and distortions resulting from the virtual displacement.

The axial stresses, σ_y , are calculated according to Eq. 4.14, in which E_y is the Young's modulus of the LC concrete and ε_y the axial strain resulting from the elongation of the tie,

$w(x)$, in relation to its original length, $y(x)$.

$$\sigma_y = E_y \cdot \varepsilon_y(x) = E_y \frac{w(x)}{y(x)} \quad (4.14)$$

The virtual strain, $\delta\varepsilon_y$, can accordingly be expressed as:

$$\delta\varepsilon_y(x) = \frac{\delta w(x)}{y(x)} \quad (4.15)$$

The shear stresses, τ_{xy} , are calculated from the LC shear modulus, G_{xy} , and the corresponding shear distortion, γ_{xy} , according to Eq. 4.16. The distortion corresponds to the difference in elongations of two adjacent ties $dw(x)/dx = w'(x)$, see Figure 4.9.

$$\tau_{xy} = G_{xy} \cdot \gamma_{xy} = G_{xy} \cdot w'(x) \quad (4.16)$$

The virtual distortion, $\delta\gamma_{xy}$, is calculated accordingly and shown in Figure 4.10:

$$\delta\gamma_{xy} = \delta w'(x) \quad (4.17)$$

4.4.2.2 Constitutive equations of the material softening

When the tensile strength of the LC is exceeded, material softening occurs as shown in Figure 4.1. To further develop the proposed model, the bilinear post-peak strength decrease is approximated by an exponential function, as shown in Figure 4.11-a for LC1000. To take the softening behavior into account in the model, an exponential decrease is assumed for E_y , similar to that obtained for the post-peak tensile strength. Thus, E_y can be expressed as a two-stage function, as shown in Figure 4.11-b, and described by Eq. 4.18:

$$E_y(w(x)) = E_{lc,m} \begin{cases} 1 & \text{for } w(x) < w_{lct}(x) \\ e^{-r[w(x)-w_{lct}(x)]} & \text{for } w(x) \geq w_{lct}(x) \end{cases} \quad (4.18)$$

where r is an exponential factor (given in Table 4.1), and $w_{lct}(x)$ is the deformation when the uniaxial LC tensile strength is reached, as expressed by Eq. 4.19:

$$w_{lct}(x) = \frac{f_{lct,m}}{E_{lc,m}} \cdot y(x) \quad (4.19)$$

It is assumed that the LC shear modulus exhibits a similar decrease to that of the Young's modulus according to Eq. 4.20:

$$G_{xy}(w(x)) = G_{lc,m} \begin{cases} 1 & \text{for } w(x) < w_{lct}(x) \\ e^{-r[w(x)-w_{lct}(x)]} & \text{for } w(x) \geq w_{lct}(x) \end{cases} \quad (4.20)$$

The initial values, $G_{lc,m}$, can be calculated from $G_{lc,m} = E_{lc,m}/2(1 + \nu)$ assuming a Poisson's ratio of $\nu = 0.2$ [ACI03]; the resulting values are listed in Table 4.1.

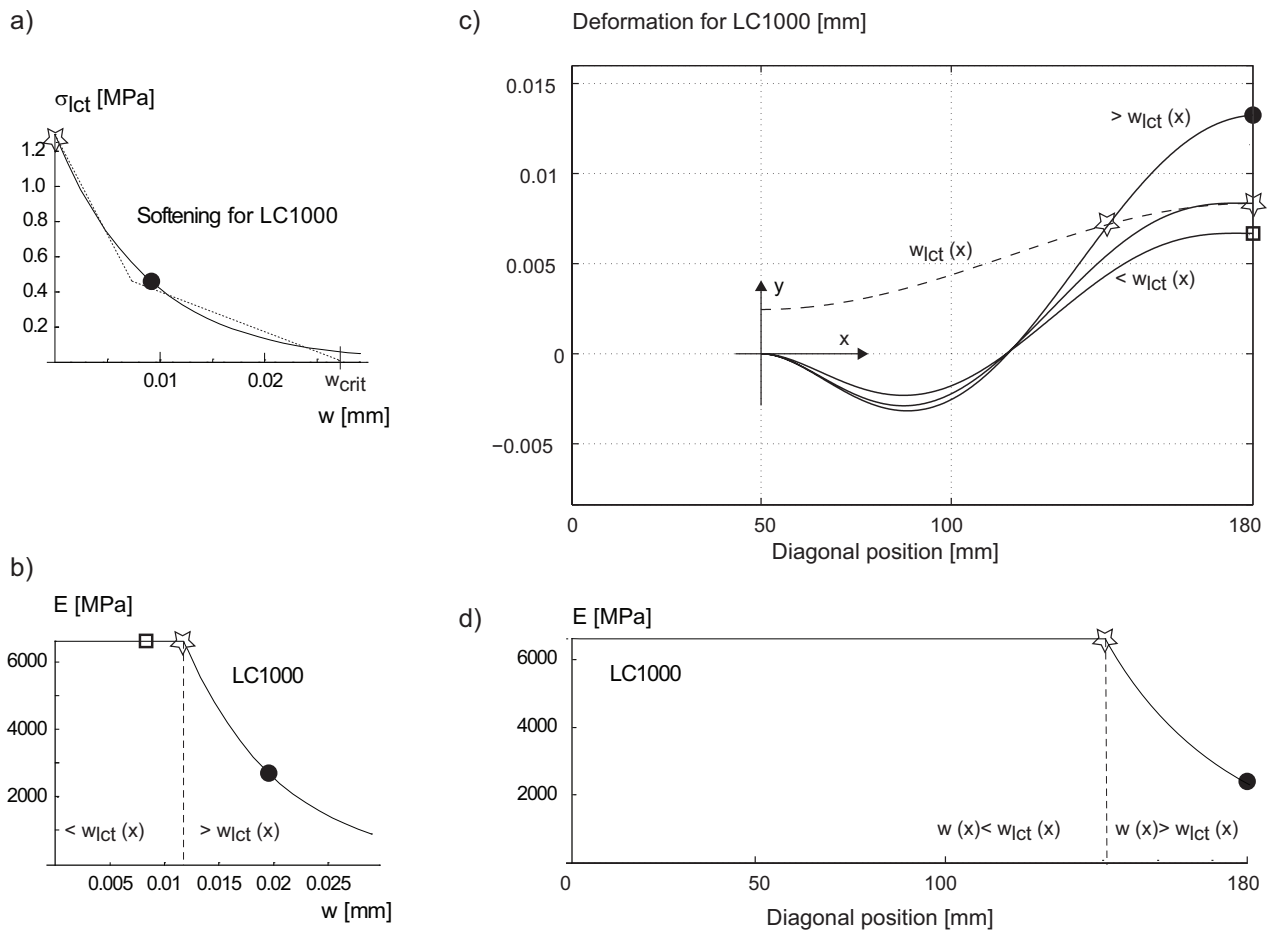


Figure 4.11: Development of material properties (a, c, d) and deformation along diagonal (b) before and after cracking for LC1000.

4.4.2.3 Solving of the equations

In order to determine the deformation $w(x)$ relative to the initial shape $y(x)$ and the corresponding compressive forces, Eq. 4.21 has to be solved:

$$\begin{aligned}
\delta\pi_i + \delta\pi_o &= 0 \\
&= \int_V \sigma_y \cdot \delta\varepsilon_y dV + \int_V \tau_{xy} \cdot \delta\gamma_{xy} dV + C \cdot \delta u \\
&= \int_V E_y \cdot \frac{w(x)}{y(x)} \cdot \frac{\delta w(x)}{y(x)} dV + \int_V G_{xy} \cdot w'(x) \cdot \delta w'(x) dV + C \cdot 2 \int_0^{L/2} y'(x) \cdot \delta w'(x) dx
\end{aligned} \tag{4.21}$$

where $w(x)$ and $\delta w(x)$ can be described as the combination of orthogonal Lagrange polynomials, $L_i(x)$ and $L_j(x)$, combined with the real and virtual constants, Φ_i and $\delta\Phi_j$, as given in Eq. 4.22 and Eq. 4.23, while the index i corresponds to the real and j to the virtual deformations:

$$w(x) = \sum_{i=1}^n \Phi_i \cdot L_i(x) \tag{4.22}$$

$$\delta w(x) = \sum_{j=1}^n \delta\Phi_j \cdot L_j(x) \tag{4.23}$$

Here $n=3$ chosen orthogonal Lagrange polynomials $L_1(x)$ – $L_3(x)$, fulfilling the geometrical boundary conditions: $L_1(x)$ restrains the strut at $x=0$ and $L_2(x)$ and $L_3(x)$ allow deformations but no strut inclination at $x=0.5L$ ([Bat82], [KW92]):

$$\begin{aligned}
L_1(x) &= 16 \cdot x^2 - 32 \cdot x^3 + 16 \cdot x^4 \\
L_2(x) &= -8 \cdot x^2 + 32 \cdot x^3 - 40 \cdot x^4 + 16 \cdot x^5 \\
L_3(x) &= 7 \cdot x^2 - 34 \cdot x^3 + 52 \cdot x^4 - 24 \cdot x^5
\end{aligned} \tag{4.24}$$

Further detailed information concerning the calculation process is given in Appendix A.1. The non-linear equation Eq. 4.21 is solved iteratively, assuming an arch rise, y_0 , and increasing the external load in small steps, as shown in Figure 4.11-c and 4.11-d for LC1000. At first, as long as the deformed shape, $w(x)$, is below $w_{lct}(x)$, the relationship between stresses and deformations remains linear (indicated with a square in Figure 4.11-a-d). Subsequently,

$w(x) = w_{lct}(x)$ is reached (indicated with a star) and when $w(x) \geq w_{lct}(x)$, E_y and G_{xy} start to decrease (indicated with a circle) and deformations rise exponentially. The stiffness of the system then progressively decreases because the extension of the zone exceeding $w_{lct}(x)$ increases. In the range of $x = 0-0.25L$, the deformations become negative due to the negative second derivate of the initial shape ($y'' < 0$), see Figure 4.11-c. This, however, is compatible with the hydrostatic compressive stress state existing in nodal zones of concrete structures.

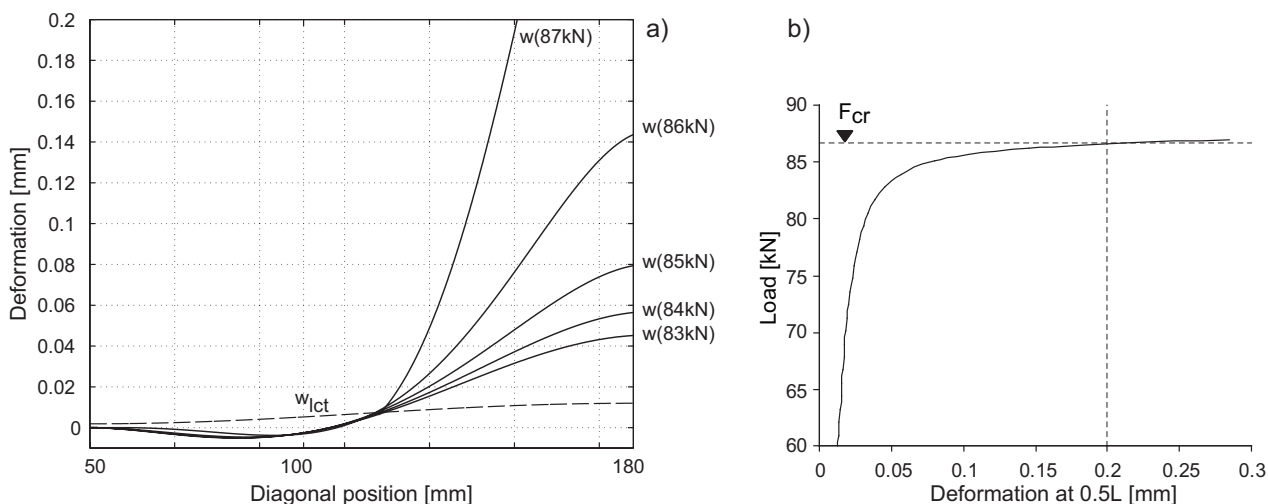


Figure 4.12: Definition of cracking load for 1300Es-1.

Depending on the assumption of the arch rise (see next paragraph), the cracking load, C_{cr} , or ultimate load, C_u , of the strut can be determined and is reached when the algorithm diverges, that is, when corresponding deformations become infinite, as shown in Figure 4.12 for determination of the cracking load of specimen 1300Es. In this example, the cracking load of the strut is already converted into the cracking load of the specimen by $F_{cr} = 2 \cdot C_{cr} \cdot \sin \alpha$. For practical reasons, calculations were stopped at a deformation of 0.2 mm in the middle of the strut, $w(L/2)$, corresponding to a large crack.

The experimental results and above-mentioned references showed that the arch rise of the strut is not a constant value, but decreases after concrete cracking. In order to apply the proposed model, the arch rises at LC cracking and at ultimate load had first to be determined by calibration to the experimental results. The arch rise was varied from 10 to 100 mm and the corresponding loads, F , at 0.2 mm deformation were calculated for the three LC types, as shown in Figure 4.13.

From these curves and the measured cracking and ultimate loads, the arch rises at cracking loads, $y_{0,cr}$, and ultimate loads, $y_{0,u}$, were determined. As assumed, the arch rises at cracking were much higher than at ultimate load, see Table 4.7.

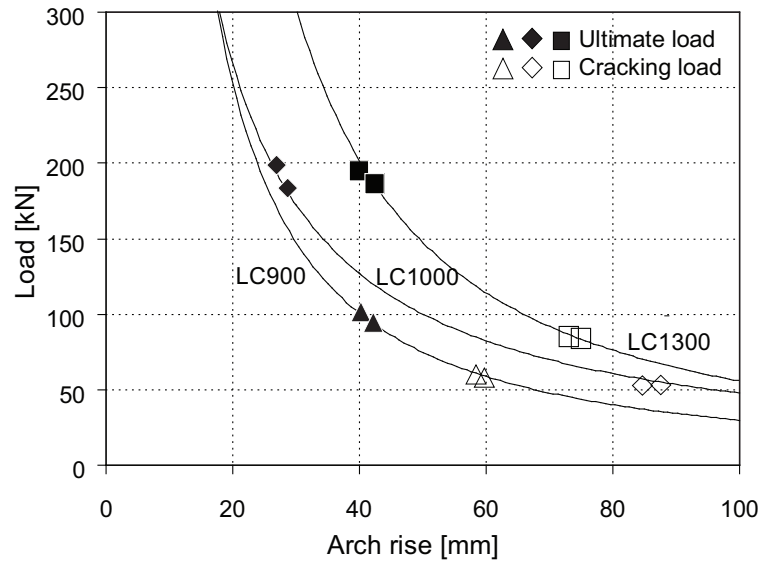


Figure 4.13: Cracking and ultimate loads vs arch rise.

Table 4.7: LC cracking loads, specimen ultimate loads, ratio between them and arch rises at cracking and ultimate loads.

Beam	Cracking load F_{cr} [kN]	Ultimate load F_u [kN]	Ratio F_u/F_{cr} [-]	Arch rise at cracking $y_{0,cr}$ [mm]	Arch rise at ultimate $y_{0,u}$ [mm]
900Es-1	60	98	1.63	60	40
900Es-2	65	83	1.28	57	42
1300Es-1	87	204	2.34	73	40
1300Es-2	80	185	2.31	77	42
1000s	45	164	3.64	90	29
1000Es	50	201	4.02	85	27

The corresponding transverse deformations (due to tension) can then be modeled at cracking as shown in Figure 4.14 for specimens 1000Es and 1300Es-2. For both LC types, good agreement with experimental results was found. Subsequent to cracking, experimental deformations increased significantly and measurements were influenced by the cracks in such a way that no coherent and conclusive distributions of deformations along and across the diagonals could be obtained at ultimate load. Therefore, predicted and measured deformations at ultimate load could not be compared.

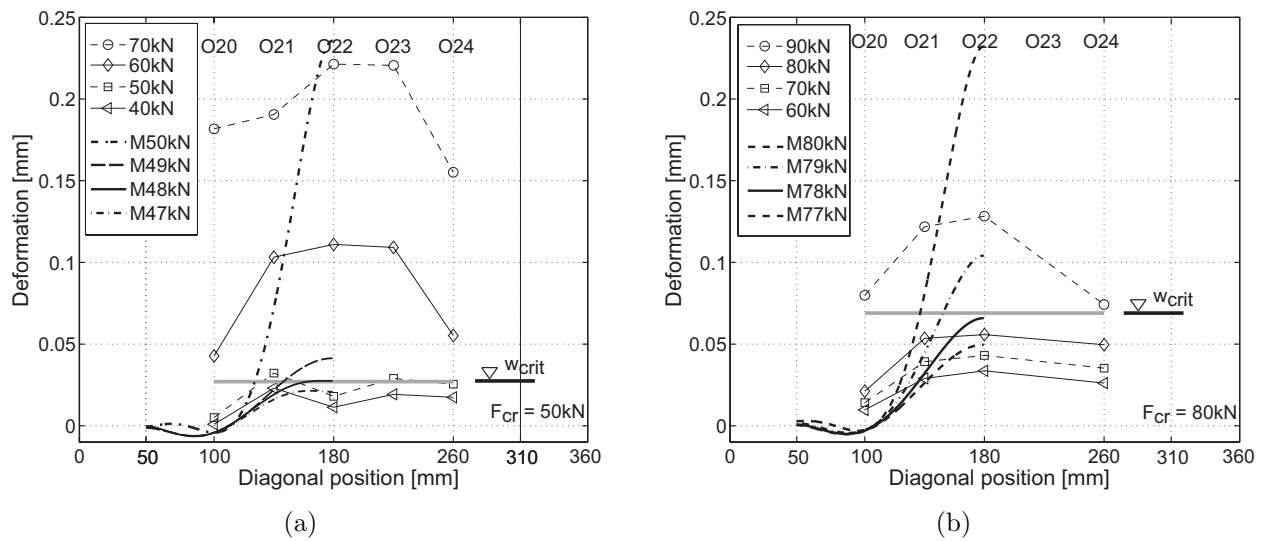


Figure 4.14: Transverse deformation along diagonal of 1000Es (left) and 1300Es-2 (right) from experiments and model (the latter denoted by M).

4.4.3 Results and discussion

4.4.3.1 Strut-and-tie models

In a first approach, the experimental results were verified with existing strut-and-tie models for normal concrete. The results and their accordance with experimental results are summarized in Table 4.6. The ultimate loads according to ACI318-05 were strongly underestimated for the SLWAC specimens while they almost matched the experimental values for the ALWAC specimens. To match the experimental results for the SLWAC, the efficiency factor would have to be in the range of $\beta_s = 1.3$ instead of 0.51, which is unrealistic since it is greater than 1.0. Therefore, even though good results were obtained for the ALWAC, the method does not seem to be generally reliable for lightweight concrete. The cracking loads were highly overestimated using the methods from Specht and Foster. Since experimental results showed that the cracking load was not correlated to the splitting tensile strength, no accordance could be found by assuming identical effective widths of the ties and deviation angles of the compressive strut for all LC types. The ratio between experimental ultimate and cracking loads varied between 1.3 and 4.0, see Table 3.9 on page 67, while Specht and Foster proposed constant values for normal concrete (2.2 and 2.5). Thus, no accordance was found between predicted and experimental ultimate loads.

4.4.3.2 Continuous direct load transmission model

The proposed model for the direct load transmission behavior is an extension of a typical statically determinate strut-and-tie model to a model consisting of a bottle-shaped strut with an infinite number of ties. The strut transmits the diagonal compressive force and, to fulfill equilibrium, generates tension in the ties. Thanks to the statically indeterminate system, the model permits the stress redistribution resulting from the non-linear LC softening behavior after concrete cracking to be taken into account. Taking the softening behavior into consideration allows accurate modeling of the differences between the SLWAC and ALWAC specimens, which exhibit different brittleness.

Although the suggested model needs to be calibrated on experimental results, i.e. the arch rises of the strut at concrete cracking and ultimate load have to be deviated from measured cracking and ultimate loads, the model is able to describe the transverse deformation of the strut during concrete cracking. The transverse deformations (due to tension) at LC cracking, shown in Figure 4.14 for specimens 1000Es and 1300Es-2, were comparable to the experimental results, including the transverse compression in the nodal zones, which could also be found by extrapolation of the experimental curves. However, the zones of deformation due to transverse tension were less extensive than those measured.

Furthermore, the model leads to arch rises - decreasing with increasing load - that compare well with experimental observations. The sum of twice the arch rise plus the offset of 55 mm of 1300Es (average of both specimens) at ultimate load, for instance, compares well with the width of the longitudinal deformations ($90-30 = 60$ mm) at ultimate load, shown in Figure 3.40 on page 73.

4.4.3.3 Influence of material properties on arch rise

The arch rise at cracking was well correlated to the LC splitting tensile strength, as illustrated in Figure 4.15 (correlation coefficient $R^2=0.99$). Thus, the splitting tensile strength gave an indication of the LC's ability to deviate the compressive stress flow: with increasing splitting tensile strengths, the load transmission occurred over a wider zone, expressed by a greater arch rise up to the cracking load. After cracking, the arch rise decreased, since the width of the compressive strut was reduced by the cracks initiating and propagating parallel to the diagonal. Accordingly, the arch rise was not correlated to the splitting tensile strength at ultimate load, as is also shown in Figure 4.15.

Figure 4.16 shows the correlation between the arch rise and LC characteristic length, l_{ch} , which represents the length of a tie in which the elastic energy required to create a transverse fracture surface is stored. The arch rise was not correlated to characteristic length at cracking, while it was well correlated at ultimate loads. The more brittle ALWAC, exhibiting a shorter

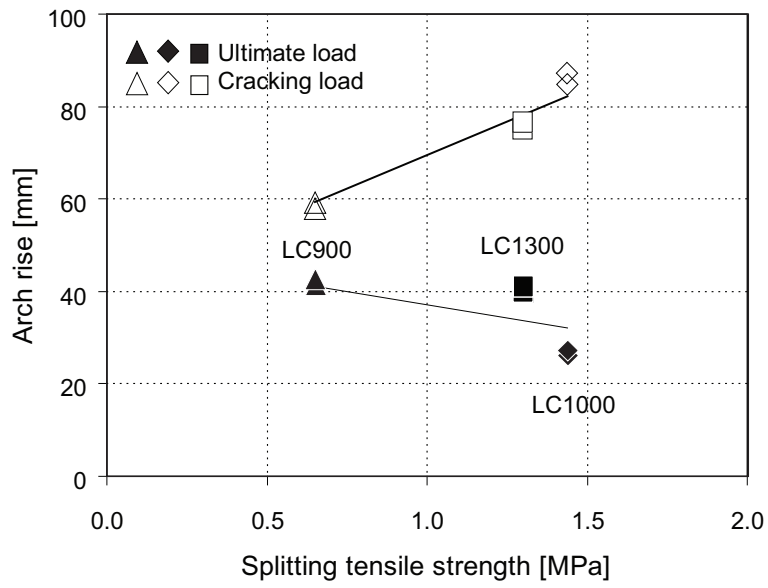


Figure 4.15: Arch rise vs splitting tensile strength.

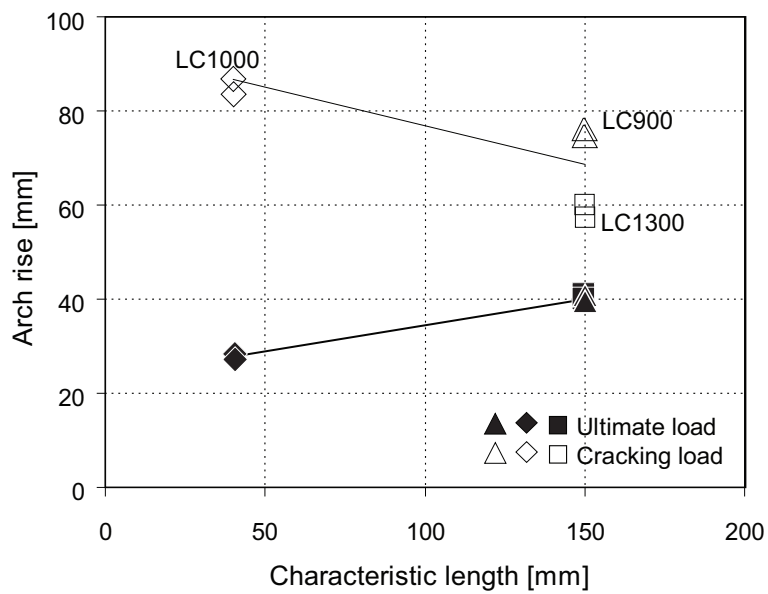


Figure 4.16: Arch rise vs characteristic length.

characteristic length and therefore shorter ties, showed smaller arch rises at failure than the SLWAC composition.

4.4.4 Conclusions

The direct load transmission behavior of hybrid sandwich beams consisting of a bottom FRP skin and a top concrete skin was investigated experimentally. The sandwich core consisted of lightweight concretes of different brittleness (SLWAC and ALWAC mixtures). Shear failure occurred in the LC core at ultimate loads which were not correlated to the compressive strength of the compressive strut between load and support axis. LC cracking and ultimate loads were first modeled with classic strut-and-tie models and then with a novel continuous load transmission model. The following conclusions were drawn:

1. The ultimate load prediction according to ACI318-05 underestimated the strength of the SLWAC specimens, while it predicted the strengths of the ALWAC specimens well. Therefore, although good results were obtained for the ALWAC mixture, the method does not seem reliable for lightweight concrete. Cracking and ultimate load prediction using classic strut-and-tie models is inaccurate since differences in material brittleness are not sufficiently taken into account.
2. The proposed continuous direct load transmission model consists of a bottle-shaped strut with an infinite number of transverse ties. The statically indeterminate system allows the stress redistribution resulting from the post-peak material softening after concrete cracking to be taken into account. This allowed accurate modeling of the differences between the load-bearing behaviors of the SLWAC and ALWAC specimens.
3. The arch rise of the bowed compressive strut decreased after cracking because the available strut width was reduced to the distance between initiating and propagating cracks parallel to the strut. The arch rise at concrete cracking was correlated to the LC splitting tensile strength while the arch rise at ultimate load was correlated to the LC characteristic length, which is a fracture mechanics property describing material brittleness.

4.5 Summary

This chapter presented the modeling of the shear resistance of the experimentally investigated hybrid long- and short-span beams with two different types of lightweight concrete core: an SLWAC mixture with expanded clay and sand aggregates and an ALWAC mixture with

expanded clay and expanded glass aggregates. The former LC exhibited a much higher fracture energy and longer fracture process zone (FPZ) than the latter. The following conclusions resulted:

- The shear resistance prediction of long- and short-span beams according to current design codes (Eurocode 2 for long-span and ACI 318-05 for short-span beams) was not reliable, since the different fracture behaviors of SLWAC and ALWAC concretes is not sufficiently taken into account. Shear strength predictions for the long-span beams could be improved by incorporating the characteristic length into the scale coefficient.
- A shear prediction method for the span was presented which takes into account the shear resistance of the fracture process zone. Due to the consideration of the different LC brittleness, good agreements between experimental results and predictions were achieved.
- In addition, a novel continuous direct load transmission model was proposed to determine cracking and ultimate loads for direct load transmission to the support. The model - a statically indeterminate system - consisted of a bottle-shaped strut with an infinite number of transverse ties. In contrast to statically determinate strut-and-tie models, the model allowed the different LC softening behaviors to be taken into account and thus the modeling of the different cracking behaviors of the SLWAC and ALWAC cores.

5 Application of hybrid slab system

The application of the hybrid FRP-concrete slab system for bridges and buildings is presented in the following chapter. A design concept is developed for a typical bridge application, including the verification of structural safety and serviceability. The verification of structural safety includes the consideration of uniformly distributed loads within the span and concentrated loads due to wheel loads. The same concept can be applied for building applications, where only uniformly distributed loads occur and the verification of punching under concentrated loads can be disregarded.

5.1 Bridge applications

In this section, a design concept is firstly developed for use of the hybrid FRP-concrete slabs for bridge decks, which includes the verification of serviceability and structural safety (flexural and shear verification). Secondly, examples of two bridge design configurations are used to study the applicability of the experimentally investigated new LC compositions. Furthermore, an optimization study discusses the influence of face material properties on the dominating failure mechanism and defines a possible material configuration for creating a ductile failure.

5.1.1 Design concept for a hybrid FRP-concrete sandwich bridge deck

5.1.1.1 Verification of structural safety

Verification of the structural safety of the hybrid sandwich bridge slab is performed for the design moments, shear forces and punching according to Eurocode 1, load model 1 [Com01]. First, verification of the bending moment is conducted in the face layers in the regions of maximum moments. Second, verification of the shear resistance is performed in three critical sections: within the span (denoted in the following as Section A-A), under concentrated loads (denoted as punching in Section B-B) and next to the support (denoted as Section C-C).

In order to obtain design values for the material resistances, the characteristic material strengths are reduced by the material resistance coefficients $\gamma_{c,M} = 1.5$ for both concretes [Com04] and $\gamma_{frp,M} = 2.0$, according to a mean value for the use of FRP profiles from the Eurocomp [Cla00].

Verification of bending moments

The bending moment is taken from the face layers and hence the verification is conducted according to Eqs. 5.1 and 5.2 in regions of maximum moments within the span and over the support. Therefore, the compressive and tensile stresses in the face layers ($\sigma_{uhpfrc,d}$ in the UHPFRC and $\sigma_{frp,d}$ in the FRP) are determined by the design moment, m_d , and the corresponding section moduli W_{uhpfrc} and W_{frp} . The stresses are then compared to the design values of the material strengths ($f_{uhpfrc,d}$ and $f_{frp,d}$), which are the characteristic material strengths reduced by the material resistance factors.

$$\sigma_{uhpfrc,d} = \frac{m_d}{W_{uhpfrc}} \leq f_{uhpfrc,d} = \frac{f_{uhpfrc,k}}{\gamma_{uhpfrc,M}} \quad (5.1)$$

$$\sigma_{frp,d} = \frac{m_d}{W_{frp}} \leq f_{frp,d} = \frac{f_{frp,k}}{\gamma_{frp,M}} \quad (5.2)$$

Verification of shear resistance within the span

The characteristic shear resistance of the slab within the span, $v_{lc,Rk(A-A)}$, is determined by using the fracture mechanics approach refined from Zink [Zin00], described in detail in Section 4.3. Subsequently, the characteristic shear resistance is reduced by the material resistance coefficient for concrete in order to obtain the design value of the shear resistance, $v_{lc,Rd}$, and compared to the design values of the shear, p_d , according to Eq. 5.3:

$$p_d \leq v_{lc,Rd(A-A)} = \frac{v_{lc,Rk(A-A)}}{\gamma_{lc,M}} \quad (5.3)$$

The components that contribute to the characteristic shear resistance of the hybrid slab are explained in detail in Section 4.3.3 (see also Figure 4.6) and expressed in Eq. 5.4:

$$v_{lc,Rk(A-A)} = v_{uhpfrc} + v_{lc} + v_{FPZ} = \left[\frac{2}{3} d_{uhpfrc} + (x_n - d_{uhpfrc}) + 0.4 \cdot d_{FPZ} \right] \cdot f_{lct,k} \geq p_d \cdot \gamma_{lc,M} \quad (5.4)$$

Verification of punching

To verify resistance to punching, the presented shear strength prediction method within the span is modified so that shear resistance is no longer calculated for one plane fracture surface but for a punching cone. For simplification, the punching load is assumed to be borne by a punching pyramid of four fracture planes, as illustrated in Figure 5.1. The shear resistance

of the simplified punching pyramid, $V_{lc,Rk(B-B)}$, is calculated according to Eq. 5.5:

$$\begin{aligned} V_{lc,Rk(B-B)} &= 4 \cdot [V_{uhpfrc} + V_{lc} + V_{FPZ}] \\ &= 4 \cdot \left[\frac{2}{3} d_{uhpfrc} \cdot b_{uhpfrc} + (x_n - d_{uhpfrc}) \cdot b_{lc} + 0.4 \cdot d_{FPZ} \cdot b_{FPZ} \right] f_{lct,k} \geq P_d \cdot \gamma_{lc,M} \end{aligned} \quad (5.5)$$

where b_{uhpfrc} , b_{lc} , b_{FPZ} = width of the punching pyramid of the respective layer, as shown in Figure 5.1. The width of each layer of the punching pyramid is calculated from the wheel side length of 400 mm (according to EC1 [Com01]), by assuming a load distribution of 1:3 within the covering ($d_{cov} = 100$ mm) and a load distribution angle of 45° within the hybrid slab.

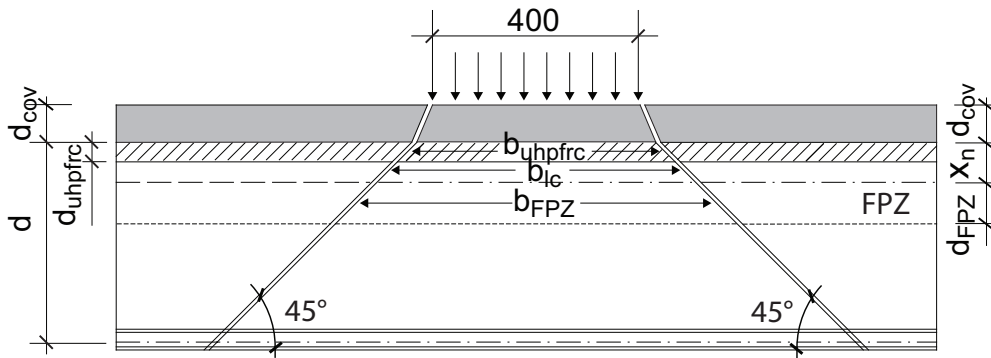


Figure 5.1: Punching

Experimental investigation on hybrid normal concrete slabs reinforced with a 23-mm-deep layer of UHPFRC in the tensile zone, recently published by Wuest [Wue07], showed that the resistance to punching loads increased by 40% compared to normal concrete slabs of the same total depth. This improvement is mainly due to positively acting membrane forces from the UHPFRC layer.

The same positive effect can be expected for the proposed hybrid FRP-concrete slab system with the FRP profile in the tensile zone. Therefore, the method presented for calculation of punching resistance should be seen as a lower limit value. An increase in the slab's punching resistance due to the additional contribution of the membrane forces of the FRP profile is disregarded at this stage of the project.

Verification of direct load transmission next to support

For the shear verification next to the support, the proposed shear strength prediction method within the span is no longer applicable since loads are directly transmitted through the compressive diagonals to the support. The proposed continuous shear model for direct load transmission regions presented in Section 4.4.2 is not applicable either, since it is based and calibrated on experimental results obtained from short-span beams of 200-mm depth.

An application of the model for greater slab depths would require further experimental investigation to confirm the calibrated input parameters for 200-mm-deep slabs. Therefore, verification of the design shear values next to the support is carried out empirically based on the experimental results reported in Section 4.3. The average ratio between ultimate beam loads and the ultimate loads for direct load transmission is 1:4.3. In this first approach, it is hence assumed that the shear resistance next to supports, $v_{lc,Rd(C-C)}$, is 4.3 times higher than the shear resistance within the span ($v_{lc,Rd(A-A)}$), as specified in Eq. 5.6. However, this simplified assumption is based on experimental results obtained from 200-mm-deep short-span beams. This hypothesis therefore represents a rough approach and should be verified for deeper slabs by further experiments.

$$v_{lc,Rd(C-C)} = 4.3 \cdot v_{lc,Rd(A-A)} \quad (5.6)$$

5.1.1.2 Verification of serviceability

For verification of the serviceability of the hybrid sandwich slab, the maximum deflection, $u_{d,span}$, is calculated within the span and compared to the maximum authorized deflection of $L/500$, according to Swisscode SIA 260 [SIA03c], where L represents girder spacing, see Eq.5.7:

$$u_{d,span} = \frac{L}{500} \quad (5.7)$$

The calculations are performed using Cedrus-4 from CUBUS [cub], and assuming an effective stiffness EI_{eff} of the cracked slab over the total bridge width. The slab would not in fact be cracked over the total bridge width, which partially increases the effective stiffness of the bridge slab. A possible decrease of the resulting values is therefore expected.

5.1.2 Design example of a 400-mm-deep, 6-m-wide bridge slab with 2-m girder spacing

The applicability of the experimentally investigated LCs (see Section 3.2) is studied in the following design example of a 6-m-wide bridge slab with girder spacing of 2 m and a slab depth of 400 mm.

5.1.2.1 Material properties

Face layers

The characteristic material strengths of the materials used are as follows: the top concrete layer consists of a 25-mm-deep UHPFRC mixture according to Habel ([HDB06], [HDB07]) and exhibits a compressive strength of $f_{uhpfrc,k} = 168$ MPa, a Young's modulus of $E_{uhpfrc} = 48$ GPa and a tensile strength of $f_{uhpfrct,k} = 11$ MPa. The bottom GFRP skin is the standard pultruded Plank profile 40HD that was used for the experimental investigation (see also Section 3.2.2), exhibiting a tensile and compressive strength of 240 MPa and a Young's modulus of 23 GPa.

LC compositions

The LC compositions from the experimental investigation are used: the two SLWAC (LC900 and LC1300) and the ALWAC (LC1000) compositions. In order to verify the shear strength of the hybrid slab system, the LC uniaxial tensile strength and the LC material brittleness, defined by the characteristic length, must be known. The LC characteristic uniaxial tensile strength is approximated with 90% of the mean splitting tensile strength determined on cylinders and summarized in Table 3.3 on page 43 in Section 3.2.1. Characteristic lengths, l_{ch} , of 150 mm and 40 mm are assumed for the SLWAC and ALWAC, see also Section 3.2.1.3.

Hybrid section properties

The sectional properties of the hybrid sandwich slab (neutral axis x_n , effective stiffness EI_{eff} , controlling section moduli of the face layers W_i) are calculated for the different LC cores based on Section 4.3.1. It is recognized that the neutral axis is very high and that the values are almost independent of the LC core, since the stiffness portion from the identical top and bottom face layers clearly dominated the slightly different stiffness portions of the different LC cores. The results are summarized in Table 5.1 for a 400-mm-deep slab, indicating that the compressive zone of the slab is only 64 mm, corresponding to only 16% of the total slab depth.

Table 5.1: Sectional properties of 400-mm-deep hybrid FRP-concrete sandwich slab of 1-m width.

	x_n [mm]	EI_{eff} [Nmm ²]	W_{uhpfrc} [mm ³]	W_{frp} [mm ³]
400-mm-deep slab	64	2.56 E+13	7.70 E+06	1.62 E+06

5.1.2.2 Load assumptions

The dead weight of the slab, including the covering, amounts to 7.5 kN/m^2 (5.0 kN/m^2 dead weight plus 2.5 kN/m^2 for the covering). The bridge deck loads are considered according to Eurocode 1, load model 1 [Com01], consisting of uniformly distributed loads (UDLs) and double-axle concentrated loads. Figure 5.2 illustrates the most critical arrangement of the loads on the 6-m-wide bridge with a girder spacing of 2 m. The UDLs are applied on lanes 1 and 2, while the wheel loads are only applied on lane 1. Each axle of the tandem system is considered with $Q_{k,i}$ multiplied by the adjustment factor, $\alpha_{Q,i} = 0.65$, for small bridges with reduced traffic loads taken from the Swisscode SIA 261, [SIA03b]. The axle comprised two identical wheels with a contact surface of $400 \times 400 \text{ mm}^2$. The UDLs are considered with $q_{k,i}$ and the adjustment factor $\alpha_{q,i} = 0.65$, according to [SIA03b]. Table 5.2 summarizes the applied loads.

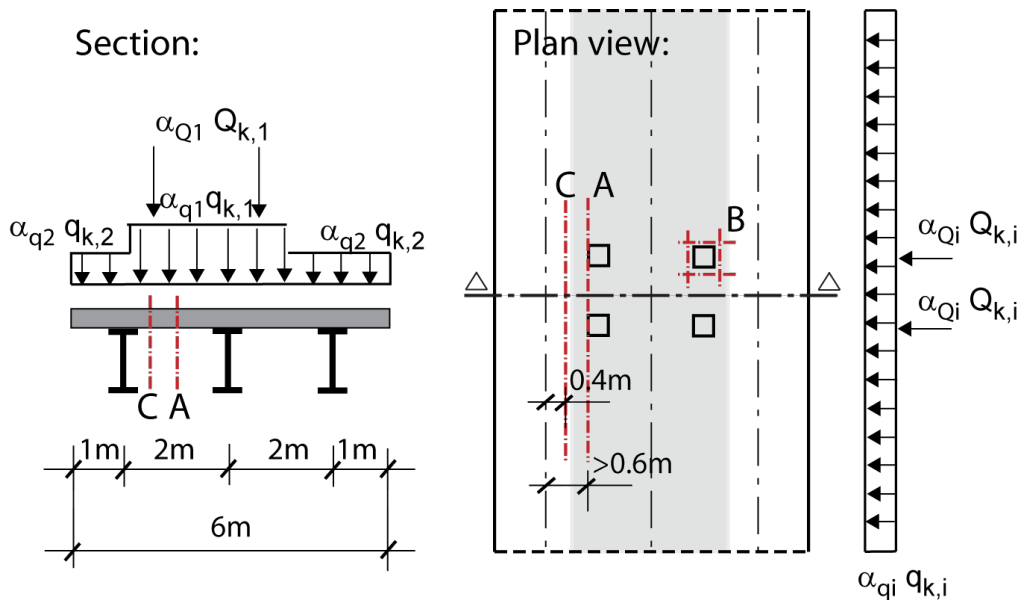


Figure 5.2: Distribution of bridge loads according to EC1 and sections for shear verification.

To determine the design shear values and moments for the safety verification, the dead load (g_k) and traffic loads ($Q_{k,i} + q_{k,i}$) are factored by the partial safety factors according to EC1 [Com01] $\gamma_G = 1.35$ and $\gamma_Q = 1.5$ respectively. For serviceability verification, the safety factors are $\gamma_G = \gamma_Q = 1.0$, while a further reduction coefficient is included for frequent loading: $\psi_G = 0.75$ according to SIA 260 [SIA03c].

The bridge slab design moments and shear values are determined using Cedrus-4 from CUBUS [cub]. The structural analysis results are illustrated in Figures 5.3 and 5.4. The

Table 5.2: Applied loads on a 6-m-wide bridge according to Eurocode load model 1 [Com01] and [SIA03b] for adjustment factors.

	Axle loads $Q_{k,i}$ [kN]	UDL $q_{k,i}$ [kN/m]	$\alpha_{Q,i}$ [-]	$\alpha_{q,i}$ [-]
First lane	300	9.0	0.65	0.65
Second lane	200	2.5	0.65	0.65

regions governing the bending moment design are within the span and over the girders, as illustrated in Figure 5.3.

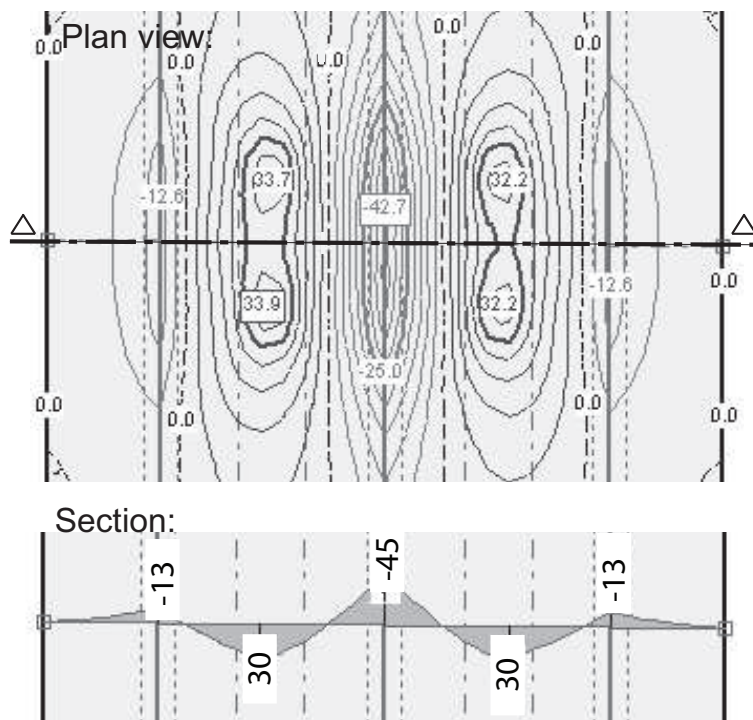


Figure 5.3: Distribution of design moments in [kNm/m], equidistance of 10 kNm/m, for a 400-mm-deep and 6-m-wide bridge with 2-m girder spacing.

The shear verification is performed in the three sections, as indicated in Figure 5.2; Section A-A representing the span area at a distance of more than 0.6 m from the support, while Section B-B represents the zone under concentrated wheel loads (punching). Section C-C is the zone next to supports at 0.4 m from the support axis, where the load is directly transmitted to the main girders by a compressive diagonal.

The design shear values occurring in Sections A-A and C-C are determined using Cedrus-4 from CUBUS [cub]. The results of the analysis are illustrated in Figure 5.4. The verification of the design punching load, P_d , (Section B-B) is conducted separately for one concentrated

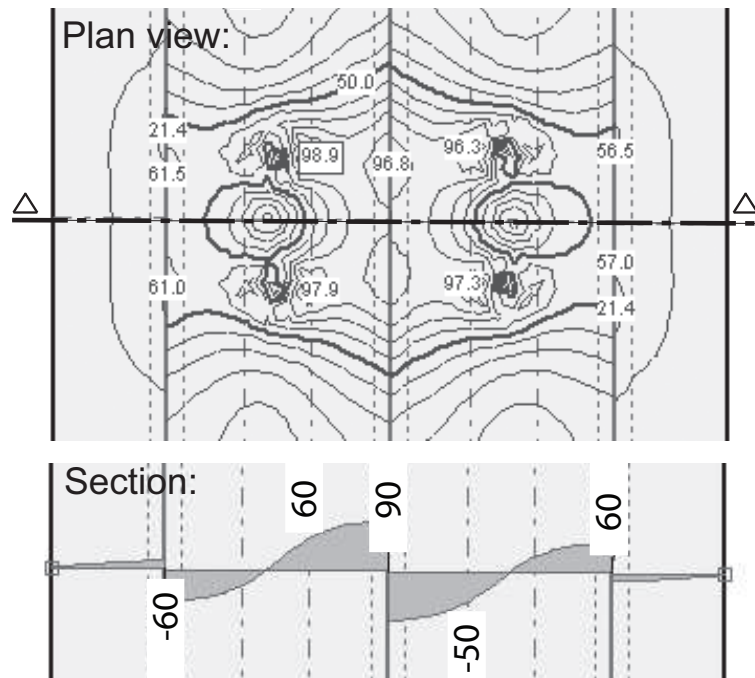


Figure 5.4: Distribution of design shear values in [kN/m], equidistance of 10 kN/m, for a 400-mm-deep and 6-m-wide bridge with 2 m girder spacing.

wheel load reduced by the appropriate adjustment factor. The design moments and shear values are summarized in Table 5.3.

Table 5.3: Design moments and shear values for a 6 m bridge with 2-m girder spacing.

Section of verification	Design moments	Design shear values	
	m_d [kNm/m]	P_d [kN]	p_d [kN/m]
A-A	80	-	60
B-B	-	$0.65 \cdot 150 \cdot 1.5 = 146$	-
C-C	-70	-	100

5.1.2.3 Verification of structural safety

Verification of bending moments

The compressive and tensile stresses due to bending in the face sheets are indicated in Table 5.4. As stated above, the analysis is independent of the LC core, since the stiffness portion from the face layers clearly predominated. Neither the compressive strength of the

top concrete layer nor the tensile strength of the FRP are reached within the span and both could be optimized; only 9% and 20% of the strength is reached respectively. In the support region, tensile stresses occur in the top concrete layer. However, the UHPFRC layer provides sufficient tensile strength to bear these stresses. The FRP profile is sufficiently resistant to compressive stresses occurring over the support.

Table 5.4: Verification of bending moments for a 400-mm-deep, 6-m-wide bridge with 2-m girder spacing (negative signs = compression).

Section of verification	$\sigma_{uhpfrc,d}$ [MPa]	$f_{uhpfrc,Rd}$ [MPa]	$(\sigma_d/f)_{uhpfrc}$ [-]	$\sigma_{frp,d}$ [MPa]	$f_{frp,Rd}$ [MPa]	$(\sigma_d/f)_{frp}$ [-]
Span	-4	-112	28 > 1.0	9	120	13 > 1.0
Support	6	7.33	1.2 > 1.0	-14	-120	8.6 > 1.0

Verification of shear resistance within the span

The shear resistance, $v_{lc,Rd}$, is calculated for the different LC types and then compared to the design shear values as described in Eq. 5.4. The results and their accordance with the design values are summarized in Table 5.5. Using the LC1300 as core material offered sufficient shear resistance to fulfill design requirements, while the LC1000 and LC900 cores provided insufficient shear resistance.

Table 5.5: Shear strength prediction within the span for a 400-mm-deep, 6-m-wide bridge with 2-m girder spacing using experimentally investigated LCs.

Lightweight concrete	v_{uhpfrc} [kN]	v_{lc} [kN]	v_{FPZ} [kN]	$v_{lc,Rk}$ [kN]	$v_{lc,Rd}$ [kN]	$v_{lc,Rd}/p_d(A-A)$ [-]
LC900	9.75	23.7	9.9	43.4	29	0.5 < 1.0
LC1300	19.50	44.5	19.9	83.8	56	1.0 = 1.0
LC1000	20.10	47.0	5.5	72.5	48	0.8 < 1.0

Verification of punching

The geometry of one fracture plane of the simplified punching pyramid is calculated according to Figure 5.1, while the effective widths of one pyramid plane are $b_{uhpfrc} = 485$ mm, $b_{lc} = 550$ mm and $b_{FPZ} = b_{lc} + 0.4 \cdot l_{ch}/\sqrt{2}$, varying between 599 - 633 mm. The shear resistances of one punching pyramid according to Eq. 5.5 and their accordance with the design shear values are summarized in Table 5.6. For all three LC compositions, the simplified punching

pyramid approach led to insufficient punching resistance (90% for LC1300, 70% for LC1000 and 40% for LC900). However, as stated above, the method presented for punching resistance calculation should be seen as a lower limit value. An increase in resistance is expected due to the additional contribution of membrane forces of the FRP profile, which is disregarded at this stage of the project. Assuming the same increase as presented in Wuest [Wue07] would increase the shear resistance by 40% to a new punching resistance value, $V_{lc,Rd}^*$, as given in Table 5.6. Consequently, LC1300 and LC1000 would offer sufficient resistance to bear the design loads.

Table 5.6: Punching resistance prediction of a 400-mm-deep bridge slab using experimentally investigated LCs.

Lightweight concrete	V_{uhpfrc} [kN]	V_{lc} [kN]	V_{FPZ} [kN]	$V_{lc,Rk}$ [kN]	$V_{lc,Rd}$ [kN]	$V_{lc,Rd}/P_d$ [-]	$V_{lc,Rd}^*$ [kN]	$V_{lc,Rd}^*/P_d$ [-]
LC900	18.9	52.1	25.2	96.2	64.1	0.4 < 1.0	96.2	0.7 < 1.0
LC1300	37.8	97.5	49.9	185.3	123.5	0.9 < 1.0	185.3	1.3 > 1.0
LC1000	39.0	103.1	13.1	155.2	103.5	0.7 < 1.0	155.3	1.1 > 1.0

Verification of direct load transmission next to the support

The results of the shear design verification next to the support are given in Table 5.7. Design requirements are fulfilled for all the experimentally investigated LCs.

Table 5.7: Shear strength prediction next to support of a 400-mm-deep, 6-m-wide bridge with 2-m girder spacing using experimentally investigated LCs.

Lightweight concrete	$v_{lc,Rk(A-A)}$ [kN]	$v_{lc,Rk(C-C)}$ [kN]	$v_{lc,Rd(C-C)}$ [kN]	$v_{lc,Rd(C-C)}/P_d(C-C)$ [-]
LC900	43.4	186.4	124.3	1.4 > 1.0
LC1300	83.8	360.6	240.4	2.7 > 1.0
LC1000	72.5	311.8	207.9	2.3 > 1.0

5.1.2.4 Verification of serviceability

The deformation of the proposed bridge slab is determined using Cedrus-4 from CUBUS [cub]. The analysis is performed with the effective stiffness uniformly distributed over the total slab width of $EI_{eff} = 2.56E+13 \text{ Nmm}^2$. The result indicates that the maximum deflection amounts to 1 mm, which is lower than the authorized deformation of $L/500 = 4 \text{ mm}$.

5.1.3 Design example of a 12-m-wide and 400-mm-deep bridge slab with 6-m girder spacing

In the following design example, a typical 12-m-wide bridge deck with a girder spacing of 6 m will be investigated. The previous design example showed that only the experimentally investigated LC1300 can be used for 6-m-wide bridges with a girder spacing of 2 m. When the girder spacing and thus the design loads increase, the material properties of the LC core need to be optimized. Therefore, the use of higher performance LC compositions is studied in the following example, while the material properties of the face layers remain unchanged.

5.1.3.1 Material properties

Face layers

The material properties and dimensions of the face layers are the same as those presented in Section 5.1.2.1.

LC compositions

The wide range of possible LC compositions exhibiting different material characteristics is demonstrated in Section 2.2.3 on page 24. Typical values of different LC types investigated by Faust [FV99], [Fau03] and Wille [WDT05] are given in Tables 2.2 and 2.3. All LC types are composed of cement, silica fume, water, expanded clay for the lightweight aggregates ($\emptyset \geq 4$ mm) and different fine aggregates ($\emptyset < 4$ mm) as specified in the tables. Since the compressive strength is measured on cubes, the values are higher than those measured on the three experimentally investigated LC cylinders described above. Specification of the densities and Young's moduli is only found for the LCs investigated by Wille [WDT05]. However, existing data shows that LC densities reach values of up to 1600 kg/m^3 , which are deemed too heavy and inappropriate for the proposed hybrid bridge slab. Investigation showed that in the LC splitting tensile strength range of 1.8–3.4 MPa, the LCs exhibited characteristic lengths of between 16 and 150 mm.

Based on these investigated LC types, four LC compositions are studied in the following design example : LC-L20, LC-L40, LC-L150, LC-L200. The denotations indicate the assumed characteristic lengths of 20, 40, 150 and 200 mm. Furthermore, the splitting tensile strengths of the LCs were adapted to precisely fulfill the design requirements for a 12-m-wide bridge slab with a girder spacing of 6 m. The LC Young's modulus necessary to calculate the neutral axis of the hybrid cross section is defined to $E_{lc,m} = 7.0 \text{ GPa}$ (based on LC1000). The assumed material properties are summarized in Table 5.8.

Table 5.8: Material properties used for the verification of the 400-mm-deep, 12-m-wide bridge slab with 6-m girder spacing.

LC type	Characteristic length l_{ch} [mm]	Splitting tensile strength $f_{lctsp,k}$ [MPa]
LC-L20	20	2.8
LC-L40	40	2.7
LC-L150	150	2.3
LC-L200	200	2.1

Hybrid section properties

The sectional properties are the same as those presented in Section 5.1.2.1, since the values are independent of the LC core due to the clearly dominating stiffness of the identical top and bottom face layers. The results are summarized in Table 5.1 on page 111.

5.1.3.2 Load assumptions

The same load assumptions as those presented in Section 5.1.2 in respect to the dead weight of the slab and bridge loads according to Eurocode 1, load model 1 [Com01], are considered. Figure 5.5 illustrates the disposition of the loads on the 12-m bridge with a girder spacing of 6 m. The UDLs are applied on four lanes, while the wheel loads are applied on lanes 1 and 2 between the girders. No concentrated loads are taken into account on the outer lanes, since they would act favorably. Each axle of the tandem system is considered with $Q_{k,i}$ multiplied by the adjustment factor for standard bridges, $\alpha_{Q,i} = 0.9$, taken from the Swisscode SIA 261, [SIA03b]. The axle comprised two identical wheels with a contact surface of 400 x 400 mm². The UDLs are considered with q_i and the adjustment factor $\alpha_{q,i} = 0.9$ according to [SIA03b]. Table 5.9 summarizes the applied loads.

Table 5.9: Applied loads on a 12-m-wide bridge according to Eurocode load model 1 [Com01] and [SIA03b] for the adjustment factors.

	Axle loads $Q_{k,i}$ [kN]	UDL $q_{k,i}$ [kN/m]	$\alpha_{Q,i}$ [-]	$\alpha_{q,i}$ [-]
First lane	300	9.0	0.9	0.9
Second lane	200	2.5	0.9	0.9
Third lane, etc.	-	2.5	-	0.9

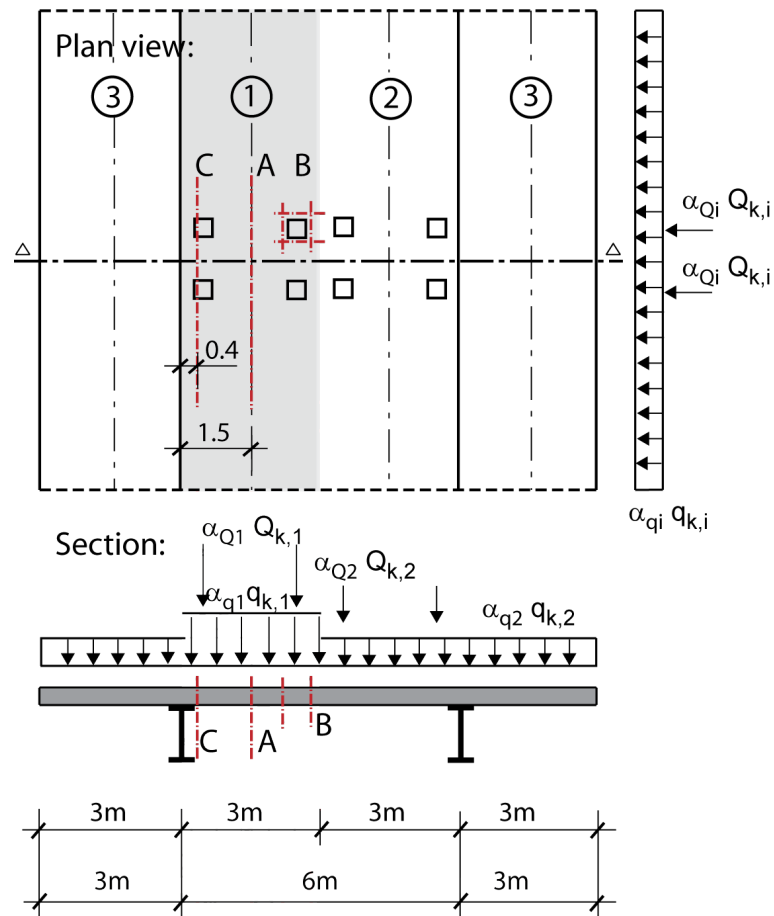


Figure 5.5: Distribution of bridge loads according to EC1 and sections for shear verification of a 400-mm-deep and 12-m-wide bridge slab with 6-m girder spacing.

The bridge slab design moments and shear values are determined using Cedrus-4 from CUBUS [cub]. The regions governing the bending moment design are within the span and over the girders, as illustrated in Figure 5.6.

The shear design values occurring in the slab are illustrated in Figure 5.7, which illustrates that the maximum shear value within the span region (Section A-A) was found at a distance of 1.5 m from the support axis and the maximum shear loads next to the support (Section C-C) at 0.4 m from the support axis. The verification of the punching load, P_d , (Section B-B) is conducted separately for one concentrated wheel load reduced by the appropriate adjustment factor. The design moments and shear values are summarized in Table 5.10.

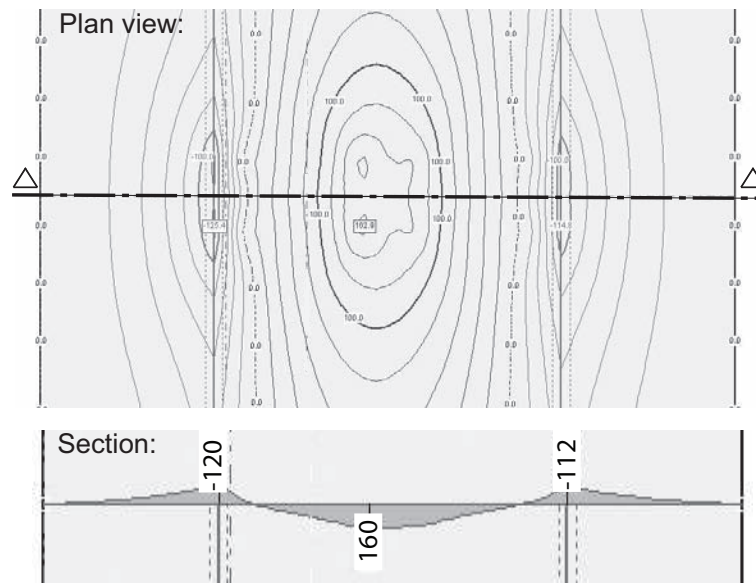


Figure 5.6: Distribution of design moments in $[kNm/m]$, equidistance of $20 kNm/m$, for a 400-mm-deep and 12-m-wide bridge slab with 6-m girder spacing.

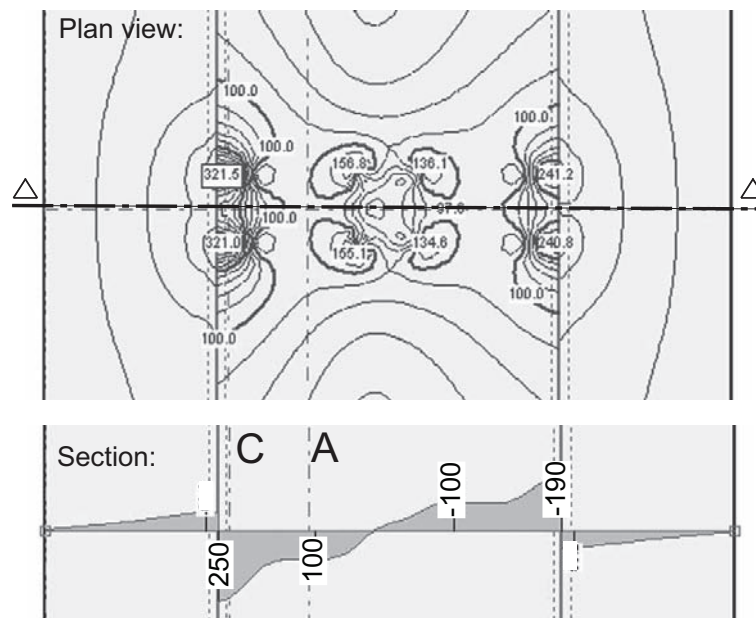


Figure 5.7: Distribution of design shear values in $[kN/m]$, equidistance of $10 kN/m$, for a 400-mm-deep and 12-m-wide bridge slab with 6-m girder spacing.

Table 5.10: Design moments and shear values for a 12-m bridge with 6-m girder spacing.

Section	Design moments		Design shear values	
	m_d [kNm/m]		P_d [kN]	p_d [kN/m]
A-A	160		-	100
B-B	-		$0.9 \cdot 150 \cdot 1.5 = 203$	-
C-C	-120		-	250

5.1.3.3 Verification of structural safety

Verification of bending moments

The verification of the compressive and tensile stresses due to bending in the face sheets is performed according to Section 5.1.1.1. The results, given in Table 5.11, showed that neither the compressive strength of the top concrete layer nor the tensile strength of the FRP is reached within the span and both could be optimized; only 15% and 36% of the strength is reached respectively. In the support region, tensile stresses occur in the top concrete layer. Since the tensile strength of the UHPFRC was insufficient to bear the tensile stresses, additional FRP reinforcement had to be incorporated into the UHPFRC layer. The FRP profile is sufficiently resistant to compressive stresses occurring over the support.

Table 5.11: Verification of bending moments for a 400-mm-deep, 12-m-wide bridge slab with 6-m girder spacing (negative signs = compression).

	$\sigma_{uhpfrc,d}$ [MPa]	$f_{uhpfrc,Rd}$ [MPa]	$(\sigma_d/f)_{uhpfrc}$ [-]	$\sigma_{frp,d}$ [MPa]	$f_{frp,Rd}$ [MPa]	$(\sigma_d/f)_{frp}$ [-]
Span	-17	-112	$6.6 > 1.0$	43	120	$2.8 > 1.0$
Support	15	7.33	< 1.0	-36	-120	$3.3 > 1.0$

FRP bars
to be added

Verification of shear resistance within the span

The material properties of the different LC types shown in Table 5.8 were chosen so that they provide precisely the required shear resistance, $v_{lc,Rd}$, according to Eq. 5.4 on page 108. The components that contribute to the shear resistance, their sums and accordance with the design shear value are summarized in Table 5.12.

Table 5.12: Shear strength prediction within the span for a 400-mm-deep, 12-m-wide bridge with 6-m girder spacing using new LCs.

Lightweight concrete	$f_{lctsp,k}$ [MPa]	v_{uhpfrc} [kN]	v_{lc} [kN]	v_{FPZ} [kN]	$v_{lc,Rk}$ [kN]	$v_{lc,Rd}$ [kN]	$v_{lc,Rd}/P_d(A-A)$ [-]
LC-L20	2.8	42.30	98.3	5.7	146.4	98	1.0 = 1.0
LC-L40	2.7	40.80	94.9	11.1	146.7	98	1.0 = 1.0
LC-L150	2.3	33.75	78.5	34.4	146.6	98	1.0 = 1.0
LC-L200	2.1	31.50	73.2	42.8	147.5	98	1.0 = 1.0

The splitting tensile strength of LC-L200 could be assumed as being 25% lower than that of LC-L20 because for a longer characteristic length, the shear resistance is transmitted through a greater depth, and thus to a higher extent by the FPZ, as shown in Table 5.12. While the FPZ of LC-L20 contributed only 4% to the shear resistance, 29% of the shear resistance was provided by the FPZ of LC-L200.

Verification of punching

The same LC types are used for the verification of punching. Punching resistance is calculated according to Eq. 5.5 on page 109 and Figure 5.1, with the effective widths of $b_{uhpfrc} = 485$ mm, $b_{lc} = 550$ mm and $b_{FPZ} = 593$ –644 mm. The results and their accordance with design values are summarized in Table 5.13.

All LCs reached a higher punching resistance than required (207.7 to 221.4 kN > 203 kN). Again, it is shown that the longer the characteristic length, the greater the contribution of the FPZ.

Table 5.13: Punching resistance of a 400-mm-deep bridge slab using new LCs.

Lightweight concrete	V_{uhpfrc} [kN]	V_{lc} [kN]	V_{FPZ} [kN]	$V_{lc,Rk}$ [kN]	$V_{lc,Rd}$ [kN]	$V_{lc,Rd}/P_d$ [-]
LC-L20	82.1	215.9	13.6	311.6	207.7	1.0 = 1.0
LC-L40	79.2	208.2	26.5	313.9	209.3	1.0 = 1.0
LC-L150	65.5	172.2	86.6	324.3	216.2	1.1 > 1.0
LC-L200	61.1	160.8	110.2	332.0	221.4	1.1 > 1.0

Verification of direct load transmission next to the support

The results of the verification of the design shear values in Section C-C are given in Table 5.14. Using LC-L20 to LC-L200, an overestimation of 70% is obtained. However, the simplified

assumption should only serve as a rough approach and be verified for deeper slabs by further experiments.

Table 5.14: Shear strength prediction next to support of a 400-mm-deep, 12-m-wide bridge slab with 6-m girder spacing using new LCs.

Lightweight concrete	$v_{lc,Rk(A-A)}$ [kN]	$v_{lc,Rk(C-C)}$ [kN]	$v_{lc,Rd(C-C)}$ [kN]	$v_{lc,Rd(C-C)}/p_d(C-C)$ [-]
LC-L20	146.4	629.5	419.6	1.7 > 1.0
LC-L40	146.7	631.0	420.6	1.7 > 1.0
LC-L150	146.6	630.3	420.2	1.7 > 1.0
LC-L200	147.5	634.3	422.8	1.7 > 1.0

5.1.3.4 Verification of serviceability

The maximum deformation of the proposed bridge slab is determined using Cedrus-4 from CUBUS [cub]. The analysis is performed with the effective stiffness of the slab, $EI_{eff} = 2.56E+13 \text{ Nmm}^2$. The result indicated that the maximum deflection was 9.9 mm, which is lower than the authorized deformation of $L/500 = 12 \text{ mm}$.

5.1.3.5 Influence of slab depths on LC material properties

The influence of slab depth on the required material properties of the new LC types is investigated for the 12-m-wide bridge with a girder spacing of 6 m by varying the slab depth between 200 and 500 mm. The bending moment verification is not critical for different slab depths. Although a reduction in slab depth leads to higher stresses in the face layers, the material strength is not achieved. A reduction to a 200-mm-deep slab increases the stresses in the face layers to $\sigma_{uhpfrc,d} = -47 \text{ MPa}$ (compression in the UHPFRC) and $\sigma_{frp,d} = 97 \text{ MPa}$ (tension in the FRP) within the span, and therefore material strengths are not reached. The moment over the girders leads to compressive stresses of 83 MPa in the FRP profile without reaching the FRP strength in compression, while the tensile stress in the UHPFRC layer of approximately 40 MPa requires additional FRP reinforcement.

The region governing the shear verification always lies within the span, as described above. The splitting tensile strengths of LC-L20 to LC-L200 are modified (by maintaining the defined characteristic length, l_{ch}) so that sufficient shear resistance is provided to precisely fulfill the design requirements for different slab depths. The results of this analysis therefore give the minimum required value for the LC splitting tensile strength. They are shown in Table 5.15 and Figure 5.8, with values for the same slab depth connected by lines. For the same slab depth, the splitting tensile strength decreases for an increasing characteristic length (from

Table 5.15: Required characteristic LC splitting tensile strength $f_{lctsp,k}$ [MPa] for new LC-types with given characteristic lengths for 12-m-wide bridges with slab depths of 200–500 mm and 6-m girder spacing.

	LC-L20 $l_{ch} = 20$ mm	LC-L40 $l_{ch} = 40$ mm	LC-L150 $l_{ch} = 150$ mm	LC-L200 $l_{ch} = 200$ mm
$h = 500$ mm	2.4	2.4	2.0	1.9
$h = 400$ mm	2.8	2.7	2.3	2.1
$h = 300$ mm	3.8	3.6	2.8	2.6
$h = 200$ mm	5.5	5.1	3.7	3.3

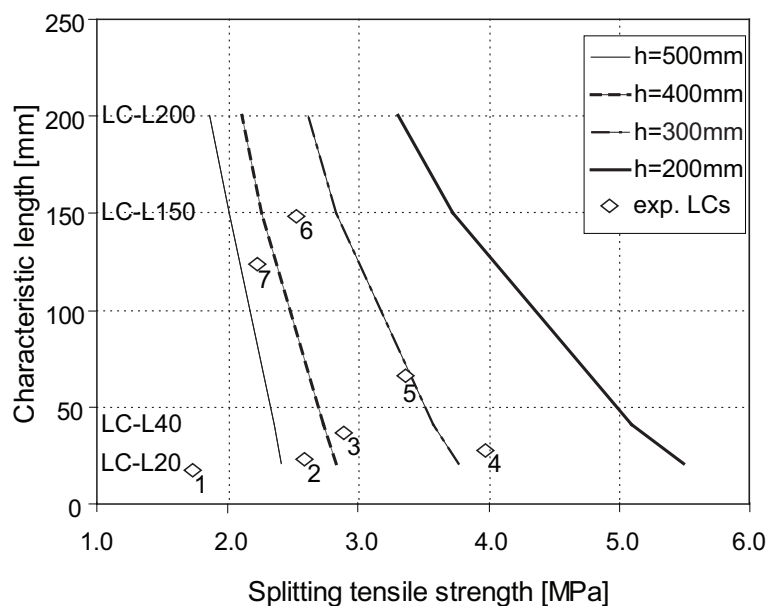


Figure 5.8: Characteristic length vs LC splitting tensile strength for 12-m-wide bridge slab with girder spacing of 6 m to fulfill design requirements for different slab depths and experimentally investigated LCs from Wille [WDT05].

LC-L20 to LC-L200), i.e. the longer the characteristic length, the longer the FPZ and thus the lower the required splitting tensile strength.

It is also noticed that for different slab depths and short characteristic lengths, the LC splitting tensile strength varies more significantly than for longer characteristic lengths. Reducing the depth from 400 to 200 mm for example almost doubles the required splitting tensile strength for $l_{ch} = 20$ mm, while it increases by only 57% for $l_{ch} = 200$ mm. This is because the characteristic length is a constant value that is independent of slab depth. The lower the characteristic length/slab depth ratio, the higher the required splitting tensile strength. Consequently, shear resistance does not increase proportionally to slab depth.

Moreover Figure 5.8 includes seven LCs (marked as diamonds and numbers) taken from Tables 2.2 and 2.3 on page 26 [FV99], [Fau03], [WDT05]. The slab depths for which these LCs could be applied can be defined by comparing them with the drawn curves; LC no. 1 would not fulfill the design requirements for a 500-mm-deep slab, while all the other LCs would provide sufficient shear resistance. LCs nos. 3 to 6 could also be applied for depths of 400 mm, while only LC no. 4 would provide sufficient resistance for use in a 300-mm slab. However, the specified LC densities reached values of up to 1600 kg/m^3 and the bridge slab would therefore not attain the target total weight of 50% of that of a normal concrete deck. To achieve this, LC densities of approximately 1100 kg/m^3 for a slab depth of 400 mm would be required.

5.1.4 Optimization study to obtain ductile failure

The aim of the slab optimization is to provide a slab configuration where a ductile failure mechanism of the hybrid FRP-concrete slab would occur.

This could be achieved by either obtaining a dominant flexural failure by concrete crushing under compression or by creating a ductile failure through progressive failure of the unbonded FRP-LC interface, as indicated by the experimental investigation on beams 1300-1/2 in Section 3.3.3.1. The latter failure mechanism needs further experimental investigation because it is seen to be influenced by the LC compressive strength and the composition of the T-upstands. The occurrence of a ductile failure mechanism due to concrete crushing in the top part of the slab is influenced by the effective stiffness and material properties of the hybrid slab and will be discussed in the following. Therefore, the face layer properties are modified while the LC material properties are kept constant throughout the optimization study. Based on the previously described design example, appropriate LC characteristic lengths and LC splitting tensile strengths are used for the study, as given in Table 5.8.

The previously described design examples lead to two major conclusions: firstly, in the verification of the flexural slab strength, neither the compressive strength of the top concrete layer nor the tensile strength of the FRP is reached. Secondly it is noticed that the compressive zone of a 400-mm-deep slab amounts to only 16% of the total slab depth and that the governing verification is the shear resistance verification within the span.

Hence, three possibilities for slab optimization will be studied: first, the reduction of the slab depth (slenderness) will be discussed, which results in increased stresses in the face layers, and thus a higher level of utilization. Second, the concrete strength of the top layer will be reduced, (normal concrete (NC) instead of UHPFRC), and third, the increasing of the compressive zone by using a stiffer FRP profile (carbon fibers instead of glass fibers) in the tensile zone will be investigated. A total of six slab types (Slabs1–6) are investigated,

as summarized in Table 5.16: two different slab depths (400 and 200 mm), two different top concrete layers (ultra-high performance fiber-reinforced concrete and normal concrete: UHPFRC and NC), and two different FRP layers (using glass and carbon fibers: GFRP and CFRP).

Table 5.16: Slab configurations for optimization study.

No.	Specification concrete layer	Specification FRP profile	Slab depth
Slab 1	UHPFRC	CFRP	400 mm
Slab 2	UHPFRC	CFRP	200 mm
Slab 3	NC	CFRP	400 mm
Slab 4	NC	CFRP	200 mm
Slab 5	NC	GFRP	400 mm
Slab 6	NC	GFRP	200 mm

5.1.4.1 Material properties

Face layers

The material properties for the top concrete layer are taken from Section 5.1.2.1 for the UHPFRC composition and from the experimental investigation (see Section 3.2) for the NC. The properties of the GFRP profile are assumed as being the same as those of the GFRP Plank profile referred to in Section 3.2. In the case of the CFRP profile, the Young's modulus is assumed to be 80 GPa, while the tensile strength is assumed to be 400 MPa. The Young's modulus and the material strengths of the face layers are shown in Table 5.17.

Table 5.17: Material properties used for optimization study of 12-m-wide bridge with 6-m girder spacing (negative signs = compression).

	Young's modulus [GPa]	Material strength [MPa]
UHPFRC	48	-168
NC	23	-50
GFRP	23	240
CFRP	80	400

LC compositions

Based on the previous design example, an LC-L200 composition is chosen for the optimization study with a characteristic splitting tensile strength of $f_{lctsp,k} = 3.0$ MPa (with $l_{ch} = 200$ mm). The LC Young's modulus is again defined as $E_{lc,m} = 7.0$ GPa.

Hybrid section properties

The sectional properties of Slab-1 to Slab-6 are summarized in Table 5.18.

Table 5.18: Sectional properties of chosen hybrid FRP-concrete sandwich slab configuration for optimization study.

	Face layer specification	h [mm]	x_n [mm]	EI_{eff} [Nmm ²]	W_{uhpfrc} [mm ³]	W_{frp} [mm ³]
Slab-1	UHPFRC-CFRP	400	132	7.09 E+13	1.12 E+07	0.55 E+07
Slab-2	UHPFRC-CFRP	200	73	1.42 E+13	0.40 E+07	0.23 E+07
Slab-3	NC-CFRP	400	166	6.16 E+13	1.61 E+07	0.12 E+07
Slab-4	NC-CFRP	200	95	1.12 E+13	0.51 E+07	0.47 E+07
Slab-5	NC-GFRP	400	138	2.19 E+13	0.70 E+07	3.62 E+07
Slab-6	NC-GFRP	200	84	0.29 E+13	1.05 E+07	1.08 E+07

5.1.4.2 Load assumptions

The same load assumptions as defined in Section 5.1.3.2 are considered. Hence, the same bridge slab design moments and shear values as given in Table 5.9 are used for the optimization study: $m_d = 160$ kNm/m and $p_d = 100$ kN/m.

5.1.4.3 Verification of structural safety

The verification of the compressive and tensile stresses due to bending in the face sheets is performed according to Section 5.1.1.1 and Eqs. 5.1–5.2, while the verification of the shear resistance in the span is performed according to Section 5.1.1.1 and Eq. 5.4. The most significant results of the analysis (design values of stresses in the face layers, σ_d , and shear resistance of the slab, $v_{lc,Rd}$) and the ratio between material resistances and design values (f/σ_d and $v_{lc,Rd}/p_d$) for the six slab types are indicated in Table 5.19.

5.1.4.4 Verification of serviceability

Based on the serviceability analysis in Section 5.1.3.4, the effective stiffness of the slab should be greater than $EI_{eff} = 2.11E+13$ Nmm² in order to respect the authorized deformation of

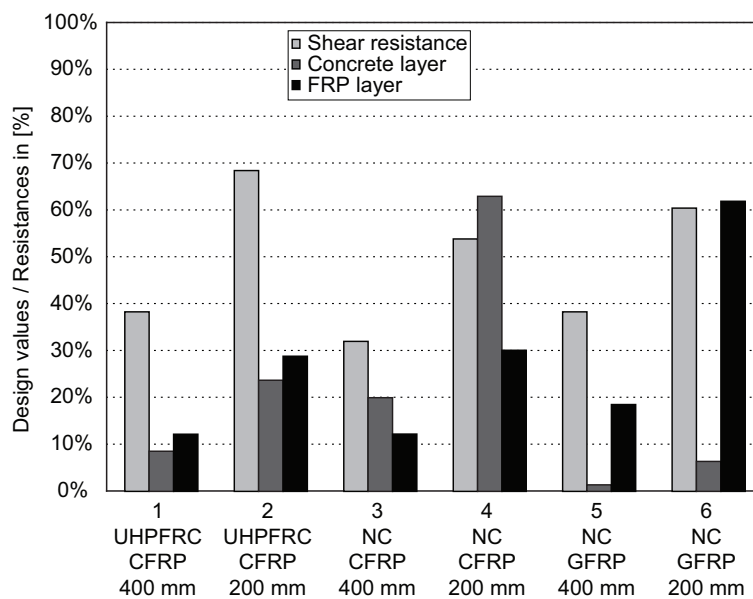
Table 5.19: Structural safety verification within the span of slab types (negative signs = compression).

	$\sigma_{c,d}$ [MPa]	$(f/\sigma_d)_c$ [-]	$\sigma_{frp,d}$ [MPa]	$(f/\sigma_d)_{frp}$ [-]	$v_{lc,Rd}$ [kN]	$v_{lc,Rd}/p_d(A-A)$ [-]
Slab-1	-14	11.8 > 1.0	48	8.3 > 1.0	211	2.6 > 1.0
Slab-2	-40	4.2 > 1.0	115	3.5 > 1.0	123	1.5 > 1.0
Slab-3	-10	5.0 > 1.0	49	8.2 > 1.0	262	3.1 > 1.0
Slab-4	-31	1.6 > 1.0	120	3.3 > 1.0	156	1.9 > 1.0
Slab-5	-2	72.7 > 1.0	44	5.4 > 1.0	219	2.6 > 1.0
Slab-6	-11	15.8 > 1.0	147	1.6 > 1.0	139	1.7 > 1.0

$L/500 = 12$ mm. Consequently, the 200-mm-deep slabs would not provide sufficient stiffness. However, a decrease in maximum deflections is expected, since the calculation is based on the simplified assumption of a uniformly distributed effective stiffness of the cracked slab over the total bridge width. Hence, the use of the 200-mm-deep slabs requires further investigation, while serviceability is verified for 400-mm slab depths.

5.1.4.5 Discussion

The utilization level (defined as the design value/resistance ratio, which is equivalent to the reciprocal of the safety value) of the face material strengths and the shear resistance is shown in Figure 5.9 for all the six slab types. As shown, all slabs provide sufficient shear and

**Figure 5.9:** Analysis of design value/resistance ratio of slab types (flexural and shear resistance).

flexural resistance to fulfill structural safety requirements for a 12-m-wide bridge slab with girder spacing of 6 m. Comparing the six slabs, Slab-4 would exhibit a ductile failure due to concrete crushing as the dominating failure mechanism. In all the other slabs, a brittle failure would occur. In Slabs-1, 2, 3 and 5, shear failure would occur before the flexural failure of the face materials. Slab-6 would be the most critical slab configuration, since first the FRP profile would reach its tensile strength, directly followed by LC shear failure - both brittle failures - while the utilization level of the compressive concrete layer is less than 10%.

Consequently, regarding the structural safety verification, Slab-4 is the most favorable slab type since it exhibits a deeper compressive zone (almost 50%), although serviceability should be more precisely verified. The 200-mm-deep slab is composed of a thin NC layer in the top zone and the stiff, high-strength CFRP profile in the bottom zone. Consequently, the use of a UHPFRC does not seem necessary due to its high strength but because of its dense and waterproof structure and its ability to bear local bending moments. In this respect, the NC composition could be further improved so that it provides similar advantages.

5.2 Building applications

5.2.1 Design example of a hybrid FRP-concrete slab in buildings

The use of the proposed FRP-concrete slab for building applications is also of interest due to its thermal insulation capacity and will be investigated in the following. For this purpose, a simply supported slab is assumed with uniformly distributed loads according to EC1 [Com01]. Two different slab depths are considered (Slabs-7 to 9: 160 and Slabs-10 to 12: 200 mm). The materials used in this study are the same as those used in the experimental investigation. The NC layer as a top concrete layer is sufficiently resistant for building requirements because no concentrated loads occur and hence no local tensile stresses. Furthermore, there are no durability-related requirements (i.e. waterproofing layer) inside the building.

5.2.1.1 Material properties

Face layers

The material properties are based on the experimental investigation described in Section 3.2.2: the top concrete layer consists of a 25-mm-deep normal concrete (NC) and has a compressive strength of $f_{c,k} = 50$ MPa and Young's modulus of $E_c = 30$ GPa. The bottom GFRP skin is the same standard pultruded Plank profile as previously described.

LC compositions

The LC compositions from the experimental investigation are used to discuss the hybrid slab system for buildings: the two SLWAC (LC900 and LC1300) and the ALWAC (LC1000) compositions. The material properties are summarized in Table 3.3 on page 43.

Hybrid section properties

The sectional properties of the slabs according to their depth are summarized in Table 5.20. Due to the dominating stiffness contribution provided by the identical top and bottom face layers, the values are independent of the LC cores.

Table 5.20: Sectional properties of chosen hybrid FRP-concrete slab configurations for building requirements.

	h [mm]	x_n [mm]	EI_{eff} [Nmm ²]	W_{nc} [mm ³]	W_{frp} [mm ³]
Slabs-7-9	160	40	2.95 E+12	2.44 E+06	8.23 E+05
Slabs-10-12	200	48	5.03 E+13	3.49 E+06	1.10 E+06

5.2.1.2 Load assumptions

The dead weight of the slab is 3 kN/m², while for building requirements, uniformly distributed loads of 5 kN/m² are assumed for areas where people may congregate (i.e. museums, exhibition rooms, access areas in public or administrative buildings), according to category C3 of EC1 [Com01].

5.2.1.3 Verification of structural safety

The maximum span length for which the hybrid slabs provide precisely the required shear resistance, $v_{lc,Rd}$, according to Eq. 5.4 on page 108 is determined for the different LC types. The resulting maximum spans are indicated in Table 5.21 and shown in Figure 5.10. Verification of the compressive and tensile stresses due to bending in the face layers is then performed according to Section 5.1.1.1. The results and their accordance with design values are summarized in Table 5.21 and indicate that neither the concrete compressive strength nor the FRP tensile strength is reached. The average utilization level of the concrete layer is 37% (safety value 3.5) while that of the FRP layer is 18% (safety value 7.2).

Table 5.21: Structural safety verification of hybrid FRP-concrete slab for buildings (negative signs = compression).

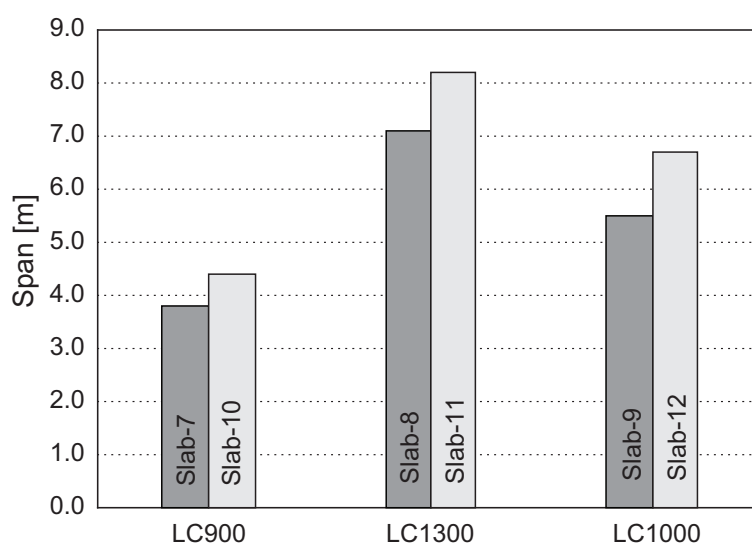
	Core specification	h [mm]	L [m]	$\sigma_{c,d}$ [MPa]	$(f/\sigma_d)_c$ [-]	$\sigma_{frp,d}$ [MPa]	$(f/\sigma_d)_{frp}$ [-]	$v_{lc,Rd}$ [kN]	$v_{lc,Rd}/p_d$ [-]
Slab-7	LC900	160	3.8	-9	$5.8 > 1.0$	19	$12.4 > 1.0$	19	$1.0 = 1.0$
Slab-8	LC1300	160	7.1	-30	$1.7 > 1.0$	68	$3.5 > 1.0$	38	$1.0 = 1.0$
Slab-9	LC1000	160	5.5	-18	$2.8 > 1.0$	41	$5.9 > 1.0$	29	$1.0 = 1.0$
Slab-10	LC900	200	4.4	-8	$6.3 > 1.0$	19	$12.4 > 1.0$	22	$1.0 = 1.0$
Slab-11	LC1300	200	8.2	-28	$1.8 > 1.0$	67	$3.6 > 1.0$	44	$1.0 = 1.0$
Slab-12	LC1000	200	6.7	-19	$2.7 > 1.0$	45	$5.3 > 1.0$	36	$1.0 = 1.0$

5.2.1.4 Verification of serviceability

The maximum slab deformations are calculated for the previously defined span lengths assuming a continuous slab. The results indicate that all slabs fulfill the requirements with smaller deformations than $L/350$, which represents that authorized by Swisscode SIA 260 [SIA03c].

5.2.1.5 Discussion

The maximum slab spans resulting from the structural safety verification for Slabs-7 to 12 are indicated in Figure 5.10. All experimentally investigated LC types can be used for building requirements and spans greater than 3.8 m in the case of Slabs-7 to 9 and spans greater than

**Figure 5.10:** Maximum spans for hybrid FRP-concrete slabs in buildings using experimentally investigated LCs resulting from structural safety verification.

4.4 m in the case of the 200-mm-deep Slabs-10 to 12. Maximum slab spans of 8 m can be attained, which is sufficient for most building applications. The material strengths of the face layers would not nearly be reached, and the dominant failure mechanism would be shear failure of the slabs. Deformation requirements are fulfilled by all investigated slabs.

5.3 Summary

5.3.1 Bridge applications

This chapter presented a design concept for the FRP-concrete hybrid bridge deck. The design concept includes the verification of serviceability and structural safety. The following conclusions can be drawn:

- The serviceability verification depends on the effective stiffness of the hybrid FRP-concrete slab, which is dominated by the stiffness of the face layers and virtually independent of the LC cores.
- The structural safety verification is firstly performed for the design moments within the span and over the supports by comparing the maximum compressive and tensile stresses in the face material layers (FRP and UHPFRC) with the respective material design strengths.
- Secondly, the shear resistance verification is conducted in three sections: within the span, under a concentrated wheel load (punching) and next to the support. The method for determining shear resistance within the span is derived from the fracture mechanics-based shear strength prediction method from Zink [Zin00], reported in Section 4.3.3. This method was experimentally validated on 200-mm-deep hybrid beams consisting of three layers: FRP-LC-NC. It is assumed that it can also be used to predict the shear strength of hybrid slabs by slightly changing layer depths and material properties. The punching resistance is determined using a simplified punching pyramid which is seen as a lower limit approach. An increase in resistance is expected due to the positively acting membrane forces of the FRP profile, which are currently not taken into consideration and need further investigation. The proposed design concept for loads next to supports is based on experimental results obtained from 200-mm-deep short-span beams and should be seen as a rough approach. Further investigation should be performed on the design concept for loads next to supports.
- The concept demonstrates the feasibility of the system and provides the basis for optimizing the LC material characteristics for any load condition. Thus, the same

range of bridge spans are possible as for conventional steel-reinforced concrete bridge slabs by adapting the LC properties (splitting tensile strength and characteristic length) to the required strength.

Furthermore, two design examples for the use of the hybrid FRP-concrete bridge slab indicated that the governing case in verification is always the shear strength prediction within the span and led to the following conclusions:

- The first design example studies the applicability of the experimentally investigated LC compositions for a 400-mm-deep, 6-m-wide bridge slab with 2-m girder spacing. The hybrid slab incorporating LC1300 provides sufficient shear resistance, while slabs incorporating LC900 and LC1000 cannot be used in this bridge configuration.
- In the second example, appropriate LC types are defined to fulfill the design requirements for a 12-m-wide bridge with 6-m girder spacing. The required LC characteristic length and LC splitting tensile strength are defined for slab depths of between 200 and 500 mm. It has been shown that these values are achievable by modification of the LC composition. As an example, several LC compositions developed and investigated by Faust [FV99], [Fau03] and Wille [WDT05] provide sufficient resistance to fulfill design criteria. Although these LCs offer the required splitting tensile strengths and characteristic lengths, the specified LC densities reach values of up to 1600 kg/m³ and the bridge deck would therefore not attain the target total weight of 50% of that of a normal concrete deck. The experimentally used LC1000 composition, offering the target weight, should thus be optimized. The addition of fibers could increase the characteristic length and splitting tensile strength while maintaining the LC density.

The chapter also included an optimization study which investigated the occurrence of a ductile failure mechanism due to concrete crushing in the compressive zone of the hybrid FRP-concrete slab. The following conclusions can be drawn:

- A desirable failure mechanism for the hybrid slab system is concrete crushing under compression, since concrete crushing leads to a ductile and not brittle failure, as is the case for shear failure of the LC core. A brittle tensile failure of the FRP layer is not desirable either. The optimization study therefore concentrates on modification of the face layer materials for a 12-m-wide bridge slab with 6-m girder spacing, while the material characteristics of the LC core are kept constant. Six slab types are investigated with two different top concrete layers (UHPFRC and NC), two different FRP layers (GFRP and CFRP) and two different slab depths (400 and 200 mm). The analysis

indicates that all slabs provide sufficient shear and flexural resistance to fulfill structural safety requirements.

- The optimization study shows that ductile failure due to concrete crushing in the compressive zone occurs only in slabs with a deeper compressive zone, relatively low compressive strength of the top concrete layer and a stiff CFRP tensile profile.
- As a result, the other possibility of creating a ductile failure mechanism by an unbonded FRP-LC interface and low LC compressive strength needs to be further investigated. The desirable ductile failure mechanism observed in unbonded beams 1300-1/2 (see also Section 3.3.3.1) should hence be studied in detail.

5.3.2 Building applications

The experimentally investigated LC types were studied for use of the hybrid FRP-concrete slab in buildings. Six slabs were investigated, comprising three different LCs (LC900, LC1300 and LC1000) and two different slab depths (160 and 200 mm), leading to the following conclusions:

- The maximum slab span is determined by the shear resistance of the hybrid slab. The material strengths of the face layers are not reached however. As already observed in the bridge application, it is not possible to create a ductile failure due to concrete crushing in the compressive zone. Further research is hence needed to investigate a desirable ductile failure mechanism.
- Maximum slab spans of 8 m can be reached with the LC types used in the experimental investigation, which is sufficient for most building applications.

6 Conclusions and future research

In this thesis a new hybrid FRP-concrete sandwich slab was developed and analyzed for potential use in bridge or building applications. The proposed hybrid slab is a sandwich structure consisting of three layers of different materials: FRP composite sheet with T-upstands for the bottom tension skin, lightweight concrete (LC) as core material and ultra-high performance fiber-reinforced concrete (UHPFRC) for the top compression skin. Experimental and analytical investigations using different LC cores and FRP-LC interfaces provided the required information concerning the load-bearing behavior of the sandwich slab. Together with the proposed design concept, design examples and an optimization study, these especially confirmed the feasibility of the hybrid slab. The concluding remarks and contribution to the state of the art are firstly summarized in Sections 6.1 and 6.2, while certain aspects of research regarding the widespread application of this slab type are discussed in Section 6.3.

6.1 Conclusions

The following conclusions drawn from the present research are structured in accordance with the objectives formulated in the Introduction.

6.1.1 Concept of hybrid FRP-concrete sandwich slab

The serviceability and structural safety of the proposed FRP-concrete hybrid sandwich slab is proved in a similar way to those of conventional steel-reinforced concrete slabs.

As far as durability is concerned, the slab offers substantial resistance to corrosion since it is steel-free and the UHPFRC layer is watertight. Hence no waterproofing layer is required and the associated complicated parapet detailing becomes unnecessary.

With regard to the economic aspects, the deck exhibits advantageous properties in fabrication and application, although the material cost of GFRP profiles is higher than that of conventional steel reinforcements. The low self-weight and planned prefabrication of large elements offer the possibility of rapid slab replacement with minimum traffic interference or simplicity of installation in the case of new constructions. Slab manufacture is also proved

to be rapid and easy since epoxy, LC and UHPFRC are applied wet-in-wet without any intermediate curing time.

6.1.2 Load-bearing behavior

An experimental program was performed in order to better understand the load-bearing behavior and failure mechanisms of the hybrid FRP-concrete sandwich slab. The first objective of this investigation was to examine whether an unbonded interface - and thus pure mechanical interlocking - between the FRP and LC through the T-upstands is sufficient to provide full composite action or whether an additional adhesive layer is required for the bonding of the FRP-LC interface.

The second objective was to investigate the influence of different LC cores on shear capacity. Two LC types were chosen, exhibiting different densities and brittleness: an SLWAC mixture with expanded clay and sand aggregates and an ALWAC mixture with expanded clay and expanded glass aggregates.

Since it has already been established that the failure mode and ultimate load change for loads next to the support and loads within the span, the third objective was to investigate the load-bearing behavior of hybrid short-span and long-span specimens. The following conclusions were drawn in accordance with the objectives:

- An unbonded sandwich slab with a low strength SLWAC concrete core starts to lose full composite action at an early stage and a ductile failure mechanism involving progressive interface failure then occurs. Sandwich slabs comprising an ALWAC concrete with a relatively high compressive strength on the other hand exhibit full composite action until a brittle shear failure of the LC core occurs. The FRP-LC interface strength due to mechanical interlocking through the T-upstands is correlated with the LC compressive strength. Slabs with an adhesively-bonded FRP-LC interface exhibit full composite action up to a brittle shear failure, independent of the LC core type. The use of anchor blocks with bonded FRP-anchor block interface can be considered an alternative to the adhesive bonding of the whole FRP-LC interface.
- The cracking and ultimate loads are significantly higher for the more ductile SLWAC compositions than for the brittle ALWAC mixture, although splitting tensile strengths are similar. Thus, in order to accurately model the cracking and failure loads, not only LC static strengths but also fracture mechanics parameters such as the LC characteristic length need to be considered.
- The slab system normally exhibits shear failure in the LC core, while the strengths of the face layers are not reached, regardless of the loading position. However, the ultimate

loads of the hybrid slabs are significantly higher next to the support than within the span.

6.1.3 Modeling of load-bearing behavior

The load-bearing behavior of the hybrid slab system needs to be modeled within the span and next to the supports. The flexural behavior of the slab can be easily predicted, while the shear resistance needs further detailed investigation. In a first approach, shear resistance prediction was performed according to codes but results proved unsatisfactory. Hence fracture mechanics-based models are presented, which are validated by the experiments. The following conclusions could be drawn from the modeling:

- Current design codes for shear resistance prediction (Eurocode2 and the ACI318-05) are frequently unreliable, since the different fracture behaviors of SLWAC and ALWAC compositions are not sufficiently considered. Within the span, shear strength prediction according to Eurocode2 could be improved by incorporating the LC characteristic length into the scale coefficient. Next to the support, only the ultimate load of the ALWAC specimens is predicted according to ACI318-05, while the strength of the SLWAC specimens is greatly underestimated.
- The proposed shear strength prediction method for the hybrid slabs within the span is based on a model originally developed by Zink for concrete members entirely composed of normal or high performance concrete [Zin00]. The revised and extended model takes into account the shear resistance of the compressive zone (composed of both concretes under compression) and that of the fracture process zone (FPZ) in the LC. The length of the FPZ is correlated to the LC characteristic length and is hence significantly longer for the SLWAC than for the ALWAC specimens. Good agreement between experimental and model predictions is achieved. The model is further extended to predict the punching shear resistance, although it does not yet take the beneficial behavior of the FRP sheet into account.
- A continuous direct load transmission model is presented to determine cracking and ultimate loads for direct load transfer next to the support. The model consists of a bottle-shaped strut with an infinite number of transverse ties, resulting in a statically indeterminate system, which allows consideration of the different LC softening behaviors.

6.1.4 Application and design method

A design concept that includes the verification of serviceability and structural safety is proposed for application of the hybrid FRP-concrete slab for bridges, although they can also be used for building applications. For bridge applications, serviceability is verified with regard to the maximum deformation of the hybrid FRP-concrete slab, while the structural safety verification is performed firstly for the design moments within the span and over the supports, and secondly for the design shear values in three sections: within the span, under a concentrated wheel load (punching) and next to the support. The following conclusions were drawn:

- Design examples according to the proposed design concept prove the feasibility of the hybrid slab concept and provide a basis for optimizing the LC and face layer properties for any load condition. Thus, the same range of bridge spans as with conventional steel-reinforced concrete bridge slabs is made possible primarily by adapting the LC properties (splitting tensile strength and characteristic length) to the required strengths.
- It has been established that slabs comprising the experimentally investigated LC compositions satisfy the design requirements for bridges with a girder spacing of up to 2 m. For greater girder spacings, LC compositions exhibiting higher tensile strengths and/or longer characteristic lengths must be used.
- In most hybrid slab configurations, a brittle shear failure of the LC core is the governing failure mechanism. A ductile failure mechanism due to concrete crushing in the top part could be achieved in thin slabs with a deep compressive zone however. A possible slab configuration for this consists of a stiff and high strength CFRP profile as the bottom layer and an NC top layer with a relatively low compressive strength.

The possibility of using the hybrid FRP-concrete slab in buildings is proved for the experimentally investigated LC types. The governing slab verification concerns the shear resistance of the LC core, while the material strengths of the face layers are normally not reached. Maximum slab spans of 8 m can be achieved, which are sufficient for most building applications.

6.2 Contribution to state of the art

The new findings contributing to the state of the art can be summarized as follows:

- The analysis of different LC cores indicates that the slab shear resistance within the span and next to the supports is not only dependent on LC static strengths, but also greatly influenced by the LC fracture mechanics properties.

- To determine cracking and ultimate loads in slabs directly loaded next to the supports, a continuous direct load transmission model in the form of a bottle-shaped compressive strut with transverse ties is proposed. The model allows consideration of the different LC softening behaviors in the ties through incorporation of the post-peak material softening after concrete cracking. Hence, an accurate modeling of the differences between the cracking and ultimate loads of the SLWAC and ALWAC specimens is achieved, something which cannot be provided by existing models.
- For the calculation of shear resistance in the span of hybrid FRP-concrete slabs with an LC core, an extension of a shear strength prediction method originally developed for normal or high performance concrete is presented. The model takes into account the shear resistance of concrete zone under compression and that of the fracture process zone (FPZ). The latter is higher in the SLWAC specimens than in the ALWAC specimens since the ALWAC exhibits a much more brittle behavior with a lower fracture energy and shorter FPZ length.
- It is confirmed that the shear strength modeling according to Eurocode 2 can be improved by incorporating the LC characteristic length into the scale coefficient, as proposed by Zink [Zin00].
- The experimental investigation proves the feasibility of the epoxy-bonded FRP-LC and LC-NC interfaces by wet-in-wet application of the layers without any intermediate curing time. In contrast to existing hybrid bridge slabs, the proposed FRP-concrete hybrid sandwich slab can be easily prefabricated in large elements, resulting in economic manufacture.
- In comparison with existing hybrid FRP-concrete slabs, the core design is improved since the shear forces are transferred by the LC core and not by the FRP webs, which are sensitive to buckling. Due to the use of an LC core with densities of up to 1100 kg/m^3 , the slab is still lightweight and offers a weight reduction of approximately 50% compared to a conventional steel-reinforced concrete slab of the same depth.

6.3 Proposal for future research

The following four research aspects need to be discussed in more detail for a widespread application of the proposed hybrid FRP-concrete slab: the validation of the shear strength prediction and design method, the development of a ductile failure mechanism, the study of certain structural details of the slab concept and the extension of the continuous direct load transmission model.

6.3.1 Validation of shear strength prediction and design method

The proposed design concept for hybrid slabs in the span uses the refined fracture mechanics-based shear strength prediction model originally developed by Zink for normal and high performance concrete [Zin00]. This model includes the shear resistance of the fracture process zone (FPZ) and was experimentally validated on 200-mm-deep hybrid specimens with different LC cores. The length of the FPZ is correlated to the LC characteristic length, which was estimated for the experimentally investigated LCs on the basis of an extensive literature review regarding the fracture mechanics properties of similar LCs. These values should be experimentally validated (e.g. by wedge splitting tests), while further sandwich experiments should confirm the design method for hybrid slabs with varying total depths, layer depths and material properties.

The method for predicting the punching resistance of the proposed hybrid slab is derived from the above presented shear strength prediction method and applied on a simplified punching pyramid. This approach is seen as a lower limit approach since a punching resistance increase is expected due to the positively acting membrane forces of the FRP profile. This effect is not taken into consideration at the moment and requires further investigation.

The use of a continuous direct load transmission model is proposed for the prediction of cracking and ultimate loads for direct load transmission next to the supports. This model is represented by a bottle-shaped compressive strut transmitting the compressive force, while tension ties transverse to the strut transmit the tensile forces. The initial arch rise of the compressive strut needs to be calibrated on experimental results. Further experimental investigation of different slab geometries (slab depth and load distance from the support) could give basic information concerning the arch rise input and prevent model calibration.

6.3.2 Development of a ductile failure mechanism

There are three possible ways of achieving a ductile failure of the sandwich slab: through the type of LC core, the choice of face layer materials and geometries or the FRP-LC interface.

- The first possibility is to improve the ductility of the LC core, characterized by the LC characteristic length. Since elongation of the FPZ enhances LC softening behavior and thus creates a more ductile system behavior, an increase of the FPZ length should be further studied. The addition of fibers to LC compositions (e.g. steel and/or polypropylene fibers) and the corresponding failure mechanisms of these LCs should be investigated via further experiments. For this purpose, wedge splitting experiments should be carried out to obtain the fracture energy values necessary for the determination of the characteristic length.

- Secondly, the face layer material properties can be chosen in such a way that a failure of the top concrete layer results. Theoretically, this would be the case in thin slabs with a deep compressive zone, while the slab consists of a top concrete layer exhibiting normal compressive strengths (approximately 50 MPa) and a stiff and high strength CFRP tensile profile in the bottom tensile zone. However, experimental investigations should validate these assumptions.
- The third possibility for creating a ductile failure mechanism was observed in unbonded hybrid specimens comprising a low compressive strength LC core with a comparatively high LC characteristic length, in which failure occurred progressively in the FRP-LC interface under high deformation. To achieve this, the LC compressive strength and T-upstand geometry should be optimized and further investigated in order to provide concrete confinement and prevent shear failure of the webs under loads next to the supports. In view of the intended bridge deck application, the reliance on pure mechanical interlocking requires more research regarding the fatigue and long-term behavior of such interfaces.

6.3.3 Structural details of slab concept requiring further study

The regions of negative moments over the main girders need further investigation. The incorporation of additional GFRP reinforcement grids in the UHPFRC layer has to be studied in the case of the occurrence of high tensile stresses in the top layer. Furthermore, more precise investigation of the transverse joints between the prefabricated slab elements is required. Different joining techniques should be discussed, such as the adhesive bonding of the elements and/or incorporation of mechanical connection systems such as groove and tongue joints along the contact surfaces.

6.3.4 Extension of continuous direct load transmission model

An extension of the continuous direct load transmission model, originally developed for modeling the cracking and ultimate loads of the hybrid FRP-concrete slabs next to the supports, is possible for the span and for any concrete type. This could lead to the creation of one single shear model valid both within the span and next to the supports and applicable on any concrete slab without shear reinforcements. The force flow in the slab is illustrated in Figure 6.1 by a strut-and-tie system: top compressive and bottom tensile forces bear the bending moments, while the shear forces are transferred by diagonal bottle-shaped compressive struts and transverse tensile ties, as indicated in Figure 6.1. Reasonable assumptions regarding the amount and form of the distribution of tensile forces

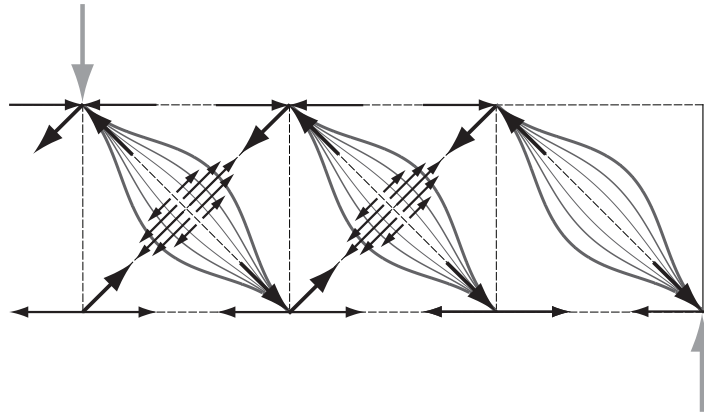


Figure 6.1: Extension of continuous load transmission model.

must be formulated. One possibility is shown in the diagram, where tension is distributed over a quarter of the length of the diagonal with a maximum in the middle of the diagonal. However, these assumptions need to be discussed in more detail in the next stage of the project.

7 Notation

Abbreviations

ACI	– American Concrete Institute
ALWAC	– All Lightweight Aggregate Concrete
CFRP	– Carbon Fiber-Reinforced Polymers
EC	– Eurocode
FRP	– Fiber-Reinforced Polymers
FPZ	– Fracture Process Zone
GFRP	– Glass Fiber-Reinforced Polymers
LC	– Lightweight Concrete
LC900	– LC with rounded density of 900 kg/m ³
LC1300	– LC with rounded density of 1300 kg/m ³
LC1000	– LC with rounded density of 1000 kg/m ³
LC1000A	– LC with rounded density of 1000 kg/m ³ used for beams with anchor blocks
NC	– Normal Weight Concrete
SIA	– Swisscode
SLS	– Serviceability Limit State
SLWAC	– Sand Lightweight Aggregate Concrete
UDL	– Uniformly Distributed Loads
ULS	– Ultimate Limit State
UHPFRC	– Ultra-High Performance Fiber-Reinforced Concrete

Latin upper case letters

A_{frp}	– FRP cross-section
A_{lc}	– LC cross-section
A_{nc}	– NC cross-section
A_{uhpfrc}	– UHPFRC cross-section
C	– compression diagonal force
C_{lc}	– compressive force in the LC layer
C_{nc}	– compressive force in the NC layer

$C_{c,Rm}$	– empirical value based on mean resistances of concrete beams in shear used in EC2
E_{frp}	– mean FRP modulus of elasticity
E_y	– modulus of elasticity in y direction
$E_{lc,m}$	– mean LC modulus of elasticity after 28 days
$E_{nc,m}$	– mean NC modulus of elasticity after 28 days
E_{steel}	– mean modulus of elasticity of steel
EI_{eff}	– effective bending stiffness of a cracked concrete member
$EI_{eff,uncr}$	– effective bending stiffness of an uncracked concrete member
EI_{exp}	– experimented effective bending stiffness
F	– force
F_{cr}	– cracking load
F_u	– ultimate load
F_{exp}	– experimentally measured load
F_{pred}	– predicted load
G_f	– fracture energy
$G_{lc,m}$	– mean LC shear modulus
G_{xy}	– shear modulus
I_i	– moment of inertia of the i -th section
$[K]$	– stiffness matrix of the equilibrium equation
L	– length of the bowed compressive strut used for direct load transmission model
L_i	– Lagrange polynomials to describe the deformation of the strut $w(x)$
M	– bending moment
M_{cr}	– cracking moment
N	– normal force
P_d	– design value for punching load
$Q_{k,i}$	– characteristic concentrated axle load on i -th lane on bridges according to EC and SIA
T	– tensile forces in the ties of a truss model
T_{frp}	– tensile force in the FRP profile
T_{lc}	– tensile force in the LC
T_b	– bursting tensile force in the tie according to Foster [Fos98]
V	– Volume enclosed by the bottle-shaped strut
V_{FPZ} and v_{lc}	– shear resistance of FPZ
V_{lc} and v_{lc}	– shear resistance of LC layer under compression
$V_{lc,Rd}$	– design value of shear resistance of LC beams

$V^*_{lc,Rd}$	– increased design value of punching resistance value
V_{nc} and v_{nc}	– shear resistance of NC layer under compression
V_{uhpfrc} and v_{uhpfrc}	– shear resistance of UHPFRC layer under compression
W_{nc}	– section modulus of the hybrid section at the top of the NC layer
W_{uhpfrc}	– section modulus of the hybrid section at the top of the UHPFRC layer
W_{frp}	– section modulus of the hybrid section at the bottom of the FRP sheet

Latin lower case letters

a	– shear span, distance between load axis and support axis
a/d	– shear span-to-depth ratio
a_i	– distance neutral axis to the center of gravity of i -th layer
b_{FPZ}	– width of the punching pyramid of FPZ
b_{lc}	– width of the punching pyramid of LC layer
b_{uhpfrc}	– width of the punching pyramid of UHPFRC layer
b_w	– width of the concrete member
c	– undeformed length of the strut
c_1	– shortening of the strut
c_2	– deformed length of the strut ($c - c_1$)
c_3	– length of strut shortening perpendicular to the undeformed strut
d	– effective depth of the concrete member
d_{cov}	– depth of road covering
d_{FPZ}	– depth of FPZ
d_{lc}	– depth of LC layer
d_{nc}	– depth of NC layer
d_{uhpfrc}	– depth of UHPFRC layer
$f_{lc,m}$	– mean LC compressive strength on cylinders after 28 days
$f_{lc,k}$	– characteristic LC compressive strength on cylinders after 28 days
$f_{lc,d}$	– design value of NC compressive strength on cylinders after 28 days
$f_{lct,m}$	– mean LC tensile strength on cylinders after 28 days
$f_{lctsp,m}$	– mean LC splitting tensile strength on cylinders after 28 days
$f_{lctfl,m}$	– mean LC flexural tensile strength after 28 days
$f_{frpt,k}$	– characteristic tensile strength of FRP
$f_{uhpfrc,k}$	– characteristic compressive strength of UHPFRC
$f_{uhpfrc,t,k}$	– characteristic tensile strength of UHPFRC
g	– dead weight of a concrete member

h	– height of concrete member
k_3	– coefficient derived from experimental results according to Specht
$k_{i,j}$	– values of the stiffness matrix $[K]$ in the i -th line and j -th row
$\{l\}$	– load vector of the equilibrium equation
l	– total span, support axis to support axis
l_{tot}	– total length of compression diagonal
l_{ch}	– characteristic length of concrete
l_b	– bursting zone of the truss model according to Foster
m_d	– moment design values
p_d	– uniformly distributed shear design values
$q_{k,i}$	– uniformly distributed characteristic load on the i -th line on a bridge according to EC and SIA
r	– exponential factor for accounting material softening
$u_{d,span}$	– design value of maximum deformation of the hybrid slab within the span
u_{cr}	– deformation of the hybrid slab at cracking
u	– horizontal displacement of the strut (in x -direction)
v_{lc}	– uniformly distributed shear resistance of FPZ
v_{lc}	– uniformly distributed shear resistance of LC layer under compression
$v_{lc,Rd}$	– uniformly distributed design value of shear resistance of LC beams
v_{nc}	– uniformly distributed shear resistance of NC layer under compression
v_{uhpfrc}	– shear resistance of UHPFRC layer under compression
$v(x)$	– horizontal displacement of the strut due to compression (in x -direction)
$w(x)$	– vertical deformation of the strut (in y -direction)
w_{crit}	– critical crack opening
x_i	– distance from the neutral axis of the specimen to the gravity center of each layer
$x_{i,uncr}$	– distance from the neutral axis of the specimen to the gravity center of each layer of uncracked concrete member
$y_{0,cr}$	– arch rise of the compressive strut at cracking load at $L/2$
$y_{0,u}$	– arch rise of the compressive strut at ultimate load at $L/2$
y_c	– constant offset of the compressive strut from the diagonal

Greek letters

α	– inclination of the compression diagonal
$\alpha_{q,i}$	– Adjustment factor on i -th lane for uniformly distributed load q
$\alpha_{Q,i}$	– Adjustment factor on i -th lane for concentrated load Q
β_S	– efficiency factor according to ACI
γ_G	– partial safety factor for dead weight
γ_Q	– partial safety factor for traffic loads
γ_M	– partial factor for material resistance
γ_{xy}	– shear distortion of ties
$\gamma_{xy,v}$	– shear distortion of ties due to strut compression
δ	– prefix indicating virtual variation
$\delta\Pi_i$	– variation of the potential of the inner energy
$\delta\Pi_a$	– variation of the potential of the outer energy
ε	– axial strains
η_1	– LC coefficient taking the oven-dry density of the LC in account
θ	– angle of deviation of the compressive strut of the truss model according to Foster
κ	– scale coefficient according to EC 2
κ^*	– alternative scale coefficient proposed from Zink
λ	– shear influence constant
ν	– Poissons' ratio
ψ_G	– reduction coefficient for frequent loading according to SIA 260
Φ_i	– constants to describe the deformation $w(x)$ in the i -th line of the vector $\{\Phi\}$
$\{\Phi\}$	– constants vector of the equilibrium equation
Π_i	– potential of the inner energy
Π_a	– potential of the outer energy
ρ	– rounded density of the LC
ρ_l	– steel reinforcement ratio
ρ_m	– mean density of LC after storage 28 days in a climate room
σ_x	– axial stress in x -direction
σ_y	– axial stress in y -direction
σ_{frp}	– axial stress in the FRP
σ_{lc}	– axial stress in the LC
σ_{nc}	– axial stress in the NC
σ_{uhpfrc}	– axial stress in the UHPFRC
τ_m	– average shear stress of the specimen
τ_{xy}	– shear stress in ties

- $\tau_{xy,v}$ – shear stress in ties due to strut compression
- $\tau_{xz,u}$ – shear strength of concrete at neutral axis

Bibliography

- [ACI03] ACI: *Guide for Structural Lightweight-Aggregate Concrete (ACI 213R-03)*, 2003
- [ACI05] ACI: *Building Code Requirements for Structural Concrete and Commentary. ACI 318-05 and ACI 318R-05*, 2005
- [Ano99] ANON: *Guide to the Structural Use of Adhesives*, 1999
- [ANW92] AL-NAHLAWI, K. A. S. ; WIGHT, J. K.: Beam analysis using concrete tensile strength in truss models. In: *ACI Structural Journal* 89 (1992), no. 3, p. 284–289
- [ASC98] ASCE: ASCE-ACI Committee 445 on Shear and Torsion: Recent approaches to shear design of structural concrete. In: *Journal of Structural engineering* 124 (1998), December, no. 12, p. 1375–1416
- [ASM02] ASM: *Handbook Composites*, 2002
- [Aur71] AURICH, H.: *Kleine Leichtbetonkunde*. Bauverlag, 1971
- [Bat82] BATHE, K. J.: *Finite Element Procedures in Engineering Analysis in Engineering Analysis*. Prentice-Hall, Inc., Englewood Cliffs, 1982
- [BBOR06] BERG, A. C. ; BANK, L. C. ; OLIVA, M. G. ; RUSSELL, J. S.: Construction and cost analysis of an FRP reinforced concrete bridge deck. In: *Construction and Building Materials* 20 (2006), no. 8, p. 515–526
- [BK84] BAZANT, Z. P. ; KIM, J. K.: Size Effect in Shear Failure of Longitudinally Reinforced Beams. In: *Journal of the American Concrete Institute* 81 (1984), September, no. 5, p. 456–468
- [BK07] BAI, Y. ; KELLER, T.: Modeling of post-fire stiffness of E-glass fiber-reinforced polyester composites. In: *Composites Part A: Applied Science and Manufacturing* 38 (2007), no. 10, p. 2142–2153
- [BK08] BAI, Y. ; KELLER, T.: Modal parameter identification for a GFRP pedestrian bridge. In: *Composite Structures* 82 (2008), no. 1, p. 90–100

- [BKN04] BASCHE, H.-D. ; KELLER, C. ; NOVAK, B.: Querkraftwiderstand betonstabbewehrter Bauteile ohne Querkraftbewehrung. In: *Beton- und Stahlbetonbau*, 99 (2004), no. 1, p. 44–51
- [BOR+06] BANK, L. C. ; OLIVA, M. G. ; RUSSELL, J. S. ; JACOBSON, D. A. ; CONACHEN, M. ; NELSON, B. ; MCMONIGAL, D.: Double-layer prefabricated FRP grids for rapid bridge deck construction: Case study. In: *Journal of Composites for Construction* 10 (2006), May, no. 3, p. 204–212
- [Bro02] BROWN, J. L.: Movable Span Deck Replacement Tests Materials' Limits. 72 (2002), February, no. 2, p. 16. – The Magazine of the American Society of Civil Engineers, www.pubs.asce.org. – ISSN 0885–7024
- [Bro05] BROWN, M. D.: *Design for shear in reinforced concrete using strut-and-tie and sectional models*, University of Texas at Austin, Diss., August 2005
- [BTT04] BAYRAMOV, F. ; TASDEMIR, C. ; TASDEMIR, M. A.: Optimisation of steel fibre reinforced concretes by means of statistical response surface method. In: *Cement and Concrete Composites*, 26 (2004), August, no. 6, p. 665–675
- [BVK08] BAI, Y. ; VALLÉE, T. ; KELLER, T.: Modeling of thermal responses for FRP composites under elevated and high temperatures. In: *Composites Science and Technology* 68 (2008), no. 1, p. 47–56
- [BW90] BRÜHWILER, E. ; WITTMANN, F. H.: The wedge splitting test, a new method of performing stable fracture mechanics tests. In: *Engineering Fracture Mechanics* 35 (1990), no. 1/2/3, p. 117–125
- [CHT99] CANNING, L. ; HOLLAWAY, L. ; THORNE, A. M.: An investigation of the composite action of an FRP concrete prismatic beam. In: *Construction and Building Materials* 13 (1999), no. 8, p. 417–426
- [Cla00] CLARKE, J. L.: *The Use of Fibre Composites in Concrete Bridges*. The concrete society, Century House, Telford avenue, Crowthorne Berkshire RG45 6YS : Concrete Bridge developemnt Group, 2000 (Technical Guide No. 3). – ISBN 0 946691 77 0
- [Com01] Comité Européen de Normalisation (CEN): *Eurocode 1 – Actions on structures*. draft nr. 3. June 2001
- [Com04] Comité Européen de Normalisation (CEN): *Eurocode 2 – Design of concrete structures - Part 1.1: General rules and rules for buildings*. EN 1992-1-1. 2004

- [cub] *Cubus AG Zurich, CEDRUS-4, Version 3.02*
- [DMT95a] DESKOVIC, N. ; MEIER, U. ; TRIANTAFILLOU, T. C.: Innovative Design of FRP Combined with Concrete: long term behaviors. In: *Journal of Structural Engineering* 121 (1995), no. 7, p. 1079–1089
- [DMT95b] DESKOVIC, N. ; MEIER, U. ; TRIANTAFILLOU, T. C.: Innovative Design of FRP Combined with Concrete: short term behaviors. In: *Journal of Structural Engineering* 121 (1995), no. 7, p. 1069–1078
- [EHM⁺02] VAN ERP, G. ; HELDT, T. ; MCCORMICK, L. ; CARTER, D. ; TRANBERG, C.: An Australian Approach to Fiber Composite Bridges / University of Southern Queensland, Australia. 2002. – Technical Report
- [ESES06a] EL-SAYED, A. K. ; EL-SALAKAWY, E. F. ; BENMOKRANE, B.: Shear capacity of high-strength concrete beams reinforced with FRP bars. In: *ACI Structural Journal* 103 (2006), no. 3, p. 383–389
- [ESES06b] EL-SAYED, A. K. ; EL-SALAKAWY, E. F. ; BENMOKRANE, B.: Shear strength of FRP-reinforced concrete beams without transverse reinforcement. In: *ACI Structural Journal* 103 (2006), no. 2, p. 235–243
- [Fau03] FAUST, T.: *Leichtbeton im konstruktiven Ingenieurbau*. Berlin: Ernst & Sohn, 2003
- [Fib04] FIBERLINE: *www.fiberline.com*. Website Fiberline Composites A/S, Nr. Bjertvej 88, 6000 Kolding, Denmark, 2004
- [Fis97] FISCHER, J. ; BEUTH (editor): Versagensmodell für schubslanke Balken / Deutscher Ausschuss für Stahlbeton. 1997 (Heft 477). – Technical Report
- [Fos98] FOSTER, S. J.: Design of non-flexural members for shear. In: *Cement and Concrete Composites* 20 (1998), no. 6, p. 465–475
- [FP68] FENWICK, R. C. ; PAULAY, T.: Mechanism of shear resistance in concrete beams. In: *Journal of Structural Division* Proceedings of the American Society of Civil Engineers, 1968, p. 2325–2350
- [FV99] FAUST, T. ; VOIGT, T.: Softening behavior of LWAC by means of wedge splitting tests / Leipzig Annual Civil Engineering Report, LACER No. 4, University of Leipzig,. 1999. – Technical Report

- [GH88] GUSTAFSSON, P. J. ; HILLERBORG, A.: Sensitivity in Shear Strength of Longitudinally Reinforced Concrete Beams to Fracture Energy of Concrete. In: *ACI Structural Journal* 85 (1988), May, no. 3, p. 286–294
- [Gri97] GRIMM, R. ; BEUTH (editor): Einfluss bruchmechanischer Kenngrößen auf das Bieg- und Schubverhalten hochfester Betone / Deutscher Ausschuss für Stahlbeton. 1997 (Heft 477). – Technical Report
- [Gür04] GÜRTLER, H.: *Composite Action of Adhesively Bonded Connections between FRP Bridge decks and Steel Main Girders*. Bât. BP, 1015 Lausanne, Switzerland, Swiss Federal Institute of Technology, Diss., September 2004
- [GV90] GAMBAROVA, P. G. ; VALENTE, G.: Smearred crack analysis for fracture and aggregate interlock in concrete. In: *Engineering Fracture Mechanics* 35 (1990), no. 4-5, p. 651–663
- [HDB06] HABEL, K. ; DENARIÉ, E. ; BRÜHWILER, E.: Structural response of elements combining ultra-high performance fiber-reinforced concretes and reinforced concrete. In: *Journal of Structural Engineering* 132 (2006), no. 11, p. 1793–1800
- [HDB07] HABEL, K. ; DENARIÉ, E. ; BRÜHWILER, E.: Experimental investigation of composite ultra-high performance fiber-reinforced concrete and conventional concrete members. In: *ACI Structural Journal* 104 (2007), no. 1, p. 93–101
- [HH01] HOLLAWAY, L. C. ; HEAD, P. R.: *Advanced Polymer Composites and Polymers in the Civil Infrastructure*. Elsevier, 2001. – ISBN 0–08–043661–7
- [HHT03] HULATT, J. ; HOLLAWAY, L. C. ; THORNE, A.: The use of advanced polymer composites to form an economic structural unit. In: *Construction and Building Materials* 17 (2003), no. 1, p. 55–68
- [Hil83] Kap. Analysis of one Single Crack In: HILLERBORG, A.: *Fracture Mechanics of Concrete*. F. H. Wittmann, Elsevier Science Publishers, Amsterdam, 1983, p. 223–249
- [HM98] HALL, J. E. ; MOTTRAM, J. T.: Combined FRP Reinforcement and Permanent Formwork for Concrete Members. In: *Journal of Composites for Constructions* 2 (1998), no. 2, p. 78–86
- [JPK99] JELIC, I. ; PAVLOVIC, M.N. ; KOTSOVOS, M.D.: Study of dowel action in reinforced concrete beams. In: *Magazine of Concrete Research* 51 (1999), April, no. 2, p. 131–141

- [KAL04] KITANE, Y. ; AREF, A. J. ; LEE, G. C.: Static and fatigue testing of hybrid fiber-reinforced polymer-concrete bridge superstructure. In: *Journal of Composites for Constructions* 8 (2004), no. 2, p. 182–190
- [Kan64] KANI, G. N. J.: The riddle of the shear failure and its solution. In: *Journal of the american concrete institute* (1964), p. 441–467
- [Kan66] KANI, G. N. J.: Basic facts concerning shear failure. In: *Journal of the american concrete institute* (1966), p. 675–693
- [Kan67] KANI, G. N. J.: How safe are our large reinforced concrete beams? In: *Journal of the american concrete institute* (67), March, p. 128–141
- [Kel03] KELLER, T.: *Use of Fibre Reinforced Polymers in Bridge Construction*. International Association for Bridge and Structural Engineering (IABSE), 2003 (Structural Engineering Document 7)
- [Kel06] KELLER, T.: Emerging markets - FRP composites in bridge superstructures. In: *Eighth World pultrusion conference, Emerging markets: globalization of the pultrusion industry, Budapest, Hungary, 2006*
- [KG05a] KELLER, T. ; GÜRTLER, H.: Composite action and adhesive bond between fiber-reinforced polymer bridge decks and main girders. In: *Journal of Composites for Construction* 9 (2005), no. 4, p. 360–368
- [KG05b] KELLER, T. ; GÜRTLER, H.: Quasi-static and fatigue performance of a cellular FRP bridge deck adhesively bonded to steel girders. In: *Composite Structures* 70 (2005), no. 4, p. 484–496
- [KG06a] KELLER, T. ; GÜRTLER, H.: Design of hybrid bridge girders with adhesively bonded and compositely acting FRP deck. In: *Composite Structures* 74 (2006), no. 2, p. 202–212
- [KG06b] KELLER, T. ; GÜRTLER, H.: In-plane compression and shear performance of FRP bridge decks acting as top chord of bridge girders. In: *Composite Structures* 72 (2006), no. 2, p. 151–162
- [Kir87] KIRMAIR, H. ; BEUTH (editor): Das Schubtragverhalten schlanker Stahlbetonbalken / Deutscher Ausschuss für Stahlbeton. 1987 (Heft 385). – Technical Report

- [KN99] KIM, D. ; N., White R.: Arch Action in Reinforced Concrete Beams-A Rational Prediction of Shear Strength. In: *ACI Structural Journal* 96 (1999), no. 4, p. 586–593
- [Kot83] KOTSOVOS, M. D.: Mechanisms of shear failure. In: *Magazine of concrete research* 35 (1983), no. 123, p. 99 –106
- [KP97] KOTSOVOS, M. D. ; PAVLOVIC, M. N.: Size effects in structural concrete: A numerical experiment. In: *Computers and Structures* 64 (1997), July, no. 1-4, p. 285–295
- [KP04] KOTSOVOS, M. D. ; PAVLOVIC, M. N.: Size effects in beams with small shear span-to-depth ratios. In: *Computers and Structures* 82 (2004), January, no. 2-3, p. 143–156
- [KT04] KELLER, T. ; TIRELLI, T.: Fatigue behavior of adhesively connected pultruded GFRP profiles. In: *Composite Structures* 65 (2004), no. 1, p. 55–64
- [KTH06] KELLER, T. ; TRACY, C. ; HUGI, E.: Fire endurance of loaded and liquid-cooled GFRP slabs for construction. In: *Composites Part A: Applied Science and Manufacturing* 37 (2006), no. 7, p. 1055–1067
- [KTZ06a] KELLER, T. ; TRACY, C. ; ZHOU, A.: Structural response of liquid-cooled GFRP slabs subjected to fire - Part I: Material and post-fire modeling. In: *Composites Part A: Applied Science and Manufacturing* 37 (2006), no. 9, p. 1286–1295
- [KTZ06b] KELLER, T. ; TRACY, C. ; ZHOU, A.: Structural response of liquid-cooled GFRP slabs subjected to fire - Part II: Thermo-chemical and thermo-mechanical modeling. In: *Composites Part A: Applied Science and Manufacturing* 37 (2006), no. 9, p. 1296–1308
- [Kup64] KUPFER, H.: *Erweiterung der Mörsch'schen Fachwerkanalogie mit Hilfe des Prinzips vom Minimum der Formänderungsarbeit*. 1964 (40), p. 44–57
- [KV05a] KELLER, T. ; VALLÉE, T.: Adhesively bonded lap joints from pultruded GFRP profiles. Part I: Stress-strain analysis and failure modes. In: *Composites Part B: Engineering* 36 (2005), no. 4, p. 331–340
- [KV05b] KELLER, T. ; VALLÉE, T.: Adhesively bonded lap joints from pultruded GFRP profiles. Part II: Joint strength prediction. In: *Composites Part B: Engineering* 36 (2005), no. 4, p. 341–350

- [KW92] KNOTHE, K. ; WESSELS, H.: *Finite Elemente, eine Einführung für Ingenieure*. Springer Verlag, Berlin/Heidelberg, 1992
- [KZT⁺05] KELLER, T. ; ZHOU, A. ; TRACY, C. ; HUGI, E. ; SCHNEWLIN, P.: Experimental study on the concept of liquid cooling for improving fire resistance of FRP structures for construction. In: *Composites Part A: Applied Science and Manufacturing* 36 (2005), no. 11, p. 1569–1580
- [Leo65] LEONHARDT, F.: Reducing the shear reinforcement in reinforced concrete beams. In: *Magazine of Concrete Research* 17 (1965), no. 53, p. 187–198
- [Lia06] LIAPOR: *www.liapor.com*. Website Liapor GmbH Co. KG, 06
- [Mör23] MÖRSCH, E.: *Der Eisenbetonbau, seine Theorie und Anwendung*. Bd. 1. 6. Wittwer, Stuttgart, 1923
- [Mur98] MURPHY, J.: *Reinforced Plastics*. 2nd. Elsevier Advanced Technology, 1998. – Handbook. – ISBN 1 85617 348 8
- [Pot97] POTTER, K.: *An Introduction to Composite Products*. Chapman and Hall, 1997
- [Rei90] REINECK, K.-H.: *Ein mechanisches Modell für den Querkraftbereich von Stahlbetonbauteilen*, Universität Stuttgart, Diss., 1990
- [Rei91] REINECK, K.-H.: Ultimate shear force of structural concrete members without transverse reinforcement derived from a mechanical model. In: *ACI structural Journal* 88 (1991), Septemeber-October, no. 5, p. 592–602
- [Rem94] REMMEL, G. ; BEUTH (editor): *Zum Zug- und Schubverhalten von Bauteilen aus hochfestem Beton / Deutscher Ausschuss für Stahlbeton*. 1994 (Heft 444). – Technical Report
- [Rit99] RITTER, W.: Die Bauweise Hennebique. In: *Schweizererische Bauzeitung* 33 (1899), no. 7, p. 59–61
- [RKKM03] REINECK, K.-H. ; KUCHMA, D. A. ; KIM, K. S. ; MARX, S.: Shear database for reinforced concrete members without shear reinforcement. In: *ACI Structural Journal* 100 (2003), no. 2, p. 240–249
- [Sei01] SEIBLE, F.: Designing with FRP Composites in the Civil Structural Environment. In: TENG, J.-G. (editor): *FRP Composites in Civil Engineering* Bd. 1, Elsevier Science. Ltd, 2001, p. 73–84

- [SIA03a] SIA: *Betonbau*. Schweizerischer Ingenieur- und Architekten- Verein, 2003
- [SIA03b] SIA: *Einwirkungen auf Tragwerke*. Schweizerischer Ingenieur- und Architekten- Verein, 2003
- [SIA03c] SIA: *Grundlagen der Projektierung von Tragwerken*. Schweizerischer Ingenieur- und Architekten- Verein, 2003
- [SMZH01] SEIBLE, F. ; M., Karbhari V. ; ZHAO, L. ; HOSE, Y.: Development and Implementation of Modular Bridge Systems. In: FIGUEIRAS, J. (editor) ; JUVANDES, L. (editor) ; FARIA, R. (editor): *Composites in Constructions*. Porto, Portugal : A.A. Balkema Publishers, Lisse, October 2001. – Proceedings of the International Conference Composites in Construction - CCC2001, p. 797–802
- [sps04] *Guide to Composites www.spsystems.com*. Website, 2004
- [SS93] Kap. Konstruieren im Stahlbeton In: SCHAICH, J. ; SCHÄFER, K.: *Betonkalender 1993*. Ernst & Sohn, 1993 (2)
- [SS95] SPECHT, M. ; SCHOLZ, H. ; BEUTH (editor): Ein durchgängiges Ingenieurmodell zur Bestimmung der Querkrafttragfähigkeit im Bruchzustand von Bauteilen aus Stahlbeton mit und ohne Vorspannung der Festigkeitsklassen C12 bis C115 / Deutscher Ausschuss für Stahlbeton. 1995 (Heft 453). – Technical Report
- [SS01] Kap. Konstruieren im Stahlbetonbau In: SCHLAICH, J. ; SCHÄFER, K.: *Beton Kalender 2001 Teil II*. Ernst und Sohn, 2001., 2001
- [SSJ87] SCHLAICH, J. ; SCHAEFER, I. ; JENNEWEIN, M.: Toward a Consistent Design of Structural Concrete. In: *PCI Journal* 32 (1987), no. 3, p. 74–150
- [TM92] TRIANTAFILLOU, T.C. ; MEIER, U.: Innovative design of FRP combined with concrete. In: *Advanced Composites Materials in Bridges and structures*, 1992, p. 491–500
- [Unk03] UNKNOWN: Design of Bridges and Highway Structures. UK, December 2003. – Technical Report
- [UO02] UDDIN, A. K. M. F. ; OHTSU, M.: Application of AE to fracture toughness and crack analysis by BEM in concrete. In: *the e-Journal of Nondestructive Testing* 7 (2002), no. 9

- [VDEZS03] VAN DEN EINDE, L. ; ZHAO, L. ; SEIBLE, F.: Use of FRP composites in civil structural applications. In: *Construction and Building Materials* 17 (2003), September, no. 6-7, p. 389–403
- [WDT05] WILLE, K. ; DEHN, F. ; TUE, N. V.: Bruchmechanische Kenngrößen hochfester Leichtbetone. In: *Bauingenieur*, 80 (2005), no. 6, p. 327–333
- [WL94a] WALRAVEN, J. ; LEHWALTER, N.: Size Effects in Short Beams Loaded in Shear. In: *ACI Structural Journal* 91 (1994), September, no. 5, p. 585–593
- [WL94b] WALRAVEN, J. ; LEHWALTER, N.: Size effects in short beams loaded in shear. In: *ACI Structural Journal* 91 (1994), no. 5, p. 585–593
- [WRB⁺88] WITTMANN, F. H. ; ROKUGO, K. ; BRÜHWILER, E. ; MIHASHI, H. ; SIMONIN, P.: Fracture Energy and Strain Softening of Concrete as Determining by Means of Compact Tension Specimens. In: *Materials and Structures/Materiaux et Constructions* 21 (1988), no. 121, p. 21–32
- [Wue07] WUEST, J.: *Comportement structural des bétons de fibres ultra performants en traction dans des éléments composés*. Lausanne, École Polytechnique Fédérale de Lausanne, PhD Thesis, 2007. – Thèse N° 3987
- [YFZ⁺03] YE, L. P. ; FENG, P. ; ZHANG, K. ; LIN, L. ; HONG, W. H. ; YUE, Q. R. ; ZHANG, N. ; YANG, T.: FRP in civil engineering in China: Research and applications. In: H., Tan K. (editor): *Fibre reinforced polymer: reinforcement for concrete structures* Bd. 2, 2003, p. 1401–1412
- [Zin00] ZINK, M. ; STUTTGART, B.G. T. (editor): *Zum Biegeschubversagen schlanker Bauteile aus Hochleistungsbeton mit und ohne Vorspannung*. 2000. – ISBN 3-519-00322
- [ZK05] ZHOU, A. ; KELLER, T.: Joining techniques for fiber reinforced polymer composite bridge deck systems. In: *Composite Structures* 69 (2005), p. 336 – 345

Curriculum Vitæ

Erika Schaumann

Date of birth: March 21st, 1975 in Mainz, D
Nationality: German
E-mail: erika.schaumann@web.de

Education

02/2004 – to date **Ecole Polytechnique Fédérale de Lausanne (EPFL), CH**
PhD student at the Composite Construction Laboratory (CCLab),
thesis: *Hybrid FRP-Lightweight Concrete Slab Systems*

10/1994 - 08/2001 **Technische Universität (TH), Karlsruhe, D**
Graduated as Master in Civil Engineering (Dipl.-Ing.), (1.9)

02/2001 - 08/2001 **Universitat Politècnica de Catalunya (UPC), Barcelona, ES**
Diploma thesis entitled: *Numerical Simulation of the Development
of Thermally Induced Stresses in Young Concrete*, (1.0)

09/1997 - 07/1998 **Institut National des Sciences Appliquées (INSA), Lyon, F**
Sokrates scholarship: exchange year

Work experience

02/2004 - to date **Composite Construction Laboratory (CCLab), Lausanne, CH**
research and teaching assistant, in charge of the project: New Road
Construction Concept (NR2C) of the 6th European Framework Program

11/2001 - 01/2004 **Consulting Engineers Bollinger u. Grohmann GmbH, Frankfurt, D**
Project management, structural design of international projects
e.g. Headquarter building of Dexia-Bil, Luxemburg

10/1998 - 01/2001 **Consulting Engineers Prof. Wenzel u. Partner, Karlsruhe, D**
Internship and part-time work, structural design

04/1999 - 09/1999 **Consulting Engineers Schlaich, Bergermann u. Partner, Stuttgart, D**

Internship as structural engineer
07/1994 - 09/1994 **Construction Company Wiemer u. Trachte, Mainz, D**
Internship on a construction site

Other skills and activities

Languages: German, French (fluent), English (fluent), Spanish (good command)
IT: MS Office, finite element programs (Sofistik, Ansys), mathematical programming (Mathematica, Matlab), current design software
Sports: Skiing (ski trainer: instructor for all levels), cycling, volleyball, mountain sports
Interests: Architecture and design, foreign languages and cultures, friends, networking, music (piano and saxophone)

Selected publications

Keller T, Schaumann E, Vallée T.

Flexural behavior of a hybrid FRP and lightweight concrete sandwich bridge deck,
Composites Part A 2007;38(3);879-889.

Schaumann E, Vallée T, Keller T.

Shear Resistance of lightweight concrete core of FRP-concrete sandwich structure,
ACI Materials Journal, submitted.

Schaumann E, Vallée T, Keller T.

Direct load transmission on hybrid FRP and lightweight concrete sandwich bridge deck,
Composites Part A, 2008;39(3);478-487.

Schaumann E, Vallée T, Keller T.

Modeling of direct load transmission in lightweight concrete core sandwich beams,
ACI Structural Journal, submitted.

Appendix A

Explanation of direct load transfer model

A.1 Description of routine

Equations 4.9–4.24 in Section 4.4.2 are solved using a routine written in Mathematica 5.2. The flow chart in Figure A.1 describes this calculation procedure which is divided into a linear calculation up to the load when the LC splitting tensile strength is reached, followed by a non-linear calculation part up to failure. The routine is used for the determination of either the cracking load, F_{cr} , or the ultimate load, F_u . The first step comprises the input of the material properties ($f_{lct,m}$, $E_{lc,m}$, $G_{lc,m}$, r), of the geometrical values (L , y_c , $y_{0,cr}$, $y_{0,u}$), of the Lagrange polynomials, L_i , and the definition of a starting value of outer load, F_0 . The material properties were taken from Table 4.1 on page 83, while the geometrical values were previously defined in Section 4.4.2.1 and the arch rises are summarized in Table 4.7 on page 101. The starting value of the outer load is defined as $F_0 = 10$ kN. In the routine, the vertical load F is always converted into the strut compression load C by $C = 0.5 \cdot F / \sin\alpha$.

Subsequently, $w(x)$ needs to be determined. As already stated in Section 4.4.2.3, $w(x)$ is described as the combination of orthogonal Lagrange polynomials (Eq. 4.24), see [Bat82] and [KW92]. In commercial FE programs, set of n general polynomials (written as $a_{i,0} + a_{i,1} \cdot x + a_{i,2} \cdot x^2 + \dots + a_{i,n-1} \cdot x^{n-1}$) are used for numerical formulation of the deformed shapes, where the unknowns $a_{i,n-1}$ for $i \in [0, n]$ are determined in the FE algorithm according to the boundary conditions. The Lagrange polynomials allow the reduction of the number of n -independent equations, since these polynomials fit the boundary conditions and the unknowns $a_{i,n}$ are already defined. This approach is used when analytical-numerical solutions are sought. In this routine, three orthogonal Lagrange polynomials are chosen from a set of six typical Lagrange polynomials. For each of these six polynomials only one of the boundary conditions, i.e. $L_i(0)$, $L'_i(0)$, $L_i(L/4)$, $L'_i(L/4)$, $L_i(L/2)$, $L'_i(L/2)$, must be equal to 1, while the remaining five conditions must be 0. For example the three chosen polynomials in Eq. 4.24 fulfill the

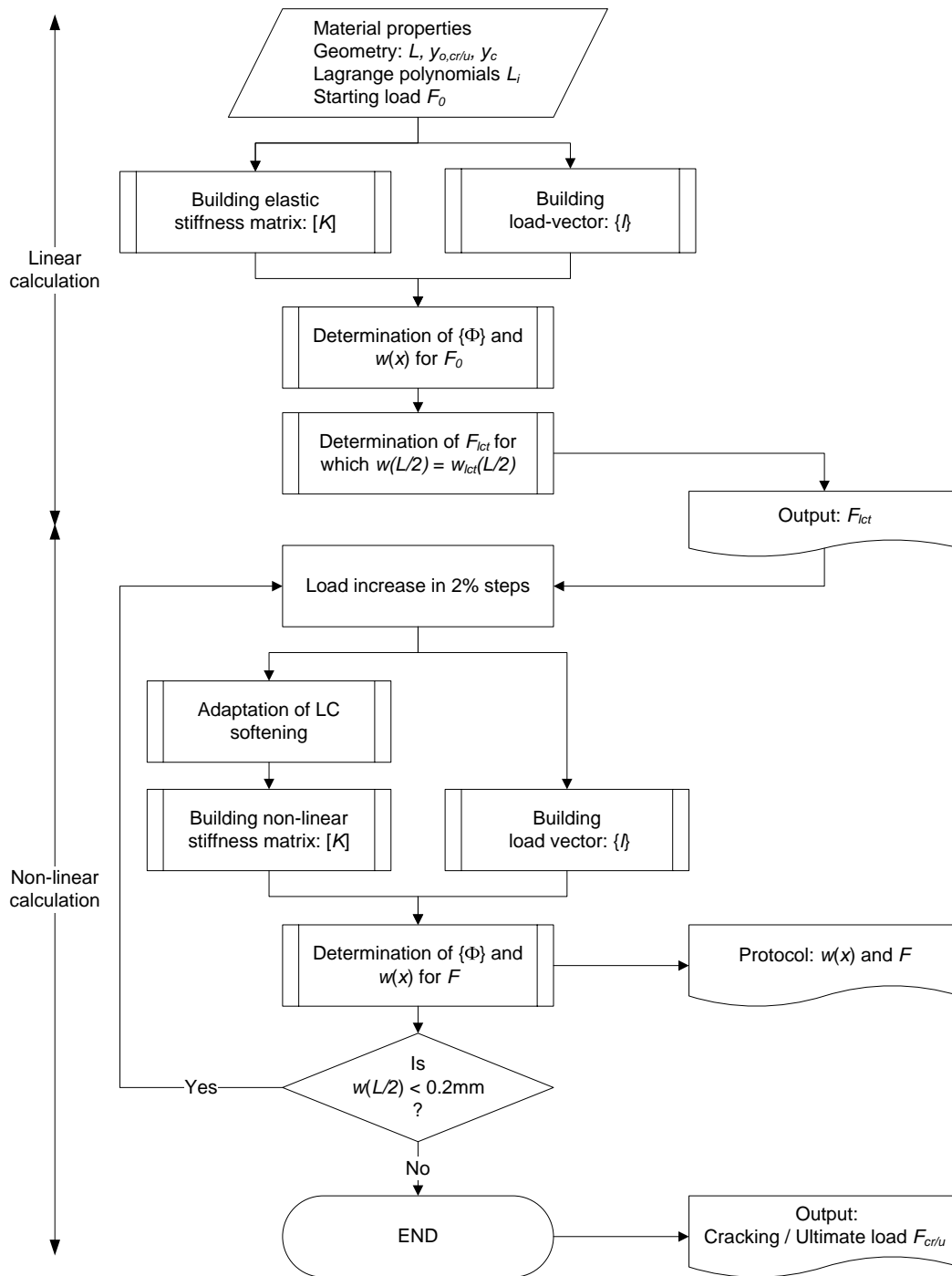


Figure A.1: Calculation process of continuous shear model.

following boundary conditions:

$$\begin{aligned}
L_1(L/4) = 1 \quad \text{while} \quad L_1(0) = L_1'(0) = L_1'(L/4) = L_1(L/2) = L_1'(L/2) = 0 \\
L_2'(L/4) = 1 \quad \text{while} \quad L_2(0) = L_2'(0) = L_2(L/4) = L_2(L/2) = L_2'(L/2) = 0 \\
L_3(L/2) = 1 \quad \text{while} \quad L_3(0) = L_3'(0) = L_3(L/4) = L_3'(L/4) = L_3(L/2) = 0
\end{aligned} \tag{A.1}$$

Mechanically formulated, $L_1(x)$ describes symmetrical deformations and restrains the strut at $x=0$, while $L_2(x)$ describes antimetrical deformations and restrains the strut at the beginning and end, and $L_3(x)$ describes free displacement at $x = L/2$.

In order to then determine the deformation $w(x)$, or more precisely the constants Φ_i , the equilibrium equation 4.10 on page 95 must incorporate the polynomial formulation of $w(x)$ and $\delta w(x)$ (Eqs. 4.22 and 4.23 on page 99) as follows:

$$\begin{aligned}
\delta\pi_i + \delta\pi_o &= \int_V E_y \cdot \frac{\sum_{i=1}^n \Phi_i \cdot L_i(x)}{y(x)} \cdot \frac{\sum_{j=1}^n \delta\Phi_j \cdot L_j(x)}{y(x)} dV \\
&+ \int_V G_{xy} \cdot \sum_{i=1}^n \Phi_i \cdot L_i'(x) \cdot \sum_{j=1}^n \delta\Phi_j \cdot L_j'(x) dV \\
&+ C \cdot 2 \int_0^{L/2} y'(x) \cdot \sum_{j=1}^n \delta\Phi_j \cdot L_j'(x) dx \\
&= \sum_{i=1}^n \sum_{j=1}^n \delta\Phi_j \cdot \left[\left(\int_V E_y \cdot \frac{L_i(x)}{y(x)} \cdot \frac{L_j(x)}{y(x)} dV + \int_V G_{xy} \cdot L_i'(x) \cdot L_j'(x) dV \right) \cdot \Phi_i \right. \\
&\quad \left. + C \cdot 2 \int_0^{L/2} y'(x) \cdot L_j'(x) dx \right] = 0
\end{aligned} \tag{A.2}$$

In Eq. A.2 the virtual displacement, $\delta\Phi_j$, can be cancelled down, so that for each $j \in [1; 3]$ the following Eq. A.3 must be fulfilled:

$$\begin{aligned}
\sum_{i=1}^n \left[\left(\int_V E_y \cdot \frac{L_i(x)}{y(x)} \cdot \frac{L_j(x)}{y(x)} dV + \int_V G_{xy} \cdot L_i'(x) \cdot L_j'(x) dV \right) \cdot \Phi_i + C \cdot 2 \int_0^{L/2} y'(x) \cdot L_j'(x) dx \right] = 0 \\
\text{for } j \in [1; 3]
\end{aligned} \tag{A.3}$$

In the routine, the set of j -equations is expressed in matrix formulation as written in Eq. A.4:

$$[K] \times \{\Phi\} + \{l\} = 0 \tag{A.4}$$

where $[K]$ = the stiffness matrix (corresponding to the first two parts of Eq. A.3), $\{\Phi\}$ = the vector of the constants, which is the unknown in the equation, and $\{l\}$ = the load vector (corresponding to the last part of Eq. A.3). The matrix formulation of the previous equation for $n = 3$ (with $k_{i,j}$ for $i, j \in [1; 3]$) is given in Figure A.2.

$$\begin{bmatrix} k_{11} & k_{12} & k_{13} \\ k_{21} & k_{22} & k_{23} \\ k_{31} & k_{32} & k_{33} \end{bmatrix} \times \begin{Bmatrix} \Phi_1 \\ \Phi_2 \\ \Phi_3 \end{Bmatrix} + \begin{Bmatrix} l_1 \\ l_2 \\ l_3 \end{Bmatrix} = \mathbf{0}$$

Figure A.2: Matrix formulation of the equilibrium condition.

Using Eqs. A.3 and A.4, the stiffness matrix, $[K]$, and the load vector, $\{l\}$, can be built up as described for $k_{1,2}$ and l_1 for example:

$$k_{1,2} = \int_V E_y \cdot \frac{L_1(x)}{y(x)} \cdot \frac{L_2(x)}{y(x)} dV + \int_V G_{xy} \cdot L'_1(x) \cdot L'_2(x) dV \quad (\text{A.5})$$

$$l_1 = C \cdot 2 \int_0^{L/2} y'(x) \cdot L'_1(x) dx \quad (\text{A.6})$$

Subsequently, the linear calculation part of the routine can be started. In a first step, the constants Φ_i , and thus $w(x)$, are determined for the starting load F_0 . This is followed by the determination of $w_{lct}(x)$ (see Eq. 4.19 on page 97) and the load, F_{lct} , at which uniaxial LC tensile strength is reached at the middle of the strut, i.e. $w(L/2) = w_{lct}(L/2)$. The value of F_{lct} is saved as the first output.

Subsequently, the non-linear calculation part starts and E_y and G_{xy} in Eq. A.3 are no longer constant but now include the softening behavior of the materials. The load is then increased stepwise in increments of 2%, which has been found to be a reasonable increase as smaller steps do not effect significant changes (i.e. changes $\leq 5\%$) in the results. At the end of each load step, the load, F , and the corresponding deformation, $w(x)$, is recorded. If $w(L/2)$ is lower than 0.2 mm, further load steps are applied and the calculation process is continued until the deformation in the middle of the strut exceeds 0.2 mm. The corresponding load defines the cracking load, F_{cr} , or ultimate load, F_u . The output F_{cr} or F_u is recorded and the calculation is stopped.

A.2 Influence of strut compression on results

As stated in Section 4.4.2.1, the influence of compression or shortening of the strut on strut deformation results, $w(x)$, and corresponding loads, F , can be disregarded. The justification for this assumption is given in the following. Therefore, calculations are performed including an additional degree of freedom in x -direction, $v(x)$ and $\delta v(x)$, which are defined by a fourth constant Φ_4 and $L_4(x)$ as follows:

$$v(x) = \Phi_4 \cdot L_4(x) \quad ; \quad \delta v(x) = \delta \Phi_4 \cdot L_4(x) \tag{A.7}$$

Here, $L_4(x) = x/L$ is chosen, assuming that the shortening is constantly increasing along the diagonal with a maximum value at the strut end. Equations A.2–A.4 must be rewritten, including the variation in inner and outer potential energy due to strut shortening. The new equilibrium equation is again formulated by the sum of the variation of inner and outer potential energy:

$$\begin{aligned} \delta \pi_i + \delta \pi_o = & \int_V \sigma_y \cdot \delta \varepsilon_y dV + \int_V \tau_{xy} \cdot \delta \gamma_{xy} dV + \int_V \sigma_x \cdot \delta \varepsilon_x dV \\ & + C \cdot (\delta u + \delta v) = 0 \end{aligned} \tag{A.8}$$

where the variation in inner energy is now composed of three parts: the first part = stresses and virtual strains in y -direction, the second part = shear and virtual distortion, and the third part = stresses and virtual strains in x -direction, and the variation in the outer potential energy is described by the product of the load, C , and the sum of δv and δu .

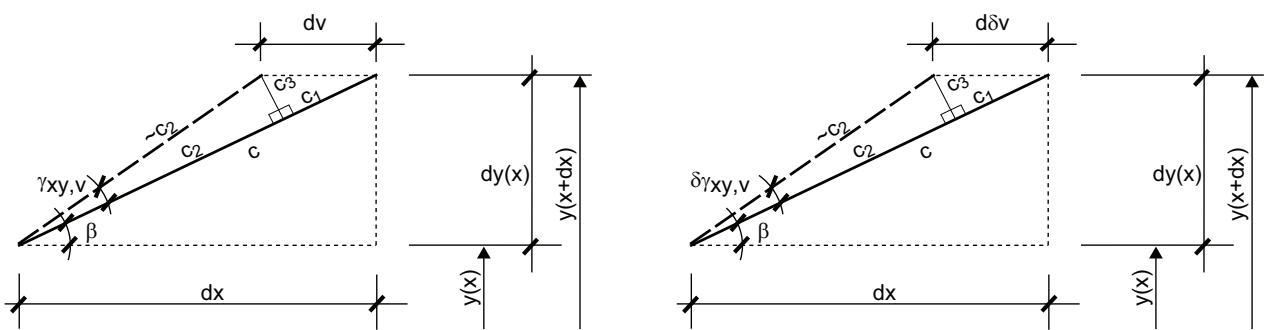


Figure A.3: Real (left) and virtual (right) kinematic relationships due to strut shortening used to determine $k_{4,4}$.

The shear stresses and distortions in the second part of Eq. A.8 result either from δu (τ_{xy} and γ_{xy} according to Eqs. 4.16 and 4.17 on page 97) or from the shortening δv . Accordingly, $\tau_{xy,v}$ is calculated from the LC shear modulus, G_{xy} , and the corresponding shear distortion,

$\gamma_{xy,v}$, defined according to Figure A.3 and Eq. A.9:

$$\tau_{xy,v} = G_{xy} \cdot \gamma_{xy,v} \simeq G_{xy} \cdot \frac{c_3}{c_2} = G_{xy} \cdot \frac{c_3}{c - c_1} = G_{xy} \cdot \frac{\sin\beta \cdot dv}{\frac{1}{\cos\beta} \cdot dx - \cos\beta \cdot d\delta v} \quad (\text{A.9})$$

The virtual distortions, $\delta\gamma_{xy,v}$, are calculated accordingly:

$$\delta\gamma_{xy,v} \simeq \frac{\sin\beta \cdot d\delta v}{\frac{1}{\cos\beta} \cdot dx - \cos\beta \cdot d\delta v} \quad (\text{A.10})$$

where c_2 = the strut increment length minus the shortening, which is equal to the deformed strut increment length, and c_3 = length according to Figure A.3.

In the third part of the equation, σ_x = axial stresses in x -direction and $\delta\varepsilon_x$ = virtual axial strains in x -direction. The axial stresses are defined by the following equation:

$$\sigma_x = E_x \cdot \varepsilon_x = E_x \frac{c_1}{c} \simeq E_x \frac{v}{L} = E_x \frac{dv}{dx} = E_x v' \quad (\text{A.11})$$

where E_x = the Young's modulus in x -direction (assumed as $E_{l_{c,m}}$), c = the length of the undeformed strut increment and c_1 = the shortening of c as indicated in Figure A.3. In this figure, the undeformed shape is represented with a constant line, while the deformed shape is illustrated with a dashed line. Accordingly, the virtual axial strains are defined by:

$$\delta\varepsilon_x = \frac{\delta v}{dx} = \delta v' \quad (\text{A.12})$$

To determine the constants Φ_i for $i \in [1;4]$ and thus the strut deformation $w(x)$ and corresponding loads, F , the equilibrium equation Eq. A.8 is expressed in matrix formulation for $i, j \in [1;4]$ as illustrated in Figure A.4. The values of the first three columns and lines

$$\begin{array}{c} \overbrace{}^{w(x)} \quad \overbrace{}^{v(x)} \\ \delta w(x) \left\{ \begin{array}{c} \left[\begin{array}{ccc|c} k_{11} & k_{12} & k_{13} & k_{14} \\ k_{21} & k_{22} & k_{23} & k_{24} \\ k_{31} & k_{32} & k_{33} & k_{34} \\ \hline k_{41} & k_{42} & k_{43} & k_{44} \end{array} \right] \times \begin{Bmatrix} \Phi_1 \\ \Phi_2 \\ \Phi_3 \\ \Phi_4 \end{Bmatrix} + \begin{Bmatrix} l_1 \\ l_2 \\ l_3 \\ l_4 \end{Bmatrix} = \mathbf{0} \end{array} \right. \\ \delta v(x) \left\{ \end{array} \right.$$

Figure A.4: Matrix formulation of equilibrium condition by including Φ_4 .

in the stiffness matrix, $k_{i,j}$ for $i, j \in [1;3]$, correspond to the combination of real stresses and virtual strains, both due to the displacement δu . The values $k_{i,j}$ for $i, j \in [1;3]$ are expressed by $w(x)$ and $\delta w(x)$ as written in Eq. 4.21 and shown in Figures 4.9 and 4.10 on page 96.

They are hence independent of δv and composed of the two first parts of the variation in inner potential energy in Eq. A.8.

In contrast, the value $k_{4,4}$ is the combination of real stresses and virtual strains, both due to the shortening of the strut, as shown in Figure A.3. Due to the horizontal deformation in x -direction the compressive strut is reduced by the length of c_1 and subjected to a distortion of $\gamma_{xy,v}$. The length of the ties remains unchanged, i.e. no elongation occurs in y -direction, so that $k_{4,4}$ is only composed of the last two parts of the variation in inner potential energy in Eq. A.8.

The values in the fourth row $k_{i,4}$ for $i \in [1;3]$ are the combination of real stresses due to the displacement u and virtual strains due to shortening of the strut δv , expressed by $w(x)\delta v$, as shown in Figure A.4. Accordingly, the values in the fourth line $k_{4,j}$ for $j \in [1;3]$

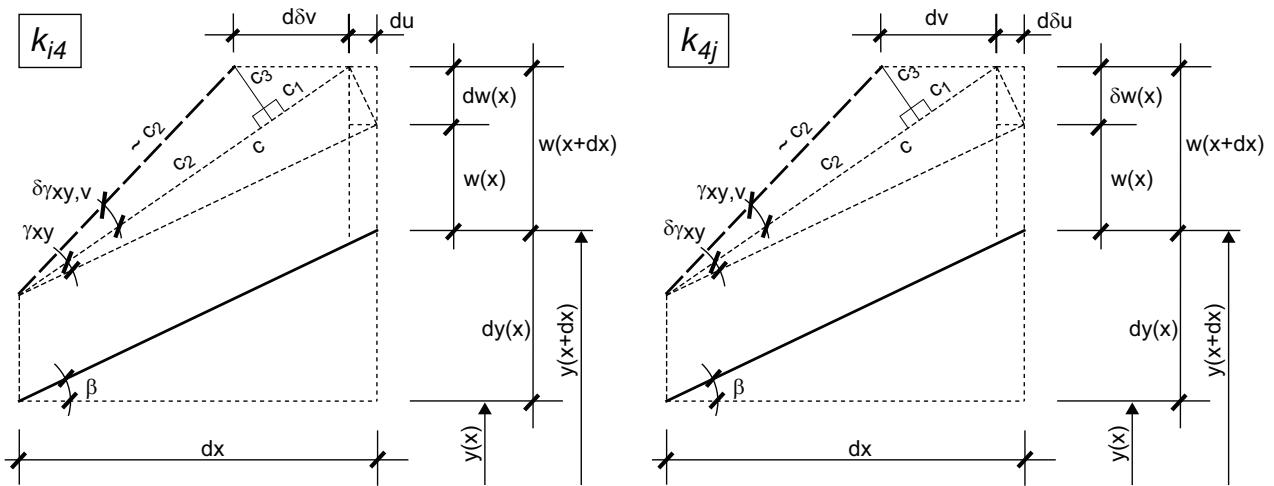


Figure A.5: Kinematic relationships due to strut shortening used to determine $k_{i,4}$ and $k_{4,j}$.

are the combination of real stresses due to shortening of the strut v and virtual strains due to the displacement δu , expressed by $\delta w(x)v$, see also Figure A.4. The kinematic relationships for the former are shown in Figure A.5 (left), while those for the latter are shown on the right. Neither would cause elongations in the ties (i.e.axial stresses/strains in y -direction) nor shortening in the strut (i.e.axial stresses/strains in x -direction). Hence, the values $k_{i,4}$ for $i \in [1;3]$ (and $k_{4,j}$ for $j \in [1;3]$) are only composed of the second part of the variation in inner potential energy in Eq. A.8 - the combination of shear stresses and virtual distortions.

By solving Eq. A.8, it can be shown that the loads are slightly higher (by less than 8%) than the results obtained by disregarding the strut shortening. The ultimate loads of three representative beam specimens are given in Table A.1. Disregarding the strut shortening hence offers a safety margin due to slight underestimation of specimen capacity. Since the

Table A.1: Specimen ultimate loads, without and with incorporation of the strut shortening.

Specimen	Ultimate load if considering δu [kN]	Ultimate load if considering δu and δv [kN]	Ratio [-]
900Es-1	98	105	1.07
1300Es-1	204	219	1.07
1000E	201	213	1.06

variation in results is less than 8%, it was reasonable to disregard strut shortening. This disregard also allows a less complex calculation procedure.